



University of
Sheffield

**Multi-Material Metal Powder Bed Binder Jetting Using PVA
Binder**

Hussam Abed H Abunar

This thesis is submitted in a partial fulfilment of the degree of
Doctor of Philosophy

The University of Sheffield
Faculty of Engineering
Department of Mechanical Engineering

December 2023

Declaration of Intent

In the pursuit of academic integrity and scholarly accuracy, I affirm that all sentences or passages extracted from external sources in this document have been acknowledged through precise cross-referencing, providing due credit to the respective author, work. Furthermore, any visual representations not originating from the author of this thesis have been appropriately cited, acknowledging and attributing credit to the respective illustrator.

I sincerely declare that the content presented in this thesis, in its entirety, has not been proffered for consideration for any other degree at any other educational institution. It is a unique and original contribution to the field, representing the result of my independent scholarly efforts.

I am cognizant of and commit to upholding the rules and regulations set forth by the University of Sheffield concerning plagiarism. I understand that any deviation from these guidelines would compromise the academic integrity of this work. In acknowledging these responsibilities, I affirm my commitment to the highest standards of academic honesty and ethical conduct throughout the duration of my academic pursuits at the University of Sheffield.

Hussam Abunar,

December 2023

Sheffield, South Yorkshire, UK

Acknowledgements

Foremost, I extend my gratitude to Allah the Almighty, the Most Gracious, and the Most Merciful, acknowledging His blessings that have illuminated my academic journey and resulted in the completion of this scholarly endeavour.

I am grateful to Professor Kamran A Mumtaz, my esteemed supervisor, for not only granting me the opportunity to collaborate but also for his constructive insights, invaluable suggestions, and consistent guidance throughout my PhD journey. His unwavering support has not only alleviated the challenges faced but has also significantly contributed to my professional and personal growth.

Also, I must express deep appreciation to my family—my parents, Hala Ismail and Abed Abunar, and my brothers, Hassan, Mohannad, and Meshal. Their enduring support and unconditional love have been the bedrock of my resilience in a journey that often led me far from the familiarity and comfort of home.

Continuing on the theme of familial support, my heartfelt gratitude extends to my beloved wife, Nura, and Two gorgeous daughters Wateen and Yaqeen. Their unwavering spiritual support, encouraging words, timely assistance, and remarkable patience during periods of separation have been indispensable to the successful completion of this researcher.

Further navigating through this intellectual expedition, I must acknowledge the fundamental guidance and unwavering support provided by my respected colleagues, Dr. Abdullah Alharbi and Dr. Mohammed Alsaddah, who have been steadfast companions on this doctoral research journey.

Special recognition is due to Dr. Abdullah Alsari and Mr. Andi Xie for their generous support in the realm of chemical characterization integral to this work. Their consistent assistance has been a cornerstone of progress in my research. Additionally, I express my thanks to friends Dr. Asim Alsenani, Faisal Alhedyan, Motaz Deebes, Zaher Alshehri and Mohammed Alotaibi for their collaborative efforts in finalizing this thesis—each playing a crucial role that is highly appreciated.

Beyond the academic sphere, the support received from the staff and fellow PhD candidates at the Royal Exchange Building has been instrumental in overcoming challenges encountered during my academic journey.

Additionally, to my dear friends in Sheffield, I extend heartfelt appreciation for their continuous support and encouraging words throughout my Ph.D. tenure. Their unwavering encouragement has not only been a source of motivation but also a testament to the strength of camaraderie that enriches the academic experience.

Lastly, I would like to express my gratitude to those who underestimated my parents, one day. Their scepticism served as the catalyst that fuelled my determination to prove them wrong. Through the unwavering support and guidance of my parents, I found the strength and resilience to overcome challenges and surpass expectations.

Abstract

This research presents a study of a novel multi-material deposition system developed for the deposition of powder and the creation of components using the Binder Jetting approach to print stainless steel and copper multi-material parts that can be used in thermal management applications. Experimental investigations into deposition nozzle diameter, head movement speed, and ultrasonic power levels of the novel multi-material deposition system reveal the effects on powder deposition heaps, establishing a correlation between ultrasonic power levels and powder heap characteristics. The derived regression equation is validated, affirming its accuracy. Polyvinyl Alcohol (PVA) is explored as a binder material, with emphasis on concentration, wettability, and thermal behaviour. Optimal structural strength and rapid powder bed infiltration are achieved with a 5% PVA concentration dissolved in deionized water. Furthermore, 38 sintering cycles have been conducted to study the dynamic interaction between 316L stainless steel and copper. Iterative adjustments in temperature and dwelling times ensure precision in parameter control, addressing challenges and maintaining structural integrity. The study extends to the evaluation of porosity as a process response, highlighting the critical importance of optimizing sintering conditions for different materials. An examination of the 316L and Cu bonding interface reveals good metallurgical bonding, supported by compositional analysis through Scanning Electron Microscopy (SEM) and Energy Dispersive X-ray Spectroscopy (EDS). Tensile testing underscores high bond strength, with brittleness in 316L and Cu components attributed to insufficient sintering. The result of this

research endeavour materialized in the successful development of a pioneering multi-material deposition system, consequently achieving a milestone in the fabrication of metal multi-material binder jetted components. Moreover, the thorough optimization of building process parameters encompassing speed, nozzle diameter, and ultrasonic power, coupled with judicious binder optimization and improved heating cycles, led to the fabrication of solid binder-jetted components made of two distinct materials characterized by disparate thermal properties. The study resulted in outcomes that show a good bonding interface between the two distinct materials. The multi-material components exhibited nearly 98% density, good interlayer connection, and improved tensile properties to copper itself, affirming the success of the proposed approach.

Table of Contents

CHAPTER 1. INTRODUCTION	1
1.1 MOTIVATION	1
1.2 AIM AND OBJECTIVES.....	3
1.3 NOVELTY STATEMENT.....	4
1.4 THESIS STRUCTURE.....	6
CHAPTER 2. LITERATURE REVIEW.....	7
2.1 ADDITIVE MANUFACTURING	7
2.1.1 <i>Basic Concepts</i>	8
2.1.2 <i>Techniques</i>	9
2.2 METAL ADDITIVE MANUFACTURING PROCESSES	10
2.2.1 <i>Binder Jetting (BJ)</i>	13
2.2.1.1 <i>Binder material</i>	20
2.2.1.2 <i>Rheological Characterisation of the Binder</i>	25
2.2.1.3 <i>Binder Burnout</i>	28
2.2.1.4 <i>Sintering</i>	29
2.2.2 <i>Laser Powder Bed Fusion</i>	32
2.2.3 <i>Directed Energy Deposition (DED)</i>	35
2.2.4 <i>Powder blown Laser Cladding (PBLCL)</i>	36
2.2.5 <i>Extrusion</i>	37
2.3 POROSITY IN ADDITIVE MANUFACTURING PROCESSES	39
2.4 MULTI-MATERIAL ADDITIVE MANUFACTURING	44
2.4.1 <i>Material Building Categories</i>	44
2.5 MULTI-MATERIAL ADDITIVE MANUFACTURING ACHIEVEMENTS.....	46
2.5.1 <i>Nonmetallic Multi-material Achievements</i>	46
2.5.1.1 <i>Vat Photopolymerization - Stereolithography (SL)</i>	46
2.5.1.2 <i>Material Jetting</i>	49
2.5.1.3 <i>Extrusion</i>	51
2.5.2 <i>Metallic Multi-material Achievements</i>	54

2.5.2.1	<i>Powder blown Laser Cladding</i>	54
2.5.2.2	<i>Powder bed fusion AM processes</i>	59
2.6	COMPARISON OF THE MULTI-MATERIAL ADDITIVE MANUFACTURING PROCESSES	69
2.7	APPLICATIONS OF MULTI-MATERIAL	70
2.8	MATERIAL POWDER DISPENSING MECHANISM.	73
2.9	SUMMARY OF LITERATURE REVIEW.....	77
CHAPTER 3. EXPERIMENTAL SETUP		79
3.1	MATERIALS	79
3.1.1	<i>Powder Material</i>	79
3.1.2	<i>Binder Material</i>	83
3.2	DESIGNING THE MULTI-MATERIAL POWDER DEPOSITION SYSTEM (MMPDS)	84
3.3	THE MULTI-MATERIAL POWDER DEPOSITION SYSTEM VALIDATION.....	89
3.4	MULTI-MATERIAL BINDER JETTING SYSTEM.....	91
3.5	POST-PROCESSING OF THE GREEN PARTS	93
3.6	SAMPLES CHARACTERISATION	94
3.6.1	<i>Preparation for Optical Microscopy</i>	94
3.6.2	<i>Porosity Analysis</i>	95
3.6.3	<i>Microstructure Characterization</i>	95
3.6.4	<i>Mechanical Tensile Testing</i>	96
CHAPTER 4. OPTIMIZATION OF THE POWDER MULTI-MATERIAL DEPOSITION SYSTEM		97
4.1	INTRODUCTION	97
4.1.1	<i>Powder Deposition Resolution</i>	100
4.1.2	<i>Design of Experiment Analysis</i>	100
4.2	RESULTS AND DISCUSSIONS	103
4.2.1	<i>Powder Deposition Resolution</i>	104
4.2.1.1	<i>Deposition trials without flattening wiper</i>	104
4.2.1.2	<i>Deposition trials with a round flattening wiper</i>	118
4.2.2	<i>Comparison of Deposited Heap Results with and without Flattening Wiper</i>	126

4.2.2.1	Utilizing a 1 mm nozzle	126
4.2.2.2	Utilizing a 0.8 mm nozzle	129
4.2.3	Full Factorial Analysis	131
4.2.4	Regression Validation	134
4.3	CONCLUSIONS	137
CHAPTER 5. BINDER SELECTION AND CHARACTERISATION		139
5.1	INTRODUCTION	139
5.1.1	PVA Concentration and Wettability Analysis.....	142
5.1.2	Thermal Characterisation of the Prepared Binder	145
5.2	RESULTS AND DISCUSSIONS	146
5.2.1	PVA Concentration and Wettability Analysis.....	146
5.2.2	Thermogravimetric Analysis of the Prepared Binder	149
5.2.3	Binder's Viscosity.....	151
5.2.4	Binder's Surface Tension	153
5.2.5	Ohnesorge Number	154
5.2.6	Z-number.....	155
5.3	CONCLUSIONS	156
CHAPTER 6. BINDER JETTING PROCESS AND PRINTING PARTS		158
6.1	INTRODUCTION	158
6.1.1	PRINTING PROCESS	161
6.1.2	SINTERING CYCLES	164
6.2	RESULTS AND DISCUSSIONS	167
6.2.1	PRINTING USING 0.6MM AND 0.1MM BINDER DEPOSITION NOZZLE.	167
6.2.2	PRINTING PARTS IN DIFFERENT BUILDING DIRECTIONS	170
6.2.3	CURING AND SINTERING CYCLES	172
6.3	CONCLUSIONS	182
CHAPTER 7. EVALUATION OF POROSITY IN SINTERED PARTS		183
7.1	INTRODUCTION	183
7.2	RESULTS AND DISCUSSIONS	185

7.3	CONCLUSIONS.....	200
CHAPTER 8. INTERLAYER CONNECTION AND TENSILE PROPERTIES OF THE MULTI-MATERIAL SINTERED PARTS		201
8.1	INTRODUCTION	201
8.2	RESULTS AND DISCUSSIONS.....	202
8.2.1	INTERFACIAL CHARACTERISTICS	202
8.2.2	TENSILE PROPERTIES	208
8.3	CONCLUSIONS.....	213
CHAPTER 9. CONCLUSIONS AND FUTURE WORK		214
9.1	CONCLUSIONS.....	214
9.2	PROPOSED AREAS OF FUTURE WORK.....	219
CHAPTER 10. REFERENCES		221
CHAPTER 11. APPENDICES.....		235
11.1	BUILDING PLATFORM BED DRAWINGS	235
11.2	SONOTRODE CALCULATIONS.....	236
11.3	SONOTRODE DRAWINGS	237
11.4	ROUND WIPER DRAWINGS.....	238
11.5	CALCULATIONS OF THE SPEED RATE ASSOCIATED WITH EACH PARAMETER SET FOR THE REGRESSION VALIDATIONS.....	239
11.6	OHNESORGE NUMBER CALCULATIONS FOR 0.1- AND 0.6-MM NOZZLE DIAMETERS	241

List of Figures

FIGURE 2.1: DIVISION OF THE AM TECHNOLOGY UNDER THE AMERICAN SOCIETY FOR TESTING AND MATERIALS (ASTM)....	9
FIGURE 2.2: AM TECHNOLOGIES WORK UNDER POWDER BED SYSTEM, POWDER FEED SYSTEM, AND WIRE FEED SYSTEM.....	10
FIGURE 2.3: A SCHEMATIC REPRESENTATION OF A CONVENTIONAL BINDER JET SYSTEM.....	13
FIGURE 2.4: SHOWS THE BINDER JETTING AM PROCESS CHAIN TO FABRICATE A PART	14
FIGURE 2.5: A 3D BINDER JETTED MOULD WAS PRINTED AND THEN EMPLOYED FOR CASTING COMPONENTS.	15
FIGURE 2.6: A SIDE VIEW OF THE 70 MM OF BINDER JETTED INCONEL PARTS, SUGGESTING MELTING AND SHAPE ALTERATION, IN CONTRAST TO THE 21 MM SAMPLE	17
FIGURE 2.7: 316L SS BINDER JETTED SOLID LATTICE.....	18
FIGURE 2.8: A BINDER JETTED OF COPPER COMPONENT WITH (A) A SATURATION RATIO OF 150% AND (B) A SATURATION RATIO OF 75%	18
FIGURE 2.9: A BINDER JETTED OF 420 STAINLESS STEEL COMPONENTS	18
FIGURE 2.10: (A) STAGE OF DENSIFICATION AND GRAIN GROWTH (B) FINAL STAGE WITH CLOSED PORE SPACES	30
FIGURE 2.11: A SCHEMATIC REPRESENTATION OF A LASER POWDER BED FUSION (LPBF) PROCESS	33
FIGURE 2.12: A SCHEMATIC REPRESENTATION OF A WIRE FILAMENT-BASED DIRECTED ENERGY DEPOSITION PROCESS	35
FIGURE 2.13: A SCHEMATIC REPRESENTATION OF POWDER BLOWN LASER CLADDING (PBLCL)	36
FIGURE 2.14: A SCHEMATIC ILLUSTRATION OF A METAL EXTRUSION-BASED AM PROCESS, AS ADAPTED FROM.....	38
FIGURE 2.15: DIFFERENT BUILDING ADDITIVELY MANUFACTURED PARTS CATEGORIES OF SINGLE AND MULTI-MATERIAL	45
FIGURE 2.16: PHOTO-POLYMERIZATION-BASED STEREOLITHOGRAPHY PROCESS OF BUILDING POLYMERIZED PARTS.....	46
FIGURE 2.17: MULTI-MATERIAL STEREOLITHOGRAPHY PROCESSING BY ROTATING VAT CAROUSEL SYSTEM.....	47
FIGURE 2.18: TWO DIFFERENT MULTI-MATERIAL ROOKS WERE BUILT USING THE MMSL PROCESS	48
FIGURE 2.19: AN ILLUSTRATION OF THE INK JETTING PROCESS, CHARACTERIZED BY MULTIPLE NOZZLES DISPENSING ZrO ₂ INK AS A BUILDING MATERIAL AND SUPPORT INKS.....	49
FIGURE 2.20: BUILDING A MULTI-MATERIAL REPLICA OF A CEREBRAL ANEURYSM FROM A PERSON.....	50
FIGURE 2.21: THREE MULTI-MATERIAL EMBEDDED FUNCTIONAL ELECTRONIC CIRCUITS OBJECTS	51
FIGURE 2.22: A SCHEMATIC DIAGRAM OF THE MULTI-HEAD TISSUE/ORGAN BUILDING SYSTEM.....	53
FIGURE 2.23: A SCHEMATIC DIAGRAM OF THE MULTI-HEAD TISSUE/ORGAN SAMPLES.....	53
FIGURE 2.24: DEPOSITING OF PRE-MIXED MULTI-MATERIAL POWDERS IN POWDER BLOWN LASER CLADDING PROCESS	54
FIGURE 2.25: A SCHEMATIC ILLUSTRATION OF THE MODIFIED LASER DEPOSITION PROCESS, AS ADAPTED FROM	56
FIGURE 2.26: DIFFERENCE IN COPPER CONCENTRATIONS (A) WIRE-POWDER METHOD (B) POWDER-POWDER METHOD	57
FIGURE 2.27: AURORA LABS STITANIUM PRO LASER POWDER BED FUSION (L-PBF) SYSTEM	59
FIGURE 2.28: THREE DIFFERENT STRUCTURES HAVE BEEN USED TO BUILD MULTI-MATERIAL SAMPLES USING PBF	60
FIGURE 2.29: OPTICAL MICROSCOPY IMAGES TAKEN AT AND AROUND THE INTERFACE	61
FIGURE 2.30: MODIFIED LASER PBF SYSTEM WITH MULTIPLE POWDER HOPPERS IN COMBINATION WITH THE POINT-BY- POINT MICRO-VACUUM SELECTIVE MATERIAL-REMOVING SYSTEM.....	62
FIGURE 2.31: THE MULTIPLE MATERIALS PROCESS FLOW CHART OF SLM, A) TRADITIONAL ROLLER DELIVERY MECHANISM, B) LASER SYSTEM, C) VACUUM CLEANED PATTERN, D) ULTRASONIC POWDER DISPENSERS	62
FIGURE 2.32: JOINT ZONES OF PRINTED SAMPLES OUT OF 316L/IN718 AND 316L/ Cu10Sn DUAL MATERIAL.....	64
FIGURE 2.33: MULTI-MATERIAL MINI HOUSE, MULTI-MATERIAL STATUE OF SPHINX, A DUAL-COLORED GRID PATTERN	64
FIGURE 2.34: 3D PRINTED STRUCTURES (A) PARTS MADE OF A SINGLE MATERIAL USING BOTH 316 L SS AND 15-5PH SS, AND (B) PARTS COMPOSED OF 316 L SS AND 15-5PH SS	66
FIGURE 2.35: CHEMICAL ELEMENT DISTRIBUTION AT THE INTERFACE OF THE 316 SS AND 15-5PH SS MULTI-MATERIAL IS ILLUSTRATED: (A) SEM IMAGE; (B, C) NICKEL (Ni) AND COPPER (Cu) ELEMENTAL DISTRIBUTIONS EDS MAPPING ...	67

FIGURE 2.36: FABRICATION OF DUAL-MATERIAL PART USING ACONITY MIDI+ L-PBF PRINTER	68
FIGURE 2.37: MULTI-MATERIAL SELECTIVE POWDER RECOATER DEVICE, DEVELOPED BY AEROSINT	68
FIGURE 2.38: SCHEMATIC OF THE MICRO-FEEDING AND MONITORING SYSTEM	76
FIGURE 3.1: SCANNING ELECTRON MICROSCOPY MICROGRAPH OF THE 316L STAINLESS STEEL POWDER	80
FIGURE 3.2: SCANNING ELECTRON MICROSCOPY MICROGRAPH OF THE COPPER POWDER.....	80
FIGURE 3.3: MEASUREMENT OF PARTICLE SIZE DIAMETER AND ITS DISTRIBUTION OF THE (A) 316L AND (B) COPPER.....	81
FIGURE 3.4: AN ILLUSTRATIVE DEPICTION IS PRESENTED HEREIN, SCHEMATICALLY PORTRAYING THE MULTI-MATERIAL DEPOSITION HEAD, SHOWING THE VARIOUS CONSTITUENT COMPONENTS INTEGRAL TO THE DISPENSATION OF THE MULTI-MATERIAL POWDERS SYSTEM	84
FIGURE 3.5: THE ULTRASONIC GENERATOR EMPLOYED IN THIS STUDY	86
FIGURE 3.6: A SCHEMATIC REPRESENTATION OF THE SONOTRODE'S DESIGN	88
FIGURE 3.7: A VISUAL REPRESENTATION OF THE VARIOUS SYSTEM COMPONENTS AND THEIR INTERACTIONS	91
FIGURE 3.8: THE SUPPLEMENTAL BUILDING ENVELOPE	92
FIGURE 3.9: THE TUBE FURNACE (STF15/180) WAS EMPLOYED FOR THE SINTERING PROCESS OF THE GREEN COMPONENTS, WHICH WERE PRODUCED THROUGH THE BINDER JETTING METHOD	93
FIGURE 4.1: THE MULTI-MATERIAL POWDER DEPOSITION SYSTEM INTEGRATED WITH THE FISNAR ROBOTIC PLATFORM IS ILLUSTRATED, HIGHLIGHTING ITS CONSTITUENT COMPONENTS.....	98
FIGURE 4.2: DISPLAYING THE SYSTEM CAPABILITY OF CONSISTENTLY DEPOSITING POWDER MATERIAL AS A CONTINUOUS, UNIFORM DEPOSITION LINE WITH VARIABLE WIDTH AND HEIGHT DIMENSIONS.....	99
FIGURE 4.3: THE INFLUENCE OF ULTRASONIC POWER LEVELS AND SPEED RATES ON THE HEAP HEIGHT OF THE DEPOSITED POWDER INVESTIGATED USING DEPOSITION NOZZLES WITH DIAMETERS OF 0.8 AND 1 MM.....	108
FIGURE 4.4: THE INFLUENCE OF ULTRASONIC POWER LEVELS AND SPEED RATES ON THE HEAP WIDTH OF THE DEPOSITED POWDER INVESTIGATED USING DEPOSITION NOZZLES WITH DIAMETERS OF 0.8 AND 1 MM.....	111
FIGURE 4.5: INVESTIGATION EXPLORES THE VARIATION IN THE HEAP HEIGHT UNDER DISTINCT ULTRASONIC POWER LEVELS, EMPLOYING A DEPOSITION NOZZLE WITH A DIAMETER OF 0.8 MM AND A CONSISTENT SPEED RATE OF 10 MM/S.....	112
FIGURE 4.6: INVESTIGATION EXPLORES THE VARIATION IN THE HEAP HEIGHT UNDER DISTINCT ULTRASONIC POWER LEVELS, EMPLOYING A DEPOSITION NOZZLE WITH A DIAMETER OF 0.8 MM AND A CONSISTENT SPEED RATE OF 30 MM/S.....	112
FIGURE 4.7: INVESTIGATION EXPLORES THE VARIATION IN THE HEAP HEIGHT UNDER DISTINCT ULTRASONIC POWER LEVELS, EMPLOYING A DEPOSITION NOZZLE WITH A DIAMETER OF 0.8 MM AND A CONSISTENT SPEED RATE OF 50 MM/S.....	112
FIGURE 4.8: INVESTIGATION EXPLORES THE VARIATION IN THE HEAP HEIGHT UNDER DISTINCT ULTRASONIC POWER LEVELS, EMPLOYING A DEPOSITION NOZZLE WITH A DIAMETER OF 1 MM AND A CONSISTENT SPEED RATE OF 10 MM/S.....	113
FIGURE 4.9: INVESTIGATION EXPLORES THE VARIATION IN THE HEAP HEIGHT UNDER DISTINCT ULTRASONIC POWER LEVELS, EMPLOYING A DEPOSITION NOZZLE WITH A DIAMETER OF 1 MM AND A CONSISTENT SPEED RATE OF 30 MM/S.....	113
FIGURE 4.10: INVESTIGATION EXPLORES THE VARIATION IN THE HEAP HEIGHT UNDER DISTINCT ULTRASONIC POWER LEVELS, EMPLOYING A DEPOSITION NOZZLE WITH A DIAMETER OF 1 MM AND A CONSISTENT SPEED RATE OF 50 MM/S.....	113
FIGURE 4.11: EXAMINATION OF THE CONSTANCY OF THE POWDER HEAP AND ITS WIDTH UNDER VARYING ULTRASONIC POWER LEVELS, EMPLOYING A DEPOSITION NOZZLE WITH A DIAMETER OF 0.8 MM AND A CONSISTENT SPEED RATE OF 10 MM/S.....	114
FIGURE 4.12: EXAMINATION OF THE CONSTANCY OF THE POWDER HEAP AND ITS WIDTH UNDER VARYING ULTRASONIC POWER LEVELS, EMPLOYING A DEPOSITION NOZZLE WITH A DIAMETER OF 0.8 MM AND A CONSISTENT SPEED RATE OF 30 MM/S.....	114
FIGURE 4.13: EXAMINATION OF THE CONSTANCY OF THE POWDER HEAP AND ITS WIDTH UNDER VARYING ULTRASONIC POWER LEVELS, EMPLOYING A DEPOSITION NOZZLE WITH A DIAMETER OF 0.8 MM AND A CONSISTENT SPEED RATE OF 50 MM/S.....	114

FIGURE 4.14: EXAMINATION OF THE CONSTANCY OF THE POWDER HEAP AND ITS WIDTH UNDER VARYING ULTRASONIC POWER LEVELS, EMPLOYING A DEPOSITION NOZZLE WITH A DIAMETER OF 1 MM AND A CONSISTENT SPEED RATE OF 10 MM/S	115
FIGURE 4.15: EXAMINATION OF THE CONSTANCY OF THE POWDER HEAP AND ITS WIDTH UNDER VARYING ULTRASONIC POWER LEVELS, EMPLOYING A DEPOSITION NOZZLE WITH A DIAMETER OF 1 MM AND A CONSISTENT SPEED RATE OF 30 MM/S	115
FIGURE 4.16: EXAMINATION OF THE CONSTANCY OF THE POWDER HEAP AND ITS WIDTH UNDER VARYING ULTRASONIC POWER LEVELS, EMPLOYING A DEPOSITION NOZZLE WITH A DIAMETER OF 1 MM AND A CONSISTENT SPEED RATE OF 50 MM/S	115
FIGURE 4.17: THE INTRODUCTION OF THE ROUND FLATTENING WIPER TO THE LOWER SECTION OF THE SONOTRODE WAS IMPLEMENTED TO ENABLE CONTROLLED DISPERSION OF THE DEPOSITED POWDER, THEREBY ACHIEVING PRECISE AND WELL-DEFINED HEAP HEIGHT DIMENSIONS.	119
FIGURE 4.18: THE INVESTIGATION DELVES INTO THE IMPACT OF ULTRASONIC POWER LEVELS AND VARIABLE SPEED RATES ON THE RESULTANT HEAP WIDTH OF DEPOSITED POWDER MATERIAL WITH A FLATTERING WIPER	122
FIGURE 4.19: THE CONSTANCY OF THE POWDER HEAP, WHEN EMPLOYING A 0.8 MM DEPOSITION NOZZLE, IS EXAMINED UNDER TWO DISTINCT HEAD MOVEMENT RATES, NAMELY 10 AND 30 MM/S WHILE MAINTAINING A CONSTANT ULTRASONIC POWER LEVEL OF 1800 W.	123
FIGURE 4.20: VISUAL ILLUSTRATION OF THE POWDER HEAP SHAPE AND CONSISTENCIES RESULTING FROM THE EXAMINATION OF THREE DIVERSE ULTRASONIC POWER LEVELS, UTILIZING 1 MM DEPOSITION NOZZLE AT A SPEED OF 10 MM/S	125
FIGURE 4.21: VISUAL ILLUSTRATION OF THE POWDER HEAP SHAPE AND CONSISTENCIES RESULTING FROM THE EXAMINATION OF THREE DIVERSE ULTRASONIC POWER LEVELS, UTILIZING 1 MM DEPOSITION NOZZLE AT A SPEED OF 30 MM/S	125
FIGURE 4.22: VISUAL ILLUSTRATION OF THE POWDER HEAP SHAPE AND CONSISTENCIES RESULTING FROM THE EXAMINATION OF THREE DIVERSE ULTRASONIC POWER LEVELS, UTILIZING 1 MM DEPOSITION NOZZLE AT A SPEED OF 50 MM/S	125
FIGURE 4.23: THE DISTINCTIONS IN POWDER DEPOSITION PATTERNS, COMPARING THE UTILIZATION OF A FLATTENING WIPER TO ITS ABSENCE.....	127
FIGURE 4.24: THE DISTINCTIONS IN POWDER DEPOSITION PATTERNS, COMPARING THE UTILIZATION OF A FLATTENING WIPER TO ITS ABSENCE.....	130
FIGURE 4.25: THE LINEAR RELATIONSHIPS BETWEEN THE THREE CRITICAL PROCESS PARAMETERS (NOZZLE DIAMETER, SPEED RATE, AND POWER LEVEL) AND THE WIDTH OF THE DEPOSITED POWDER HEAP.	132
FIGURE 4.26: THE LINEAR RELATIONSHIPS BETWEEN THE THREE CRITICAL PROCESS PARAMETERS (NOZZLE DIAMETER, SPEED RATE, AND POWER LEVEL) AND THE HEIGHT OF THE DEPOSITED POWDER HEAP.	133
FIGURE 4.27: VALIDATION OF THE REGRESSION EQUATION OF THE DEPOSITION OF A 2 MM HEAP WIDTH WAS CONDUCTED UNDER DIFFERENT PARAMETERS.....	136
FIGURE 4.28: VALIDATION OF THE REGRESSION EQUATION OF THE DEPOSITION OF A 2 MM HEAP WIDTH WAS CONDUCTED UNDER DIFFERENT PARAMETERS.	136
FIGURE 5.1: AN ILLUSTRATIVE REPRESENTATION IS PROVIDED HEREIN DEPICTING THE EXPERIMENTAL APPARATUS EMPLOYED FOR THE FORMULATION OF THE LIQUID BINDER	141
FIGURE 5.2: THE EQUIPMENT USED IN THIS STUDY TO DEPOSIT THE PVA BINDER AND EVALUATE THE PRINTABILITY USING A DROP-ON-DEMAND APPROACH	143
FIGURE 5.3: REPRESENTATION OF THE DROPLET UPON CONTACT BETWEEN THE DROPLET AND THE SUBSTRATE, THE INTERPLAY OF THREE SURFACE TENSION VECTORS BECOMES EVIDENT	144
FIGURE 5.4: THE VARIATION IN USING TWO DIFFERENT PVA CONCENTRATIONS.....	147
FIGURE 5.5: SESSILE DROP EXPERIMENT	148
FIGURE 5.6: THERMOGRAVIMETRIC ANALYSIS OF THE FORMULATED PVA BINDER REVEALS THE ALTERATIONS IN MATERIAL WEIGHT AS A CONSEQUENCE OF THERMAL DECOMPOSITION DURING THE TEMPERATURE ELEVATION.....	149

FIGURE 5.7: DYNAMIC VISCOSITY MEASUREMENTS WERE CONDUCTED ON THE 5% PVA BINDER IN CONJUNCTION WITH DEIONIZED WATER. THESE MEASUREMENTS REVEAL A NOTABLE REDUCTION IN VISCOSITY VALUES AS A DIRECT CONSEQUENCE OF ELEVATED TEMPERATURES	151
FIGURE 5.8: IMPACT OF TEMPERATURE VARIATIONS ON THE SURFACE TENSION OF THE PREPARED PVA BINDER OF 5%	153
FIGURE 5.9: OHNESORGE NUMBER OF THE PREPARED BINDERS COMPRISED OF 5% MOLECULAR WEIGHTS OF PVA DISSOLVED IN DEIONIZED WATER FOR THE BINDER DEPOSITION NOZZLE OF 0.1 AND 0.6 MM	154
FIGURE 5.10: Z NUMBER OF THE BINDERS CONSISTED OF 5% MOLECULAR WEIGHTS OF PVA DISSOLVED IN DEIONIZED WATER AT ELEVATED TEMPERATURES FOR THE BINDER DEPOSITION NOZZLE OF 0.1 AND 0.6 MM.....	155
FIGURE 6.1: FISNAR ROBOTIC SYSTEM USED FOR MULTI-MATERIAL BJ PROCESSING WITH THE INTEGRATION OF A LIQUID DISPENSING PEN AND A MULTI-MATERIAL POWDER DISPENSING SYSTEM	158
FIGURE 6.2: BINDER DISPENSING PEN WITH THE TWO DIFFERENT DEPOSITION NOZZLES (A) 0.6 MM AND (B) 0.1 MM.....	159
FIGURE 6.3: DIFFERENT MULTI-MATERIAL STRUCTURES APPROACHES.....	160
FIGURE 6.4: THE STAGES OF BUILDING MULTI-MATERIAL COMPONENTS IN THE X-Y AXIS.....	163
FIGURE 6.5: (A) ILLUSTRATING THE WEAK GEOMETRIC PRECISION AT THE SAMPLE'S EDGES ACHIEVED THROUGH THE UTILIZATION OF A 0.6 MM NOZZLE FOR PVA BINDER DISPENSING. (B) QUANTIFYING THE DROPLET SPREADING SIZE RESULTING FROM THE PVA BINDER DISPENSING THROUGH A 0.6 MM NOZZLE.....	167
FIGURE 6.6: (A) EMPLOYING A 0.1 MM NOZZLE HAS YIELDED BETTER GEOMETRIC PRECISION IN THE GREEN PART IN COMPARISON TO THE 0.6 MM NOZZLE. (B) THE USE OF A 0.1 MM NOZZLE HAS RESULTED IN A REDUCTION IN DROPLET SPREADING SIZE TO 1.5 MM.	168
FIGURE 6.7: VARIOUS INSTANCES OF PRINTED GREEN COMPONENTS CONFORM TO THE VERTICAL (Z-AXIS) ORIENTATION .	171
FIGURE 6.8: MULTI-MATERIAL GREEN PARTS MANUFACTURED IN THE (X-Y-AXIS) ORIENTATION DURING	171
FIGURE 6.9: SAMPLES SUBJECTED TO SINTERING PROCESSES AT A MAXIMUM TEMPERATURE OF 1200°C FOR (A) A DURATION OF TWO HOURS, AND (B) A DURATION OF ONE HOUR.	173
FIGURE 6.10: SAMPLES SUBJECTED TO SINTERING PROCESSES AT A MAXIMUM TEMPERATURE OF 1150°C FOR (A) A DURATION OF TWO HOURS, AND (B) A DURATION OF ONE HOUR.....	174
FIGURE 6.11: SAMPLES SUBJECTED TO SINTERING PROCESSES AT A MAXIMUM TEMPERATURE OF 1150°C FOR (A) A DURATION OF TWO HOURS, AND (B) A DURATION OF ONE HOUR.....	175
FIGURE 6.12: THE SEPARATION OF THE TWO DIFFERENT MATERIALS BECAUSE OF LOW DWELLING TIME	177
FIGURE 6.13: THE EFFECT OF THE NON-UNIFORM HEAT DISTRIBUTION ON THE COPPER SIDE	180
FIGURE 6.14: CONSECUTIVE CYCLES DEMONSTRATE THE COMMITMENT TO ENHANCING THE QUALITY OF THE COMPONENTS	181
FIGURE 7.1: THE SYSTEMATIC EVALUATION OF POROSITY VARIATIONS ACROSS DISCRETE SINTERING CYCLES WAS UNDERTAKEN TO SHOW THE INTERPLAY BETWEEN SINTERING PARAMETERS AND THE RESULTANT POROSITY OF THE MATERIAL.....	187
FIGURE 7.2: MICROGRAPHS OF THE SINTERED SPECIMENS SHOWING THE HIGH RATE OF POROSITIES AS THE BLACK PORTIONS IS THE POROSITY	189
FIGURE 7.3: VISUALIZATION OF MICROSCOPY IMAGES AS THE BLACK PORTIONS IS THE POROSITY	190
FIGURE 7.4: MICROSCOPIC IMAGERY AS THE BLACK PORTIONS IS THE POROSITY.....	191
FIGURE 7.5: CONSEQUENT TO THE MODIFICATIONS MADE TO THE OPERATIONAL CYCLES, A SIGNIFICANT REDUCTION IN POROSITY LEVELS IS DISCERNIBLE AS THE BLACK PORTIONS IS THE POROSITY, WITH VALUES DECREASING FROM 16.8% IN (A) TO 10.8% IN (B) FOR THE STAINLESS-STEEL SIDE AND FROM 27% IN (A*) TO 16.6% IN (B*) FOR THE COPPER SIDE.....	193
FIGURE 7.6: MICROSCOPY PICTURES OF THE IMPROVEMENT IN THE POROSITIES AS THE BLACK PORTIONS IS THE POROSITY. (A) THE STAINLESS-STEEL SIDE AND (A*) THE COPPER SIDE THROUGHOUT MODIFYING SINTERING CYCLES.....	194
FIGURE 7.7: MICROSCOPY MICROGRAPHS OF THE SINTERED SPECIMENS SHOWING THE REDUCTION IN THE POROSITY VALUES IN (A) THE STAINLESS-STEEL SIDE AND (A*) THE COPPER SIDE	195

FIGURE 7.8: MICROSCOPY MICROGRAPHS OF THE SINTERED SPECIMENS SHOWING THE (A) HIGHER POROSITY ON THE STAINLESS-STEEL SIDE DUE TO THE REDUCTION IN THE MAXIMUM REACHED TEMPERATURE FROM 360 TO 180 MINUTES, (A*) THE POROSITY ON THE COPPER SIDE WAS LOWER.....	196
FIGURE 7.9: THE MICROGRAPHIC REPRESENTATIONS VISUALLY CAPTURE THE ENHANCEMENTS ACHIEVED THROUGH A DELIBERATE ALTERATION OF THE SINTERING CYCLES, TRANSITIONING FROM 31 TO 34 CYCLES. THIS TRANSFORMATION RESULTED IN A NOTABLE REDUCTION IN POROSITY, SPECIFICALLY FROM 7.3% IN (A) TO 5.5% IN (B) FOR THE STAINLESS-STEEL SIDE, AND FROM 8.9% IN (A*) TO 5% IN THE COPPER SIDE(B*).....	197
FIGURE 7.10: THE MICROGRAPHIC REPRESENTATIONS VISUALLY CAPTURE THE ENHANCEMENTS ACHIEVED THROUGH A DELIBERATE ALTERATION OF THE SINTERING CYCLES, TRANSITIONING FROM 31 TO 34 CYCLES. THIS TRANSFORMATION RESULTED IN A NOTABLE REDUCTION IN POROSITY, SPECIFICALLY FROM 4.6% IN (A) TO 2.4% IN (B) FOR THE STAINLESS-STEEL SIDE, AND FROM 3.7% IN (A*) TO 2.6% IN THE COPPER SIDE(B*).....	198
FIGURE 7.11: TEMPERATURE DISTRIBUTION AND DWELLING TIME OF THE BEST SINTERING CYCLE TO THE GREEN PARTS THAT ENHANCE THE BEST STRUCTURAL QUALITY AND LOWER POROSITY VALUES.	199
FIGURE 8.1: SEM IMAGE ILLUSTRATING THE 316L AND CU BONDING INTERFACE IN THE MULTI-MATERIAL SAMPLE PRODUCED BY THE MODIFIED BINDER JETTING (BJ) SYSTEM. THE RED DOTTED LINES REPRESENT THE BORDERS OF THE TRANSITIONAL REGION BETWEEN THE TWO MATERIALS.....	202
FIGURE 8.2: EDS MAPPING ANALYSIS REVEALING MICROCONSTITUENT COMPOSITIONS IN MULTI-MATERIAL BINDER JETTED SAMPLES OF 316L STAINLESS STEEL (TOP PART) AND COPPER (LOWER PART), HIGHLIGHTING ELEMENT DISTRIBUTION WITHIN THE SPECIMENS.	205
FIGURE 8.3: QUANTITATIVE EDS LINE SCANS ILLUSTRATING COMPOSITIONAL VARIATIONS OF CU AND FE ELEMENTS ALONG THE INTERFACE IN THE BINDER-JETTED MULTI-MATERIAL SAMPLE. THE HORIZONTAL YELLOW LINE DESIGNATES THE SCANNED REGION, WITH CU (BLUE) AND FE (ORANGE) ELEMENTAL COMPOSITIONS PLOTTED BELOW.	206
FIGURE 8.4: THE TENSILE TEST COUPONS FABRICATED UNDER THE SPECIFICATIONS OUTLINED IN THE BS EN ISO 6892-1:2016 STANDARDS. THESE SPECIMENS HAVE BEEN PREPARED TO UNDERGO ULTIMATE TENSILE STRENGTH (UTS) TESTING.	208
FIGURE 8.5: STRESS VERSUS STRAIN ANALYSIS OF THE MULTI-MATERIAL TENSILE SPECIMEN FABRICATED THROUGH THE BINDER JETTING APPROACH. THE GRAPH SHOWS THE MAXIMUM UTS VALUE THAT THE MULTI-MATERIAL SPECIMEN CAN STAND BEFORE BREAKAGE OCCURS.....	210
FIGURE 8.6: THE FRACTURED SAMPLES ANALYSIS OF 316L AND CU MULTI-MATERIAL COMPONENTS POST-TENSILE TESTING. THE PICTURE ILLUSTRATES THE FEATURES OF THE TENSILE BARS, HIGHLIGHTING UNEXPECTED BRITTLINESS AND LIMITED PLASTIC DEFORMATION, ATTRIBUTED TO AN INSUFFICIENT SINTERING PROCESS.....	212
FIGURE 11.1: THE DESIGN DRAWINGS OF THE MANUAL POWDER BED USED AS A POWDER BED IN SOME 3D PRINTING BUILDINGS.....	235
FIGURE 11.2: THE DESIGN DRAWINGS OF THE SONOTRODE USED IN THE MULTI-MATERIAL POWDER DEPOSITION SYSTEM.	237
FIGURE 11.3: THE DESIGN DRAWINGS OF THE SONOTRODE USED IN THE MULTI-MATERIAL POWDER DEPOSITION SYSTEM.	238

List of Tables

TABLE 2.1: ACHIEVED GREEN AND SINTERED PART DENSITIES AT 100% BINDER SATURATION LEVEL AS ADAPTED FROM ...	19
TABLE 2.2: A WIDE RANGE OF BINDER MATERIAL USED IN BINDER JETTING TECHNOLOGY, AS ADAPTED FROM	20
TABLE 2.3: COMPARISON OF THE MULTI-MATERIAL AM ACHIEVEMENTS OVER THE DIFFERENT PROCESS DISCUSSED	69
TABLE 2.4: MULTI-MATERIAL COMBINATIONS AND THEIR APPLICATIONS.....	70
TABLE 2.5: COMMON SONOTRODE SHAPES USED IN HIGH-POWER ULTRASONIC SYSTEMS AND THEIR LENGTH CALCULATIONS.	75
TABLE 3.1: THE POWDER MATERIAL COMPOSITION TABLE FOR 316L STAINLESS STEEL POWDER USED IN THIS RESEARCH ..	79
TABLE 3.2: THE DESIGN OF THE MULTI-MATERIAL SYSTEM ADHERES TO A SET OF PURPOSE-DRIVEN SPECIFICATIONS. FURTHER ELABORATION ON NOZZLE DIAMETERS, VELOCITY PARAMETERS.	85
TABLE 3.3: SPECIFICATIONS OF THE USED DERUI ULTRASONIC GENERATOR.....	87
TABLE 3.4: EXPERIMENTAL DESIGN IS SUMMARIZED AND PRESENTS THE THREE PARAMETERS, DEPOSITION NOZZLE DIAMETER SIZE, SPEED RATE, AND THE ULTRASONIC POWER LEVEL ACROSS THREE DISTINCT LEVELS: LOW, MEDIUM, AND HIGH...	90
TABLE 4.1: A LAYOUT OF THE FULL FACTORIAL EXPERIMENTAL DESIGN SHOWING A TABULAR REPRESENTATION OF THE THREE PARAMETERS SYSTEMATICALLY RANGING ACROSS THREE DISCRETE TIERS: LOW, MODERATE, AND HIGH.	102
TABLE 4.2: THE OUTCOMES PERTAINING TO HEAP WIDTH AND HEIGHT VALUES DERIVED THROUGH THE UTILIZATION OF TWO DISTINCT PARAMETERS, EACH COMPRISING THREE DISCRETE LEVELS	106
TABLE 4.3: THE OUTCOMES OF HEAP WIDTH AND HEIGHT VALUES THROUGH THE UTILIZATION OF TWO DISTINCT PARAMETERS, EACH COMPRISING DIFFERENT DISCRETE LEVELS.....	121
TABLE 4.4: DISPARITIES IN WIDTH MEASUREMENTS INVESTIGATED IN THE CONTEXT OF POWDER DEPOSITION USING A 1 MM NOZZLE COMPARING INSTANCES WHERE A WIPER WAS EMPLOYED TO THOSE WHERE IT WAS NOT.	128
TABLE 4.5: DISPARITIES IN WIDTH MEASUREMENTS INVESTIGATED IN THE CONTEXT OF POWDER DEPOSITION USING A 0.8 MM NOZZLE, COMPARING INSTANCES WHERE A WIPER WAS EMPLOYED TO THOSE WHERE IT WAS NOT.....	130
TABLE 4.6: CORRELATION COEFFICIENTS SERVE AS NUMERICAL INDICES DELINEATING THE LINEAR RELATIONSHIPS AMONG THE THREE FUNDAMENTAL PROCESS PARAMETERS, NAMELY NOZZLE DIAMETER, SPEED RATE, AND POWER LEVEL.	131
TABLE 4.7: THE FOUR DISTINCT PARAMETER SETS WERE ESTABLISHED FOR ANALYSIS TO CONDUCT THE VALIDATION OF THE LINEAR REGRESSION ASSUMPTIONS.	135
TABLE 5.1: THREE DIFFERENT LEVELS OF PVA CONCENTRATION USED IN THE TEST EXPERIMENT WERE CARRIED OUT TO ENSURE THE OVERALL STRENGTH AND DURABILITY OF THE GREEN BODY.....	143
TABLE 6.1: BINDER JETTING BUILDING PARAMETERS EMPLOYED IN THE FABRICATION OF MULTI-MATERIAL STRUCTURES.	163
TABLE 6.2: VARIOUS THERMAL TREATMENT CYCLES EMPLOYED FOR THE SINTERING OF MULTI-MATERIAL COMPONENTS...	166
TABLE 6.3: THE OUTCOMES OF DIFFERENT SINTERING CYCLES AND THEIR IMPACT ON THE GEOMETRIC INTEGRITY OF 3D PRINTED SINTERED SAMPLES INVESTIGATED IN THIS STUDY.	172
TABLE 7.1: THE OPERATIONAL CYCLES WERE CHOSEN BASED ON THEIR OPTIMAL GEOMETRIC ATTRIBUTES, AND THEIR IMPACT ON POROSITY WAS SYSTEMATICALLY EVALUATED.	184
TABLE 7.2: THE INFLUENCE OF THE SELECTED SINTERING CYCLES, BASED ON THEIR FAVORABLE GEOMETRIC INTEGRITY OUTCOMES, ON THE POROSITY CHARACTERISTICS OF BOTH MATERIALS WAS EXAMINED.	186
TABLE 8.1: A SUMMARY OF THE ULTIMATE TENSILE STRENGTH (UTS) VALUES OF THE DIVERSE ARRAY OF MATERIALS UNDER INVESTIGATION	209
TABLE 11.1: A THOROUGH AND IN-DEPTH EXPLORATION OF DESIGN CALCULATIONS OF THE SONOTRODE'S MANUFACTURING, WHICH OFFERS AN EXTENSIVE REPOSITORY OF DETAILED INFORMATION AND SPECIFICATIONS.	236
TABLE 11.2: OHNESORGE NUMBER OF THE PREPARED BINDERS COMPRISED OF 5% MOLECULAR WEIGHTS OF PVA DISSOLVED IN DEIONIZED WATER FOR THE BINDER DEPOSITION NOZZLE OF 0.6 MM.....	241
TABLE 11.3: OHNESORGE NUMBER OF THE PREPARED BINDERS COMPRISED OF 5% MOLECULAR WEIGHTS OF PVA DISSOLVED IN DEIONIZED WATER FOR THE BINDER DEPOSITION NOZZLE OF 0.1 MM.	241

Nomenclature

AM	Additive manufacturing
ASTM	The American Society for Testing and Material
BJ	Binder jetting
CAD	Computer-aided design
DED	Directed energy deposition
DOD	Drop on demand
FDM	Fused layer modelling
HIP	Hot isostatic pressing
LOM	Sheet lamination
L-PBF	Laser powder bed fusion
ME	Material extrusion
MIM	Metal injection moulding
MJT	Material jetting
MMPDS	Multi-material powder deposition system
MMSL	Multi-material stereolithography
MtoBS	Multi-head tissue/organ-building system
PBF	Powder bed fusion
PM	Powder metallurgy
PVA	Polyvinyl alcohol
SEM	Scanning electron microscope
SL	Stereolithography
SLM	Selective laser melting
SLS	Selective laser sintering
TGA	Thermogravimetric analysis
UTS	Ultimate tensile strength
VPP	Vat photopolymerization

Chapter 1. Introduction

1.1 Motivation

Additive manufacturing (AM), often referred to as three-dimensional (3D) printing, has gained prominence in the realm of production and manufacturing. It presents a compelling alternative to traditional manufacturing methods, offering enhanced design flexibility, faster prototyping, and shortened development cycles. AM processes operate by creating products layer by layer, with each new layer added to the previously deposited one. The American Society for Testing and Materials (ASTM) classifies AM technologies into seven primary categories: Powder Bed Fusion (PBF), Vat Photopolymerization (VPP), Binder Jetting (BJ), Material Extrusion (ME), Directed Energy Deposition (DED), Material Jetting (MJT), and Sheet Lamination (LOM) (1). While the fundamental concept of these processes remains consistent, their mechanisms vary, contingent on three key elements: the state of building material, heat source, and feeding systems. In addition, certain AM processes necessitate pre-production, during-production, and/or post-production processes. Furthermore, some AM techniques are better suited for specific polymer applications, while others excel with metals. In the realm of metal AM, processes can be categorized into three groups: powder bed, powder feed, and wire feed. Among these, powder bed methods are considered one of the most commonly employed. In the powder bed, metal powder is distributed as a bed, and specific areas are solidified to create bonds between powder particles, typically via laser or electron beams or binders. Laser-PBF and BJ are examples of PBF processes, with SLM using a laser for direct heating and melting, while BJ relies on sintering the green part for particle bonding.

Despite the extensive use of AM technologies, limitations persist in the fabrication of advanced printed components. Quality can vary due to manufacturing parameters unique to each process. Additionally, many AM processes necessitate supplementary steps, such as pre-heating, inter-layer heat treatment, burnout and sintering cycles,

and surface finishing. Consequently, it is essential to establish an understanding of the interplay between manufacturing constraints, including building materials, additive materials, and additional processes. While numerous projects and research endeavours have explored the relationship between material and process parameters, relatively few have focused on multi-material structures, especially within the context of powder bed AM techniques. The challenge lies in processing multi-material components, demanding a precise dispensing mechanism capable of selectively feeding different powder types to enable multi-material construction. Furthermore, different materials exhibit varied responses to heat treatment. In the BJ process, sintering the green part serves as a method to heat and partially melt the printed parts, constituting an indirect heat processing approach within the printing process. This differs from other AM processes where inter-layer heat is applied by a laser or electric beam to melt and fuse powder particles, constituting a direct heat processing method within the printing process. Direct heat treatment can occasionally cause thermal expansion and subsequent layer delamination, which is a concern that indirect heat processes may alleviate. Delamination due to thermal expansion in some AM processes occurs when the application of direct heat causes localized expansion within a layer of the printed object. While it may seem intuitive that the new layer would adhere to the previous layers, rapid heating and cooling cycles can induce thermal stresses within the material, especially if the thermal expansion coefficients of the layers differ significantly. This stress can weaken the bonding between layers, leading to delamination. Moreover, the critical shortage of accessible and cost-effective multi-material AM systems has presented a significant obstacle to the advancement and widespread implementation of multi-material AM processing. Thus, there is a lack of understanding of the complexities of different metal materials in BJ processing, which will undoubtedly enhance the quality and performance of printed components across applications. Therefore, understanding the relationship between processing metal multi-material parts in BJ and the sintered parts' properties is of utmost importance in advancing the field of metal multi-material AM printing.

1.2 Aim and Objectives

The aim of this research is to develop a novel multi-material deposition system for Binder Jetting (BJ) technology capable of dispensing two different powder materials, optimize processing parameters for enhanced component quality, and demonstrate the feasibility of fabricating specific multi-material combinations through the developed multi-material Binder Jetting system. To achieve the research purpose, the following objectives need to be accomplished:

- Multi-material work in additive manufacturing: To explore the multi-material techniques used in additive manufacturing to identify the state of the art in multi-material additive manufacturing processing, especially powder bed approaches.
- Multi-material application: To explore metal material combination, of two different materials, that is used in a specific application.
- Multi-material deposition system: To design and development of novel multi-material deposition system to dispense two or more powder materials.
- Validating the multi-material deposition system: To validate the designed system to check the capability of repeatably dispensing different types of powders and the controllability of the system parameters.
- Selection of binder material: To select the binder used in the BJ printing process and characterize them to investigate its wettability, rheological characterisation, and thermogravimetric analysis.
- Multi-material components printing: To print parts with BJ approaches and evaluate the effect of the sintering cycles to parts' porosity. Residual stress analysis and shrinkage analysis are not part of the research.
- Characterisation of the printed multi-material components: To investigate the parts' microstructural and tensile properties.

1.3 Novelty Statement

This Ph.D. research constitutes the first work in the realm of additive manufacturing, specifically focused on advancing multi-material 3D printing through the use of binder jetting technology. A principal challenge that is addressed is the absence of accessible and cost-effective multi-material binder jetting processes, an obstacle that has held back the advancement and broader adoption of multi-material binder jetting technology. At the heart of this work lies a novel achievement—the design of a cost-effective multi-material powder deposition system.

The limitations in the capability to deposit multiple metal material powders, within a single part, have significantly restricted the exploration of diverse materials in 3D printing. This novel approach shows a promising result with the introduction of a new system which is powder multi-material deposition system. This system not only extends the possibilities of experimentation in metal multi-material parts but also delivers a significant impact on material waste. Achieving accurate powder material deposition has proven challenging, constraining the development of functionally graded components. Here, the novel system, through its involved mechanisms, adeptly overcomes this challenge, allowing for the exact placement of powder materials at designated locations on the building platform. In addition, the inability to recycle unused powder is resulting in material wastage. Yet, with the innovative system, the requirement to completely cover the entire build platform with powder for the production of small parts becomes unnecessary. This efficient approach not only reduces costs but also contributes to the reduction of material waste. Moreover, thermal expansion issues in some of the additive manufacturing processes have long obstructed the production of multi-material parts. Thus, the multi-material system introduces an approach building multi-material parts using binder jetting techniques. The controlled heating furnaces in the sintering cycle control the cooling rate, redefining the concept of thermal expansion control and enabling the creation of good functionally graded multi-material components. The thermal fusing of dissimilar materials, a remarkable challenge in the multi-material printing field, is improved in

this study. The novel system influences the powder multi-material deposition system to construct multi-material parts, followed by a thorough sintering process which results in an understanding of the dissimilar material fusion (stainless steel and copper), expanding the boundaries of what can be achieved in this field. Lastly, the effect of the thermal sintering cycles on the porosity of the multi-material samples has been investigated. The exploration of sintering cycles for binder jetted multi-material parts within this study yields invaluable insights into the art of controlling these parameters, elevating the quality and reliability of multi-material 3D-printed components to new heights.

1.4 Thesis Structure

This research paper consists of 9 chapters:

Chapter 1: The introduction. It consists of the motivation of this thesis, the purpose of the study, the research objectives, the novelty statement, and the thesis structure.

Chapter 2: In this chapter, a review and investigation are conducted for the AM topic in general, some of the AM techniques, binder jetting, and the promising approaches of multi-material AM materials and processes.

Chapter 3: Experimental Methods and Materials. It mainly covers the chosen materials and equipment used in this thesis.

Chapter 4: Powder deposition system: In this chapter, the design and validation of the deposition system are discussed.

Chapter 5: Binder Selection and Characterisation. This chapter focuses on the Selection, preparation, and analysis of the binder.

Chapter 6: Binder jetting process and Printing Parts: In this chapter, the use of the binder jetting technique to build multi-material parts and the effects of the sintering cycle on the final shape are discussed.

Chapter 7: Evaluation of porosity in sintered parts: In this chapter, the effect of sintering cycles on the multi-material parts' porosity is discussed.

Chapter 8: Microstructure and mechanical behavior: In this chapter, the results of the interlayer connection and mechanical tensile properties are discussed.

Chapter 9: Conclusion and future work. It focuses on the conclusive summaries of the previous chapters, and it provides future work recommendations.

Chapter 2. Literature Review

This chapter will focus on reviewing and investigating the topic of AM selective laser melting and binder jetting as the main interest. Additionally, some of the AM techniques will be reviewed particularly in the context of 3-dimensional printing of metals and powder metal. Furthermore, this chapter will contain a literature review of the promising approaches of multi-material AM materials and processes to explore the state of the art in this area.

2.1 Additive Manufacturing

Additive manufacturing (AM), also called 3D printing, is an automated system that is mainly used to build rapid prototyping parts or in some cases end-user products. This technology was established in the middle of the 1980s as the first AM machine ever known was called Stereolithography Apparatus. This machine was built in 1984 and then introduced by Charles W. Hull of 3-D Systems Corporation two years later (2). It has been extensively used in the field of production and manufacturing as it has become the most game-changing method for Rapid Prototyping, tooling purposes, and manufacturing small to medium end-user products around the world due to the clear advantages over all the traditional manufacturing methods. Most of these advantages are, increasing complexity of designed parts at no additional cost, shorter lead time, individual product customization, reduction of wasted material, and less human interaction (3). However, until the last decade, AM has not entirely achieved the industry's expectations as its performance is almost limited to prototyping and low-value products. Positively, in recent days the actual performance of additive technologies has exponentially grown because of a wider understanding of the fundamental mechanisms behind AM techniques. Advanced additive methodologies have been discovered along with improving the old additive techniques (4). The American Society for Testing and Materials (ASTM) has defined the AM approach as the way it functions as a single layer on top of a previously deposited layer to reach

the final product. This approach is opposite to the conventional subtractive manufacturing methods (1). AM technologies give the flexibility of making parts from a different range of materials such as metal, polymer, glass, and ceramic (5). Furthermore, one of the advantages of AM techniques is the ability to produce complex shapes as a complete part of a single building process unlike the situation in conventional manufacturing techniques where sometimes it is almost impossible to achieve complex shapes using one manufacturing process. Thus, this advantage permits optimising the assembly designs which directly leads to the reduction in manufacturing time, cost, the material used, and final weight. Furthermore, AM technologies have been integrated into a wide range of sectors that require flexible design freedom along with customisation capabilities such as R&D, medical, and aerospace (6).

2.1.1 Basic Concepts

Despite the differences in the manufacturing processing of AM technologies, they all function as a layer-by-layer fabrication to make the final product and mostly share similar process steps. According to Fernández et al (4), these process steps start with putting up the final geometry and dimensions of the part that is to be manufactured and then transferring it to a CAD file. Then, this file is converted to one of the common AM file formats such as the STL file extension. Thirdly, the design file is manipulated and transferred to the AM system where its scale, rotation, and positioning are checked and finalised to allow the creation of more than one object at one time if possible. Next, the machine specifications and commands are defined to finalise the layer thickness and building trajectories. After that, the system starts building a layer on top of the layer to reach the final product. Once the building process has finished, the manufactured part is extracted from the building platform cleaned from any loose powder, and removed from any support structures. The last step is post-processing where additional processes are taken place such as removing edges, and in some techniques, binder or additives burnout and sintering processes are done in this stage.

2.1.2 Techniques

The American Society for Testing and Material standard also categorises AM technologies into seven main categories. These categories are Powder Bed Fusion (PBF), Vat Photopolymerization (VPP), Binder Jetting (BJ), Material Extrusion (ME), Directed Energy Deposition (DED), Material Jetting (MJT), and Sheet Lamination (LOM) as shown in Figure 2.1. Each category of these seven is further broken up into two or more processes depending on the state of the material and source of heat. Although the main concept of these processes is identical, the production mechanism of each technique varies. Moreover, some of these methods require pre-production, -production and/ or post-production processing. Furthermore, each technique or sub-category is adequate for certain applications. To put it in other words, some of these processes better work with polymer while others work well with lite metal. In addition to that, some of the AM processes give semi-full density whereas others vary from low to medium density.

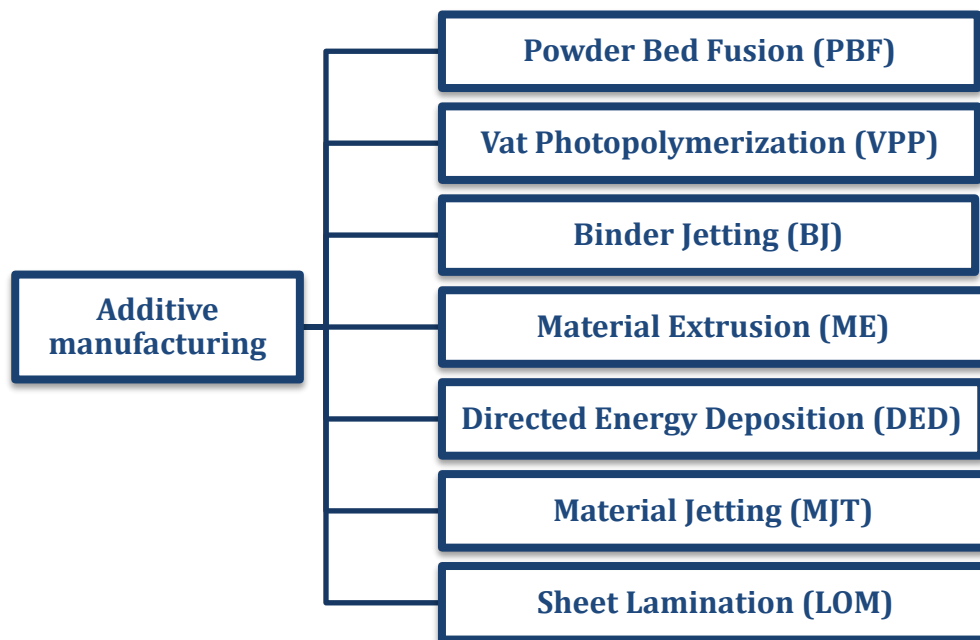


Figure 2.1: Division of the AM technology under the American Society for Testing and Materials (ASTM).

2.2 Metal Additive Manufacturing Processes

According to ASTM standards, AM is further divided into metal AM (MAM) and Non-metal additive manufacturing. MAM has three main systems which are the powder bed system, powder feed system, and wire feed system (6). Figure 2.2 shows the AM technologies that work under each system. Although metal AM can provide a wide range of advantages to the industrial sector, it still has some limitations that restrict its rapid growth in some cases. Approximately all these limitations are related to the job which needs to be done such as component size, component quality, cost, and time to be produced (6). Other limitations are the capability of specific AM processes to reach certain mechanical properties and process availability.

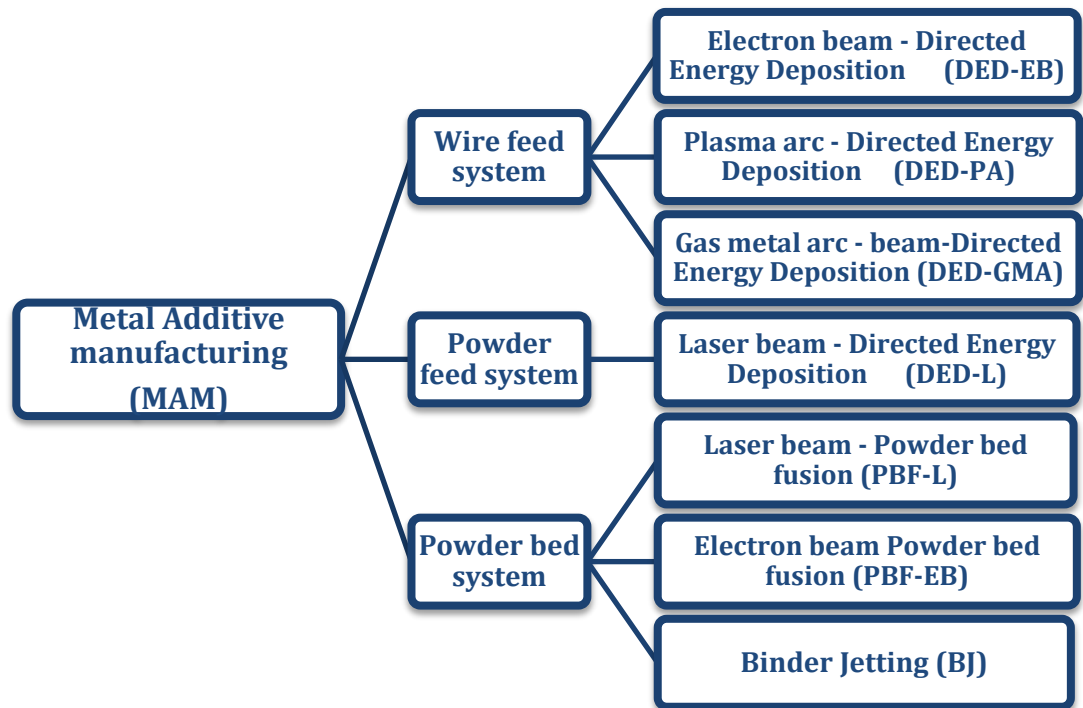


Figure 2.2: shows the AM technologies that work under the powder bed system, powder feed system, and wire feed system.

Since the last decade, new commercial metallic powder availability has increased dramatically. currently, there are more than 29 common types of alloys that are in the market. These types include titanium, stainless steel, nickel-based alloys, aluminum-based alloys, and cobalt-chrome. In AM technologies, all these types of metallic powder material's performance properties are strongly influenced by the powder characteristics. To say it, in other words, particle size distribution (PSD), morphology, and porosity affect the powder packability and flowability which leads to the lack of feasibility in fabricating the high-resolution powder layer which also affects the final printed part's homogeneity and properties. This absence of an entire understanding of the influence of the powder characteristics in the manufacturing process can result in fabricating a part with poor properties (7). According to Le Néel et al (8), in using two systems of the powder bed AM, namely binder jetting and selective laser sintering, to fabricate sand moulds (8). This work defines the structural material as the significant material used to fabricate the mould, hence it must be selected sensibly as choosing the right structural material will give the right mould properties that lead to fabricating a well-casted part. This work also itemised the mechanical properties of an acceptable mould into the following factors: surface finish, permeability, cohesiveness, refractoriness, flowability, availability, collapsibility, and chemical inertness. Thus, using accurate structural materials relatively contributes to optimizing the final part characteristics as each material has its specific properties (8). However, structural material selection is not the only measure to achieve a high-quality part. Other powder material parameters must be considered such as particle diameter size and particle shape. ExOne corporation has presented that powder particles, which are provided by ExOne corporation, ranging between 75 and 250 μm in diameter are a standard range for binder jetting practices where the powder particle size must be smaller than the slice height to perform a flowable layer surface (9). On the other hand, Rao et al (10) have indicated that the particle size must not be finer than 5 μm as finer particles will be affected by their lightweight and fly into the air. Additionally, these fine particles flying in the air could lead to lung fibrosis in the

surrounding workers because of the inhalation of these particles. Furthermore, the fine particles could lead to powder particle agglomeration on the building device that directly results in an inaccurate result and/or a decrease in the equipment uptime, therefore, the ideal minimum mean particle size can be 20 μm (11).

Another area of concern is the particle shape where it is ideal to be spherical to attain smooth flowability (12). Lores et al (6) indicate that achieving adequate part properties depends on the suitable process performance and one factor to achieve the suitable process performance is to use spherical-shaped powder particles in binder jetting. To put it in other words, non-spherical particles and/or irregular particles display lower random packing density caused by the higher interparticle friction, thus this affects the green part's density as well as the sintered part density and shrinkage. So far, the particle shape measurement is not regulated by any guidelines or standards, however, a few national standards are labeling and categorising the powder particle shape. One good example of these powder shape national standards is the Russian GOST 25849 which categorises the shape into spherical, spheroidal, angular, rod-like, needle-like, plate-like, flaky, dendritic, and particles with internal voids (6). Verlee et al (13) have experimented to analyse how powder particle sizes affect the final part density, permeability, and porosity characteristics. In this experiment, the methodology was to test six dissimilar powder batches with ranging particle size diameters and different particle shapes. The printed parts were then kept in the sintering cycle for 90 minutes at an extending temperature from 1200 to 1430°C. The results of the experiment showed that higher particle sizes resulted in lower densification influence with higher pore sizes and lots of open porosity shapes. It also showed that minor powder bed packing occurred when the powder particles were in a non-spherical shape which resulted in extra porosity after the sintering cycle thus shrinkage. Finally, the study concluded that the non-spherical particles show a rough porosity surface after the sintering cycle. This rough porosity surface leads to decreases in the permeability of the final part by promoting more fluid pressure loss.

2.2.1 Binder Jetting (BJ)

Binder Jetting (BJ) is considered one of the AM processes that use metal or nonmetal powder particles to produce parts. This technique was invented and patented by the Massachusetts Institute of Technology (MIT) at the beginning of 1990. At that time, this technique was called the 'Three-dimensional printing technique' (11). In the Binder Jetting building process, the state of the print material has to be in powder form. According to Farzadi et al (14), in a typical binder jet system, each layer of a part is created by spreading a layer of powder, often with a counter-rotating roller. Subsequently, a print-head deposits a liquid binding agent onto the powder bed, forming a 2D pattern for the layer. While some systems may use heaters for moisture control and curing, heat is not inherently necessary. After each layer, the build platform descends to accommodate the next layer, and this process repeats. The resulting printed parts are usually delicate and undergo post-processing to enhance their mechanical properties (15). Figure 2.3 provides a representation of a conventional binder jet system.

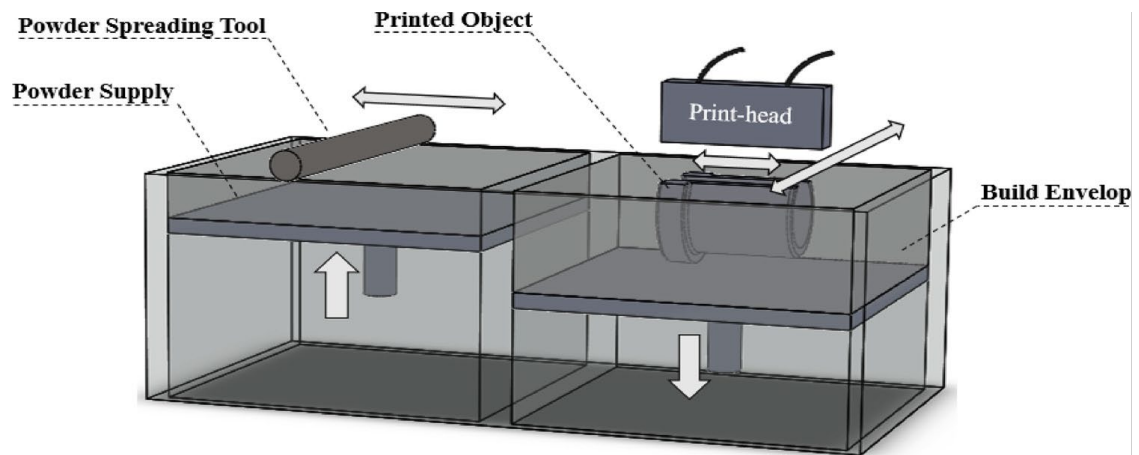


Figure 2.3: A schematic representation of a conventional binder jet system (16).

A more detailed Binder Jetting manufacturing process chain is illustrated in Figure 2.4 as the powder is fed from one or more nozzles followed by a roller that spreads the powder equally into the work envelope. Followed by a binder dispenser that jets the binder material selectively at the top of the previously deposited layer of powder to make a bond between the powder particles at these particular areas to create the first layer. Then, a UV light is subjected to the work envelop to dry the dispensed binder. The process is then repeated for several iterations that equate to the number of slices until the green part is fully produced. Next, the powder bed is placed into an oven to remove the moisture that existed inside the green part and heated for a specific time and temperature that depends on the type of binder. After the curing cycle, the surrounding loose powder is removed to extract the green part. Lastly, the green part is sintered inside a furnace to first cure the binder material and then recrystallise the powder material to create a metallurgical bonding.

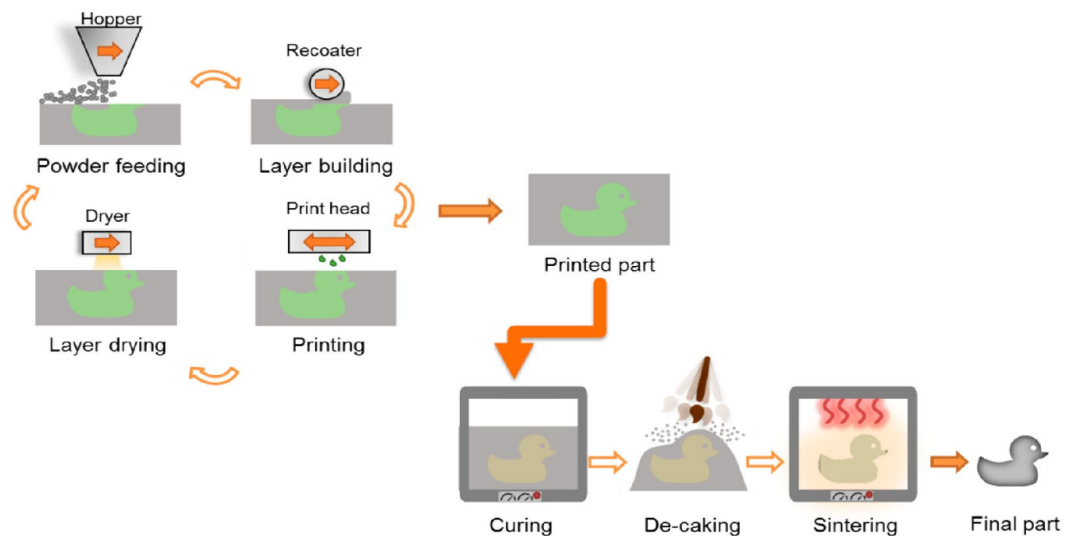


Figure 2.4: Shows the Binder Jetting AM process chain to fabricate a part (6).

Binder Jetting (BJ) is a useful technique that has been widely adapted to process various powder materials for diverse applications, including casting, medicine, and electronics. Particularly, BJ has found more use in the 3D printing of casting moulds and cores. Upadhyay et al (17) have conducted a review on the use of the binder jetting process in rapid sand casting highlighting its significance. Upadhyay et al (18) have concluded that the porosity inherent in the binder jetted parts is advantageous for moulds and cores, as it facilitates gas transport and provides a sufficient feature for the easy removal from the final part. Hoosier Pattern Inc. reported that 3D binder jetted moulds have been successfully printed using both sand and ceramic materials, although the practice of using sand moulds is more common as seen in Figure 2.5. 3D printing moulds not only significantly reduce geometric constraints and lead times associated with pattern fabrication but also ensures that the final part's properties match those produced through traditional manufacturing methods (19) (20). Snelling et al (21) stated that in some instances, binder jetted moulds have demonstrated superior results compared to traditional sand moulds.

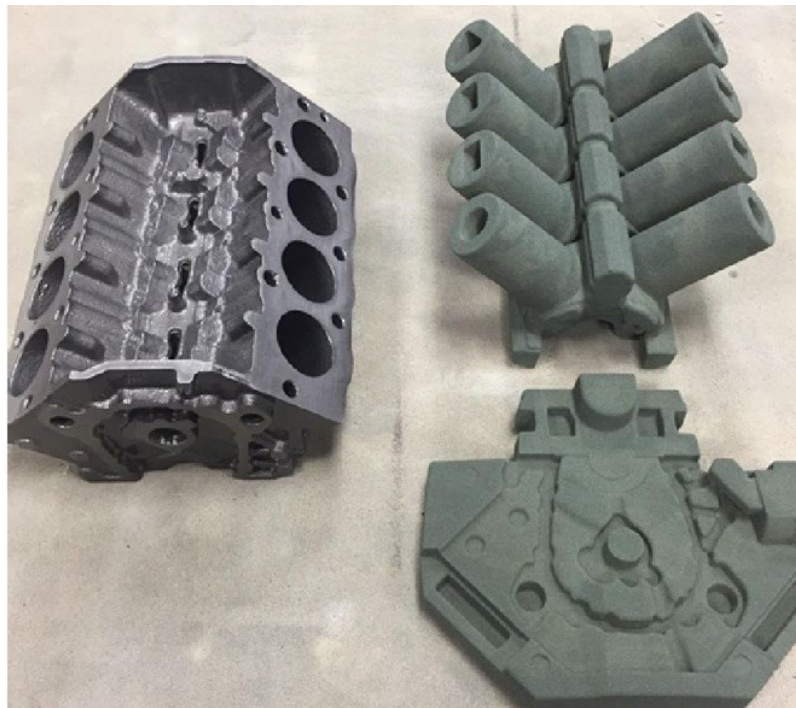


Figure 2.5: A 3D binder jetted mould was printed and then employed for casting components (18).

Unfortunately, until recent years BJ technique has been mainly considered as a process used to fabricate cores and moulds for the metal casting industry. Currently, high-productivity machines and research works in BJ have attracted more attention. Thanks to the published works that have established good know-how knowledge which contributed to the growth of using BJ and helped in the development of this technology. When comparing the BJ process and conventional powder metallurgy (PM) processes in fabricating metal parts, it can be noticed that BJ is still facing a primary challenge which makes it hard to achieve the equal density to those conventional PM processes have achieved due to the lack of compacting force during the manufacturing process which leads to low powder packability in the final part. Additionally, another cause of lower density is the shrinkage that occurs during the post-processing cycles of the printed part which affects the dimensional tolerances (6). One cause of the dimensional shrinkage is the amount of binder dispensed during the printing process. Thus, it has become a technical goal to dispense as low as possible across each layer. One main purpose of binder reduction is to control the emitted gases during the manufacturing process or sometimes during the use of the manufactured part as casting moulds. Therefore, it is an important process to sensibly choose the appropriate binder material.

Presently, a significant portion of the prevailing industrial Binder Jetting (BJ) production involves manufacturing metal components. The majority of this effort concentrates on conventional powder metallurgy alloys, particularly stainless steel. Although there is some use of bronze-infiltrated stainless steel, the norm in industrial applications is for standard alloys with high density. Despite achieving satisfactory density levels in various materials, the persistent challenge lies in minimizing defects and ensuring geometric precision. The common density attained for steel powders with gas atmosphere sintering ranges from 92% to 95%, primarily due to the trap of the residual gas from the build material or binder material (22). To further enhance the density of powder-based binder jetted components beyond 99%, Hot Isostatic Pressing (HIP) is widely employed as a standard practice (23).

Binder jetting shows great promise in processing materials traditionally challenging to machine, such as Inconel and Cobalt-chrome alloys. Notably, Nandwana et al (24) have reported a binder jetted Inconel 718 parts, as seen in Figure 2.6, with 99.9% theoretical density. This density result is greater than the reported density of 97% achieved through powder injection moulding by Özgün et al (25).

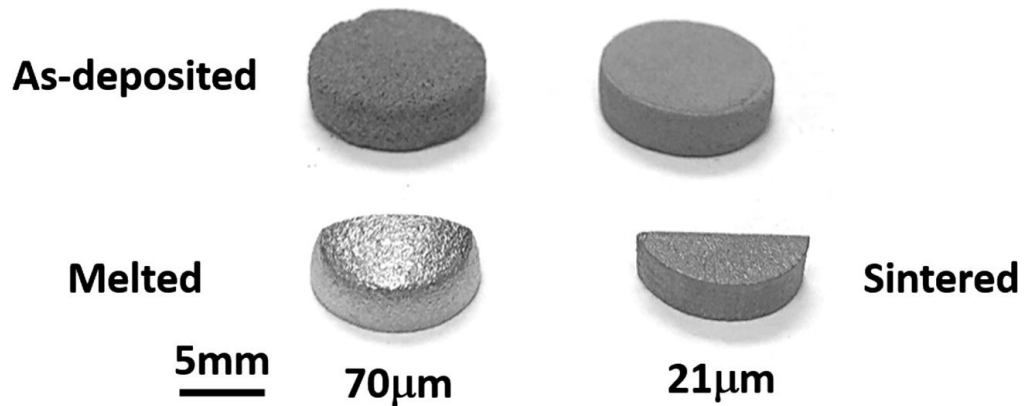


Figure 2.6: A side view showing the curvature of the 70 μm of binder jetted Inconel parts, suggesting melting and shape alteration, in contrast to the 21 μm sample, which retains sharp edges following processing at 1330 °C for 5 hours (24).

Additionally, Stoyanova et al (26) have reported a binder jetted Cobalt-chrome (Co-Cr) prints exhibit nearly twice the wear resistance compared to cast parts, attributed to the favourable microstructure of the part. Binder jetting has successfully produced other various metals, such as Stainless Steel -316L as seen in Figure 2.7, Copper as seen in Figure 2.8, and Stainless Steel -420 as seen in Figure 2.9.

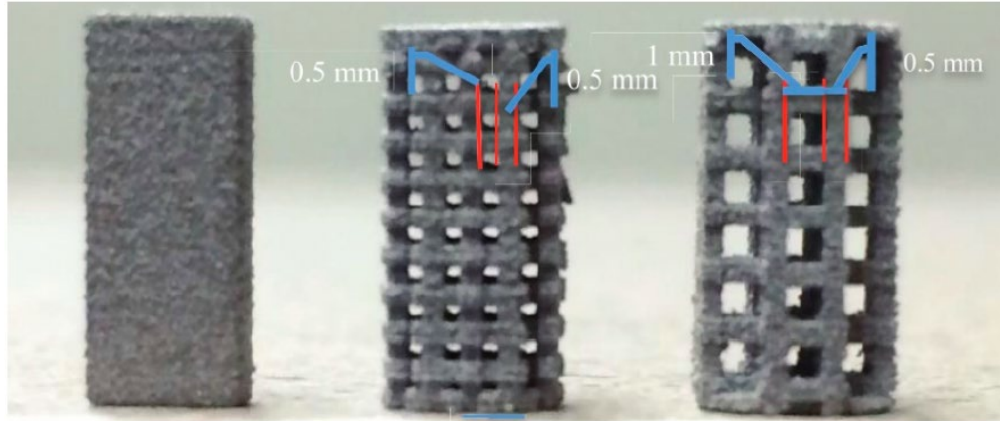


Figure 2.7: 316L SS binder jetted solid lattice, a grid lattice with a spacing of 1.0 mm, and a grid lattice structure with a spacing of 1.5 mm (27).

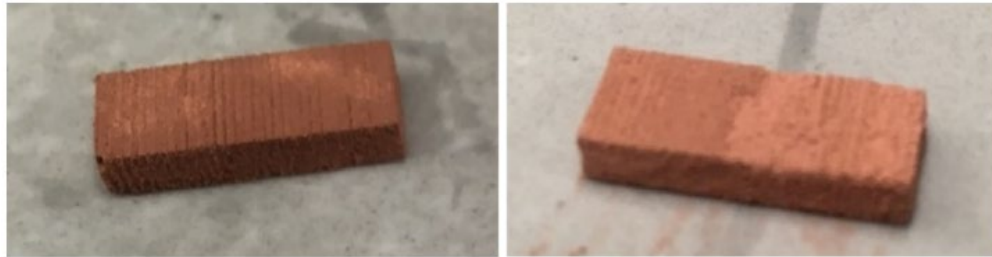


Figure 2.8: A binder jetted of copper component ($18 \times 6 \times 3$ mm) with (a) a saturation ratio of 150% and (b) a saturation ratio of 75%, observed after removal from the powder bed before sintering (28).



Figure 2.9: A binder jetted of 420 stainless steel components (29).

A study has been performed by Huang et al (30) on the binder jetting process to investigate what influences of layer thickness and binder on the printed part density and bonding strength. The study resulted in showing that the green part surface roughness is influenced by the layer thickness and binder saturation level. In addition, the experiment shows that reducing the layer thickness along with an increase in the binder saturation ratio within a certain range can give a higher green density Table 2.1. Finally, the use of excessive binder saturation could lead to poor green part density as well as layer-shifting geometry distortion.

Sample	Layer thickness (mm)	Green density (%)	Density after sintering (%)	Bending strength (MPa)	Shrinkage in X/Y/Z (%)
A2	0.1	40.1	46.7	60.8	7/9/17
B2	0.12	38.6	42.3	55.4	9/8/23
C2	0.14	36.2	40.9	42.5	11/10/26

Table 2.1: Achieved green and sintered part densities at 100% binder saturation level as adapted from (30).

2.2.1.1 Binder material

Currently, several types of binder material can be used integrated with the BJ process. The most common group of binder materials in use in contact with BJ-MAM are Ethylene glycol (EG) based binders due to their lower market price, water solubility, and burnout properties. Another group of binder formulas is that is provided by BJ system manufacturers where they make their binder formulas according to their devices. The wide range of binder material that is commonly used in BJ technology is shown in Table 2.2 along with the curing temperature and curing time of each binder material.

Binder	Materials used with	Curing temperature	Curing time
EGBE/IPA/EG (2-butoxyethanol/isopropanol/ethylene glycol)	316 SS	195	2h
EGBE/IPA/EG (2-butoxyethanol/isopropanol/ethylene glycol)	420 SS	195	2h
EG/DEG (ethylene glycol/diethylene glycol)	316L SS	200	2h
DEG (diethylene glycol)	Glass iron	200	2h
LB04 (ExOne's product)	420 SS With Cu nano	200	2h
PM-B-SR1-01 (ExOne's product)	420 SS With Si3N4	170	2h
PM-B-SR1-04 (ExOne's product)	Ti With Al	200	2h
PM-B-SR1-04 (ExOne's product)	Cu	190	2h
PM-B-SR2-05 (ExOne's product)	Cu	190	2h
Dextrin/Glycerine	Ti ₃ SiC _s	70	24h
DEG (diethylene glycol)	NdFeB	100-150	4-6h

Table 2.2: A wide range of binder material used in binder jetting technology, as adapted from (6).

It can be seen that almost all the binder materials are cured at a temperature range between 70 and 200, however, the curing time for each binder varies. Thus, it is an essential process to ensure that an appropriate binder material is being used to achieve the best green part strength that can behold together until the sintering process without any damage. Despite that polymer-based binders are considered reliable binders; they peculiarly tend to display certain limitations. The first limitation is that it is essential when burning out the polymer binder to have a refined sintering atmosphere that promotes polymer high temperatures decomposition and degassing. Second, high temperatures decomposition of polymer binder results in carbon residual which distinctly influences the final part purity thus, thermal, electrical, and mechanical properties (31). However, according to Lores et al (6) in some cases, carbon residual has great importance such as the use of residual carbon of dextrin-based binder in the fabrication of Ti_3SiC_2 composites where it permits the reaction between Ti and Si.

The differences in these binder types must be considered more in detail to achieve a better understanding of each binder approach's performance. Thus, there are several published works have also been done recently regarding the use of other types of solution as a binder material in BJ. Some of these works are metal nanoparticle suspension material, metal salts solution, and metal-organic decomposition inks which could lead to the advantage of no residual material in the process, and the solution does not require a curing cycle. The other side of using metal nanoparticle suspensions is particles tend to clog the dispensing nozzle which leads to effects on the binder dispensing process. Other disadvantages are the difficulty of dispersion of the metal nanoparticle as well as the oxidation of nanoparticles. In contrast, using metal salt will reduce the effect of the material Clogging on the nozzle. Additionally, the shelf life of metal salt is longer than other types of solutions. However, the metal content is limited to salt solubility. Moreover, Metal-organic decomposition has the advantages of Lower metallisation temperature than the previous types aside from

Controlling the precipitated particle size and better solubility. Yet, the metal content in this solution is limited and it gives low green part strength.

A recent study made by Williams et al has experimented with the use of copper nanoparticle suspension instead of the use of traditional organic binder in a modified BJ process called by the authors 'Binderless Jetting' (28). In this study, the main purpose of the authors was to replace the organic binder with nanoparticle suspensions to benefit from the advantages of eliminating the need for a specific sintering atmosphere to properly burn out the binder and release unwanted gases. Other advantages are, eliminating the need for a de-binding cycle and the absence of binder residuals. Additionally, the authors have used an adjusted BJ system that includes inter-layer drying and curing conditions for 2 minutes at a temperature of 260 °C. this interlayer process is done by passing an overheating heater above the powder bed and maintains the powder bed surface at a certain temperature to sufficiently dry the printed layer. The results of this study indicate that the sintering necks of the used copper nanoparticles can be generated at a temperature just below 300 °C due to the use of additional inter-layer drying and curing conditions. The study also resulted in an increase in the green part strength of 150% at a 140% copper nanoparticle suspension saturation. however, the sintered density of green nanoparticle bonded parts showed slightly lower density results compared to green parts of organic binder bonds (6). In the sand-casting industry, the binder types that are applicable for fabricating sand moulds are itemised into nine different types which are organic liquids, solvents, metal salts, inorganics, in-bed adhesives, sintering aids/inhibitors, acid/base systems, phase-changing materials, and hydration systems (32). Néel et al (8) indicate that the choice of binder material sometimes depends on the 3D printer's capability. A good example is, Voxeljet and ExOne machines approve the use of an organic binder, phenol-based binder, and furan-based binder.

Another binder material used in the BJ process is the use of sodium silicate as a binder material. Sodium silicate, commercially known as sodium water glass, is a liquid solution that contains some dissolved glass in water. This solution has a low market price compared to its excellent adherence properties. Thus, it has been widely used as a resin material, sealant formula, and binder in the AM processes. As it is considered an electrolyte solution, it is a typical inorganic polymer solution that shows the properties of both electrolytes and polymers. Research work was made by Yang et al (33) to measure the static and dynamic viscosities of the solution using a range of concentrations where the authors have used a commercial sodium silicate solution (made by Wuhan Longda sodium silicate Co. Ltd., China). The study has resulted in showing that static and dynamic viscosities increase dramatically with the variation in concentrations from 15 to 55% and they decrease with the raising temperature from 15 to 70 °C. Snelling et al (34) have conducted a series of experiments to investigate the potential differences, created by using four different commercially available binders' systems, in the material properties. The four commercially available binders are ExOne Sand Materialization (Furan Resin with Binder Catalyst), Alkyd 18-415 with Alkyd 23-217 Coreactant (Alkyd Resin and Catalyst), Super Set 942 with TW30 (Furan Resin and Acid Catalyst), Chem Bond 490 with Chem Bond 260 (Sodium Silicate Resin with Glycerin Catalyst) and Phenoset-RB Part 1 with APR-015 Part 2 (Phenolic Resin with Acetate Ester Catalyst). The experiments focused on tensile strength by testing the mechanical characteristics of the particle bonding of the 3D printed parts and the burnout characteristics as the amount of released gas was measured during the binder burnout cycle. The experiments showed that the ExOne systems, containing a furan binder with a binder catalyst, present a stronger yield due to a well-controlled binder and building material distribution. However, the experiment proved that ExOne systems had a higher burnout temperature as compared to the remaining binder systems.

An effort has been made that compare two commercially used resins to bond Nd-Fe-B magnets which are sodium silicate and epoxy resin (35). The study resulted in that; better properties were achieved in the Nd-Fe-B magnet structure built with sodium silicate. A year later, Liu et al (36) have made a study that investigates the effect of the sodium silicate binder's curing time and temperature on bonded Nd-Fe-B-based permanent magnets. The study mainly focuses on three principal properties which are mechanical strength, part microstructure, and magnetic properties. In this work, the sodium silicate was used as a binder to fabricate Nd-Fe-B magnets that enhanced better mechanical strength and improved thermal stability. As a result of this experiment, sodium silicate was completely cured at a temperature of 175 °C for 40 minutes this was observed by the fracture surface morphology. Additionally, the magnet parts that are prepared under this condition have exhibited optimal properties. Moreover, it has been noticed that as the curing time and temperature increase, the combination of the structural powder material and the sodium silicate binder turns out to be more constricted thus the structure grows into a stronger and crumblier structure.

Another type of binder material used in the binder jetting process is Polyvinyl alcohol (PVA). PVA finds diverse applications ranging from the textile industry to specialized biomedical applications (37). Using PVA as a polymer binder at an approximately 5% weight concentration is environmentally safe and non-toxic. Granulated PVA is commercially available with molecular weights ranging from 10,000 to 200,000 g/mol and is offered in various degrees of hydrolysis (38). Hydrolysis measures the extent to which a polymer dissolves in water. Fully hydrolysed PVA, resulting from extensive hydrolysis, exhibits dissolution temperatures above 80°C and requires a prolonged period for dissolution, especially when the PVA has a high molecular weight. Once fully dissolved, the OH groups of entirely hydrolysed PVA form robust hydrogen bonds with water molecules, contrasting with the OH groups of PVA with lower hydrolysis levels.

In the context of Binder Jetting (BJ) additive manufacturing, the ideal binder should possess high infiltration capacity, optimal levels of vertical infiltration, and effective lateral spreading. During powder bed processing, the surface tension and viscosity of the binder play crucial roles in determining its lateral distribution and vertical penetration. These properties are directly influenced by the molecular weight of PVA (39). A study by Paul et al (40) examined low, medium, and high molecular weight PVA-based liquid binders with respective molecular weights of 10,000, 25,000, and 84,000 g/mol. It was found that the medium molecular weight PVA-based binder outperformed the other two due to its lowest contact angle with the powder (27 degrees). The optimal polymer chain of the medium molecular weight PVA and the relatively low viscosity of the binder's water base contributed to its effective hydration action compared to other PVA-based binders.

2.2.1.2 Rheological Characterisation of the Binder

Binder's viscosity

The primary objective to assess the binder's viscosity at various temperatures, is to understand how the binder interacts within the context of vertical infiltration and lateral spread upon contact with a powder bed. To accomplish this, the dynamic viscosity of the binder can precisely determine, employing a Modular Compact Rheometer (MCR 502e, Anton Paar GmbH, Virginia, United States (41)).

As a point of reference, standard water properties were considered, under The International Association for the Properties of Water and Steam (IAPWS) (42) (43). This analysis of the binder's dynamic viscosity under different thermal conditions not only contributes to a deeper comprehension of its behaviour but also provides insights into the benchmark properties of water. The substantial reduction in water viscosity across the tested temperature range highlights the sensitivity of this property to variations in temperature, an aspect that is particularly relevant for a wide array of applications where precise control over binder characteristics is important.

Binder's surface tension

In BJ, it is identified that the central role that surface tension plays in the properties and performance of the binder sample. As such, a thorough investigation and analysis of this parameter to gain a deeper understanding of its implications is necessary. surface tension can be determined by using the Tensiometer (BP100 manufactured by Krüss in Hamburg, Germany (44)). This device is designed to provide precise measurements of surface tension, making it an ideal choice for research needs. The methodology commenced with a thorough calibration process. Calibration is a critical step to establish the baseline for accurate measurements. During this phase, a precise determination of the capillary diameter has been done by calculating the surface tension of a calibration liquid with a known and well-established value. The use of deionized water in its liquid state as the reference substance ensured the accuracy and reliability of the calibration process. This reference substance, with its well-understood properties, allowed to validate the performance of the Tensiometer and served as a benchmark for the measurements of the binder sample.

Ohnesorge number

The fundamental aim of this rheological analysis of the binder, encompassing measurements of viscosity and surface tension, is to ascertain the binder's suitability for consistent dispensing through a variety of nozzle orifice sizes and over extended periods. It is essential to determine whether the binder could maintain its dispensability under varying conditions and time frames. To achieve this objective, the Ohnesorge number, indicated as "Oh" is used (45). The Ohnesorge number is an essential dimensionless parameter in fluid dynamics, enables to assess and predict the behaviour of the binder under various conditions by using the following equation (46):

$$Oh = \frac{\mu}{\sqrt{\sigma \rho L}}$$

In this equation, μ symbolizes the dynamic viscosity of the liquid. Additionally, σ represents the surface tension of the liquid. ρ is the symbol that represents the density of the liquid. L is the symbol that represents the diameter of the nozzle orifice. By evaluating this number, valuable insights into the ability of the binder to be consistently dispensed through nozzles of different sizes can be gained while accounting for sequential variations.

Z-number

Z number is a numerical value holds significant importance in characterizing the behaviour of liquid droplets in the context of 3D printing processes. Researchers have proposed a dependable range for Z values, implying that $10 > Z > 1$ represents a reliable domain for droplet formation based on the investigations conducted by Derby et al (47). This suggests that as the Z value approaches or equals one, the ejection of drops becomes hindered due to the effects of viscous dissipation. Conversely, when the Z value equals or approximates ten, the primary drop is accompanied by a considerable number of satellite droplets (47). Nevertheless, in practical scenarios, it is feasible to 3D print with liquid materials possessing Z values significantly higher than 10, provided that the satellite droplets effectively coalesce with the primary droplet. Various studies have demonstrated the possibility of printing using common liquid materials characterized by low viscosities ranging from 0.4 to 2 mPa.s and surface tensions spanning from 23 to 73 mN/m. In these cases, the Z number values for these liquid materials fall within the range of 21 to 91 (48).

2.2.1.3 Binder Burnout

Due to the use of liquid binder material in the binder jetting process, the green printed body must be subjected to a calculated temperature for a considered time to remove most of the binder used in geometry generation. The unburned or trapped binder material can lead to part failure where it holds the binder in between the part powder material. One example of affecting the final casting part quality is the experiment done by Meisel, Williams, and Druschitz. In their experiment, they failed to cast a complex cellular structure by using 3D-printed moulds in their initial attempts due to partial filling of the mould at the bottom of the cellular structure. The main reason for this issue was the evaporation of the binder material when it was exposed to the melting temperatures of the cast metal (49). For this reason, the appropriate burnout time and temperature must be considered when using each binder material to insure the full burnout of the binder. Truong et al (50) made an experiment where they used a binder mixture of isopropanol (IPA), ethylene glycol monobutyl ether (EGBE), and ethylene glycol (EG). These three binder materials are burned out at a temperature of below 198 °C. IPA and EGBE were evaporated at lower temperatures, 80.4 °C, and 171 °C respectively. The third material of the mixture has boiled at a temperature of 197.3 °C. Another effort has been made by Snelling et al (34) where the authors made a comparison of four different commercially available traditional chemically bonded sand binders. These four commercial binders are ExOne Sand Materialization, Alkyd 18-415, Alkyd 23-217 Coreactant, Super Set 942 and TW30, and Chem Bond 490 and Chem Bond 260. The motivation of their experiment was to study the effects of binder material in 3D printed sand moulds on castings. The results of this study have shown the differences in the binder burnout temperature as they were 300 °C, 250 °C, 300 °C, and 450 °C for ExOne Sand Materialization, Alkyd 18-415, and Alkyd 23-217 Coreactant, Super Set 942 and TW30, and Chem Bond 490 and Chem Bond 260 respectively.

2.2.1.4 Sintering

According to Rahaman, the sintering process is an essential stage in three main disciplines of manufacturing industries which are the ceramics manufacturing industry, powder metallurgy manufacturing, and the agglomeration of ore fines (pelletising) (51) and (52). Thanks to recent research and development which made the powder metallurgy and ceramics industries have been developed systematically to a large extent in the last decade which gives the chance to the development of the BJ technology (53). Thümmeler, 1967 has summarised the sintering process into three main stages which are, the early stage of neck growth, the stage of densification and grain growth, and the final stage with closed pore spaces. In the first stage, the particles of the powder material are in an individual manner as there is no strong grain growth occurring takes place. The neck growth happens according to an exponential time law. Due to the surface tension, the tensile stresses sustain the grain boundaries between two adjacent particles, but new grains are likely to be occasionally formed and particles' midpoints can be slightly approaching each other. In the second stage, most of the distinct particles change their behaviour and start to act to lose their individuality. Then, the formation of a coherent network occurs causing full-body shrinkage Figure 2.10a. Once 90% of the density is exceeded, a notable increase takes place in the proportion of closed pore spaces. at the final stage, the isolated pores start to form a spherical shape and the densification process is proceeding slowly to form a densified body Figure 2.10b (52).

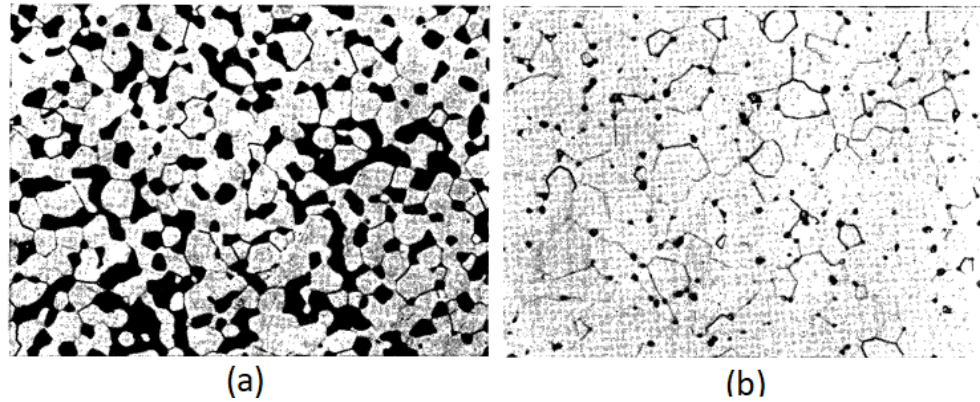


Figure 2.10: (a) The stage of densification and grain growth (b) The final stage with closed pore spaces (52).

According to the Company of Inovar Communications Ltd, the sintering process is a process that applies a heat treatment process to an unfinished previously manufactured powder compact, where powder particles are held together by cold welding, to improve the connection between the powder particles of the green body. This heat treatment temperature is just below the melting point of the powder material. At the specific sintering temperature, the diffusion process leads to the formation of necks, and then these nicks grow at these contact points. The sintering process is generally achieved in a continuous furnace that usually is chosen by cautious choice due to the sensitivity of the furnace atmosphere and temperature profile throughout the furnace (54).

To show the influence of the sintering process on the final part properties, McKenna et al (55) have conducted research that focuses on the permeability and compressive strength of printed parts. The experiment method was to 3D print 13 samples of Zcast 501 powder and resin binder of ZB56 then change the curing time and temperature of each sample to investigate the influences of these parameters on mechanical characteristics, such as strength and permeability. As a result of this experiment, a mathematical model was developed that allows optimising curing time and temperature to get the required permeability and compressive strength. Truong et al

(50) have reported a modified BJ process that can fully sinter the powder particles after the binder burnout phase under an isothermal condition. In this study, Material Research Furnace was used to sinter the compact powder after the binder burnout phase. The powder materials used in this experiment were two different stainless-steel material grades, SS 420, and SS 316. In general, the sintering of the stainless-steel powder part is usually done in a furnace with a hydrogen environment yet, the authors preferred to use argon or nitrogen gas instead. The reason for using nitrogen or argon gases was to avoid the decarburization of graphite liners inside the furnace. However, using the nitrogen gas in a closed environment furnace could form nitride in the stainless-steel powder which leads to affect its corrosion resistance properties. On the other hand, the use of Argon gas as an inert gas in sintering metal materials like stainless steel and copper has been reported in many published works. Goudah et al (56) have successfully sintered copper parts produced with metal injection molding using argon as an inert gas. Comparably, Shaari et al (57) have used argon gas in the sintering process to investigate the impact of sintering parameters on the Cu/CNTs composite material. Moreover, another work has been made by Serafini et al (58) where the green compacts underwent sintering in an argon atmosphere, utilising a thermal cycle that involved heating up to a sintering temperature of 1240 °C. Furthermore, the effects of sintering temperature and the addition of TiH₂ on the sintering process of Cu have been investigated by Hao et al (59). Thus, argon has been used as an inert gas in sintering the processed samples In this work.

2.2.2 Laser Powder Bed Fusion

Laser Powder bed fusion (L-PBF) is considered one of the AM processes that use metal powder particles to produce final components. The L-PBF processes, including Selective Laser Sintering (SLS) and Selective laser Melting (SLM), are mainly used to additively manufacture metal parts. Recently, L-PBF has attracted more attention due to the lower production time and production costs, lower capital investment, and less technological complexity. This gained interest helps the laser-based powder bed system to become wider than the electron beam-based systems (EB-PBF). Besides, the building envelopes of the L-PBF have been developed and reached 1m^3 which allows the manufacturing of larger parts compared to EB-PBF. However, the use of EB-PBF is preferred in the case of dealing with high-cost crack-susceptible alloys such as TiAl alloys due to lower residual stresses. Thus, in this case, the high production cost is balanced by the higher added value to the final component (60). In L-PBF processes, the state of the manufacturing material is powder particle material. Additionally, L-PBF techniques must have a controlled building environment, a container of powder material, a powder spreading system, a roller to keep the powder layer aligned and a laser to sinter or melt the selected powder area Figure 2.11.

Selective Laser Melting is simply a method in which the powder is fed from a powder delivery box followed by a roller or rake that spreads the powder equally into the powder bed envelope. Next, a beam of lasers is selectively subjected to the distributed powder to melt and fuse the powder particles. These particles solidify as soon as the laser beam passes through the selected area and then the creation of the first layer occurs. The process is then repeated for several iterations that equate to the number of slices until the component is fully produced. After the completion of the process, the unused/un-melted powders are removed leaving the finished final component. The entire manufacturing process can be summarised into six steps. The first step is the powder spreading to form the first powder layer. Then, level the previously spread powder in the building envelope. After that, direct the laser for

melting and solidification of the selected area. Following, the building platform goes down for a distance equates to layer thickness. Next, the repetition of the previous steps until the building process finishes. Finally, the removal of the unused powder and then extracting the final component. Due to the simplicity and the general AM advantages, the use of the SLM process has become wider due to its unique advantages. The first advantage is the capability to obtain better geometrical tolerances, dimensional tolerances, and the ability to achieve high relative densities compared to other AM processes. Another advantage is the low waviness in the final component surface which leads to minimum post-processing works. Also, the SLM process is capable of manufacturing parts with thin and thick cross-sections (60). Thanks to these advantages have led to establishing know-how knowledge which contributed to the development of SLM technology.

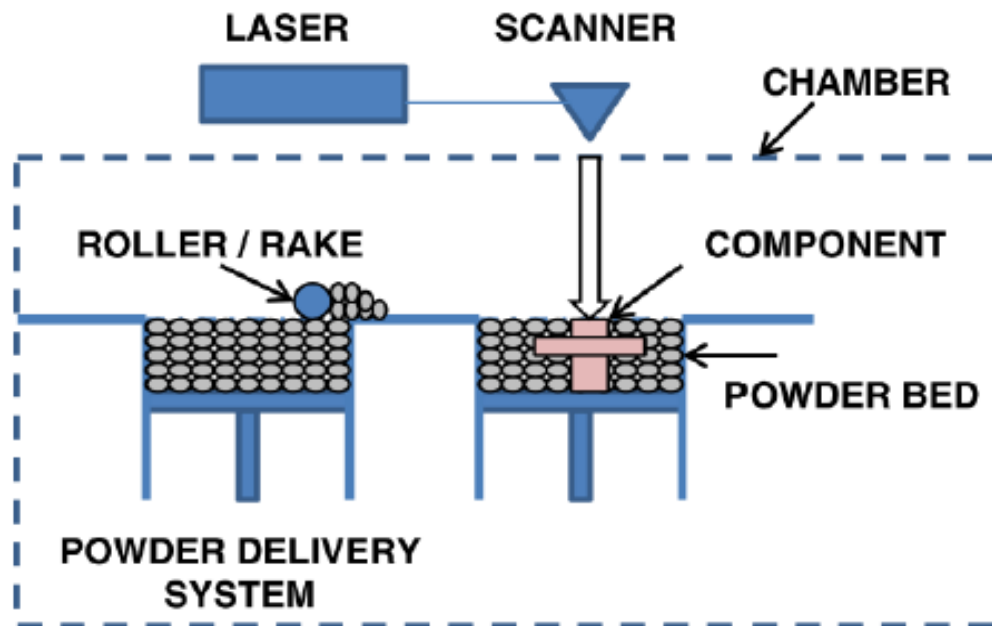


Figure 2.11: A schematic representation of a laser powder bed fusion (LPBF) process (61).

However, the SLM process can lead to the occurrence of some effects caused by process-related defects. These defects are summarised as follows (60);

- The incompleteness of the fusion between powder particles and the appearance of porosities at the part's surface.
- The occurrence of high residual stresses leads to cracks, distortions, or delamination of the final manufactured component.
- The occurrence of cracks in susceptible alloys and metastable microstructures resulted from high cooling rates.

Other process-related defects can occur by using a recycled powder, the powder that was unused/un-melted in the previous manufacturing process. Using the remaining non-used powder that was removed from a previous building process could result in some part defects as the powder is believed to have developed different mechanical and chemical properties such as morphology, particle size distribution, and chemical composition. These changes in properties could affect the powder flowability during the building process and the packing density of the final part. An effort has been made by Cardiff University and Renishaw Plc where the authors investigated the effects of additively manufactured parts using recycled Ti-6Al-4V powders in SLM. In this study, the authors conducted a series of experiments where they used the recycled Ti-6Al-4V powder across five repeated builds. In the beginning, they loaded 40kg of virgin Ti-6Al-4V powder into the SLM machine and built the first component. After the first build, the unused powder has been collected and filled in the powder container to re-introduce it in the next building. Next, the introduced powder is used to produce another identical component. The process was repeated until producing the fifth component. The five components have been tested to determine the change in the mechanical and chemical characteristics. The study concluded with, an observation of an increase in the diameter values and change of particle shape through repeated recycling. Additionally, minor changes to the chemical composition of the Ti-6Al-4V powder (62).

2.2.3 Directed Energy Deposition (DED)

The Directed Energy Deposition technique (DED) is one of the AM processes that employ an electron beam, plasma arc, or laser beam as thermal energy to melt and then fuse the fed material to build the final shape as seen in Figure 2.12. The feeding material can be a powder material dispensed from a nozzle or a wire filament injected by a heated nozzle. The DED technique is also known as metal deposition or directed metal deposition due to the popularity of the process for producing metal parts, although some DED sub-processes are used for non-metal production. The DED system has gained the reputation of the ability to deposit feeding material along four or five axes. This feature makes the DED process become one common AM technology used for repairing worn parts and tools. The DED technique is divided into several sub-processes regarding the delivery of the focused thermal energy. The most common sub-processes are Laser Engineered Net Shape (LENS), Electron Beam Additive Melting (EBAM), Rapid Plasma Deposition (RPD), and Powder Blown Laser Cladding (PBLCL) (63).

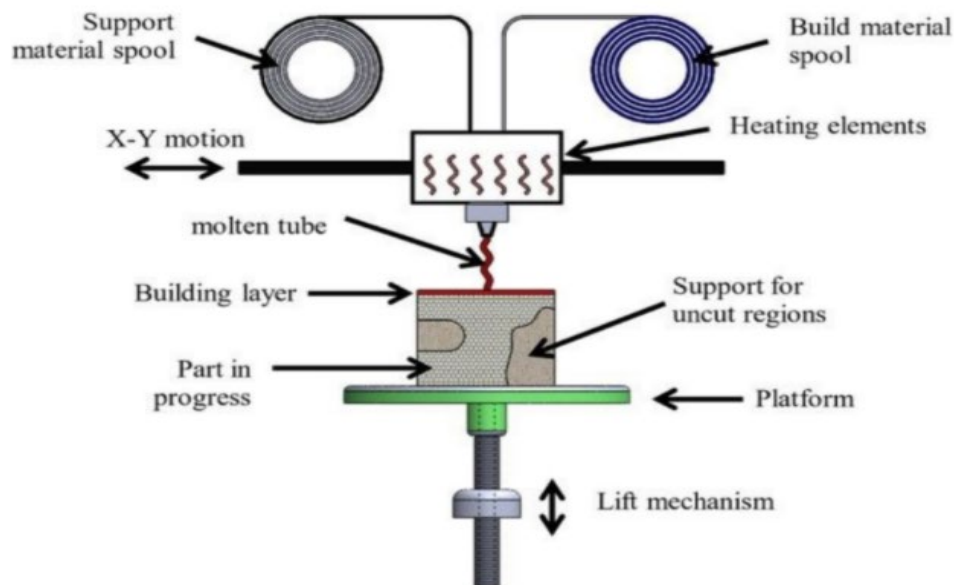


Figure 2.12: A schematic representation of a wire filament-based Directed Energy Deposition (DED) process (63).

2.2.4 Powder blown Laser Cladding (PBLCL)

The process of PBLCL, also known as Powder Feeding Technology or Laser Melting Deposition, is a process that employs an extremely focused laser beam as thermal energy to selectively melt the feeding powder material jetted into the heated chamber. area. The process operation is described, first, the powder material is blown via one or more side feeding nozzles or powder feeders into a melting pool generated by the laser as seen in Figure 2.13. Then, the powder melts and makes a bond to the neighboring powder when fused. After the bonding occurs, the process continues to build up the part in a layer-by-layer manner (64).

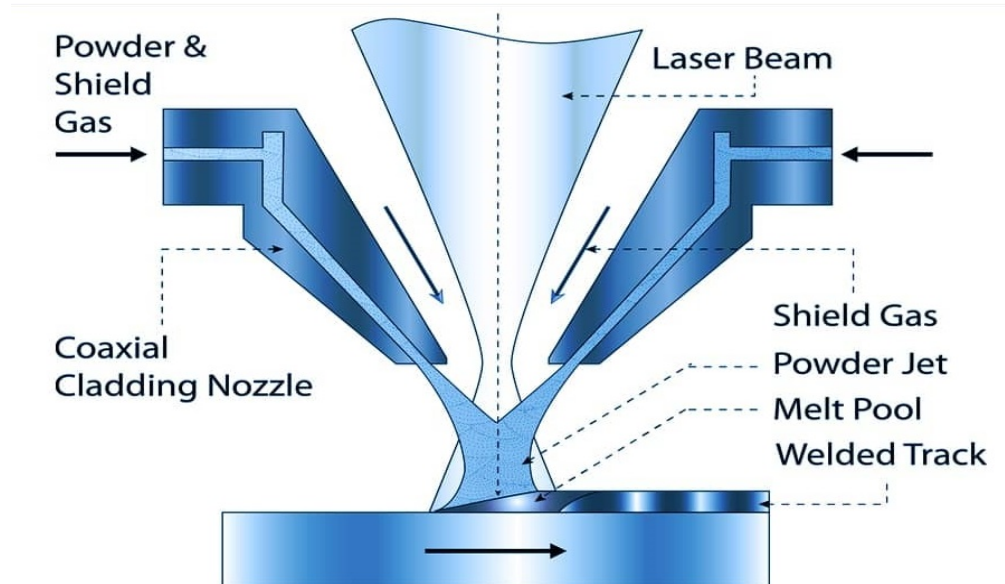


Figure 2.13: A schematic representation of Powder Blown Laser Cladding (PBLCL) (65).

According to J. Liu and his team, the PBLCL system is commonly used due to the advantages of the production of lightweight components, short production time, and unique design freedom. Additionally, this process has the capability of repairing existing parts using the same or different powder material. Furthermore, one of the PBLCL's applications is aerofoil production where it is capable of producing lower-

weight components with a high strength-to-weight ratio which leads to a reduction in the process manufacturing time by around 80% and a 20-50% decrease in cost. In comparison with the conventional manufacturing processes, PBLC has better corrosion and wear-resistance coatings, thus it is used in the automotive industry with engine manufacturing by General Electric and Rolls-Royce (64). Another effort has been made by Song. et. al to investigate the capability of using PBLC to coat a boiler tube in which this coating resists the fireside corrosion of the tube and to study the ability of the process to build a structure on an existing part of a different material. As a result of this study, the PBLC process has proven the ability to successfully build a Ni50Cr structure on an existing 304 stainless steel part (66).

2.2.5 Extrusion

The AM Material extrusion process is considered one of the most common ways to produce plastic and metal parts for prototyping and can be used to extrude metallic and non-metallic materials. The extrusion process is also known as Fused deposition Modelling (FDM), Melt Extrusion Manufacturing (MEM), and Fused Filament Fabrication (FFF). Material extrusion was first introduced in 1989 by Scott Crump when he patented the new AM technique. Followed by the introduction of the FDM process in 1990 by Stratasys company, the co-founder of Scott Crump (67). At that time, the process was meant to be a process to produce rapid prototyping as most of the AM-produced parts have been for presentation models and visual aids, however not necessarily used as functional prototypes. In 2010, Stratasys extrusion-based AM technology, FDM, became the most widely AM technology. Lately, in 2010, 15,000 FDM machines were installed world widely. Stratasys then started to provide several commercial FDM systems, large to small-scale machines, producing different materials, colours, and grades. Recently, FFF systems have mostly dominated the personal fabrication market due to the rapid growth in demanding personal desktop AM systems as well as the open-source RepRap project. This growth and popularity of

the extrusion process started after the expiration of the initial Stratasys patents registered in 1989, in addition to the simplicity and low cost of extrusion system construction (68). The extrusion process operates in the same concept as the hot glue gun where a rod is injected inside a heated chamber and then it is deposited in a semi-solid condition. To explain it more, it functions mainly to extrude a semi-solid filament through a modified nozzle that contains pinch roller mechanisms by applying mechanical or pneumatic pressure. The filament material that crosses the nozzle is heated by a heated liquefier to a calculated temperature depending on the feedstock material to adapt the flow properties of the extruded material. The nozzle then moves in the horizontal x-y plane while extruding the material into the building platform which moves in the Z-axis as seen in Figure 2.14 (4).

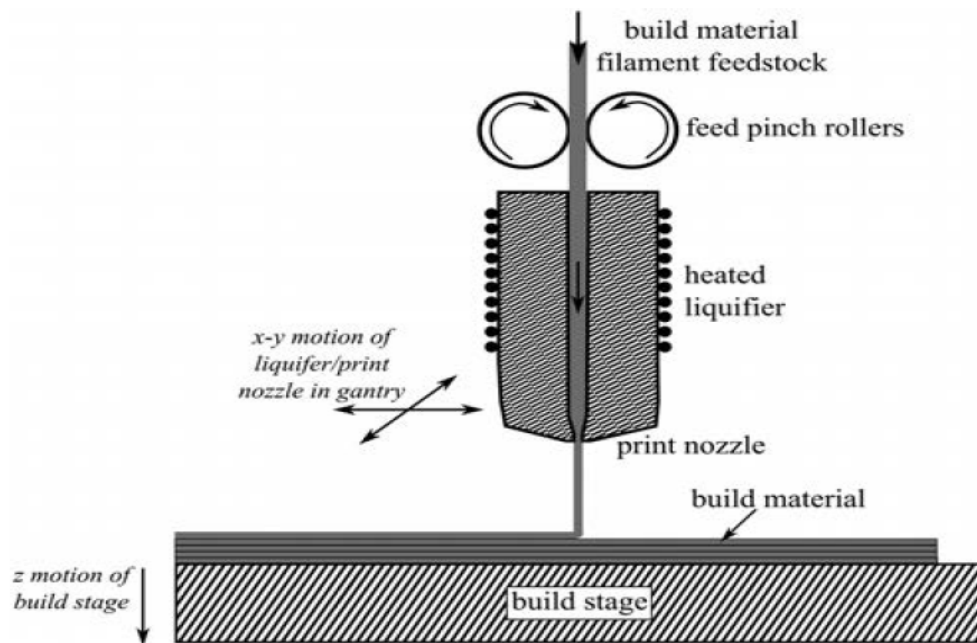


Figure 2.14: A schematic illustration of a Metal Extrusion-based AM process, as adapted from (68).

2.3 Porosity in Additive Manufacturing Processes

Porosity is a phenomenon characterised by the presence of cavities and voids dispersed throughout the volume of a sample, resulting in affecting the final density of the sample bulk. The influence of internal pores on the mechanical properties of metal is widely acknowledged in the literature (69). Pores can result in stress concentration, reduction in the loading area, and the initiation and propagation of cracks (70) (71). This occurrence, of cavities and voids, has been recognised as a significant difficulty encountered in the context of various manufacturing processes and operations (72). Processes unfailingly involve the solidification of a molten pool which have the size of which can vary considerably ranging from large dimensions, such as castings, to more diminutive proportions in the domain of a variety of welding techniques. Generally speaking, the formation of cavities and voids in these manufacturing procedures and techniques is attributed to the entrapment of gaseous impurities released from the molten metal reservoir during solidification (73). Katayama et al (74) investigated the welding process applied to stainless steel by using a laser to melt the metal, ultimately identifying porosity as a result of the entrapment of bubbles within the weld pool as a result of interaction with the solidifying front. These bubbles, ascribed to the evaporation of metals resulting from the complex interaction between the laser and the metal, were identified as a contributing factor. Matsunawa et al (75) have observed that the occurrence of porosity in the laser welding process can be attributed to the presence of unstable keyhole phenomena, as well as identifying a significant correlation between void formation and the choice of shielding gas configurations. Similar principles apply to using SLM where a study has been done and reported that pore trapping after the laser was switched off for stationary laser melting (76). Similarly, Khairallah et al (77) also evaluated the possibility of key-hole closure as an explanation for the production of porosity. On the other hand, in the Binder Jetting process, there is an absence of pores in the green component throughout the printing process. The occurrence of minuscule pores are binder-jetted components is often observed after the sintering

stage. In contrast to other techniques such as Selective Laser Melting (SLM) and Electron Beam Melting (EBM), Binder Jetting does not include the process of direct material melting and pool formation. Thus, the mechanisms through which porosity develops in SLM and EBM are not applicable in the context of Binder Jetting. Sintering plays a crucial role in the final quality of Binder Jetted objects, exhibiting similarities to the operational principles employed in Metal Injection Moulding (MIM). Both techniques include the use of binders, followed by subsequent operations like binder removal, sintering, and maybe additional heating procedures following printing (40). Sung et al (78) conducted a study on the effect of the sintering cycle on stainless steel products' porosities manufactured by the Metal Injection Moulding (MIM) process. The researchers discovered that the presence of pores in the sintered products decreased significantly from 39% to just 1% using a sintering temperature range from 900°C to 1350°C in the stainless-steel products. It has been observed that elevated sintering temperatures resulted in enhanced particle cohesion, leading to improved component quality and reduced porosity. A study conducted by Machaka et al (79) have investigated the potential influence arising from the size of powder particles and their interaction with the binder material using powder particle sizes around 5 µm. The presence of extremely fine powders led to the occurrence of agglomeration when they came into contact with the binder. This agglomeration hindered the uniform removal of the binder (de-binder), leading to the creation of voids throughout the bulk of the produced samples. Nevertheless, there exist some factors that have significance in MIM but lack relevance in the context of BJ. In the context of the MIM process, many aspects such as material ejecting temperature, flow behaviour, and slurry rheology significantly influence the outcome when compared to the BJ process. In the BJ process case, some studies stated that the cause of the occurrence of voids can be attributed to the powder morphology, extreme binder saturation level, and inter-layer spacing (80) (81). However, some other studies, which focused on the issue of density and porosity of 316L stainless steel parts manufactured using the BJ process, have concluded that the presence of voids in the fabricated components may

often be attributed to the sintering procedure when research conducted by Mirzababaei et al (5) investigated the potential causes for the presence of voids in components produced using the Binder Jetting additive manufacturing technique, with a special focus on 316L stainless steel. The observed occurrence of holes can be attributed to inadequate particle cohesion during the sintering process.

Sintering temperature affects densification during sintering through transformational phase shifts in the material. For the 316L stainless steel, a dramatic structural transition occurs at temperatures above 1200°C when austenite, which has a face-centered cubic (FCC) crystal structure, becomes delta-ferrite, which has a BCC crystal lattice. Due to its faster diffusion rate than austenite, delta-ferrite enhances densification, making this phase transition crucial (82). When the sintering temperature exceeds 1395°C, another densification process activates. The material's liquid phase enhances this. Capillary forces affect the solid matrix due to this liquid phase. To reduce the interfacial area between solid components, capillary forces reduce solid material porosity. Thus, the sintering temperature is crucial to densification. Understanding how sintering temperature, phase transformations, and liquid phase formation interact is crucial to optimising sintering processes and improving material densification, which has broad implications for the production of advanced materials with tailored properties.

According to Verlee et al (83), as the temperature rises to almost the melting point, the material's pores shrink and become localised inside grains. This heat shift increased the system's total free energy due to the physical separation of pores from grain boundaries. This separation created new material interfacial regions. This microstructural behaviour depends on the main diffusion process. Volume diffusion was found to be crucial to these phenomena after extensive investigation. The fact that relative grain growth outpaced relative densification in this scenario suggests that volume diffusion is more important. Note that volume diffusion is slower than grain boundary diffusion. Thus, the isolated holes in the grains prevented complete densification. As temperature rises, pores expand and reappear at grain boundaries.

Importantly, this shift did not reduce the material's total pores. The main change was pore size increasing as temperature rose (84).

To show the effect of the sintering time and temperature of the final product, Verlee et al (85) conducted an experimental study to determine how sintering factors, such as temperature and holding time, affect component qualities. The main focused material in this study was 316L stainless steel. The sintering process took place in a batch furnace with regulated hydrogen. The sintering temperatures ranged from 1200°C to 1430°C, and fixed temperatures were held for different periods. After that, the Archimedes technique was used to evaluate density and open and closed porosity. The authors found that the sintering temperature and time have a direct effect on the sintered components' density. The study indicated that raising the sintering temperature increased final density as it increased from 77% to 98.7% when changed the sintering temperature from 1200°C to 1425°C. In addition, the authors systematically adjusted the sintering time from 1 to 300 minutes at 1315°C, 1335°C, and 1345°C within their experiment. Accordingly, their research showed a strong correlation between sintering time and material density. At a given sintering temperature, final density correlated linearly with sintering duration up to 89%. Densification decreased after this crucial point, indicating a slower material density rise as sintering time increased. Remarkably, the ultimate stage of sintering, characterized by maximum density, required a minimum dwelling time of 90 minutes at each specified sintering temperature. Consequently, Verlee et al (85) found that the sintering profile—including time and temperature—determines the product's porosity. Importantly, sintering time and temperature determine the range and distribution of pores, including open and closed porosity percentages. Another effort has been made by Juan et al (86) who examined the impact of sintering dwelling time on the final density of the samples of 316L stainless steel. The sintering procedure encompassed different durations of 90 minutes, 360 minutes, and 1440 minutes, carried out at three discrete temperatures: 1300°C, 1356°C, and 1380°C. The research findings provided significant insights into the correlation between the duration of

holding time and the ultimate density of the sample. The experimental results indicate that an increased dwelling time during the sintering process at a temperature of 1300°C resulted in a notable improvement in the ultimate density of the 316L samples. To clarify, it may be stated that extended durations of exposure to this specific temperature led to an increase in material density, which suggests a higher level of densification. In contrast, a distinct pattern was seen for samples that underwent sintering at a temperature of 1356°C. The maximum attainable density was achieved during a holding duration of 360 minutes. Interestingly, the sintered density did not exhibit any further improvement when the holding duration was extended beyond this crucial threshold. The aforementioned observation might be ascribed to the phenomena of pore coarsening, which involves the enlargement of pores within the material without a concomitant decrease in their total count. The prolonged duration of holding at a temperature of 1356°C seems to facilitate the expansion of pores, thereby impeding any further augmentation in material density. These presented investigations highlight the significant influence of the duration of sintering holding time and sintering temperature on the final parts' densities. The duration of holding time required for best results is dependent on the sintering temperature since distinct processes drive the densification process at different temperature ranges. The results of the previous studies provide significant insights into the field of materials science and sintering processes. They explain the complex relationship between sintering temperature, holding time, and pore behaviour, which is crucial for enhancing material densification and maintaining the quality of sintered products across various industrial sectors.

2.4 Multi-material Additive Manufacturing

This section reviews several multi-material additive manufacturing deposition techniques. These techniques are reviewed concerning their requirements, possibilities, and limitations to better understand the manufacturing process. Some AM systems are natively capable of additively producing multi-material of two or more material parts without altering the process such as 3D printing with extrusion or jetting direct material. In contrive, other 3D printing systems such as Powder bed fusion (PBF), Stereolithography (SL), or Binder jetting (BJ) require some process adjustments to achieve multi-material products.

2.4.1 Material Building Categories

The primary success of fabricating a high-quality part in AM technologies is to select the accurate materials combination to be used in the building process. Materials used in the building process can be structural material (powder or wire) and additive material (binder). Utela et al (32) summarise the process of the relevant steps to develop a well-made 3D printed part fabricated by BJ technology into five steps which are powder formulation, binder method selection, binder formulation, and testing, printing process specification, and post-processing specification. Recently, the AM of multi-material has been one of the main scopes in different groups around the world. So far, it has been achievable to build multi-material parts thanks to the focused research and efforts. For example, fused layer modelling (FDM) and stereolithography (SL) are being used to make polymer based multi-material components. On the other side, metallic multi-material components can be produced by using powder bed fusion (PBF). However, there has been a big variance in understanding the term of multi-material.

The multi-material term is a general term of many different material building categories. In other words, these categories all have almost the same concept of combining different materials in one building process, but the differences can be in the way that two or more materials are joined during the manufacturing process. As shown in Figure 2.15, four building categories point out the differences in the 3D printing. In mono-material, the same material is being used to 3D print the components. In the 2D Hybrid part, the building process is on top of a different material. This process is called hybrid as it makes it possible to additively build on the top of a previously manufactured part that has been built with a conventional or subtractive manufacturing process. The third category is 2D multi-material, this category mainly focuses on changing the material in one dimension that is perpendicular to the building platform. Whereas in the 3D multi-material category, the material change occurs selectively at any axis of the building process (87).

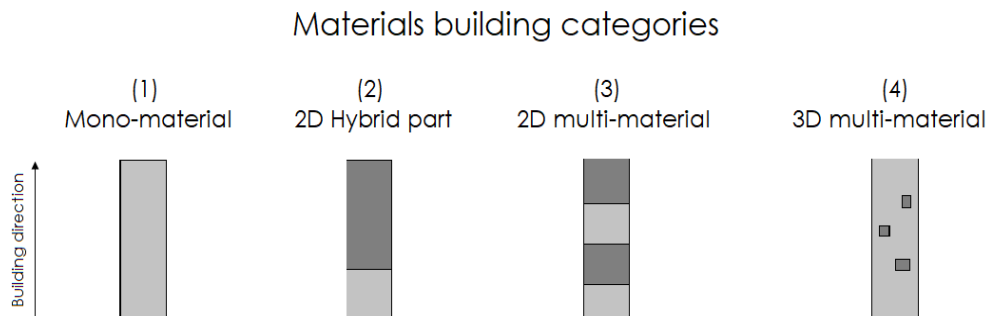


Figure 2.15: Different building additively manufactured parts categories of single and multi-material.

2.5 Multi-material Additive Manufacturing Achievements

2.5.1 Nonmetallic Multi-material Achievements

2.5.1.1 Vat Photopolymerization - Stereolithography (SL)

The stereolithography (SL) is one of the AM categories of Vat Photopolymerization technique, which uses a UV laser beam to solidify a sensitive oligomer resin material inside a curable atmosphere as seen in Figure 2.16. In the SL printer, the resin is cured and consolidated by passing an ultraviolet (UV) laser beam selectively to form the first layer while leaving other resin in vicious conditions on a work platform located below the resin surface (88). Next, the work platform incrementally goes down into a vat filled with epoxy or acrylate by a distance equal to the chosen layer thickness value. The SL process is one of the oldest techniques of rapid prototyping production as it goes back to 1986 when it was invented by Charles Hull (89). Recently, SL technique has gained more attention in producing microelectronic components where it gives high dimensional accuracy (90).

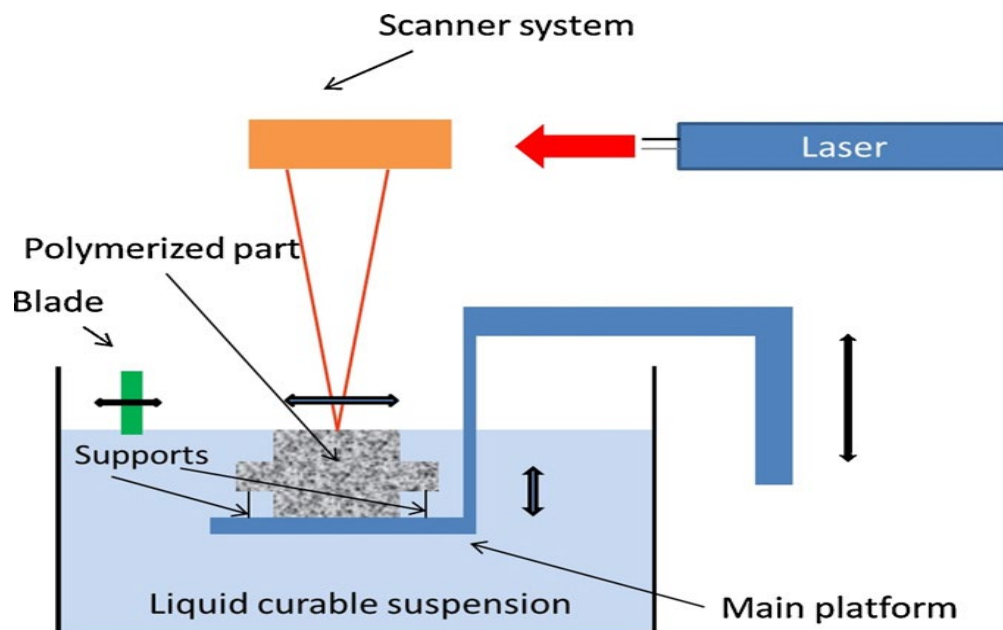


Figure 2.16: Photo-polymerization-based Stereolithography process (SL) of building polymerized parts (90).

Choi et al (91) reported the multi-material stereolithography (MMSL) printing using a new platform assembly, a rotating vat carousel system, and an automatic levelling system, as can be seen in Figure 2.17.

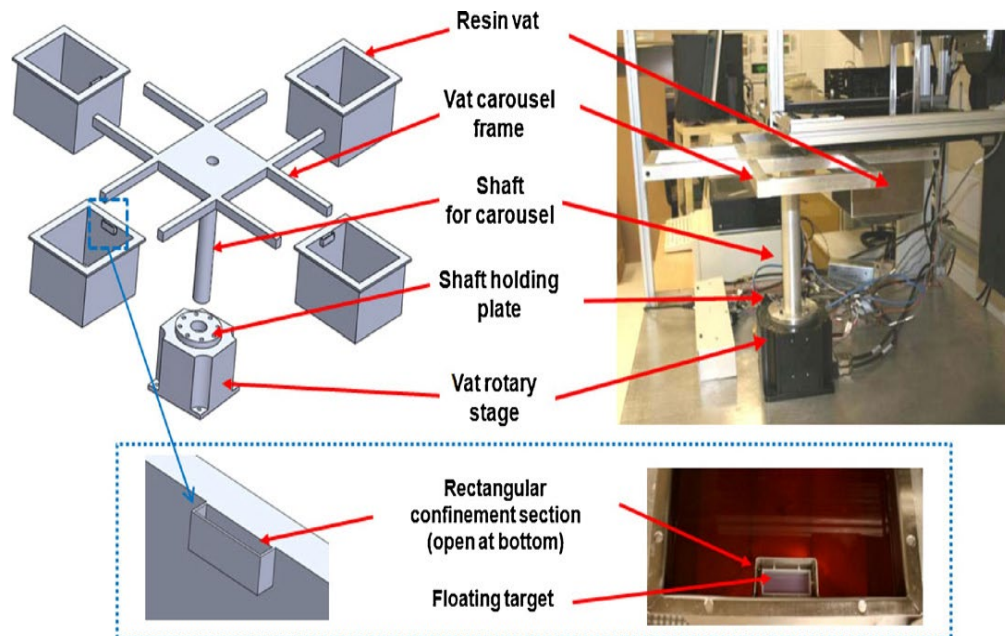


Figure 2.17: Multi-material Stereolithography Additive Manufacturing processing by rotating vat carousel system (91).

The main motivation of this experiment was to test and demonstrate the fabrication capabilities of the multi-material stereolithography process using three low-viscosity resins. The authors have chosen to fabricate pieces of the chess game, the rook, as building a rook is considered a common structure to demonstrate the capability of a single material SL process. To test the capability of the MMSL, two rook structures have been prepared as shown in Figure 2.18. Figure 2.18 shows the models which consists of three different structures and is made from three types of diluted resin materials. The process, to build the two rook structures, requires three resin vat changeovers. Between each changeover, it is necessary to clean the platform and part with isopropyl alcohol before immersing the platform into the next resin vat.

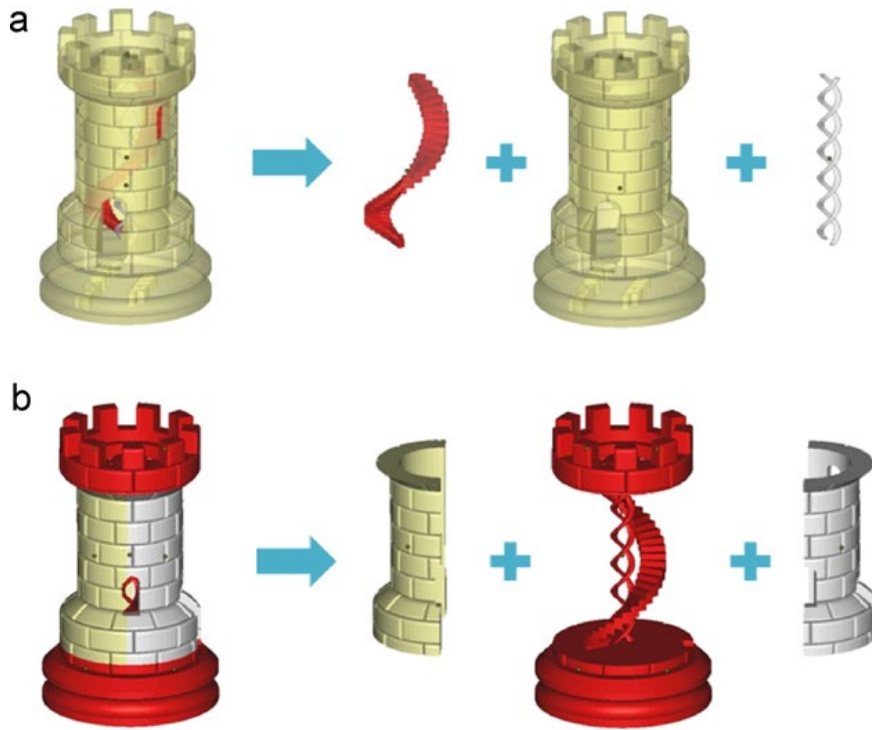


Figure 2.18: Two different multi-material rooks were built using the MMSL process (91).

On the other hand, this multi-material process has some building limitations which are, laser shadowing, contaminating material due to the switch of the different vats, trapped volumes, and surface tension issues. Laser shadowing will occur due to the previously printed layer that physically blocks the laser beam. Trapped volumes occur due to the cup or region that is created within one material on top of the other material.

2.5.1.2 Material Jetting

Material jetting, also referred to as "inkjet 3D printing" or "drop-on-demand 3D printing," is one of the additive manufacturing techniques. The system works by firstly dispensing small droplets of ink materials onto a build platform, subsequently solidifying them using UV light, as seen in Figure 2.19 (92). The process iterates layer by layer to construct a three-dimensional object. A notable advantage of material jetting lies in its capacity to produce highly detailed and accurate parts with a smooth surface finish. This capability makes it well-suited for applications like generating lifelike prototypes, models, or components demanding precision. Moreover, material jetting facilitates the incorporation of multiple materials and colours within a single print. This versatility enables the creation of parts with diverse mechanical properties or the production of full-colour prototypes, accomplished by employing multiple print heads for different materials or colours. Despite these advantages, material jetting has its limitations. The process can be relatively slow, and the materials utilized may incur higher costs. Additionally, the removal of support structures, necessary for supporting overhanging features during printing, can be challenging and may result in a rough surface finish object (93).

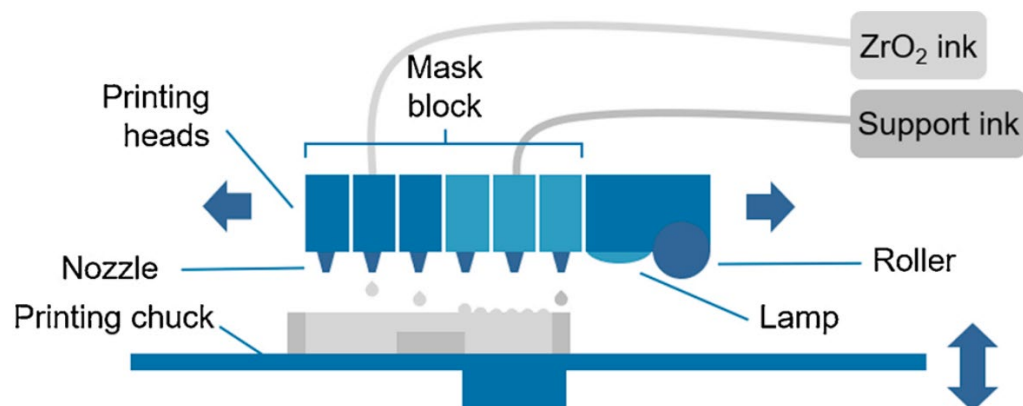


Figure 2.19: An illustration of the ink jetting process, characterized by multiple nozzles dispensing ZrO₂ ink as a building material and support inks. Adjunct to this, a lamp is employed to facilitate the drying of the printed ink, while a roller serves the dual purpose of smoothing the upper surface and sustaining vertical printing precision (92).

Multi-material fabrication using the material jetting process has been reported by Dr. David Frakes, Principal Investigator at Image Processing Applications Laboratory, Arizona State University. Dr. Frakes has used a Solid-scape material jetting machine to 3D print a core blood vessel model and then translate it into a transparent flow model for Cerebral aneurysms research as seen in Figure 2.20. Dr. Frakes commented that cerebral aneurysms affect only 2 % of all people. The death rate in the USA is nearly 20,000 every year and the numbers are stark. In addition, if an aneurysmal sac ruptures in the brain it becomes a highly lethal condition with a 50% mortality rate per rupture says Dr. Frakes. According to Dr. Frakes, the result of their 3D modelling was achieving a transparent block that has a lost-core or a hollow portion of the model which is a replica of a human cerebral aneurysm. This multi-material structure was built using modelling wax to fabricate the core blood vessel model and transparent polyurethane to build the transparent flow model (94). However, this process is not suitable for high-performance components.

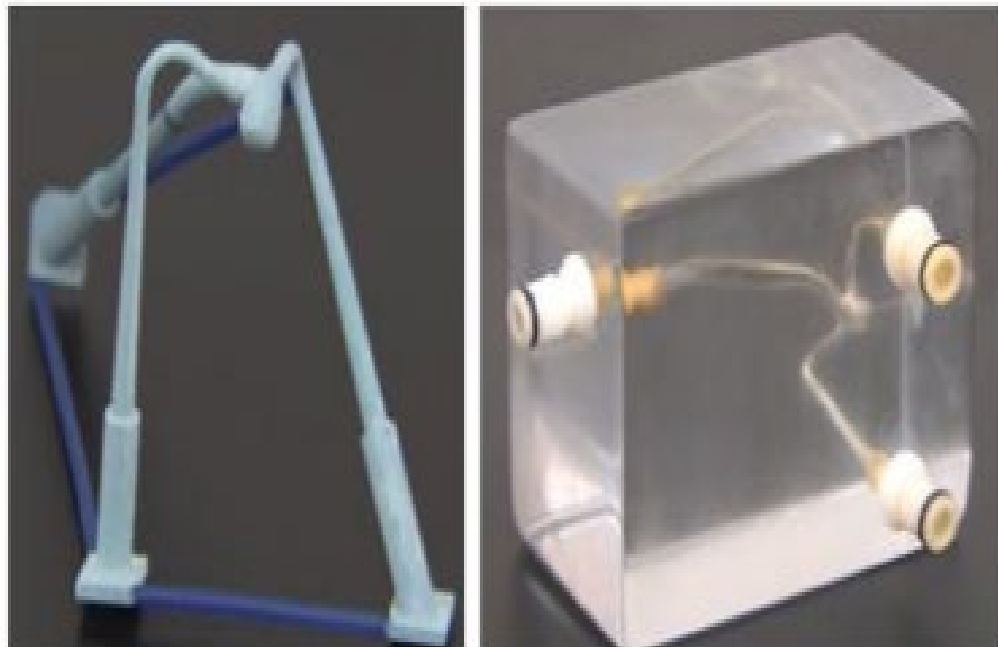


Figure 2.20: Building a multi-material replica of a cerebral aneurysm from a person (94).

2.5.1.3 Extrusion

One example of using the extrusion to build multi-material structures is the manufacturing of electronics-based objects that have been reported by Periard et al (95). The ability to dispense conductive silicone drops into silicone and epoxy structures has been demonstrated. Three embedded functional electronic circuit objects have been built, as seen in Figure 2.21, in a single building process. The first object, a children's toy, was printed using the substrate silicone with a groove to dispense the conductive silicone into. Then green LED eyes were fitted into the electronic circuit that lights up when the toy's chest is pressed. The second object, a circuit board, was built using the substrate silicone to produce the isolation channels to ensure the isolation of the conductive silicone traces. Then, the conductive silicone materials were deposited into the isolation channels that later were covered by layers of silicone to form the full printed circuit. The last object, LED flashlight, was built using silver-filled silicone for the electrically conductive parts and pure silicone for the flashlight body.

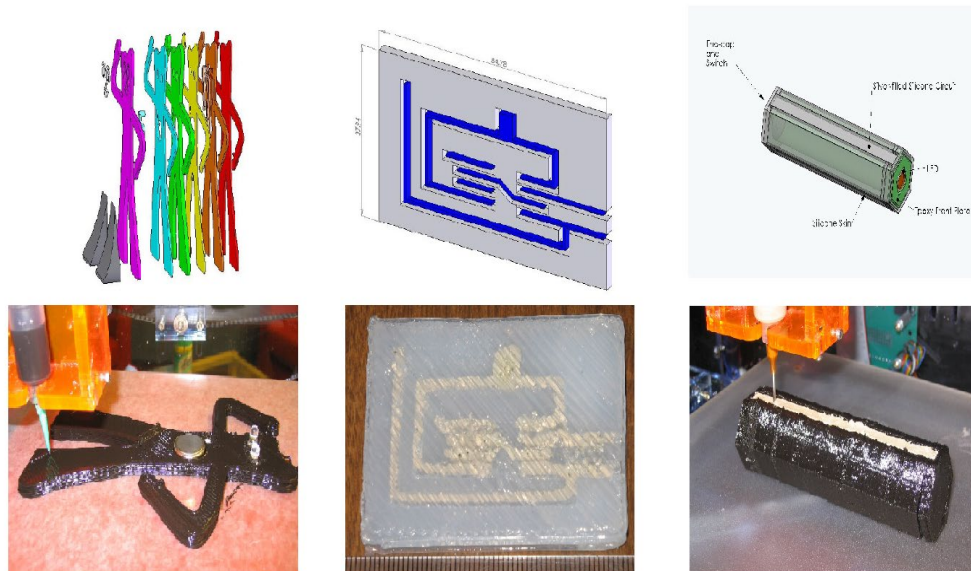


Figure 2.21: Three multi-material embedded functional electronic circuits objects (95).

Silver conductive ink deposition was initially attempted throughout a syringe but encountered issues with low viscosity and solidification in the needle, preventing uniform deposition. Subsequently, conductive silicone material was tested and found to maintain shape well, suitable for dispensing through the needle. Additionally, 2-part epoxies and silicone were employed for creating isolation grooves and the object's outer body. This led to the successful production of multi-material components with specific resistivity and dimensions.

Another attempt was made by Shim et al (96) to build a mechanically enhanced 3D bio-printed construct for osteochondral tissue regeneration, involving various cell types. They utilized polycaprolactone (PCL) as a framework to bolster mechanical stability, as it offers superior mechanical properties compared to hydrogel. The authors noted the challenge of achieving ideal 3D tissue printing using hydrogel alone due to its inadequate stability. To address this, they combined solid-state synthetic biomaterials with hydrogel, successfully depositing PCL and alginate to achieve mechanical stability and cellular arrangement, respectively. This was facilitated by a newly developed multi-head tissue/organ building system (MtoBS) designed to handle materials with different rheological properties as shown in Figure 2.22.

The MtoBS system, comprising six dispensing heads, utilized various biomaterials including gel-state hydrogels and solid-state synthetic biomaterials. Two nozzles were equipped with a heating system to semi-melt thermoplastic biomaterials like PCL and PLGA at 150°C, followed by extrusion using pneumatic pressure. After dispensing, the thermoplastic biomaterials were rapidly cooled. The remaining four dispensers were used for gel-state hydrogel deposition. Additionally, the MtoBS enabled tissue or organ fabrication in both centimeter and micrometer scales, with user-definable line width and pore size.

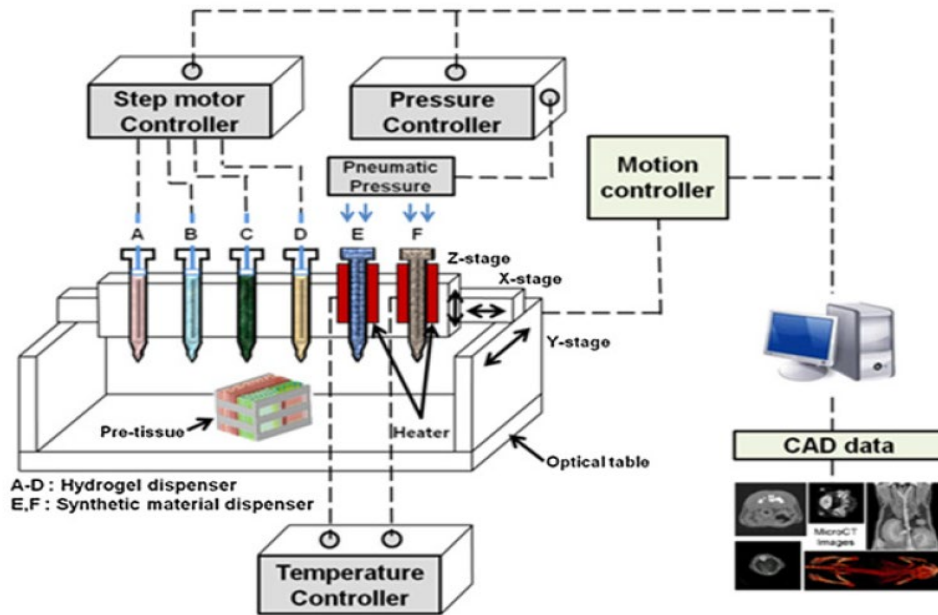


Figure 2.22: A schematic diagram of the multi-head tissue/organ building system (96).

As a result, a cell-laden structure consisting of a PCL framework, chondrocytes, and osteoblasts was processed using the novel MtoBS as seen in Figure 2.23. The top regions display cartilage and are filled with red-stained alginate and the lower regions are bones filled with blue-stained alginate. Separate dispensing nozzles were used to deposit the chondrocytes and osteoblasts into the PCL framework.

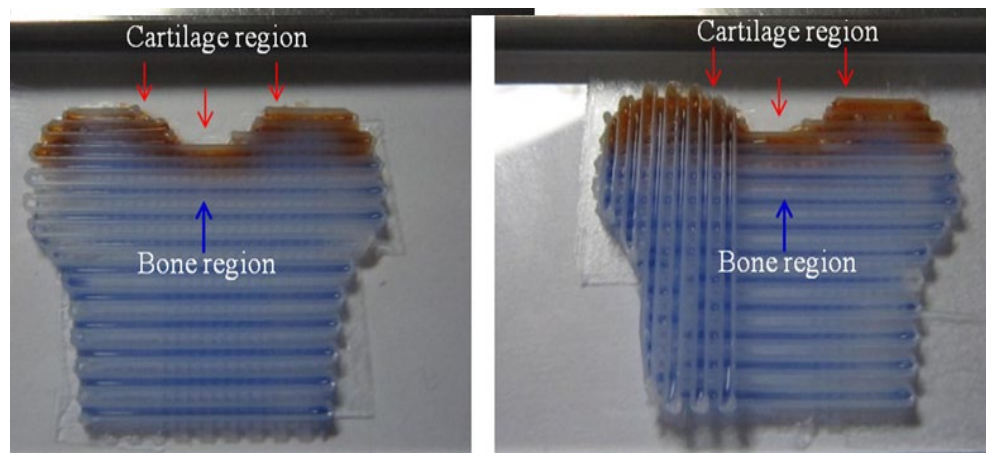


Figure 2.23: A schematic diagram of the multi-head tissue/organ samples (96).

2.5.2 Metallic Multi-material Achievements

2.5.2.1 Powder blown Laser Cladding

To achieve multi-material components with PBLC, Wei Li and his team have done a study to deposit pre-mixed powders (97). In this study, the authors have used two experimental methods to observe the importance of the separation of pre-mixed powder in the PBLC system to fabricate Functionally Graded Material (FGM) as seen in Figure 2.24. The main motivation of this study was to deposit multi-material pre-mixed powder to create components with user-definable areas. They also aimed to investigate the effect of the powder particle size on the deposition rate.

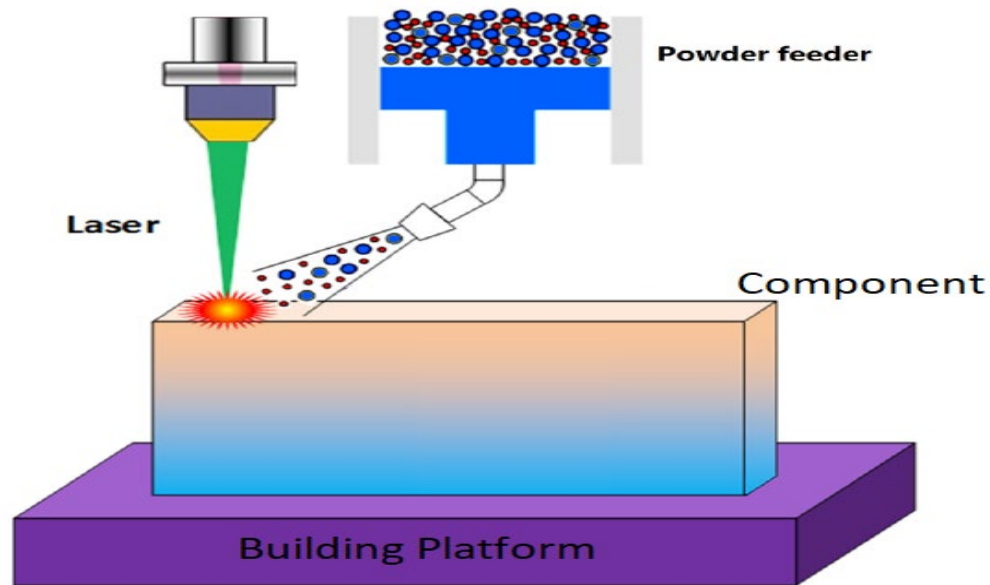


Figure 2.24: Depositing of pre-mixed multi-material powders in the Powder Blown Laser Cladding process (97).

The authors have conducted two experiments to test the powder flow from the nozzle and its effect on the particle size on the ejecting order of the mixed powders. In these experiments, multi-material components have been fabricated by pre-mixing two or more alloy or metal elemental powders inside a powder feeder. The pre-mixed powder is then pushed by an inert gas to be deposited throughout a dispenser. The combination ratio of the different materials is calculated concerning the composition

requirement of the multi-material structure. The experiments involved the use of pure 4047 Aluminium and Copper powders with a size range between 45 and 106 microns. The two different powders were pre-mixed for 30 minutes, with a commercial shaker mixer for the homogeneous mixing of powders, to be deposited to perform the first experiment. In the first experiment, the authors used aluminium particle diameters ranging from 45 to 75 microns and copper particle diameters from 75 to 106 microns. As a result of the first experiment, it was notable that a huge percentage of 4047 Al particles exited before the Cu particles for the first 21 seconds, and then the Cu particle percentage increased for the remaining time of the experiment. In the second experiment, a novel optimisation of the particle separation system was introduced to reduce the undesired existence of the powder separation. In this try, the aluminium particle diameter used ranged from 75 to 106 microns, and the copper particle diameter from 45 to 75 microns. The introduced optimisation can be described as finding an ideal value which was the square root of the powder's density ratio. As a result of applying the optimised technique, the flow of the two powder materials has been constant in almost equal volume.

The authors have concluded that in using pre-mixed powder materials that have two types of powder with dissimilar densities it is expected to show powder separation occurrence. Due to the change in particle size and density of each material, the small and light-weight particles could transfer faster than big and heavy-weight particles in the feeding pipes. This non-uniform powder dispensing could lead to regular fluctuation in the material composition ratio though ruins the required structural performance. Therefore, it is essential to optimise the particle diameter ratio to an ideal value. In spherical or very close to a spherical shape, the particle diameter ratio should be equal to or close to the square root of the powder density ratio to achieve the same particle acceleration inside the powder feeder pipe. Thus, very little powder separation will happen.

Another effort has been made by Lin Li and his team, to compare the fusibility of two dissimilar materials by processing them using powder-powder and wire-powder experiments of two different materials in a Directed Laser Deposition process in a single building process as seen in Figure 2.25. The main aim of this study was to build a multi-material structure from dissimilar materials, copper, and nickel on top of an H13 tool steel substrate by using a 1.5-kW diode laser for the build-up process.

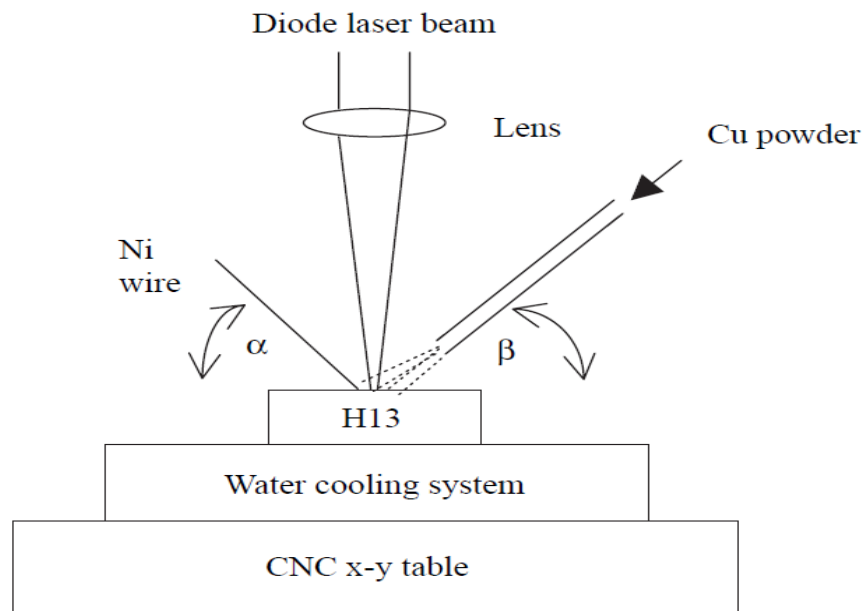


Figure 2.25: A schematic illustration of the modified Laser Deposition process, as adapted from (98).

In the first experiment, a 1500 W laser beam power was used to melt and fuse the two dissimilar powder materials. The powder delivery nozzle angle was 45 degrees from the two sides of the laser beam with a powder delivery rate of 0.017 -0.193 g/s for Cu and 0.036 -0.18 g/s for Ni. The deposition speed for the two experiments was 4 mm/s. In the second experiment, the same laser beam power of 1500 W was used with a powder delivery nozzle angle of 50 degrees and wire delivery nozzle angle of 30 degrees with wire delivery rate of 0.010 -0.041 g/s. Comparing the two experiments' results of wire-powder and powder-powder, it has been noticed that the

presence of a copper-rich thin layer on top of the clad exists in the two experiments with a slight change to the layer composition concentration. In the wire-powder method, the uniform distribution of nickel and irons in concentrations of 78-82% copper has been shown in Figure 2.26a. On the other hand, the powder-powder method presents an extremely higher concentration of more than 90% Cu with an agglomeration of nickel powders split in random places Figure 2.26b.

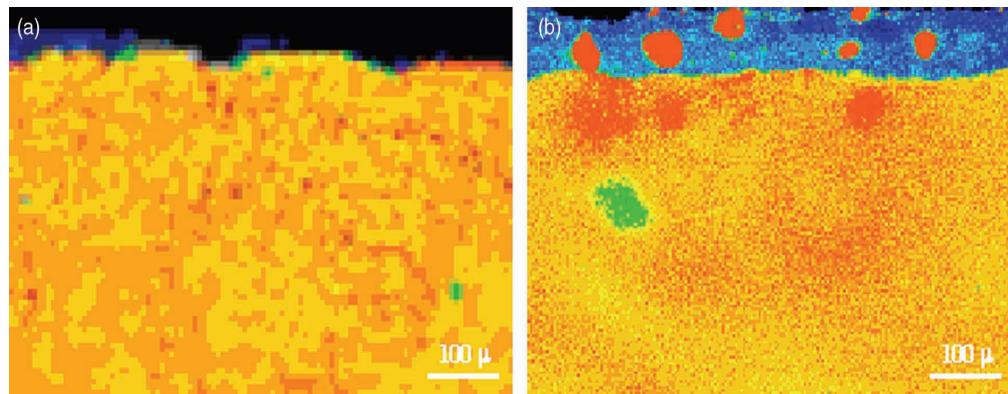


Figure 2.26: The difference in copper concentrations from (a) wire-powder method, and (b) powder-powder method (98).

Besides, a copper-rich layer has been shown on the top part of the deposit in both methods due to the temperature at the top of the melt pool, generated by the laser, being an adequate temperature to melt only the copper powder as it has a lower melting temperature value than nickel and iron which are 1,085 °C, 1,455 °C, and 1,538 °C respectively. In the powder-powder method, the different powder materials are subjected to the same laser irradiation thus copper powder particles will reach the melting temperature in less heat than the other material. This means any temperature less than 1400 °C the nickel and iron powder particles would not be melted while copper powder particles would be melted. Therefore, nickel isolation has been reported as shown in Figure 2.26b. However, In the wire-powder method, the nickel wire has a diameter of 0.5mm, and the wire remains in contact with the

melt pool thus it is heated up due to conduction before entering the melt pool. Therefore, no high isolated nickel areas were shown at the cladding. Furthermore, the wire-powder method has also proven the elimination of several multi-material process drawbacks which are, the recyclability of the un-used multi-material powders and the need for multiple passes in building functionally graded structures. Finally, the authors have recommended the use of lower melting temperature material as a powder material leaving the higher melting temperature material in the form of wire (98).

2.5.2.2 Powder bed fusion AM processes

In the powder-based processes, the use of multi-material is limited and until the last decade, multi-material parts that have been produced using these processes were manufactured with controlled porosity that was infiltrated with different coloured dyes after the fabrication. Different powder materials have different mechanical properties thus, Also, they also have various thermal properties such as conductivity, specific heat capacity, latent heat, and melting temperatures. Therefore, one extremely relevant property in PBF-manufactured parts is the mismatch in the thermal expansion coefficient of the different materials. This mismatch naturally rises the stresses of each interface. An effort has been made by Nadimpalli et al (99) where multi-material of stainless steel 316L and Maraging Steel MS1 have been built using an open-architecture L-PBF system from Aurora Labs, as shown in Figure 2.27.

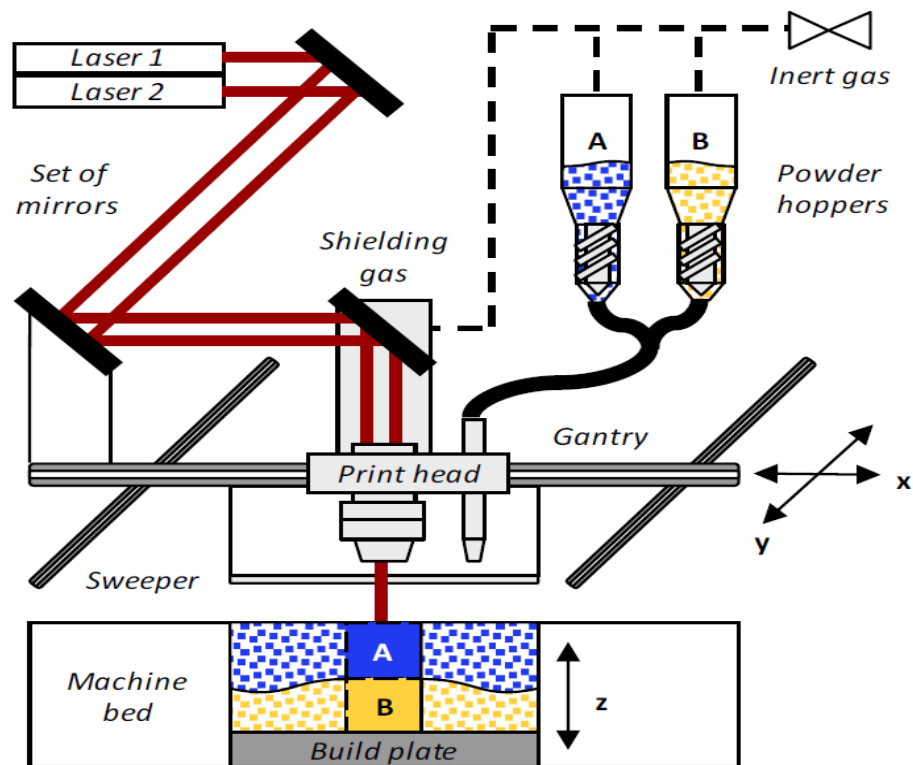


Figure 2.27: Aurora Labs STitanium Pro laser powder bed fusion (L-PBF) system (99).

The reason to choose the Aurora Labs system is its unique powder deposition mechanism which uses a set of individual powder hoppers located above the build chamber. The decision to use this combination of materials stemmed from the superior strength of MS1 and its corrosion resistance when paired with 316L. The methodology of this experiment was to build two multi-material cuboids, combining 316L and MS1 material, on three different levels as seen in Figure 2.28. The cuboids' dimensions are to be 10mm in length, 10mm in width, and 7mm in height. On the first level, MS1 powder is to be deposited on top of a previously manufactured 316L build plate. At the second level, MS1 is to be printed on top of printed 316L cuboids on top of a previously manufactured 316L build plate. At this level, the powder material was suddenly changed at the interface between MS1 and 316L structures. At the third level, the change at the interface between MS1 and 316L powder happened gradually on the printed cuboids.

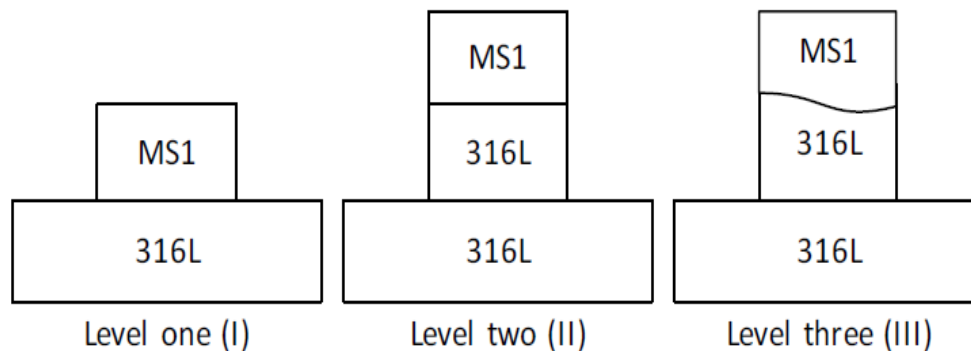


Figure 2.28: Three different structures have been used to build multi-material samples using PBF AM, as adapted from (99).

The microstructure of level two and three material interfaces was investigated using light optical microscopy. As a result, 316L material has shown better etchant sensitivity when compared to MS1 material. In addition, a gradual change from one material to another has been noted in Figure 2.29.

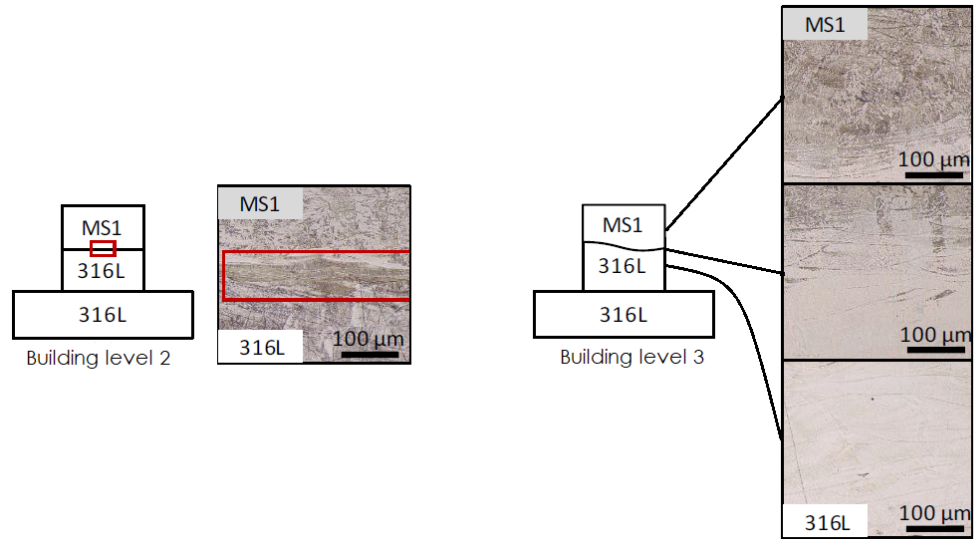


Figure 2.29: Optical microscopy images taken at and around the interface (99).

In a similar manner, Wei et al (100) have developed a multi-material system that enables the building of a multi-material structure using an installed vacuum device to the 3D printing process which removes the first material unwanted powder before depositing the second material powder on the top of the printed surface. The authors have introduced the modified laser PBF system with multiple powder hoppers in combination with a point-by-point micro-vacuum selective material-removing system as seen in Figure 2.30. The multiple powder system was comprised of a powder supply chamber and a traditional roller delivery mechanism spreading the main building powder material and a laser system to melt the selected area Figure 2.31 (a, b). Additionally, it has a point-by-point micro-vacuum that works as a removal system to remove a precision single layer of the main building powder at specific locations Figure 2.31 (c). Furthermore, the system includes several ultrasonic powder dispensers that selectively dispense the other powder materials according to the required design pattern Figure 2.31 (d). Two different multi-material combinations

have been built. The first combination is Cu10Sn copper alloy and 316L stainless steel. The second multi-material combination is In718 nickel alloy and 316L stainless steel.

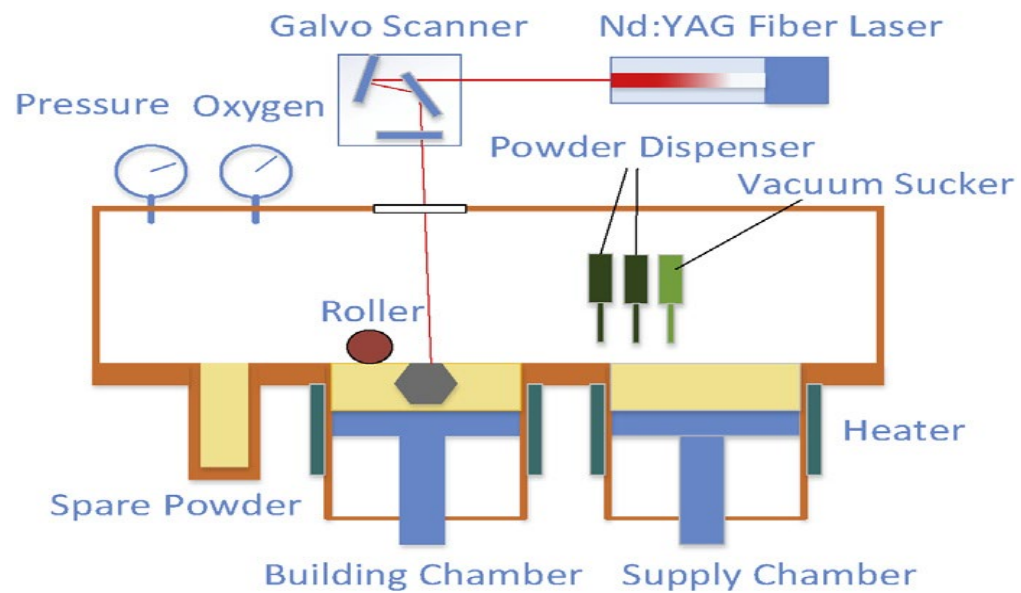


Figure 2.30: Modified laser PBF system with multiple powder hoppers in combination with the point-by-point micro-vacuum selective material-removing system (100).

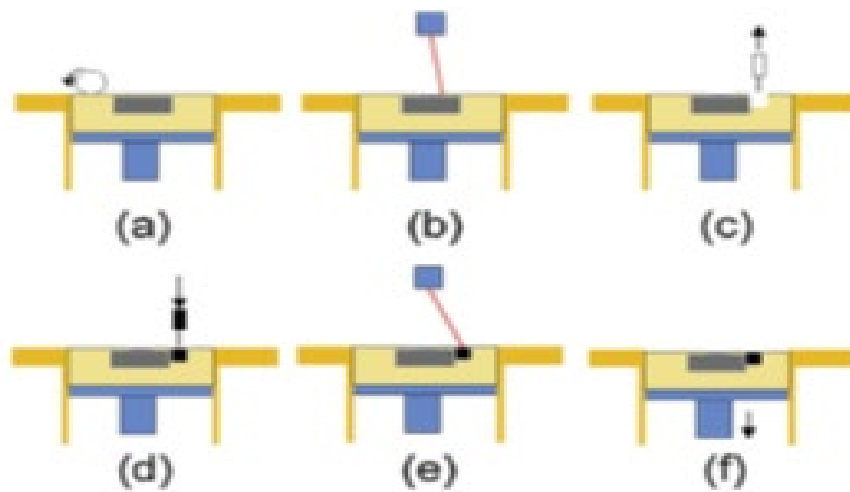


Figure 2.31: The multiple materials process flow chart of SLM, a) traditional roller delivery mechanism, b) laser system, c) vacuum cleaned pattern, d) ultrasonic powder dispensers (100).

This multi-material building process is conducted in an inert gas environment, typically argon or nitrogen, with an oxygen level kept below 0.3%, monitored using a real-time oxygen sensor. It involves spreading a layer of the primary powder material, typically 316L, over the building platform and levelling it with levelling blades. The laser then melts and fuses the powder in the selected area. A micro-vacuum system removes a single layer thickness of powder in defined areas, after which ultrasonic powder dispensers fill these areas with the second or third powder material. These dispensed powders are then melted by the laser beam to bond with the first powder material. The building platform moves down by the defined layer thickness to manufacture the next layer of the component. This process repeats for each layer until the entire specified 3D model is achieved. The powder materials used in this experiment include spherical gas atomized 316L stainless steel powder, In718 nickel alloy powder, and Cu10Sn copper-alloy spherical powder. All the three powder materials come with diameters ranging from 10 to 45 μm .

The printed parts have been prepared to be cross sectioned by cutting, mounting, and grinding with 400, 800, 1000, and 1200 grid emery papers, and finally polished using 1.0 μm diamond polishing paste. Then, the samples have been checked using the Leica DM2700-M microscope to get optical microscopic images of material interfaces. In addition, Vickers microhardness on the samples has been measured using a Durascan-80 hardness tester with an applied load of 0.3, 0.5, and 0.5 kgf on Cu10Sn, 316L, and In718 parts respectively. Finally, a scanning electron microscope from SEM, Zeiss Sigma VP FEG SEM has been used to examine the interfaces between the different materials. The joint between the two materials is a “finger cross” joint zone as seen in Figure 2.32. The study resulted in proving the feasibility of successfully depositing multiple materials of 316L/In718 and 316L and Cu10Sn samples on the same building layer as can be seen in Figure 2.33.

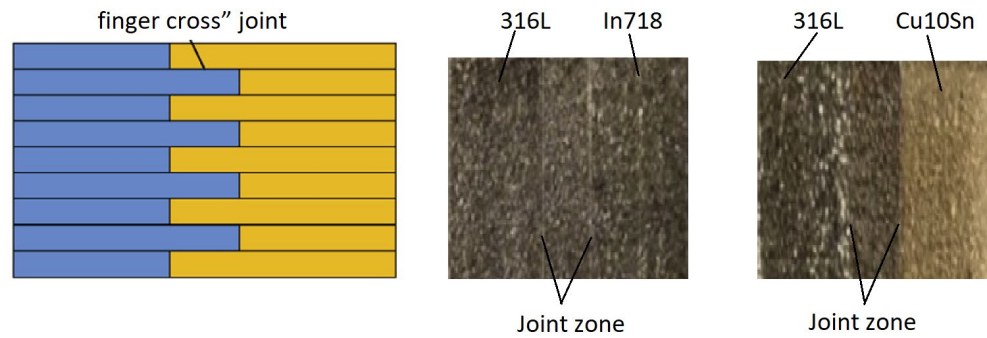


Figure 2.32: Joint zones of printed samples out of 316L/In718 and 316L/ Cu10Sn dual material (100).

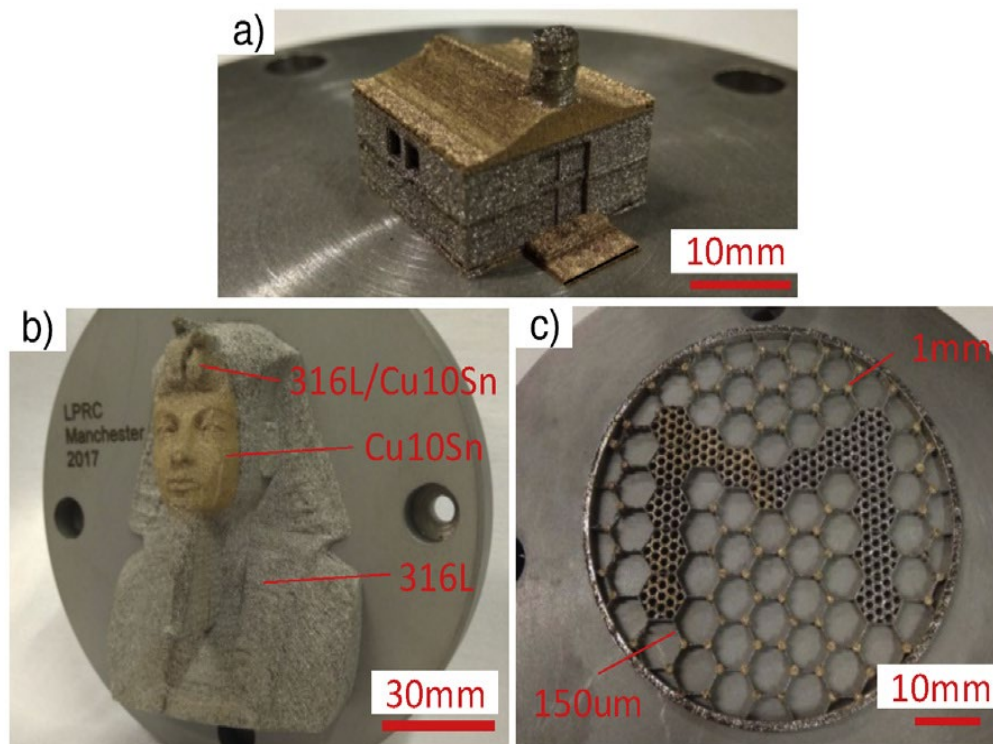


Figure 2.33: Multi-material mini house, b) multi-material/ dual-colored statue of Sphinx, c) a dual-colored grid pattern (100).

The result of the optical microscopic images of the cross-sectional showed some pores at the multi-material interfaces specifically at the ultrasonic deposited powder area. In these areas, it was found that the occurrence of uneven surfaces due to the ridges between each dispensing track leads to lower packing density and higher porosity. Besides, it was found that a good bond occurred between the 316L SS layer and the Cu10Sn layer. Some parts of Cu migrated into the previously molten 316L layer. By examining one of the SEM images of the 316L and In718 samples, some cracks were observed. Furthermore, The EDS mapping results have shown that most of the defects were distributed in the In718 alloy powder region deposited by the ultrasonic nozzle as powder particles from the ultrasonic feeding nozzle have not been subjected to external pressure. Thus, cracks and porosity appeared during material phase changes in the laser fusing process. Unlike the roller-assisted spread areas, there were fewer cracks and porosity observed as the packing density of the powder bed was enhanced by the roller compressing. The same reason described above has resulted in some cracks and porosity in the ultrasonic deposited Cu10Sn powder region in the 316L and Cu10Sn specimen. Also, there is no cracks or porosity were observed in the fused 316L region which has been spread using the powder-spread roller. The other material characterisation test is the Vickers hardness test. The results of the hardness test showed that the hardness values ranged between 237 HV and 251HV for the 316L part. In718 part hardness values ranged from 301 HV to 310 HV with the transition zone having hardness values between those of the two materials. Meanwhile, the 316L and Cu10Sn sample has shown a range from 227 HV to 247 HV for the 316L part with 149 HV to 160 HV at the Cu10Sn section.

Likewise, Liang et al (101) have reported a multi-material 3D printed part, made from a different grade of stainless steel, using the Selective laser Melting approach. In this investigation, the author concentrates on utilizing Laser Powder Bed Fusion to combine 316 L austenitic stainless steel and precipitation-hardening 15–5PH martensitic stainless steel as seen in Figure 2.34. The study resulted in the solidification of both 316 L austenitic stainless steel (SS) and 15–5PH martensitic SS exhibited similar elongated grain orientations. In terms of interlayer connection, the interface of the 316 L/15–5PH multi-material exhibited dense bonding without visible pores or cracks as seen in Figure 2.35. It featured a wavy interface, varying by approximately $57.4\ \mu\text{m}$ (about twice the layer thickness) in the building direction.

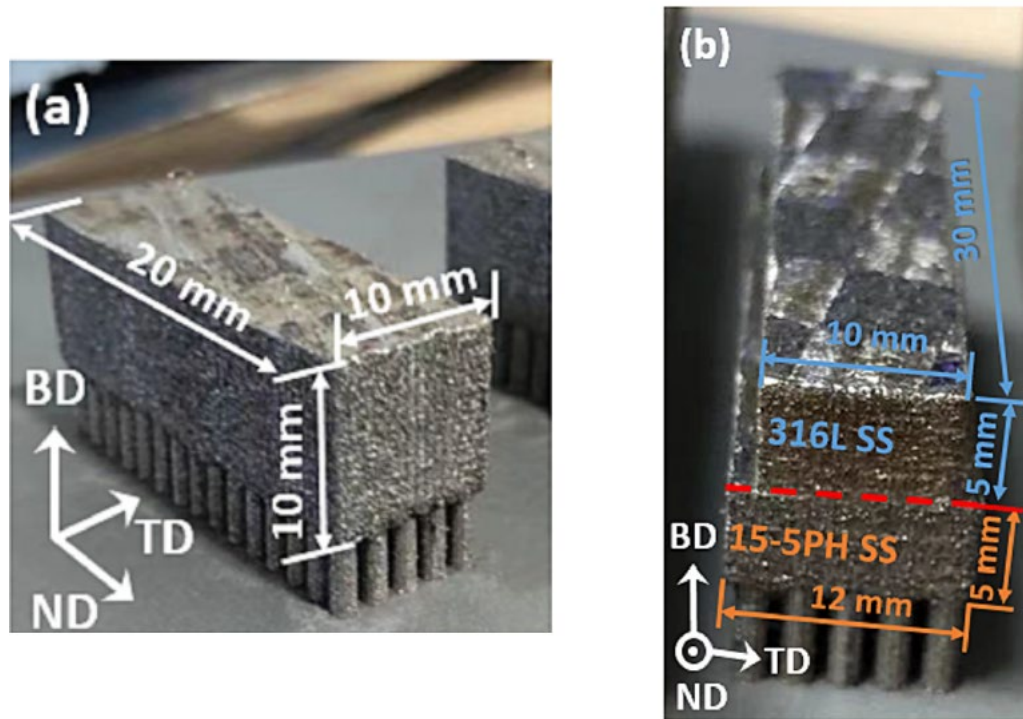


Figure 2.34: 3D printed structures (a) parts made of a single material using both 316 L SS and 15–5PH SS, and (b) parts composed of 316 L SS and 15–5PH SS. The arrow indicates the building direction (BD) approach (101).

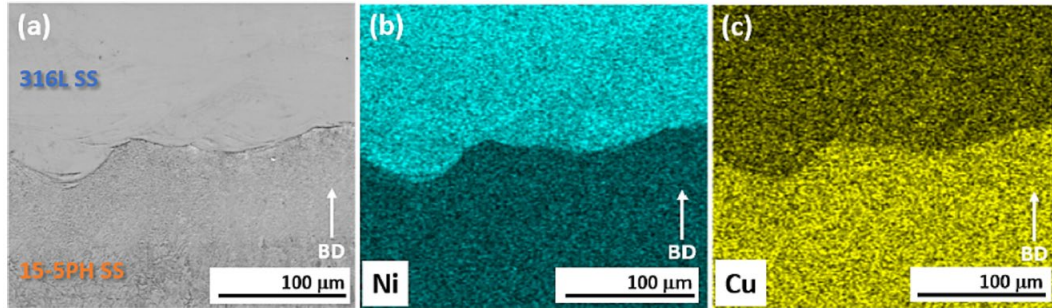


Figure 2.35: Chemical element distribution at the interface of the 316 SS and 15-5PH SS multi-material is illustrated: (a) SEM image; (b, c) Nickel (Ni) and Copper (Cu) elemental distributions, as determined by Energy Dispersive Spectroscopy (EDS) mapping. The arrow denotes the building direction (BD) (101).

Other multi-material contributions have been registered by Aerosint, where a unique milestone in fabricating multi-material parts applications (102). Aerosint is known as a developer of a zero-waste polymer powder bed 3D printing technology. This unique milestone is the introduction of a robust commercial multi-material powder deposition recoater mechanism that has the ability to build multi-material parts in a single building process. Powders of metal, ceramic, and polymer can be used in accordance with the new recoater. In March 2020, the company tested its multi-material powder deposition technology in the Aconity Midi+ L-PBF printer and successfully fabricated a dual-material part as seen in Figure 2.36. This dual material recoater operates by selectively dispensing the required type of material into a specific place Figure 2.37. The dual-material component has been printed by the Aconity Midi+ L-PBF 3D printer. Due to the collaboration between Aerosint and Aconity 3D, the new multi-material powder depositor can be integrated with the Midi+ 3D printer as it is considered an attachment to the Midi+ 3D printer that can be bought as an extra option. According to Aerosint, this multi-material powder depositor is a strong opportunity for new use cases and applications (102).

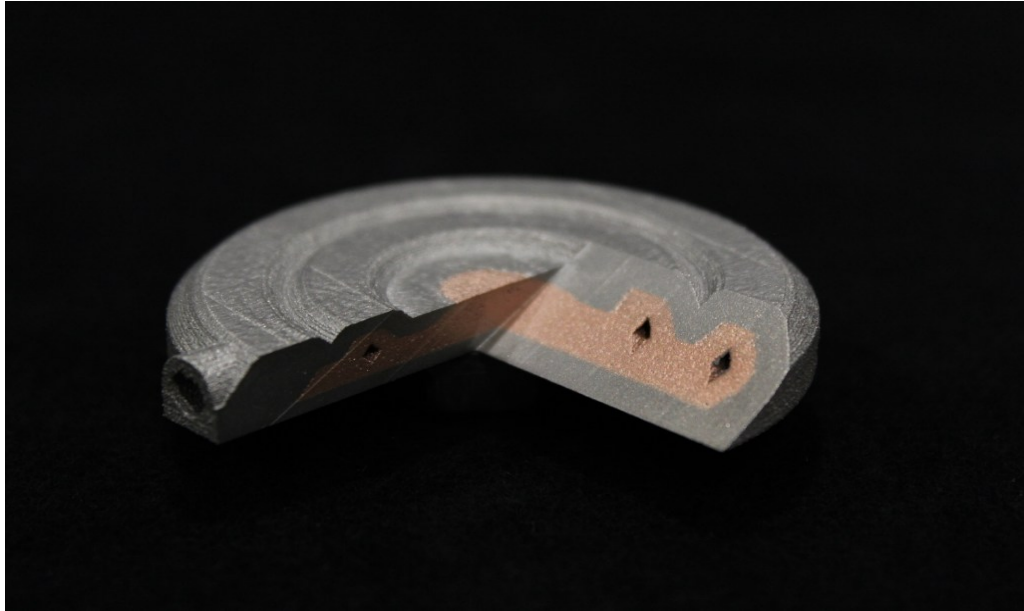


Figure 2.36: Fabrication of dual-material part using Aconity Midi+ L-PBF printer (102).

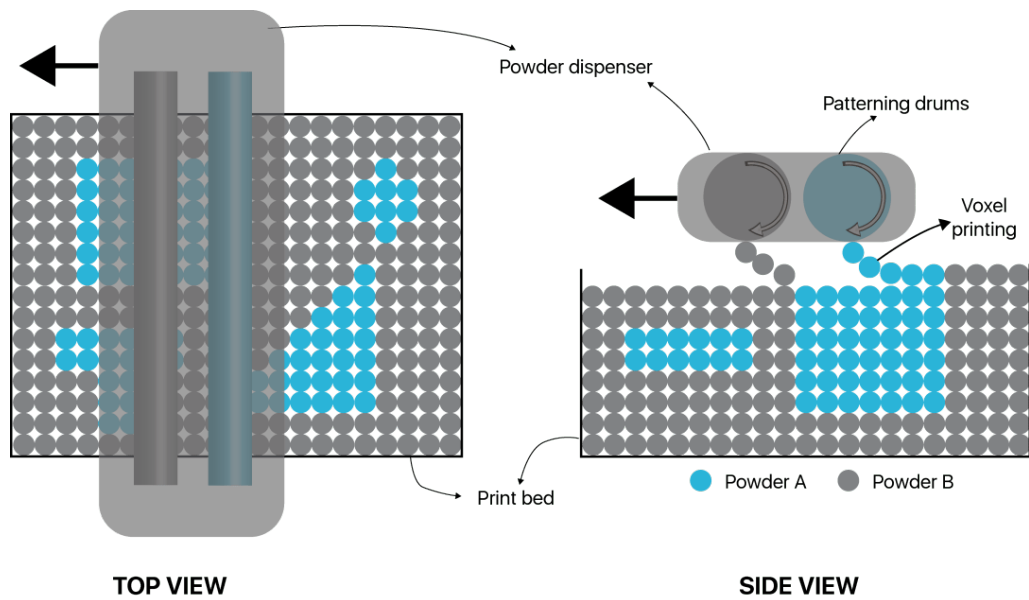


Figure 2.37: The image shows the multi-material selective powder recoater device, developed by Aerosint (103).

2.6 Comparison of the Multi-material Additive Manufacturing Processes

Process	Part quality	Ease of processing	Limitations
Vat photopolymerization	Achieved good final multi-material quality	Time and Material consuming.	Not suitable for high performance components.
Material jetting	Achieved good final multi-material quality	Hard to process metal materials.	Not suitable for high performance components.
Material extrusion	Achieved good final multi-material quality	Cannot achieve very complex parts using extrusion.	Not suitable for high performance components.
Directed energy deposition	Achieved good final multi-material quality	Hard to achieve very complex parts using extrusion. Power consuming.	Powder separation occurrence. Recyclability of the used powder.
Powder Bed Fusion	Achieved good final multi-material quality	Defects porosity at the final component caused by un-compressed powder.	The restriction of the use some multi-material dispenser with other AM processes The high price of this recoater is over £ 150,000

Table 2.3: Comparison of the multi-material AM achievements over the different process discussed.

2.7 Applications of Multi-material

The capability to fabricate multiple material parts is improving AM technologies by optimising the mechanical properties of the parts and providing additional functions to the final parts such as lightweight products, corrosion protection, thermal management, electrical conductivity, and orthopaedic. Besides, joining two metallic materials can result in a high-performance product that has a cost-effective alternative to solid mono-material. Table 2.4 shows some of the most common multi-material combinations and their applications.

Material 1	Material 2	Applications	References
Titanium	Aluminium	Lightweight	(104)
Copper	Aluminium	Lightweight	(105)
Copper	Nickel	Corrosion resistance	(106)
Copper	Titanium	Corrosion resistance	(107)
		Orthopaedic and dental applications	
Titanium-based alloys	Cobalt–chromium–molybdenum alloy (Co-Cr-Mo)	Orthopaedic	(108)
Copper	Stainless steel 316	Corrosion resistance	(109) (110)
		Thermal management	

Table 2.4: Multi-material combinations and their applications.

Lightweight construction is most desirable in the automotive industry, especially in reducing the total car body weight. Another area that benefits from the lightweight structures is the airplane industries where a combination of aluminum alloy and titanium alloy is used in producing the airplane wings. Lightweight can be achieved by using steel, aluminum, magnesium, and fibre-reinforced materials. For instance, the combination of C18400 copper alloy with AlSi10Mg would give the features of

lightweight high conductive components, Al/Cu components are 50% lighter than similar singular copper alloys, due to the lightweight of the aluminum and the high conductivity of copper. Another advantage is the lower cost of aluminum compared to copper alloys. One good example of using Al integrated with Cu to minimize the material weight is the manufacturing of bus bars. Further interest in using this combination lies in e-mobility batteries where copper and aluminum act as electrodes inside the battery (105). Another combination of metal alloys that uses copper with another element is the use of copper integrated with nickel to reach a good corrosion resistance and wear resistance alloys. This combination is resistant to moisture, alkali, and salt, solutions on-oxidizing acids, hydrogen fluoride, organic acids, and gases such as oxygen, chlorine, hydrogen chloride, carbon dioxide, and sulphur dioxide. Additionally, due to the low tendency to selective corrosion and pitting corrosion, Cu-Ni alloys have no risk of stress corrosion cracking. Thus, Cu-Ni alloys are commonly used in the food industry especially with the highly stressed multi-stage evaporators, conveying and processing foodstuffs, and pipelines of all kinds (106). Furthermore, combining copper with titanium could give strong and excellent corrosion resistance properties that can be used in several high-performance applications in technology, manufacturing, and medicine. Titanium is well-known as the material that has the highest strength-to-density ratio among all the metallic elements as well as it has outstanding corrosion resistance. As copper is known for its anti-bacterial effect, it makes copper and titanium a good fit alloy to be used in biomedical industries such as orthopaedic and dental applications (107). It has also been reported that the use of titanium along with stainless steel, cobalt-chromium–molybdenum alloy (Co-Cr-Mo) is an area of interest to the biomedical industries as this combination is one of the most important materials used in orthopaedic applications (108). Another combination of metallic alloys used in improving the corrosion resistance is the addition of copper to the 316L SS particularly in seawater and sulfuric acid-containing environments, as copper is well recognized for the suppression of anodic dissolution by elemental Cu deposition on the surface of the steel. Adding copper to 316 L has the effect of

eliminating the initiated pitting corrosion sites in the stainless-steel surface. As a result of the dissolution of copper at the surface, the surface is then coated with insoluble copper sulphide (Cu_2S) compound (109). Another area of interest is plating stainless steel material with copper material. Copper material is known for its softness and malleability, whereas stainless steel is known for its poor electrical conductivity. However, the price of the stainless-steel material is much less expensive when compared to copper. Thus, combining the two materials would result in part with very high thermal conductivity, good hardness properties, good electrical conductivity, and high tensile strength. Copper-plated steel can be used in applications such as double-walled tubes and bearings in the automotive industry and in producing electrical components including circuit breakers and switches (110).

2.8 Material Powder Dispensing Mechanism.

To be able to fabricate a multi-material structure in an additive manufacturing process, it is required to develop a multi-material deposition system that enables the dispensing of two or more different types of material selectively in a single building process. One way to dispense a single powder material is to use a high-power ultrasonic system to send ultrasonic waves to deposit the powder. The ultrasonic system is a system that is used to generate vibration energy from electrical energy. This vibration energy has a high frequency that can be transmitted into the ultrasonic range (111). Currently, the common use of the high-power ultrasonic system is lying in applications such as dispensing single powder material (111) (112) (113), ultrasonic atomizer or mixer, sonar devices, ultrasonic cleaners, ultrasonic welding, ultrasonic machining process, and vibratory motors (114). In general, in a high-power ultrasonic system, controlled electrical energy is generated by the use of a controller that sends vibration energy to the ultrasonic transducer then the vibration is transmitted by a transmitting cone. The transmitting cone is attached to a horn, also known as a sonotrode, which amplifies the amplitude of vibration at the end of the tool. The vibration's magnitude can be varied depending on the ultrasonic system's application. In most cases, the ultrasonic transducer vibrates at an amplitude ranging from 4 to 10 μm . An application like ultrasonic machining can require from 10 to 100 μm amplitude. Another application is using the ultrasonic system in welding. In this application, an amplitude from 25 to 150 μm is required. This range in amplitude is related to the material being processed. The ratio between the transducer amplitude and the sonotrode amplitude is called the amplification factor. The sonotrode design plays an important role in achieving better amplification factors. In most cases, the slenderness factor increases when decreasing cross-section and increasing slenderness, the largest diameter in the sonotrode divided by the total length of the sonotrode. In addition, a basic requirement for the size of the amplification factor is to be greater than 1.

One rule of thumb in designing and fabricating a sonotrode is to make it with materials that have low acoustic losses and high fatigue strengths such as stainless steel, titanium, and aluminium to ensure that the sonotrode has a resonance frequency and resonance wavelength corresponding to the used ultrasonic transducer. Furthermore, the resonance frequency of a sonotrode is related to the sonotrode shape. Common sonotrode shapes are cylindrical, tapered, exponential, and stepped shapes Table 2.5. The resonant frequency of the cylindrical sonotrode shape can be easily determined analytically, whilst the other complicated shapes must use the finite element method to calculate their resonant frequency. Designing and fabricating a sonotrode requires special attention as an incorrectly designed sonotrode can cause the destruction of the vibration system and could lead to damage to the ultrasonic generator. It is essential to carefully calculate the sonotrode length for the specific material used in the fabrication of the sonotrode. Also, the sonotrode must have a symmetric design to focus the sonotrode frequency on the axis of the sonotrode. Symmetric design principles hence force the input channel to be at least two. Positioning the nozzle's tip in-line with the axis of the sonotrode would support the nozzle to achieve the maximum ultrasonic movement (115). For designing a sonotrode, the primary step is to calculate the resonance length of the sonotrode from the formula derived from Webster's horn equation (116):

Webster's horn equation

$$\frac{\partial^2 u(x,t)}{\partial x^2} + \frac{\partial u(x,t)}{\partial x} \frac{\partial}{\partial x} (\ln S_x) = \frac{1}{c^2} \frac{\partial^2 u(x,t)}{\partial t^2},$$

From Webster's horn equation,

$$C_l = \sqrt{E/d} \quad , \lambda = \frac{C_l}{F}$$

Where:

E: Young's Modulus of Material (GPa)

C_L : Sound velocity of material (m/s)

d: Density of material (kg/m³)

F: Operating frequency (kHz)

λ : wavelength (mm)

Then, the dimensions and shape of the sonotrode can be determined using the following equations (116):

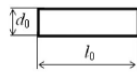

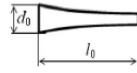
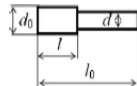
SONOTRODE SHAPE	LENGTH	AMPLIFICATION RATIO	SLENDERNESS RATIO	OTHER
cylindrical		$L = \frac{\lambda}{2}$		$\delta = \frac{d_0}{l_0}$
tapered		$L = 1.1 \frac{\lambda}{2} \times \sqrt{1 + \left(\frac{D_1}{D_2}\right)^2}$	$\frac{D_1}{D_2}$	$\delta = \frac{d_0}{l_0}$
exponential		$L = \frac{\lambda}{2} \times \sqrt{1 + \left(\frac{D_1}{D_2}\right)^2}$	$\frac{D_1}{D_2}$	$\delta = \frac{d_0}{l_0}$
stepped		$L = \frac{\lambda}{2}$	$\left(\frac{D_1}{D_2}\right)^2$	$\delta = \frac{d_0}{l_0}$

Table 2.5: Common sonotrode shapes used in high-power ultrasonic systems and their length calculations.

An effort has been made to use a high-power ultrasonic system to deposit powder material at the Department of Mechanical Engineering at the University of Wisconsin-Madison. The ultrasonic-based micro-powder feeding mechanism was developed and implemented to deposit powders (112). In this study, the authors have used a low-cost micro capillary tube with an inner diameter of 125 μ m and a length of 16 mm to deposit dry micro powders. This capillary tube has a tapered hole and was assembled into a small aluminium block that is then has been glued on a piezoelectric transducer plate. The other end of the piezoelectric transducer was connected to a function generator to control the frequency and the amplitude of the ultrasonic waves as seen

in Figure 2.38. The authors have used a resonant frequency of the piezoelectric transducer of 40 kHz to feed dry powders through the capillary tube.

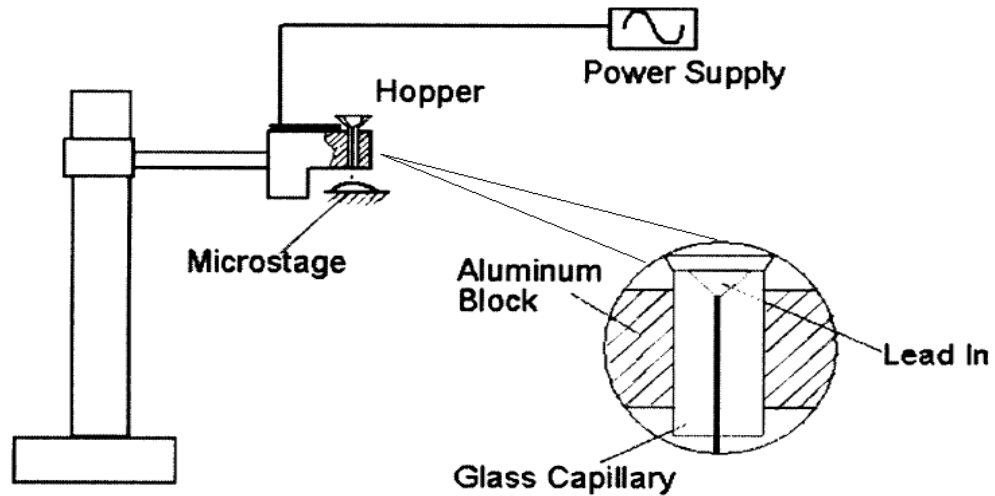


Figure 2.38: Schematic of the micro-feeding and monitoring system (112)

As the deposition width, thickness, and continuation are relatively affected by flow rate, the authors have measured the flow rates using a highly sensitive electric balance. Two types of powder material have been used which are copper powder and stainless-steel powder. Both powder types were spherical shapes and had a nominal diameter of 3 μm . The results show that a continuous discharge of the two powders was achieved at a flow rate of 10-5 g/s. In addition, using a moving velocity of 4 mm/s and a gap distance of 85 μm would result in a continuous and thin powder line.

2.9 Summary of Literature Review

In additive manufacturing, the production of multi-material components is confronted with numerous challenges. These challenges encompass the lack of cost-effective system, accessible multi-material solutions and a lack of knowledge about the fusion of dissimilar materials. Furthermore, the production of multi-material 3D-printed parts is disadvantaged by the absence of suitable building systems and limited published research that pertains to conventional binder jetting techniques.

Multi-material additive manufacturing parts have been reported using vat photopolymerization- stereolithography, material jetting, material extrusion, directed energy deposition, and selective laser melting techniques as have been investigated in the literature. However, most of the work conducted in this area is encumbered by certain constraints, including unsuitability for high-performance components, the consumption of substantial time and materials, the inability to fabricate complex parts, issues with powder separation, a lack of recyclability for used powders, heightened energy consumption, elevated porosity in the final components, restrictions imposed by the powder recoater system when integrated with other additive manufacturing systems, and the lack of cost-effective and accessible processing methods. The literature shows that only a few multi-material works are focusing on using powder bed AM processes. Thus, there is a missed opportunity which is people are not paying enough attention to building metal multi-materials using the BJ approach.

Remarkably, there has been a gap in research works involving the utilization of the binder jetting technique for multi-material applications as there is no capable device for delivering two types of materials for the BJ approach. To be more specific, the application of Binder Jetting with multi-materials in a single layer through dry powder delivery has not yet been documented within the area of scientific literature. An effective approach for this endeavour involves the implementation of a point-by-point powder deposition mechanism to deposit each powder material. This technique

is of paramount importance in the context of dispensing multiple materials within the same layer during the binder jetting process.

The principal novelty of this PhD research resides in the development of knowledge relating to the optimal processing of Binder Jetted multi-material constructs using 316L stainless steel and copper powder. This study investigates the feasibility of fusing two dissimilar materials when subjected to indirect heat processing, the influence of sintering cycles on porosity, interlayer connections, and mechanical tensile properties. To achieve these goals, a novel, cost-effective multi-material deposition system is employed. Through the implementation of this innovative multi-material powder deposition system, a multitude of prevailing limitations can be effectively mitigated. These enhancements cover the challenges associated with depositing two or more metallic materials, the exploration of sintering possibilities for dissimilar materials, the reduction of unutilized powder, and the mitigation of thermal expansion issues observed in the layers of dissimilar materials due to different coefficients of thermal expansion of each material.

Chapter 3. Experimental Setup

3.1 Materials

3.1.1 Powder Material

Within the scope of this investigation, a thorough selection procedure was conducted to acquire a collection of two different materials for their properties and applications. Particularly, careful consideration was given to the use of gas-atomized spherical 316L stainless steel powder (316L, Alfa Aesar, UK) with particle diameters ranging from 10 to 45 μm . Table 3.1 shows the main material elements composition table (percentage of elements) for the 316L stainless steel powder used in this research (117). The second material is a spherical copper powder from Technology Ltd., UK, with particle diameters ranging from 10 to 45 μm .

Elements	Percentage (%)
Fe	67.5
Cr	17
Ni	13
Mo	2.5

Table 3.1: The powder material composition table (percentage of elements) for the 316L stainless steel powder used in this research.

Both powder materials are in spherical shapes, as seen in Figure 3.1 and Figure 3.2, as a spherical powder shape is an important powder characteristic for reaching excellent flowability (118). Additionally, excellent flowability is required for achieving adequate powder layer deposition as well as to make sure that the powder particles are being dispensed properly while the ultrasonic vibration is applied (112).

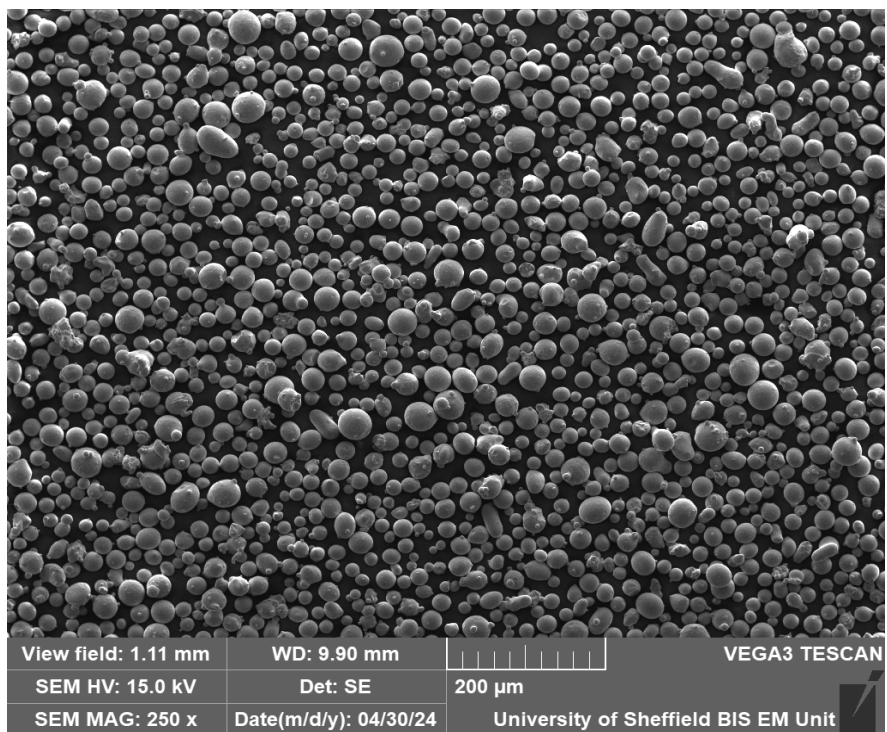


Figure 3.1: Scanning Electron Microscopy micrograph of the 316L stainless steel powder.

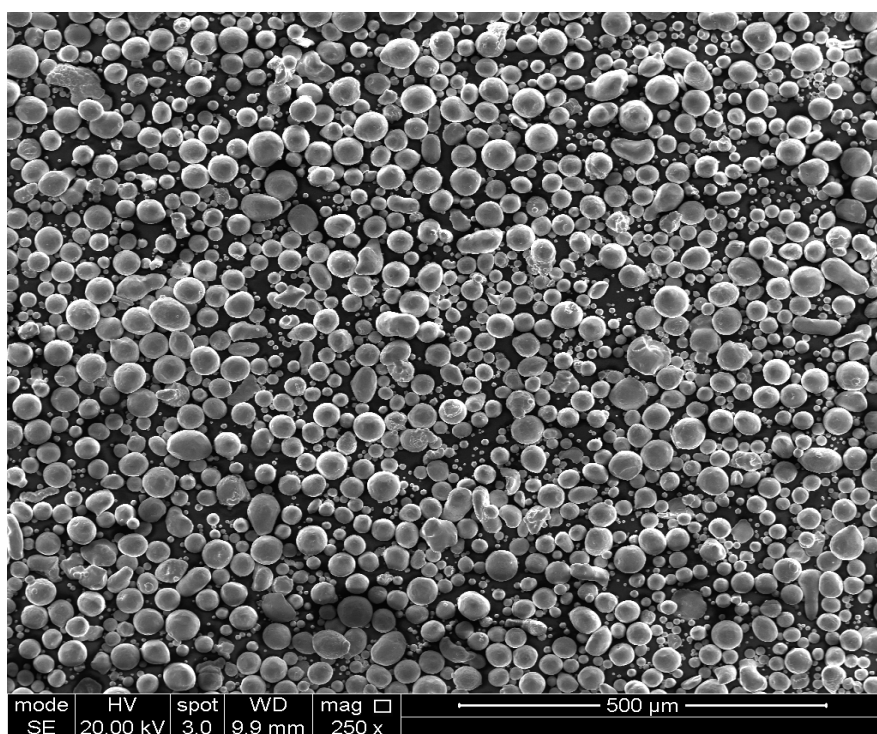


Figure 3.2: Scanning Electron Microscopy micrograph of the copper powder.

Figure 3.3 illustrates the average particle size diameter of the powder along with its distribution. The median particle diameter (D50) was found to be 25.6 μm for the 316L and 22.6 μm for the Cu, aligning with the powder's provided particle size distribution (PSD) from the supplier.

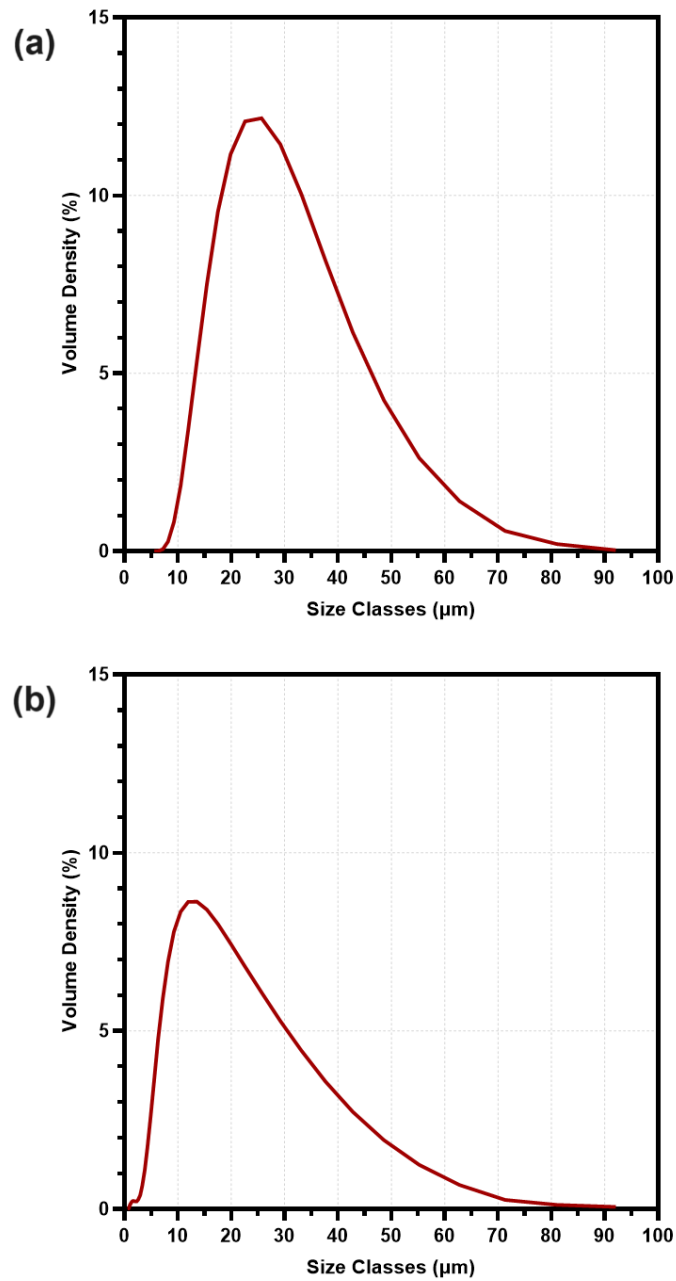


Figure 3.3: Measurement of particle size diameter and its distribution of the 316L stainless steel (a) and copper (b).

The selection of these specific materials stemmed from previous research focusing on the utilization of multi-material components. The investigation has been conducted to explore the potential of using copper and stainless-steel multi-material components in a thermal management application to get an enhanced thermal performance. Multi-material parts, consisting of 316L and Cu, within a heat exchanger can present an interactive approach. This material combination could be utilized in various types such as plate heat exchangers, shell-and-tube heat exchangers, or finned tube heat exchangers. One specific application could be in automotive cooling systems, where the combination of copper's high thermal conductivity and stainless steel's corrosion resistance can enhance heat transfer efficiency and durability in demanding operating conditions. Also, in aerospace, similar multi-material components might find use in aircraft heat exchangers, such as those employed in aircraft engines for cooling purposes. The combination of copper and stainless steel could help improve heat transfer efficiency while maintaining structural integrity under high temperatures and harsh environmental conditions.

3.1.2 Binder Material

In this study, medium molecular weight Polyvinyl Alcohol (PVA) powder was used. PVA has many applications from the textile industry to the niche biomedical industry (37). Using PVA as a polymer-based binder at a concentration of approximately 5% by weight is safe for the environment and non-toxic. In addition, granulated PVA is commercially available with molecular weights ranging from 10,000 to 200,000 g/mol and these molecular weight ranges is also available in various degrees of hydrolysis (38). Hydrolysis quantifies the degree to which a polymer is water-soluble. PVA that has undergone extensive hydrolysis is also known as "fully hydrolysed" PVA. This form of PVA tends to have dissolution temperatures above 80°C and requires a lengthy time for dissolution, especially for PVA with a high molecular weight. After complete dissolution, the OH groups of entirely hydrolysed PVA form strong hydrogen bonds with water molecules, in contrast to the OH groups of PVA with a lesser degree of hydrolysis. The optimum binder for the BJ additive manufacturing process would have a high infiltration capacity and optimal levels of vertical infiltration and lateral spreading. During the powder bed processing of a material, the surface tension and viscosity of the binder play a significant role in determining how far a binder will distribute laterally and how deeply it will penetrate vertically. These properties may be directly influenced by the PVA's molecular weight (39). Paul et al (40) have conducted a study that involved low, medium, and high molecular weight PVA-based liquid binders with respective molecular weights of 10,000, 25,000, and 84,000 g/mol. Accordingly, it was discovered that the PVA-based binder with medium molecular weights performed considerably better than the other two binders because it had the lowest contact angle with the powder, 27 degrees. The optimal polymer chain of the medium molecular weight PVA and the relative lack of viscosity of the binder's water base contributed to its good hydration action compared to other PVA-based binders.

3.2 Designing the Multi-material Powder Deposition System (MMPDS)

One of the objectives of this research effort is the design and fabrication of a multi-material powder deposition system tailored for the deposition of two distinct powder metal materials. This innovative system has been methodically evaluated within the context of Binder Jetting techniques. The multi-material deposition system, as delineated in this work, comprises three essential components: the ultrasonic transducer, the sonotrode (commonly referred to as the horn), and a FDM capillary nozzle (deposition nozzle), serving as the outlet for powder distribution (see Figure 3.4). The introduction of powder into the hopper is facilitated through a pair of symmetrical orifices located at the sonotrode's sides.

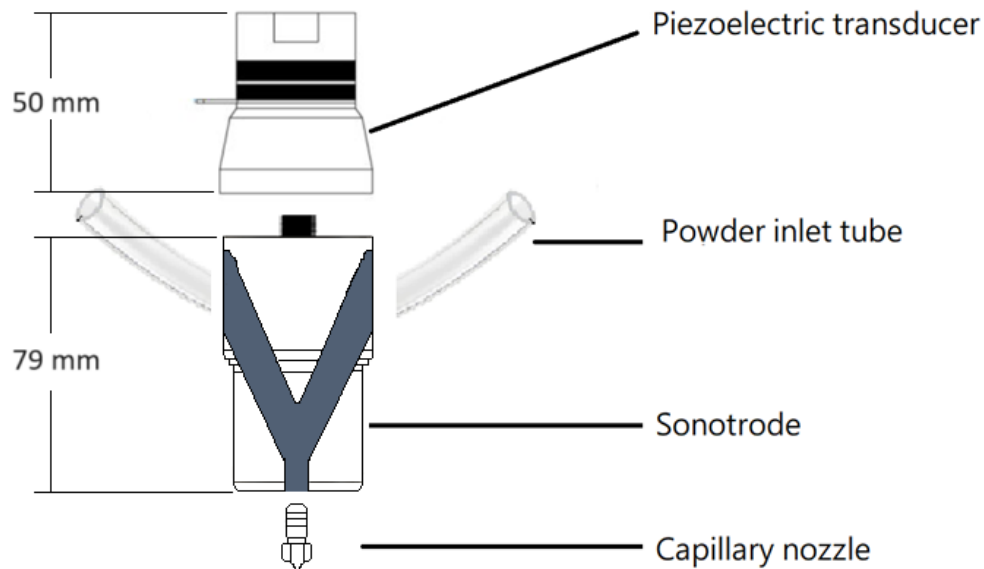


Figure 3.4: An illustrative depiction is presented herein, schematically portraying the multi-material deposition head, showing the various constituent components integral to the dispensation of the multi-material powders system. The system is initiated by an ultrasonic transducer, followed by the sonotrode, which is characterized by the presence of two symmetrically positioned orifices on its sides. The final element in the system is the deposition nozzle.

This design concept could represent an advancement from the conventional single-powder deposition hoppers prevalent in some powder deposition AM methodologies like Blown Powder Directed Energy Deposition, as discussed in the literature review. Notably, this design incorporates the utilization of a replaceable deposition nozzle at the lower portion of the deposition system. Furthermore, this deposition apparatus is engineered to dispense two dissimilar powder materials from a single outlet orifice, the deposition nozzle. The purpose specifications, which have been derived from the literature review, of the deposition system and the employed powder materials are presented in Table 3.2. The particle size ranging from 15-45 μm is used due to the most common powders used with most PBF AM systems. The shape of powder is chosen due to the performance of the spherical particle shape. The sonotrode frequency value is recommended by the literature. The measured outcomes of the chosen parameter values are to deliver consistent powder stream.

Parameter	Value
Particle Size	15-45 μm
Average Particle Shape	Spherical shape
Sonotrode Frequency	40 kHz
Nozzle Diameter	0.6, 0.8, and 1 mm (different nozzle diameters will be trialled)
Nozzle Toolpath Speed	10, 20, and 30 mm/s (different speeds will be trialled)
Ultrasonic power	600, 1200, and 1800 W (different power will be trialled)

Table 3.2: The design of the multi-material system adheres to a set of purpose-driven specifications. Further elaboration on nozzle diameters, velocity parameters, and ultrasonic power settings is provided in Chapter 4 for analysis and discussion.

An initial component of the designed system comprises a 60W, 40 kHz ultrasonic piezoelectric transducer, notable for its high conversion efficiency. This transducer was sourced from the Freshie Wind Store, Guangdong, China (119). The selection of an ultrasonic frequency of 40 kHz has been informed by the prior research and

experimentation concerning the use of ultrasonic powder dispensing methodologies. The preponderance of scholarly works consistently recommends the adoption of an ultrasonic frequency exceeding 39 kHz to establish a controlled flow of powder particles (references (111), (112), (113), (120), (121) and (122)). Thus, in this study, the ultrasonic generator utilized was sourced from Shenzhen Derui Ultrasonic Equipment Ltd, Shenzhen, China, known for its expertise in ultrasonic technology (see Figure 3.5) (123). The seamless integration of this ultrasonic generator into the experimental setup involved connecting it to the system through a transducer. This key step in the experimental configuration allowed the ultrasonic generator to efficiently transmit its ultrasonic vibrations, ensuring precise and controlled application in the study.



Figure 3.5: The ultrasonic generator employed in this study was procured from Shenzhen Derui Ultrasonic Equipment Ltd, Shenzhen, China, and is characterized by its high-quality digital ultrasonic generator, offering an ultrasonic power output of 1800 W at a frequency of 40 kHz.

Table 3.3 presents the technical specifications of the Derui ultrasonic generator that was utilized. The capability to generate ultrasonic vibrations at a frequency of 40 kilohertz (kHz) is possessed by this ultrasonic generator, accompanied by a maximum ultrasonic power output of 1800 watts (W). The ultrasonic generator featured an ability to produce ultrasonic vibrations with good precision and efficiency. In addition,

the generator operates at a frequency of 40 kHz and it has an maximum ultrasonic power output of 1800 watts (W). The combination of its high-frequency operation and substantial power output makes this ultrasonic generator a powerful and versatile tool that can meet the good dispensing of the powder materials.

Specifications	
Brand name	Derui
Product name	ultrasonic generator DR-4018
Ultrasonic frequency	40Khz
Transducer PC	36
Maximum ultrasonic power	1800w
Power supply	240V

Table 3.3: Specifications of the used Derui ultrasonic generator. This ultrasonic generator possesses the capability to generate ultrasonic vibrations at a frequency of 40 kHz, coupled with a maximum ultrasonic power output of 1800 W.

Another initial component is the sonotrode. The sonotrode has undergone engineering to function as an amplifier, serving to transduce the vibrational energy generated by the ultrasonic transducer, thereby enhancing, and focalizing the discharge of powdered material. The sonotrode exhibits a symmetrical design, featuring two precisely aligned powder inlet channels, each possessing a diameter of 10 mm and inclined at an angle of 25 degrees to facilitate the smooth ingress of powder material into the sonotrode, as depicted in Figure 3.6. In the context of this research, the sonotrode is constructed from aluminum, chosen for its economical pricing and favourable acoustic properties, notably its sound propagation speed. Furthermore, the sonotrode is designed as a stepped shape, with an upper diameter of 45 mm, a dimension that corresponds to the diameter of the bottom surface of the ultrasonic transducer, which measures 45 mm. The bottom diameter of the sonotrode is set at 39 mm. The precise widths of these diameters are calculated based on a

specific formula as discussed in the literature, section 2.6 in Table 2.5. Additionally, the sonotrode's total length is systematically determined to be 78.75 mm, ensuring it is equivalent to half the calculated wavelength. This calculation is derived from the sound velocity of Aluminium 6061-T6 over the operating frequency. For a more exposition of the sonotrode's design, please refer to appendix 1. Notably, the inlet channels have been engineered to maintain a high degree of smoothness, as per request from the supplier, to prevent any potential jamming of the powder material during its conveyance. Powder is transported to the nozzle's tip via an inlet channel. The final element of the powder deposition system is a replaceable nozzle, offering a range of outlet diameters. The utilization of replaceable nozzles allows for flexibility in accommodating various powder diameters in future applications, as the nozzles are available in different sizes.

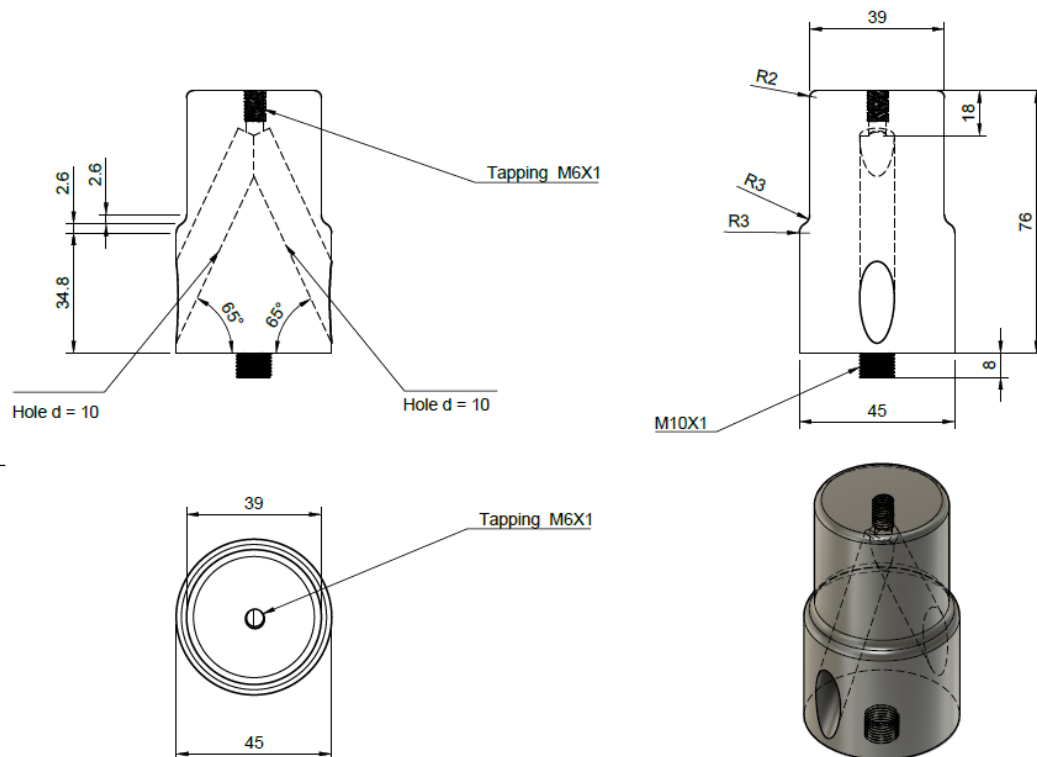


Figure 3.6: A schematic representation of the sonotrode's design, which depicts the calculated dimensions, and geometrical configuration, and shows the inclusion of dual powder inlet orifices positioned on either side.

3.3 The Multi-material Powder Deposition System Validation

Following the exploration of the literature and thorough observations taken during the development of the multi-material deposition system, three fundamental variables have been discerned for subsequent investigation. These variables encompass the deposition nozzle diameter, the deposition rate of speed, and the ultrasonic power level.

Deposition Nozzle Diameter: This parameter refers to the orifice diameter of the Fused Deposition Modelling (FDM) nozzle affixed at the lower terminus of the sonotrode. The specific value of this parameter can be ascertained from the available sizes offered by the manufacturers. In this study, the parameter levels have been designated as 0.6, 0.8, and 1 mm, reflecting the constraints imposed by FDM printer manufacturers. Moreover, it is noteworthy that the literature reports powder deposition out of nozzle diameters ranging from 0.58 to 1.26 mm (111).

Deposition speed rate (Moving Speed Rate): This pertains to the velocity at which the Fisner robot moves the MMPDS during powder deposition. For this investigation, the factor levels have been stipulated as 10, 30, and 50 mm/s. A review of pertinent literature reveals a diverse range of motion speeds, spanning from 5 to 70 mm/s, used for powder deposition, with an observed optimal deposition velocity of approximately 30 mm/s. Consequently, this study encompasses a lower limit of 10 mm/s and an upper limit of 50 mm/s for the rate of motion.

Ultrasonic Power Level: This variable is indicative of the power output, measured in Watts, applied to the ultrasonic transducer during the powder deposition process. For this research, the factor levels have been designated as 600, 1200, and 1800 Watts.

To assess the multi-material deposition system's deposition consistency and measure the dimensions of the resultant powder heap's width and height, a series of trials have been conducted. These trials employ gas-atomized 316L stainless steel powder characterized by a Particle Size Distribution (PSD) falling within the range of 15 - 45 μm , dispensed from a height of 20 mm. The experimental configuration is encapsulated in Table 3.4, where the three previously mentioned parameters are

delineated at three discrete gradations: specifically, low, intermediate, and high levels. This tabular representation serves as an overview of the experimental structure, incorporating the variations in these key parameters to facilitate a more detailed analysis of the effect of each parameter.

Input parameter	Level-1	Level-2	Level-3
Nozzle diameter size (mm)	0.6	0.8	1
Deposition speed rate (mm/s)	10	30	50
Ultrasonic power level (W)	600	1200	1800

Table 3.4: The experimental design is summarized and presents the three parameters, deposition nozzle diameter size, speed rate, and the ultrasonic power level across three distinct levels: low, medium, and high.

3.4 Multi-material Binder Jetting System

To facilitate the successful implementation of a multi-material Binder Jetting (BJ) process, a specialized system was purpose-built for this study. The central component chosen to precisely coordinate the movement of the multi-material deposition system was a Fisnar robot (Fisnar I&J7400-LF) obtained from INTERTRONICS, UK (124). This robot system features 3-axis maneuverability (the robot reaches the same given position with 0.1mm precision), allowing for control of the multi-material deposition system's trajectory. The Fisnar robot is equipped with a liquid dispensing pen utilized for the precise application of the liquid binder, featuring an interchangeable nozzle tip of varying diameters. To regulate the deposition of liquid binder droplets, a DC50 Benchtop Digital Liquid Dispensing Controller, also from INTERTRONICS, UK, was employed. Figure 3.7 provides a visual representation of the various system components and their interactions, showing the equipment involved in achieving a successful multi-material BJ process.

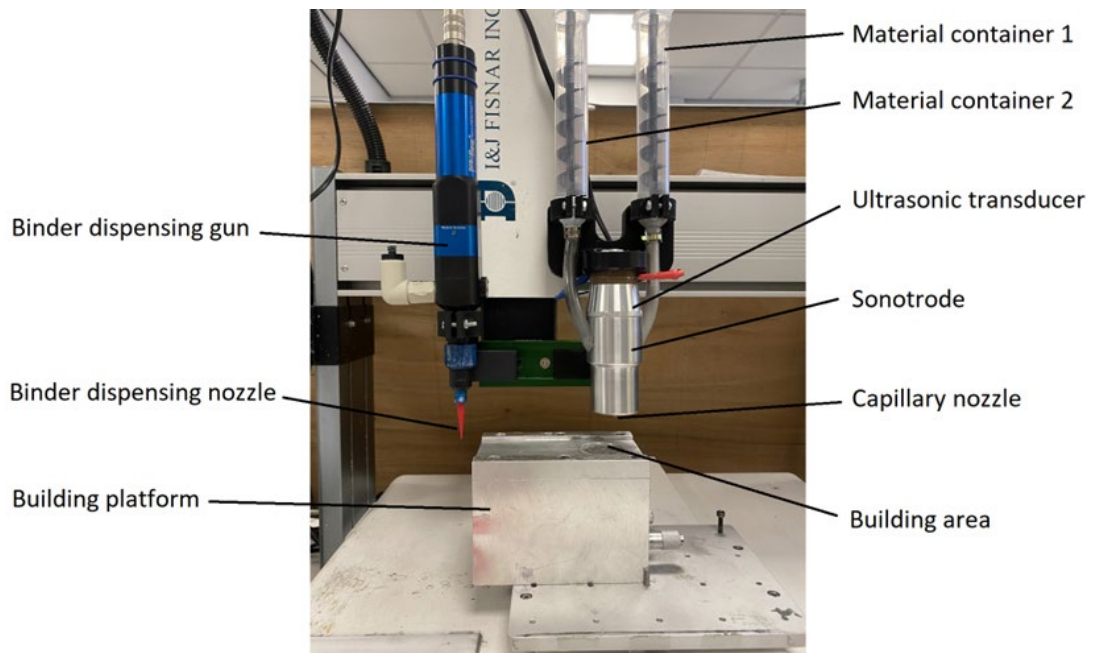


Figure 3.7: A visual representation of the various system components and their interactions, showing the equipment involved in achieving a successful multi-material BJ process.

In addition, a supplemental building envelope was introduced within the process. This component is deployed to be lowered after the printing of each layer. It operates in conjunction with a Z-axis linear trimming platform procured from Shenzhen Chuangjicheng Wangluo Keji Youxian gongsi, China (see Figure 3.8). The platform is square-shaped, measuring 60 x 60 millimetres, and features a 42 mm graduated dial thimble on one side. The platform offers a total height of 46 mm, which includes a maximum stroke length of 10 mm and a minimum stroke distance of 10 micrometres. This platform was specially fabricated to serve as a manual building envelope for 3D printing purposes and was tested to validate its functionality as a building platform within the mechanical engineering workshop at the University of Sheffield. The integration of these components and their operational dynamics collectively form a crucial framework for the successful execution of multi-material Binder Jetting in this research work.

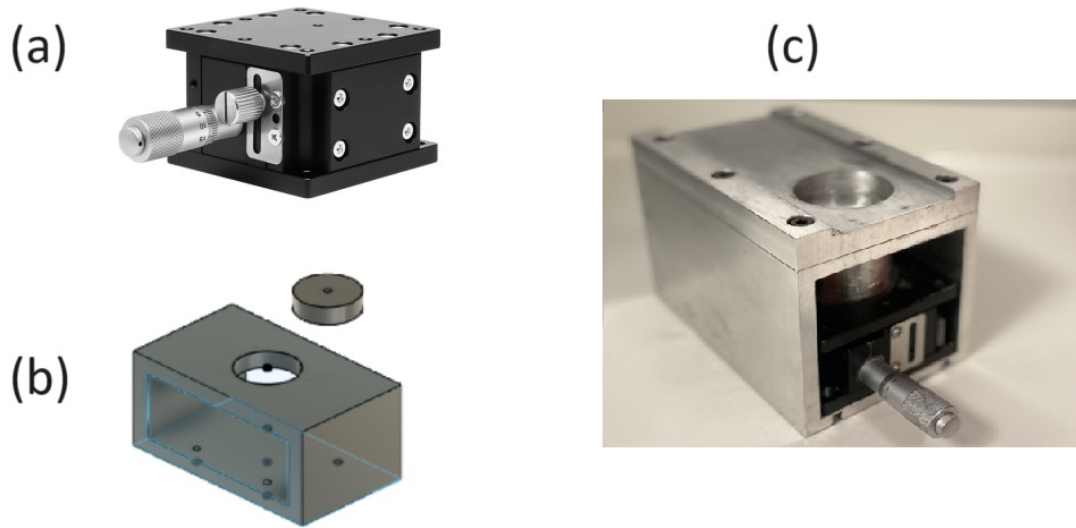


Figure 3.8: The supplemental building envelope. (a) shows the Z-axis linear trimming platform, (b) fabrication of the powder bed block with a moving Z-axis, and (c) the final powder bed building envelope.

3.5 Post-processing of the Green Parts

The post-processing steps are fundamental in BJ 3D printing. In the post-processing, the binder is burnt off and the metallic powder is sintered to fuse the loose powder to form the final shape. Sintering is considered the most crucial post-processing stage as it plays an essential role in the final part's density and strength (5). The green components were sintered in a tube furnace (STF15/180, Carbolite Gero (125)) according to a specific thermal cycle (see Figure 3.9). For each sintering cycle, the specimens were prepared and then the sintering process was conducted in an Argon (Ar) inert atmosphere, as recommended by the published research (56), (57), (58), (59) using a tube furnace to ensure consistency and reproducibility. In addition, in some cases, when the inert gases are used in the sintering atmosphere, gases can become trapped within the material as it undergoes densification, leading to the formation of pores or voids. This gas entrapment can compromise the density of the sintered part. Therefore, adjusting sintering parameters such as temperature and dwell time can help mitigate gas entrapment.

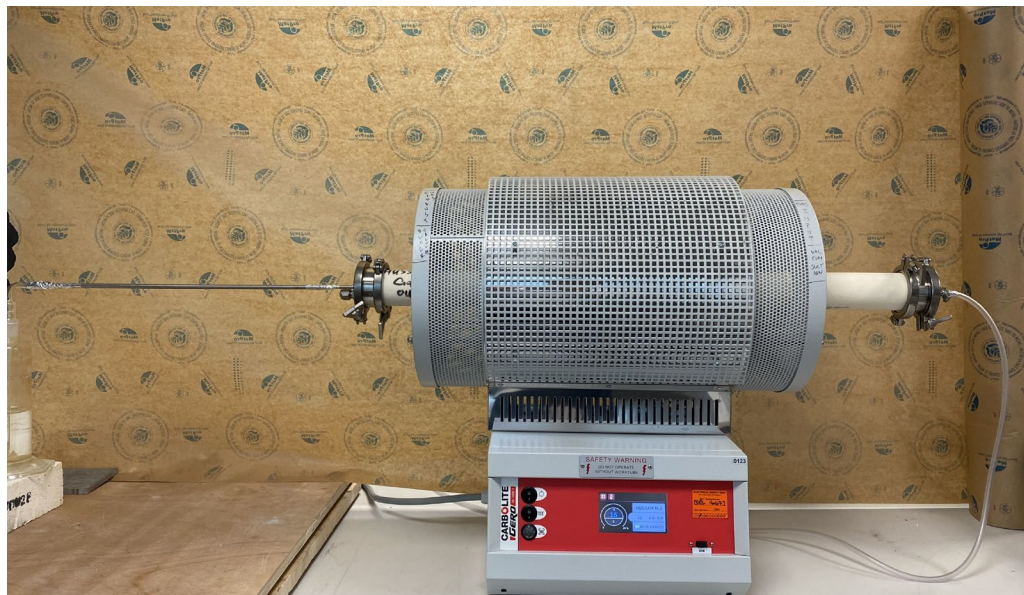


Figure 3.9: The tube furnace (STF15/180) was employed for the sintering process of the green components, which were produced through the binder jetting method.

3.6 Samples Characterisation

3.6.1 Preparation for Optical Microscopy

In preparation for optical analysis, the samples underwent a controlled processing regimen. Initially, a precision abrasive saw machine was employed to perform sample cutting. To facilitate secure fixation, the samples were embedded using the SimpliMet 4000 mounting equipment (from Buehler Limited (126)), employing conductive Bakelite materials. Subsequently, a Buehler Automet Grinder-Polisher device (AUTOMET® 250 GRINDER-POLISHER, from Buehler Limited (127)) was utilized to undertake a series of grinding and polishing steps. The grinding process involved the sequential use of increasingly finer grit papers, specifically P250, P600, P1200, and P2500. Operating at a plate speed of 300 rpm and a head speed of 55 rpm, a constant force of 23 N was applied over a 60-second interval. It is worth noting that a head rotation counter to the direction of the plate was judiciously employed to ensure uniformity in the grinding process. In the pursuit of a smooth finishing, unblemished surface, the samples were subsequently subjected to polishing with colloidal silica polishing fluid with a particle size of 0.06 micrometer for a duration of 5 minutes, maintaining the same operational parameters as the preceding grinding phase. A counter-directional polishing technique was implemented in this step to achieve the desired outcome of a flat, highly reflective surface. Concluding the sample preparation, a thorough rinsing procedure was executed for a duration of 3 minutes, utilizing a ChemoMet polishing cloth and water. This thorough cleaning phase was essential for the removal of any residual polishing debris, ensuring optimal clarity for subsequent optical microscopy analysis. The prepared samples were then rendered ready for examination via optical microscopy, allowing for a thorough inspection of their porosity features.

3.6.2 Porosity Analysis

The utilization of optical microscopy, employing a Nikon microscope ECLIPSE LV150 (from Nikon Industrial Microscopy (128)), enabled a thorough examination of the material interfaces, quality of bonding, and porosity. The assessment of sample porosity was carried out employing ImageJ, a specialized image processing software tailored for scientific analysis. Optical microscopy micrographs obtained from the polished cross-sectional samples served as the basis for porosity evaluation. Initially, these micrographs were converted into 8-bit grayscale images, a transformation that was instrumental in enabling subsequent image analysis. The conversion into the 8-bit format effectively rendered the original micrographs as grayscale images, with variations in contrast that predominantly reflected the surface's topographical features, particularly the presence of pores and voids. Within this framework, ImageJ was instrumental in establishing the contrast threshold necessary for pore detection as the procedure method inspired by prior research works (40) (129). The contrast threshold was chosen by inspecting the segmented image resulting from different threshold values and select the one that provides the most accurate representation of the features of interest while minimizing background noise. This approach facilitated precise porosity determination by quantifying pore density within the micrograph, offering valuable insights into the material's structural characteristics.

3.6.3 Microstructure Characterization

In the context of this study, Scanning Electron Microscopy (SEM) analysis was conducted using an InspectF50, a scanning electron microscope designed to generate high-resolution images of samples through the scanning of a focused electron beam. SEM utilizes the interaction of electrons with the sample to produce various signals that are detected by electron microscope detectors, providing critical insights into the surface topography and composition of the sample (130). The Inspect F50 SEM instrument is equipped with an Energy Dispersive Spectroscopy (EDS) system,

Secondary Electron (SE), and Backscattered Electron (BSE) detectors. These instrumental features enable the analysis of diverse sample types, including longitudinal and transverse cross-sections, powder cross-sections, as well as both polished and as-built surfaces (131). The utilization of SEM was employed to assess the quality of bonding, detect any potential anomalies or defects, and assess the uniformity of the 316L and Cu 3D-printed parts' interfaces. Augmented by EDS capabilities, the SEM facilitated elemental mapping, allowing for the identification and visualization of the distribution of distinct elements at the material interfaces. This approach yielded valuable information regarding their chemical composition and potential interdiffusion phenomena, as was similarly documented in previous research by Wei et al (100) involving the inspection of multi-material selective laser melting printed samples.

3.6.4 Mechanical Tensile Testing

Furthermore, in accordance with the stipulations outlined in the BS EN ISO 6892-1:2016 Standards (132), dog-bone-shaped tensile test specimens were fabricated. These specimens were intended for assessing the tensile properties of the multi-material composition consisting of copper (Cu) and 316L stainless steel (SS) at ambient room temperature. The evaluation of tensile strength was carried out using a universally recognized testing apparatus, the Model H5K from Tinius Olsen Ltd equipped with a maximum load of 5 KN as specified by the manufacturer. Conforming to the protocols outlined in the BS EN ISO 6892-1:2016 Standards, the determination of strain rate was carefully executed and precisely maintained within a range of 2 mm per minute. To ensure the reliability of the results, the tensile tests were performed in triplicate for each material, enabling the calculation of average values and standard deviations, which serve to enhance the precision of the acquired data.

Chapter 4. Optimization of the Powder Multi-material Deposition System

4.1 Introduction

In the field of additive manufacturing (AM), and more especially in the field of powder bed AM printing techniques, it is of the greatest significance to achieve a consistent and even distribution of the powder material. When it comes to eliminating discontinuities and flaws in the final printed items, this consistency is a crucial component to have. The printing process as a whole can be greatly slowed down by any resistance that the powder deposition encounters as it is being distributed inside the machine. The implications of such resistance might emerge as incomplete or incorrect prints, which in turn result in items with poor geometrical and dimensional tolerances. These types of issues are characteristic of AM technologies and are commonly encountered while using these technologies. The study in question centered on the design and manufacture of a specialised multi-material powder deposition system to help solve these problems. This system was designed to assist the regulated distribution of two different kinds of loose powders, 316L stainless steel powders, and pure copper powders, respectively. As shown in Figure 4.1, this deposition system is made up of numerous essential components, including the following:

- Powder containers: The system consists of two containers, each of which is used to hold a type of raw powder material. The containers also equipped with a screw feeder to allow the powder to be pushed into the sonotrode.
- An ultrasonic transducer: A 40 kHz ultrasonic piezoelectric transducer is used. This transducer's job is to produce ultrasonic vibrations of a certain magnitude.
- Sonotrode: The vibrations that are generated by the ultrasonic transducer are transferred to the sonotrode, which then causes it to vibrate as well. This vibrational motion is essential for permitting the regulated release and deposition of the powder.

- Deposition nozzle: The deposition nozzle is located at the end of the sonotrode and provides the vital role of regulating the volume of powder material that flows from the sonotrode onto the construction platform. Its position at the end of the sonotrode allows it to perform this important duty. Notably, this deposition nozzle was created to be detachable and interchangeable. This characteristic enables the orifice size to be modified to handle a wide range of powder particle sizes.

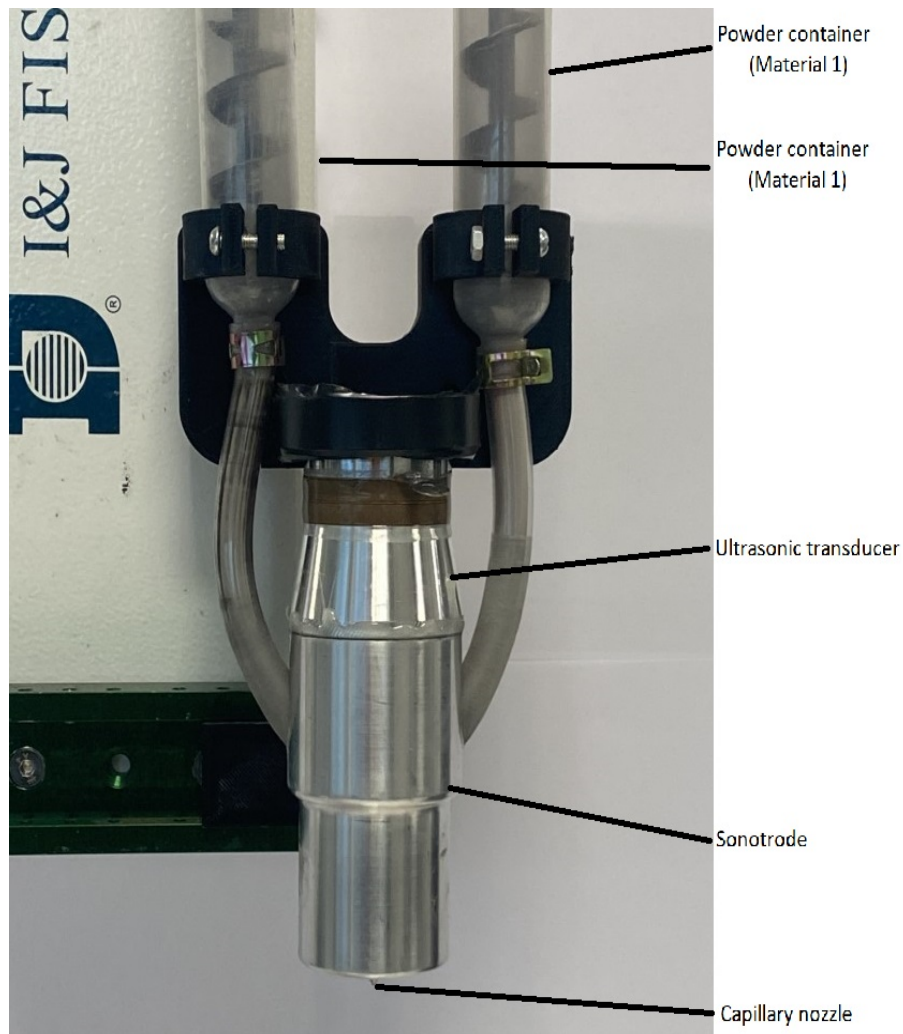


Figure 4.1: The multi-material powder deposition system integrated with the Fisnar robotic platform is illustrated, highlighting its constituent components. These components encompass individual powder containers for each material, an ultrasonic transducer, a sonotrode, and a deposition nozzle.

Subsequent to the assembly of the multi-material powder deposition system, it was seamlessly integrated into the Fisnar I&J 7400-LF robotic platform. The precise control and positioning of the deposition head were achieved through the direct coordination of this robotic system, playing a fundamental role in the process. Leveraging the robot's capacity for fine adjustments in the multi-material powder deposition system orientation and movement speed, the powder deposition process was executed with accuracy and consistency. A precise program code was developed to validate the efficacy of the novel deposition mechanism. This program was designed to instruct the movement of the deposition system as it dispensed powder onto a plastic substrate, effectively serving as a guiding mechanism. The primary objective of this testing phase was to ascertain the system's capability to dispense metal powder consistently and reliably. During the depositing trials, 316L stainless steel powder with particle sizes ranging from 15 to 45 μm was utilized. The decision to utilize this range for the trials is primarily based on considerations of market availability and common industry practices in AM. This range represents a widely accessible and commonly used powder size distribution in the additive manufacturing market. As a result of these trials, the system demonstrated its proficiency in the dependable deposition of powder material, showing a continuous and uniform deposition line characterized by varying dimensions in both width and height, as depicted in Figure 4.2.

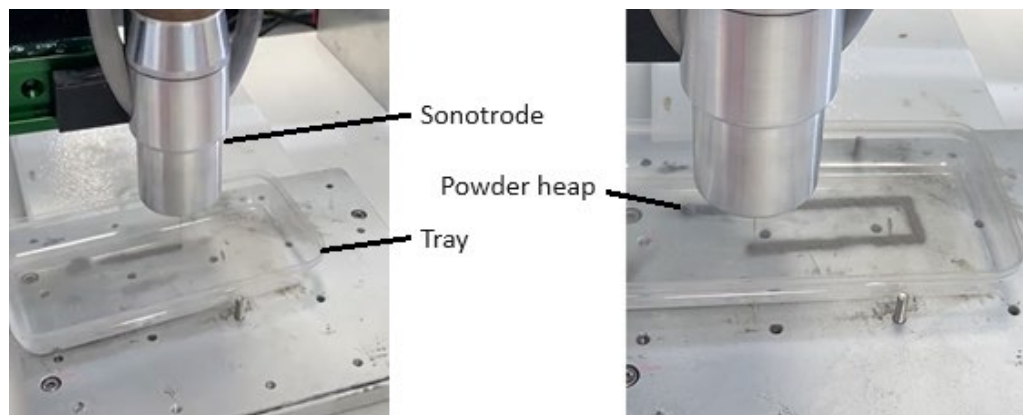


Figure 4.2: Displaying the system capability of consistently depositing powder material as a continuous, uniform deposition line with variable width and height dimensions.

4.1.1 Powder Deposition Resolution

Following the published research of the powder material deposition system's developmental stages, three fundamental variables have been identified for investigation. These factors, namely the deposition nozzle diameter, head movement speed, and ultrasonic power level, have been chosen due to their anticipated significance and potential impact on the multi-material deposition system, as outlined in Table 3.3 (chapter 3.3). By scrutinizing and manipulating these variables, valuable insights can be gleaned concerning their effects on the overall performance and quality of the MMD system.

To assess the finest resolution achievable by the deposition head, two distinct series of experimental trials were conducted. In the initial series of experiments, powder material was dispensed from a 20 mm height, representing the distance between the build platform and the deposition nozzle, resulting in a zigzag pattern. In the second series of trials, an additional round flattening wiper was affixed to the lower side of the sonotrode to level and evenly distribute the deposited powder to a predetermined height.

4.1.2 Design of Experiment Analysis

The optimisation of process parameters is a technique that is frequently used in a variety of additive manufacturing (AM) techniques to improve the qualities of the manufactured parts. The application of statistical analysis involves utilizing the design of experiments (DOE) technique allows researchers to pinpoint the significant factors within a process by conducting a predetermined number of experiments. For instance, Taguchi analysis enables faster conclusion drawing, thereby conserving valuable time and resources when compared to a full factorial design, which necessitates testing all possible combinations. However, full factorial design takes into consideration an interpretation of the different parameters and their levels. The primary goals of a statistical analysis encompass three important aspects: firstly, identifying the "main

effects" of each factor to ascertain their influence on the output; secondly, exploring the factor levels that yield the most favourable results; and thirdly, evaluating the contributions made by each factor to the overall outcome. One way to accomplish the final goal, the statistical method known as Analysis of Variance (ANOVA) can be used as a tool to determine which aspects are more important than others (133). Recent research has shown that one of the beneficial ways of process parameters' optimisation is to use any approved statistical analysis, for instance, in the field of fused deposition modelling (FDM), Taguchi analysis was used to explore the impact of various parameters on enhancing dimensional accuracy such as layer thickness, orientation angle, and filling pattern (134). Additionally, the ANOVA efficiently optimised five separate aspects and their corresponding parameters through the analysis of only 27 tests, which enabled the construction of an ideal trade-off among these factors. Similarly, Wankhede et al (135) used this statistical analytic approach to evaluate the influence of FDM process parameters on surface roughness and build time of the finished parts. They were able to get optimal parameter levels with only 8 experimental combinations by using this approach. In addition, Zhu et al (136) were able to successfully improve surface features and minimise porosity in the context of high-speed sintering (HSS) by applying Taguchi analysis to optimise HSS process parameters. An alternative method for optimizing the system involves the application of a regression equation. A regression equation is employed to study the relational dynamics between distinct sets of data (137). These examples demonstrate how successful and efficient it is to use statistical analysis for optimising process parameters in additive manufacturing. As a result of the presence of the three chosen parameters, each of which can be broken down into three distinct levels (low, medium, and high) a full factorial DOE has been adopted for this investigation. An overview of the experimental setups, including the levels of the respective parameters, is presented in Table 4.2.

Experiment Set	Parameter-1	Parameter -2	Parameter -3
1	0.6	10	600
2	0.6	10	1200
3	0.6	10	1800
4	0.6	30	600
5	0.6	30	1200
6	0.6	30	1800
7	0.6	50	600
8	0.6	50	1200
9	0.6	50	1800
10	0.8	10	600
11	0.8	10	1200
12	0.8	10	1800
13	0.8	30	600
14	0.8	30	1200
15	0.8	30	1800
16	0.8	50	600
17	0.8	50	1200
18	0.8	50	1800
19	1	10	600
20	1	10	1200
21	1	10	1800
22	1	30	600
23	1	30	1200
24	1	30	1800
25	1	50	600
26	1	50	1200
27	1	50	1800

Table 4.1: A layout of the full factorial experimental design showing a tabular representation of the three parameters systematically ranging across three discrete tiers: low, moderate, and high.

4.2 Results and Discussions

The multi-material deposition system has been trialled to check its deposition consistency and to measure the height and width of the powder heap. The material used in these trials is gas-atomized 316L stainless steel powder and copper with a 15 - 45 μm powder particle size and will be dispensed from a height of 20 mm. A zigzag pattern was created by depositing the powder material from a height of 20 mm. The height of 20 mm was fixed throughout the experimentation. Maintaining a fixed height ensures that the powder material is deposited consistently in each trial, minimizing variability due to changes in deposition parameters. This consistency helps in accurately assessing the effects of other variables or factors being investigated in the experiment. Fixing the deposition height at 20 mm provides a standardized condition for the initial trial series, facilitating reliable comparisons and interpretation of results. The zigzag lines' widths have been measured for three different samples for each parameter arrangement by a vernier calliper. The measurement have taken place at the middle part of the deposited line. The average value of the three readings has been chosen as the parameter arrangement's value. On the other hand, the deposition height was established by placing a known-sized object adjacent to the zigzag lines and capturing an image. Subsequently, the height was calculated using ImageJ software.

The parameters have been adjusted depending on the results attained in the first experiment series. In other words, some inputs have been eliminated in the second series of experiments due to the poor deposition line pattern results that they showed in the previous test group. Next, the powder heap's height and width have been measured to show the differences and effects of the three parameters on the deposition head. The measurements have been calculated by using ImageJ software where a known dimension reference object, as a dimension calibration tool, has been placed close to the powder heaps while taking the picture for each deposition line.

4.2.1 Powder Deposition Resolution

4.2.1.1 Deposition trials without flattening wiper.

In the initial trial series, deposition nozzles with diameters of 0.6, 0.8 and 1 mm have been used in addition to different head movement speeds of 10, 30, and 50 mm/s. Moreover, ultrasonic power levels of 600, 1200, and 1800 W have been trialled. During these tests, it was discovered that the 0.6 mm deposition nozzle, even when applying all three different ultrasonic power levels, would cause powder jam and prevent the powder from being ejected from the sonotrode. This nozzle size might have been too narrow for efficient powder flow, leading to clogging and jamming, even when subjected to higher ultrasonic power levels. This confirms that even with the aid of ultrasonic vibration, the 316L stainless steel powder with particle sizes ranging from 15 to 45 μm cannot pass through the narrow deposition orifice. The outcomes of the conducted experiment, as shown in Table 4.3, afford an understanding of the dynamic interplay between ultrasonic power levels and the resulting dimensions of the powder heap height.

Notably, a proportionate relationship is evident, wherein an increase in ultrasonic power is positively correlated with an increased heap height. The phenomenon observed can be explained by the interaction of mechanisms controlled by the motion vibration of the transducer. This motion, regulated by the ultrasonic generator, initiates ultrasonic vibrations, facilitating the controlled dispensation of powder material through the sonotrode. Higher power levels prompt a faster vibrational response from the transducer, leading to increased powder deposition.

An additional influential factor impacting powder height is the velocity of the deposition head along the building platform. The velocity of the deposition head across the building platform emerges as a consequential variable influencing powder height. The outcomes obtained from an array of distinct speed rates underscore notable disparities in both heap height and morphological attributes, particularly concerning the two nozzle sizes subjected to scrutiny (0.8 and 1 mm). The systematic analysis of these results also reveals a negative correlation between the movement

speed and the resultant heap height. Stated differently, a rise in speed is associated with a concomitant reduction in heap height.

Figure 4.3 serves as an illustrative representation show the impact of varying parameters on powder heap height within the context of the experimental setup. Specifically, the utilization of a 0.8 mm deposition nozzle, accompanied by a head speed rate of 10 mm/s at the lowest ultrasonic power setting, showed a discernible heap height of 245 μm . Intriguingly, as the ultrasonic power levels increased—from the lowest to medium and ultimately to the highest setting—the resultant heap heights demonstrated a proportional escalation, reaching 270 μm and 370 μm , respectively. In parallel investigations, the deployment of a 1 mm deposition nozzle, concomitant with a head speed rate of 10 mm/s at the lowest ultrasonic power level, yielded a notable heap height of 710 μm . The subsequent exploration of medium and highest ultrasonic power settings (1200 W and 1800 W, respectively) at the same nozzle size and head speed revealed corresponding heap heights of 721 μm and 760 μm . These results collectively underscore the interplay of ultrasonic power levels and nozzle dimensions in dictating the powder deposition dynamics.

The observed dependencies affirm the critical influence of ultrasonic power and nozzle specifications in achieving good control over powder deposition outcomes.

The other factor that influences the powder height is the deposition head's moving speed across the building platform. In rendering the experimental outcomes with numerical precision, a thorough examination of parameter interactions is crucial. Employing a deposition nozzle possessing a diameter of 0.8 mm, place alongside with the highest ultrasonic power setting and a head movement speed rate of 10 mm/s, yielded a discernible heap height of 350 μm . Subsequently, sustaining the identical nozzle size and ultrasonic power level while adjusting the movement speed to 30 mm/s yielded a consequential reduction in heap height to 315 μm . Further variation in the movement speed parameter, specifically at 50 mm/s under analogous conditions, resulted in a diminished heap height of 240 μm . An in-depth comparative

analysis reveals that the adoption of a movement speed of 50 mm/s generated approximately two-thirds of the heap height achieved at 10 mm/s.

Nozzle diameter (mm)	Speed rate (mm/s)	Power level (W)	Heap Width (mm)	Heap height (μm)
0.8	10	600	3.9	245
		1200	3.6	270
		1800	3.4	350
	30	600	3.5	190
		1200	3.2	210
		1800	3.1	315
	50	600	3.1	150
		1200	2.7	210
		1800	2.5	240
	10	600	4.6	710
		1200	4.4	721
		1800	4	760
1	30	600	4.3	503
		1200	3.9	517
		1800	3.6	562
	50	600	4.1	231
		1200	4	283
		1800	3.5	365

Table 4.2: The outcomes pertaining to heap width and height values derived through the utilization of two distinct parameters, each comprising three discrete levels. These parameters systematically applied within the context of a validation study conducted on a multi-material system without wiper.

Conversely, employing a deposition nozzle with a 1 mm diameter, in tandem with the highest ultrasonic power level and a head movement speed rate of 10 mm/s, yielded a pronounced heap height of 760 μm . In exploration, the application of the maximum ultrasonic power level, 1800 W, at the same nozzle size and varied head motion speeds of 30 and 50 mm/s resulted in heap heights of 562 μm and 365 μm , respectively. Comparative scrutiny underscores that at a movement speed of 50 mm/s, the resultant heap height is slightly less than half of that achieved at 10 mm/s. These findings underscore the profound influence of deposition parameters, offering valuable insights into the optimization strategies for achieving precise control over powder deposition in the realm of additive manufacturing processes.

An additional visible factor exerting a substantial influence on the powder height within the deposition system is the deposition nozzle diameter. This parameter emerges as a critical variable, playing a fundamental role in shaping the resultant powder heap. The systematic scrutiny of these outcomes reveals a discernible and statistically significant positive correlation between the deposition nozzle diameter and the ensuing heap height. To understand this relationship more precisely, an increase in the deposition nozzle diameter exhibits a proportional rise in the resultant heap height. In other words, a discernible rise in deposition nozzle diameter is associated with a simultaneous elevation in heap height. This observed correlation underscores the interplay between the geometric characteristics of the deposition nozzle and the resulting powder deposition dynamics, offering valuable insights into the optimization of deposition parameters for enhanced control and precision of the system.

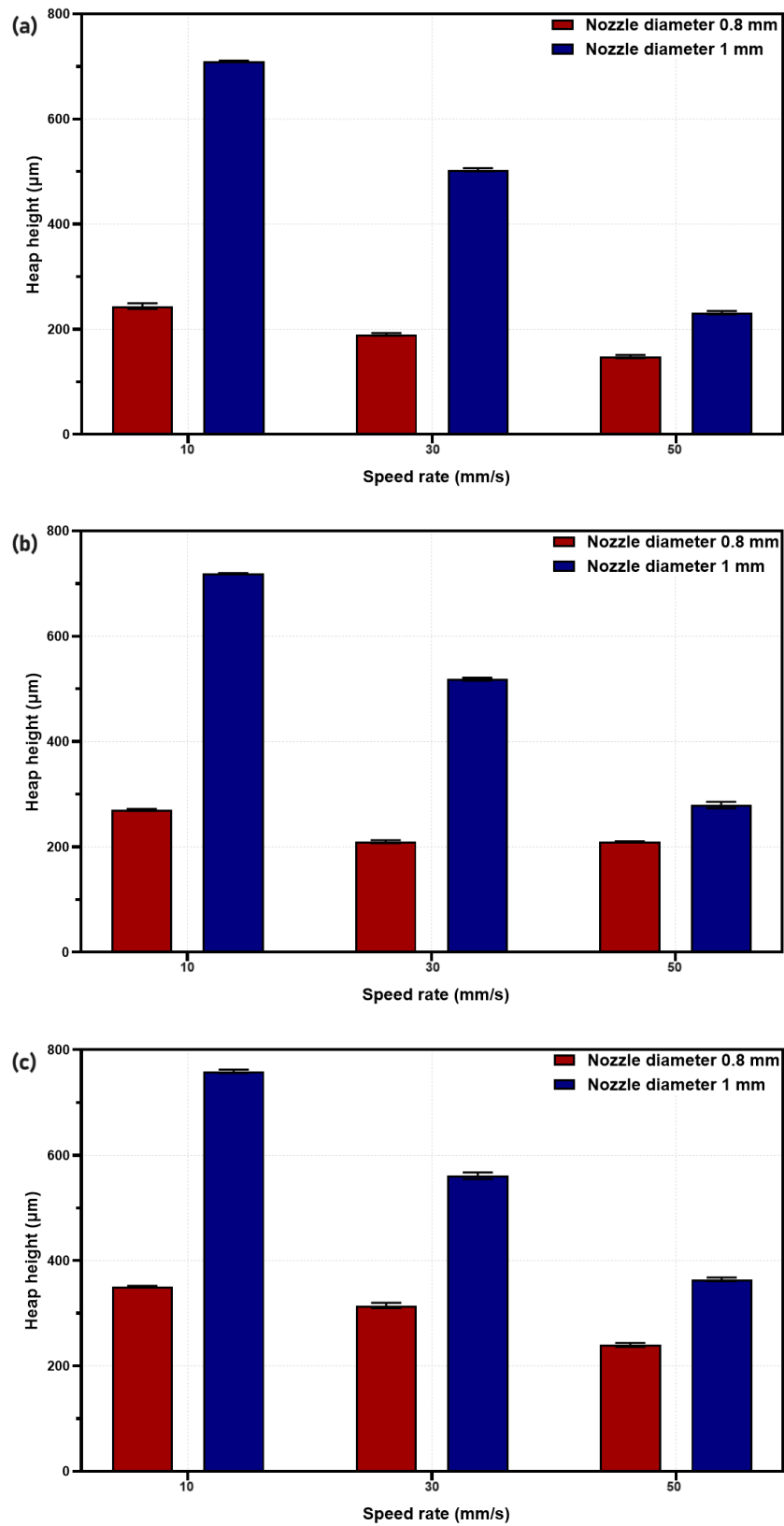


Figure 4.3: The influence of ultrasonic power levels and speed rates on the heap height of the deposited powder investigated using deposition nozzles with diameters of 0.8 and 1 mm. Graph (a) indicates a power level of 600W, whereas graph (b) correspond to the 1200W power level and (c) shows the power level of 1800W.

In Figure 4.4, an in-depth analysis of the influence of ultrasonic power levels on the width values of deposited powder heaps is presented. The experimental findings distinctly reveal a negative correlation between ultrasonic power levels and the resultant heap width. This phenomenon signifies that with an increase in ultrasonic power, there is a consequential reduction in the observed heap width. The origin of this correlation lies in the vibrational dynamics orchestrated by the transducer. These vibrational patterns are subsequently transmitted to the sonotrode, thus regulating the dispensing characteristics of the powder material. As the power level intensifies, the transducer undergoes accelerated vibrations, resulting in a more focused powder stream, and conversely, decreased power levels yield broader powder deposition. Illustratively, employing a 0.8 mm nozzle with a movement speed rate of 50 mm/s at the lowest ultrasonic power level yields a heap width of 3.1 mm. Contrastingly, under analogous conditions but with medium and highest ultrasonic power levels, the heap width diminishes to 2.7 mm and 2.5 mm, respectively. Additionally, the utilization of a 1 mm deposition nozzle at the lowest ultrasonic power level, paired with a movement speed rate of 50 mm/s, produces a heap width of 4.1 mm. In contrast, when applying the same nozzle size and speed but at medium and the highest ultrasonic power levels, the resulting heap widths are 4 mm and 3.5 mm, respectively. These detailed findings underscore the relationship between ultrasonic power levels and powder heap dimensions, providing essential insights for the optimization of the deposition system.

Simultaneously, an investigation into the influence of movement speed on the width characteristics of deposited powder heaps is important within the context of the optimization of the deposition system. The insights derived from the experimental results reveal a compelling inverse relationship between movement speed and the resulting heap width, wherein an increase in head speed precipitates a discernible reduction in the observed heap width. This interplay is examined through the controlled application of a 0.8 mm deposition nozzle, operating at a precise

movement speed rate of 10 mm/s, concomitant with the highest ultrasonic power level, yielding a heap width of 3.4 mm.

Contrasting scenarios unfold when subjecting the system to varying movement speeds under identical nozzle size and ultrasonic power conditions, revealing heap widths of 3.1 mm and 2.5 mm at 30 mm/s and 50 mm/s, respectively. This systematic exploration not only accentuates the sensitivity of the deposition process to movement speed variations but also sheds light on the complex dynamics governing powder heap dimensions.

Furthermore, an examination extends to the utilization of a 1 mm deposition nozzle, operating at a movement speed rate of 10 mm/s under the highest ultrasonic power level. This configuration yields a substantial heap width of 4 mm. However, under altered conditions of movement speed, specifically at 30 mm/s and 50 mm/s, the resultant heap widths are notably reduced to 3.6 mm and 3.5 mm, respectively. These findings, rooted in experimental accuracy, contribute to a profound understanding of the relationship between movement speed and powder heap dimensions. This knowledge, essential for strategic optimization, develops the scientific foundation of the powder deposition system.

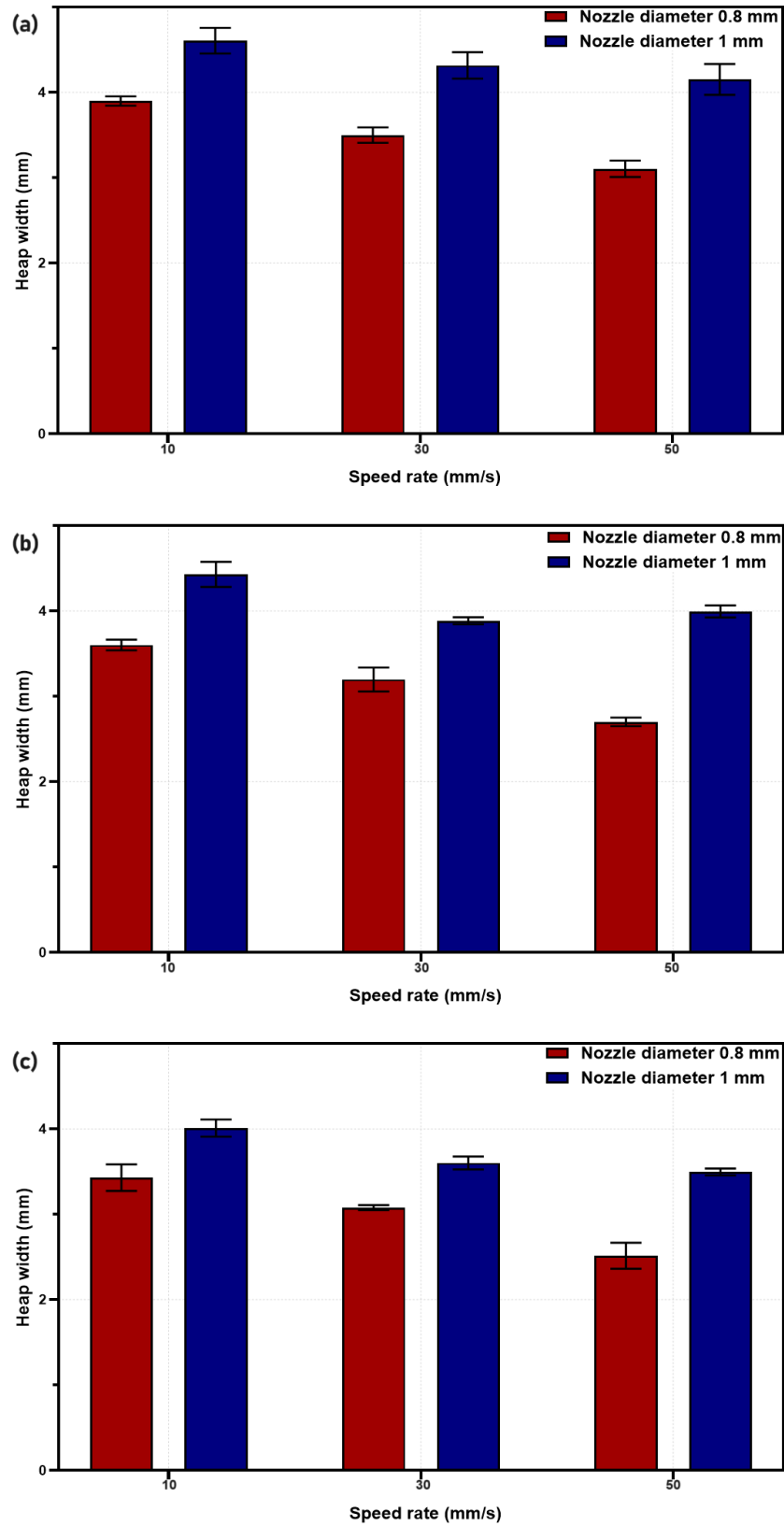


Figure 4.4: The influence of ultrasonic power levels and speed rates on the heap width of the deposited powder investigated using deposition nozzles with diameters of 0.8 and 1 mm. Graph (a) indicates a power level of 600W, whereas graph (b) correspond to the 1200W power level and (c) shows the power level of 1800W.

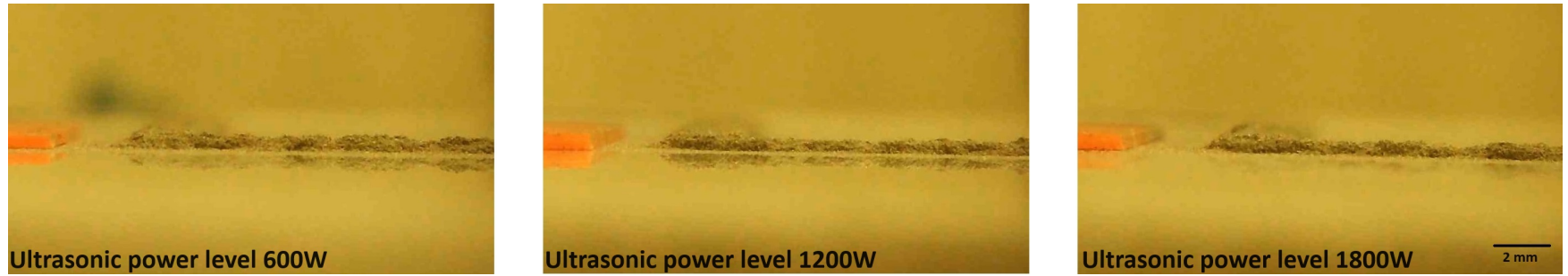


Figure 4.5: The investigation explores the variation in powder heap height under distinct ultrasonic power levels, employing a deposition nozzle with a diameter of 0.8 mm and a consistent speed rate of 10 mm/s.

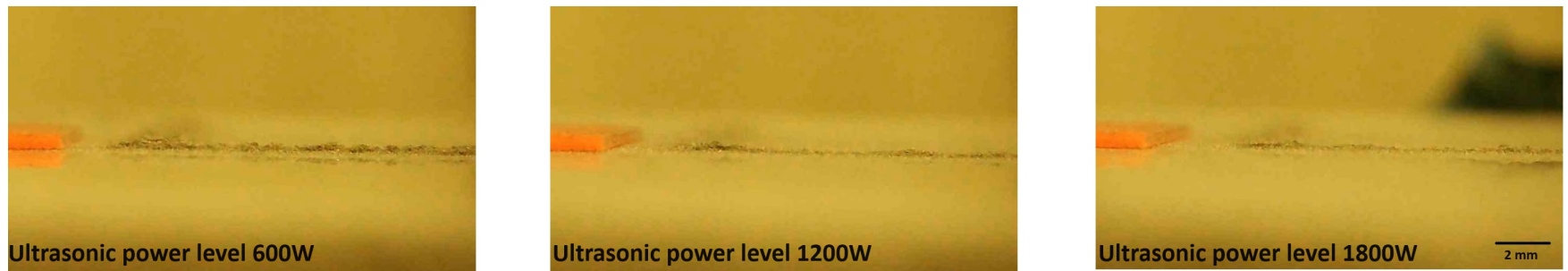


Figure 4.6: The investigation explores the variation in powder heap height under distinct ultrasonic power levels, employing a deposition nozzle with a diameter of 0.8 mm and a consistent speed rate of 30 mm/s.

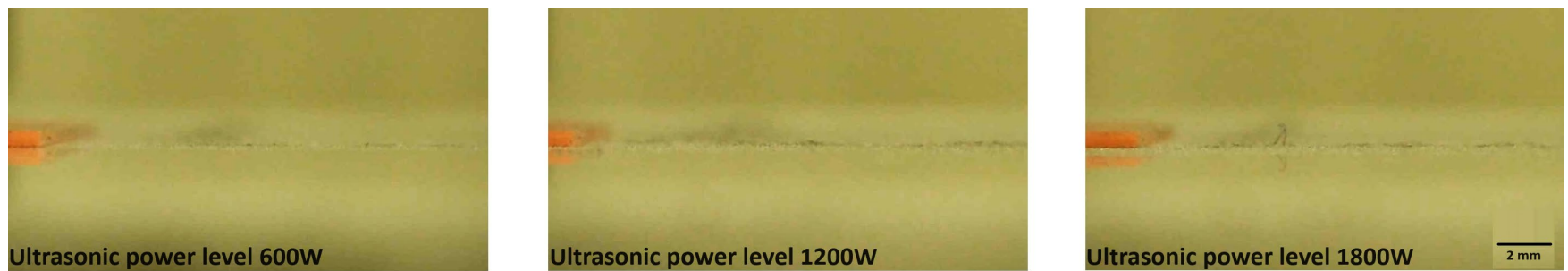


Figure 4.7: The investigation explores the variation in powder heap height under distinct ultrasonic power levels, employing a deposition nozzle with a diameter of 0.8 mm and a consistent speed rate of 50 mm/s.

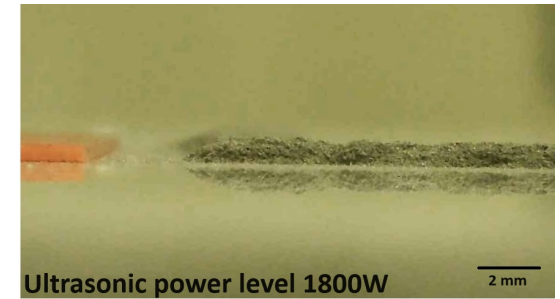
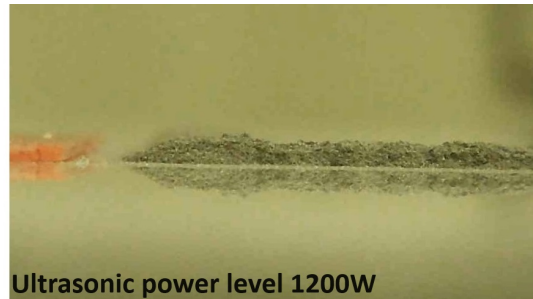
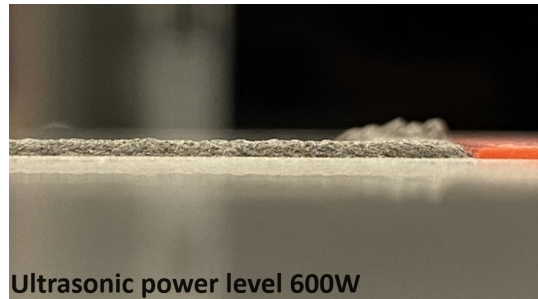


Figure 4.8: The investigation explores the variation in powder heap height under distinct ultrasonic power levels, employing a deposition nozzle with a diameter of 1 mm and a consistent speed rate of 10 mm/s.

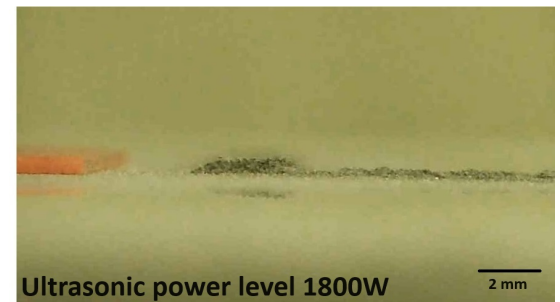
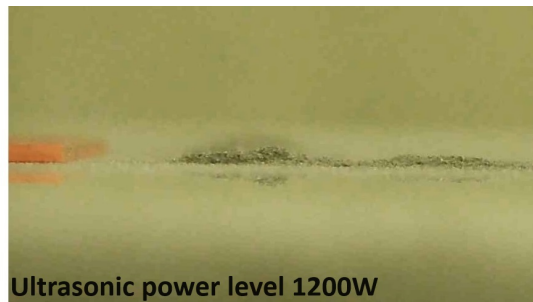
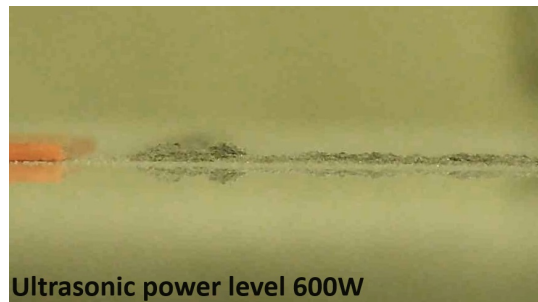


Figure 4.9: The investigation explores the variation in powder heap height under distinct ultrasonic power levels, employing a deposition nozzle with a diameter of 1 mm and a consistent speed rate of 30 mm/s.

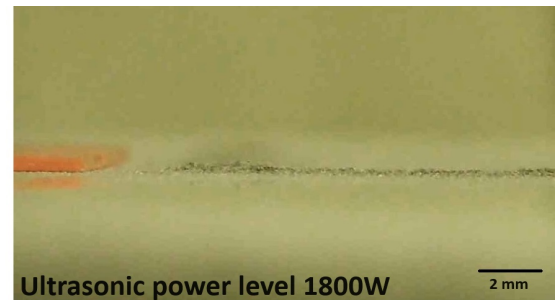
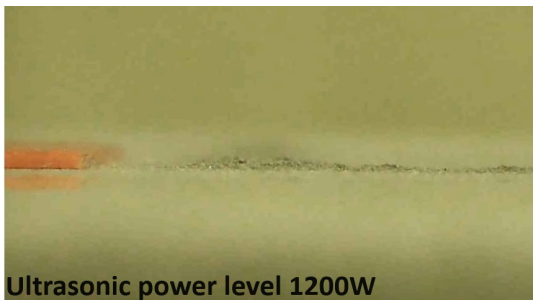
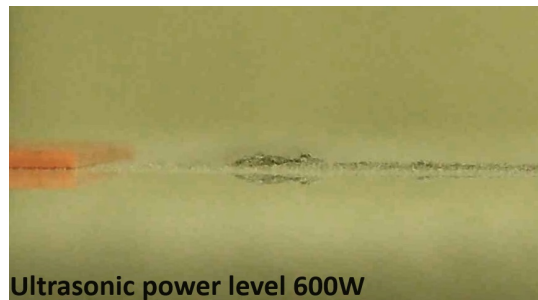


Figure 4.10: The investigation explores the variation in powder heap height under distinct ultrasonic power levels, employing a deposition nozzle with a diameter of 1 mm and a consistent speed rate of 50 mm/s.

For all three different speed rates and the three ultrasonic power levels, the powder has been deposited constantly in some cases showing a continuous powder heap when using a 0.8 mm deposition nozzle as shown in Figures 4.11, 4.12 and 4.13.

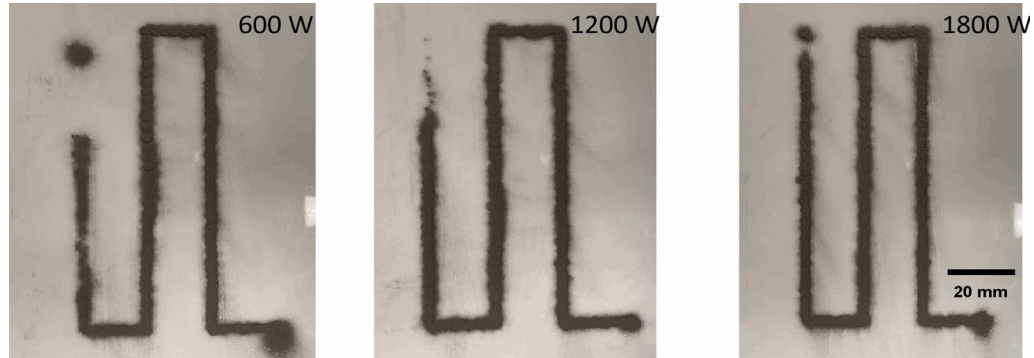


Figure 4.11: Examination of the constancy of the powder heap and its width under varying ultrasonic power levels, employing a deposition nozzle with a diameter of 0.8 mm and a consistent speed rate of 10 mm/s.

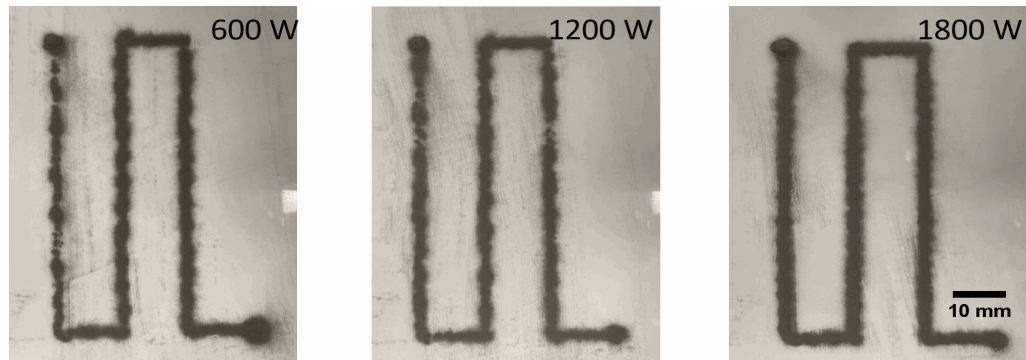


Figure 4.12: Examination of the constancy of the powder heap and its width under varying ultrasonic power levels, employing a deposition nozzle with a diameter of 0.8 mm and a consistent speed rate of 30 mm/s.

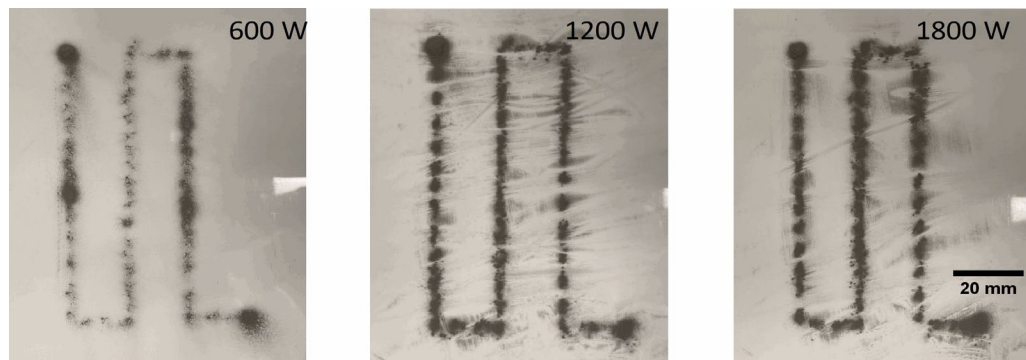


Figure 4.13: Examination of the constancy of the powder heap and its width under varying ultrasonic power levels, employing a deposition nozzle with a diameter of 0.8 mm and a consistent speed rate of 50 mm/s.

The same experimental trials have been conducted using the 1 mm deposition nozzle. The powder has been deposited constantly showing a continuous powder heap as seen in Figure 4.14, 4.15 and 4.16.

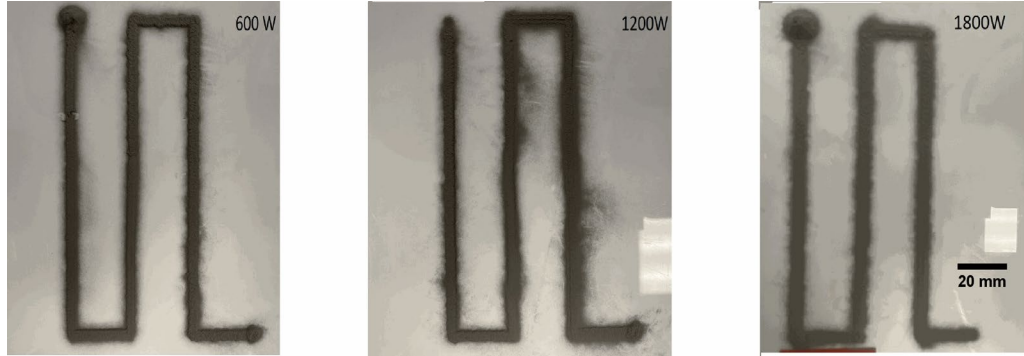


Figure 4.14: Examination of the constancy of the powder heap and its width under varying ultrasonic power levels, employing a deposition nozzle with a diameter of 1 mm and a consistent speed rate of 10 mm/s.

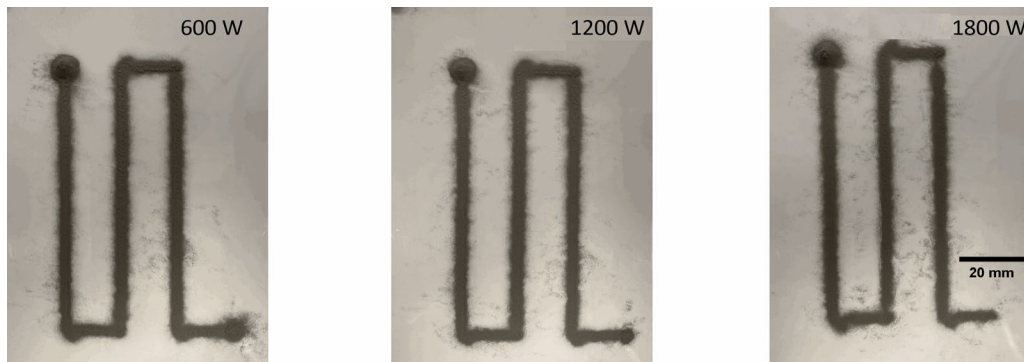


Figure 4.15: Examination of the constancy of the powder heap and its width under varying ultrasonic power levels, employing a deposition nozzle with a diameter of 1 mm and a consistent speed rate of 30 mm/s.

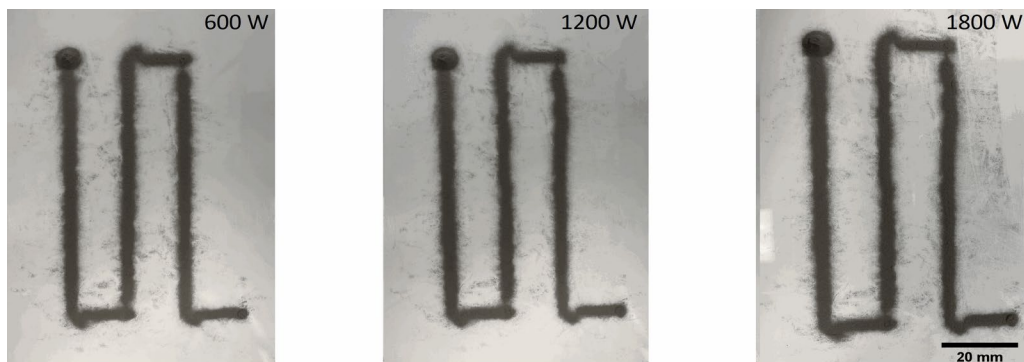


Figure 4.16: Examination of the constancy of the powder heap and its width under varying ultrasonic power levels, employing a deposition nozzle with a diameter of 1 mm and a consistent speed rate of 50 mm/s.

The 0.8 mm deposition nozzle demonstrates a propensity for exhibiting relatively uniform powder heap formations when subjected to head movement speeds of 10 and 30 mm/s, particularly notable under specific ultrasonic power levels, namely 1200 W and 1800 W. However, an examination reveals that the application of a 600 W ultrasonic power setting, both at 10 and 30 mm/s, introduces discernible irregularities and discontinuities in the deposited lines. This phenomenon is illustrated in Figure 4.11 and Figure 4.12, where evident powder discontinuities emerge at the initiation of the deposited line, indicative of the challenges associated with lower ultrasonic power deployment during the deposition process. Notably, this variance is observed in lines deposited at 10 mm/s from a 0.8 mm nozzle diameter, where disparities arise from the distinct application of 600 W and 1200 W power settings Figure 4.11.

Furthermore, Figure 4.12 shows the suboptimal heap lines observed at a speed of 30 mm/s when utilizing ultrasonic power levels of 600 W and 1200 W. The findings emphasize the interaction between ultrasonic power settings, head movement speeds, and resultant powder heap characteristics.

The investigation extends to Figure 4.13, which delineates the differential line characteristics resulting from varying ultrasonic power levels at a head movement speed of 50 mm/s. Under an ultrasonic power of 600 W, the deposition head encounters challenges in effectively dispensing powder due to diminished transducer vibration and the high movement speed, resulting in compromised line quality. Conversely, the application of 1200 W ultrasonic power yields a deposition line pattern better than that obtained with 600 W, although not immune to slight discontinuities that may influence the powder spreading process. Despite a marginal enhancement at 1200 W, the deposition lines still fall short of the desired standard. Intriguingly, discontinuities persist in lines even at the highest ultrasonic power level when employing a head movement speed of 50 mm/s. This observation underscores the impediment posed by rapid head movement, preventing the formation of a seamless and continuous straight-line pattern in the deposited powder.

In the depositions without wiper experimental outcomes, it is evident that the selection of a 1 mm nozzle configuration may offer a consistent heap line pattern; nevertheless, this advantage is counterbalanced by the generation of notably elevated powder heap heights, occasionally exceeding 500 μm . In stark contrast, the orifice dimensions of the 0.8 mm nozzle consistently exhibit good heap deposition line patterns when using lower movement speed and high ultrasonic power level. Furthermore, this configuration consistently yields reduced height and width dimensions in comparison to that achieved with a 1 mm nozzle diameter.

In a conclusive evaluation, it can be inferred that the optimum compromise between line pattern quality and dimensional considerations is achieved through the implementation of a 0.8 mm nozzle size, concomitant with an 1800 W power setting and a head movement speed of 30 mm/s. Under these selected deposition parameters, the system demonstrates commendable performance by achieving a continuous line that has the narrowest width of 3.1 mm. This judicious configuration not only attains a good line pattern but also ensures dimensional attributes that align with desirable specifications, thereby offering valuable insights for the strategic optimization of the multi-material deposition systems.

4.2.1.2 Deposition trials with a round flattening wiper

In the subsequent phase of experimental trials, a round flattening wiper was introduced to the lower section of the sonotrode, facilitating the controlled dispersion of deposited powder to achieve well-defined heap height dimensions, as illustrated in Figure 4.17. The schematic representations and dimensional data about the circular flattening wiper are available for reference in appendix 11.4. In this sequential set of experimental iterations, the determination of heap height is linked to the interplay between the round flattening wiper's distance from the building platform—an aspect precisely governed by the Fisnar robot. To ensure methodological accuracy and to maintain a standardized approach, the heap height parameter was regulated at a constant 150 μm throughout the experimental series. Consequently, the primary focal point of this phase lies in the scrutiny of powder heap width. Within this experimental framework, due consideration was accorded to key parameters, including deposition nozzle diameter, movement speed, and ultrasonic power level, in addition to the newly introduced variable of the powder wiper. However, mindful of the priority to streamline the investigative process, specific configurations within these parameters were selectively excluded based on prior observations of unsatisfactory outcomes during the preliminary round of trials. Specifically, configurations involving a movement speed of 50 mm/s coupled with a 0.8 mm nozzle diameter were deliberately omitted from further consideration. This decision was grounded in the antecedent finding that such a configuration had consistently yielded suboptimal deposition lines across a spectrum of ultrasonic power levels. Furthermore, a discerning analysis of the experimental outcomes revealed instances of powder discontinuities at the commencement of deposited lines when employing lower ultrasonic powers (600 and 1200 W) at both 10 mm/s and 30 mm/s speeds. These discontinuities were attributed to the insufficiency of ultrasonic power during the deposition process, a critical insight that informed the refined parameters for subsequent investigations. Hence, in the context of the 0.8 mm deposition nozzle, a singular ultrasonic power level is employed, specifically set at

1800 W. Additionally, the investigation is delimited to head movement speed rates of 10 mm/s and 30 mm/s for the 0.8 nozzle diameter, ensuring a targeted and controlled exploration of relevant parameters. On the other hand, the exploration of three distinct head movement speeds is conducted in tandem with the deployment of the 1 mm deposition nozzle. Furthermore, a trial encompasses the evaluation of all available ultrasonic power levels, systematically applied in conjunction with the 1 mm deposition nozzle. The desired width and heap height most suitable for deposition and the resulting part quality are 300 μm in width and 150 μm heap height.

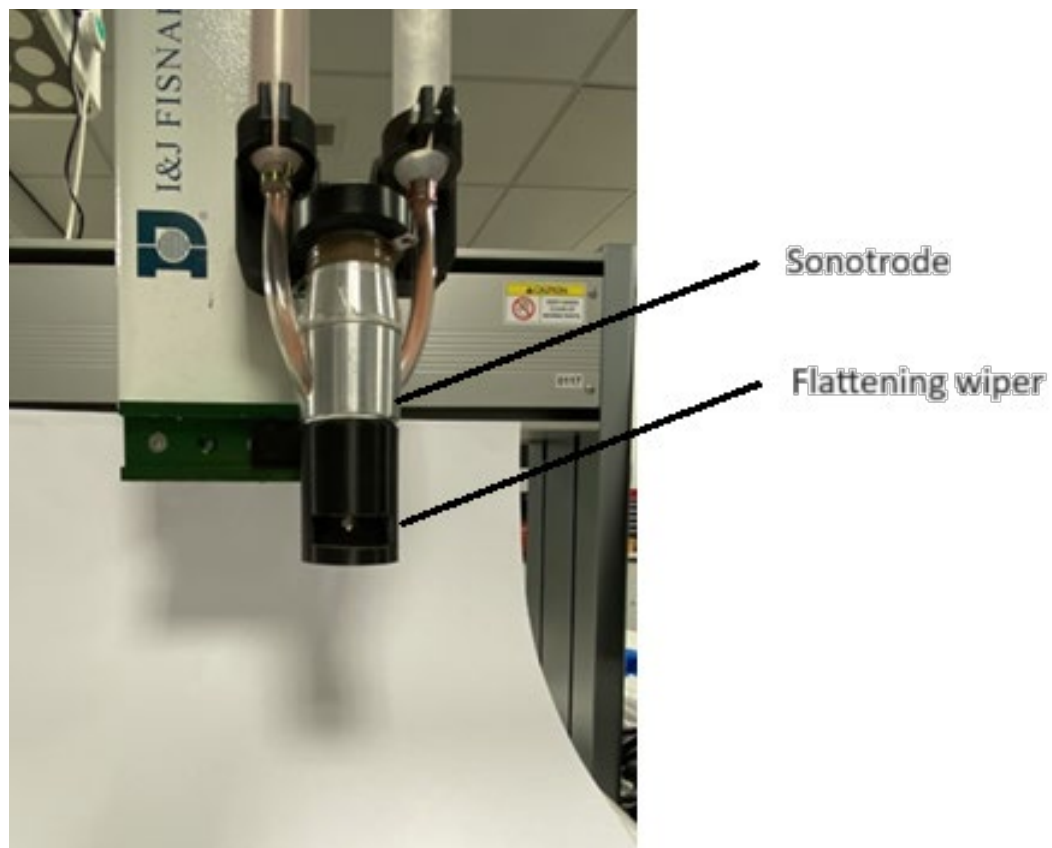


Figure 4.17: The introduction of the round flattening wiper to the lower section of the sonotrode was implemented to enable controlled dispersion of the deposited powder, thereby achieving precise and well-defined heap height dimensions.

As presented in Table 4.4, an array of heap width values was systematically observed under the constant condition of maintaining the powder heap height at 150 μm . The inquiry sought to study the influence of varying ultrasonic power levels on the lateral expansion of the powder heaps, particularly when concomitant with the deployment of the round flattening wiper. The data establishes a discernible positive correlation between ultrasonic power levels and heap width, underscoring the fundamental role played by the round flattening wiper in enforcing heap height and uniformly redistributing deposited powder across the uppermost region of the heap. Examining the outcomes delineated in Table 4.4, the utilization of a 1 mm deposition nozzle at a head movement speed of 10 mm/s and the lowest ultrasonic power level yielded a heap width of 4.5 mm. In contrast, a progressive augmentation of ultrasonic power to 1200 W under identical nozzle size and speed conditions led to a considerable widening, resulting in a heap width of 11 mm. Remarkably, the application of the highest ultrasonic power level resulted in a substantial expansion, yielding a heap width of 17.5 mm. This systematic escalation in heap width across the three ultrasonic power levels underscores the efficacy of the round flattening wiper in facilitating judicious powder spreading, thereby influencing the lateral dimensions of the deposited powder at the apical region of the heap.

Concomitantly, an analytical exploration into the interdependence of head movement speed on the width of powder heaps reveals a distinctive inverse relationship. The findings show that, with an escalation in movement speed, a corresponding decrement in heap width is consistently observed. This correlation is evident in the results presented in Table 4.4, showcasing the dynamic interplay between head movement speed and the resultant width dimensions of the deposited powder heaps. The observed variations in heap width resulting from different movement speeds can be attributed to the dynamic flow concentration of the powder as the deposition head traverses the building platform. This phenomenon underscores the relationship between the controlled motion of the head and the dynamics of the dispensed powder flow, contributing to the detailed morphological changes in the deposited

heaps. To exemplify, employing a 1 mm deposition nozzle at a methodically controlled movement speed of 10 mm/s under the highest ultrasonic power level resulted in a substantial heap width of 17.5 mm. Contrarily, maintaining the same nozzle size and ultrasonic power level but increasing the movement speed to 30 mm/s yielded a diminished heap width of 7.9 mm. Furthermore, at an elevated head movement speed of 50 mm/s, the heap width experienced a further reduction to 7.3 mm. Similarly, analogous observations were made for the 0.8 mm nozzle configuration. In this scenario, a heap width of 9.8 mm was attained at a methodically regulated movement speed of 10 mm/s under the highest ultrasonic power level. Conversely, maintaining identical parameters but elevating the movement speed to 30 mm/s resulted in a reduced heap width of 6.2 mm. These discernible outcomes provide an understanding of the relationship between head movement speed and the lateral dimensions of the powder heaps, contributing invaluable insights into the dynamics of the deposition system.

Nozzle diameter (mm)	Speed rate (mm/s)	Power level (W)	Heap Width (mm)	Heap height (μm)
0.8	10	1800	9.8	Height is controlled by setting the distance between the wiper and the building platform which was 150 μm
		600	4.6	
	30	1200	11	
		1800	17.5	
		600	4.5	
		1200	7.2	
1	30	1800	7.9	
		600	3.9	
		1200	4.7	
	50	1800	7.3	

Table 4.3: The outcomes of heap width and height values were derived through the utilization of two distinct parameters, each comprising different discrete levels. These parameters were systematically applied within the context of a validation study conducted on a multi-material system with a wiper.

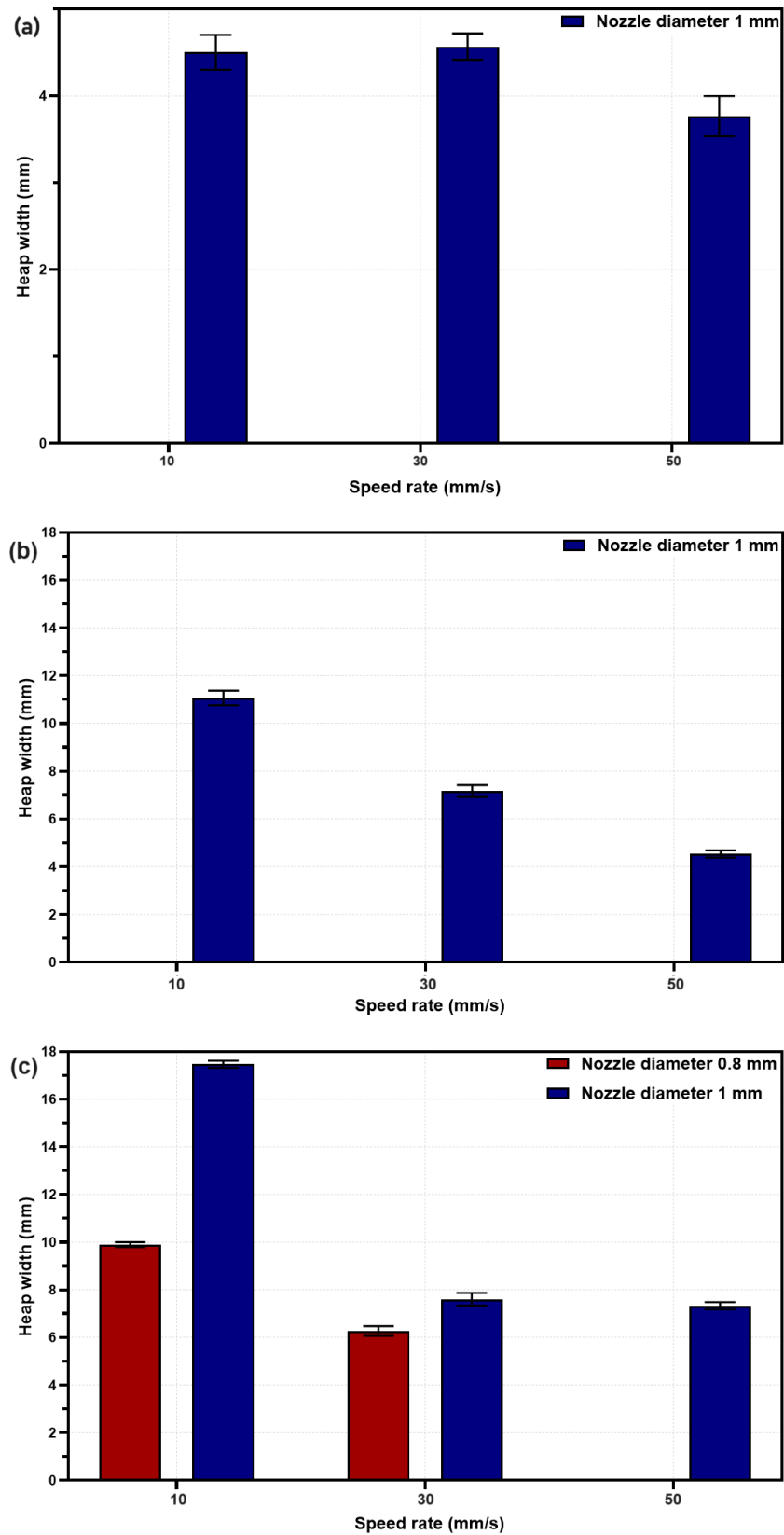


Figure 4.18: The investigation delves into the impact of ultrasonic power levels and variable speed rates on the resultant heap width of deposited powder material with a fluttering wiper. The study employs deposition nozzles characterized by diameters of 0.8 mm and 1 mm. Graph (a) indicates a power level of 600W, whereas graph (b) corresponds to the 1200W power level and (c) shows the power level of 1800W.

Figure 4.19 visually shows the discernible distinctions in powder heap morphologies and consistencies achieved through an exploration of two distinct head movement rates (10 and 30 mm/s) in conjunction with one ultrasonic power level (1800 W), utilizing the 0.8 mm deposition nozzle.

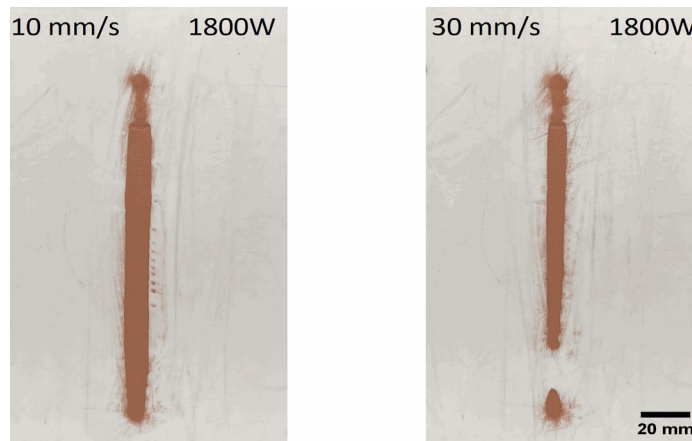


Figure 4.19: The constancy of the powder heap, when employing a 0.8 mm deposition nozzle, is examined under two distinct head movement rates, namely 10 and 30 mm/s while maintaining a constant ultrasonic power level of 1800 W.

The performance of the 0.8 mm deposition nozzle in generating powder heaps was investigated under controlled conditions, focusing on two distinct head movement speeds—10 mm/s and 30 mm/s—while maintaining a constant ultrasonic power level of 1800 W and using the fluttering wiper. The results revealed a noteworthy consistency in the powder heap profiles when subjected to the aforementioned conditions. Specifically, at a head movement speed of 10 mm/s, the generated powder heap exhibited a sustained uniformity, as depicted in Figure 4.19. In contrast, at a speed of 30 mm/s, slight variations in the heap morphology were observed. It is noteworthy that when employing 1800 W ultrasonic power at a speed of 10 mm/s, the resulting powder heap exhibited an expanded width in comparison to the heap generated at 30 mm/s. This observation prompts a quantitative analysis, revealing heap widths of 9.8 mm and 6.2 mm for head movement speeds of 10 mm/s and 30 mm/s, respectively.

In the context of powder deposition dynamics from a 1 mm deposition nozzle and using the fluttering wiper, Figures 4.20, 4.21 and 4.22 provides a portrayal of powder heap morphologies, delineating the impact of distinct ultrasonic power levels (600 W, 1200 W, and 1800 W) when paired with head movement speeds of 10, 30 and 50 mm/s. Evidently, in Figure 4.20, when using 600 W ultrasonic power, the powder heap assumes a nonuniform configuration owing to the attenuated ultrasonic vibration. In stark contrast, the deployment of 1200 W yields a consistent and continuous heap, while the utilization of 1800 W introduces a dynamic: an initial thin deposition line that gradually widens over the course of movement. This evolution in width is attributed to the surplus powder volume deposited and subsequently compelled to lateral spreading. Upon escalating the movement speed to 30 mm/s (Figure 4.21), an interplay between ultrasonic power and speed becomes apparent. At 600 W, the powder heap exhibits inferior irregularities in the deposition lines compared to lower speeds, underscoring the sensitivity of the process to the combined influence of power and speed. In contrast, the deployment of 1200 W at this speed results in a uniform heap line, offering a noteworthy contrast to the outcomes observed at 10 mm/s. Further scrutiny of Figure 4.22, depicting powder heap patterns at a head movement speed of 50 mm/s, reveals additional insights. Notably, the presence of discontinuity in the deposited line suggests suboptimal heap lines at this elevated speed, particularly evident with ultrasonic power levels of 600 W and 1200 W. This phenomenon can be attributed to the compounded effect of lower ultrasonic power and the swift trajectory of the deposition head.

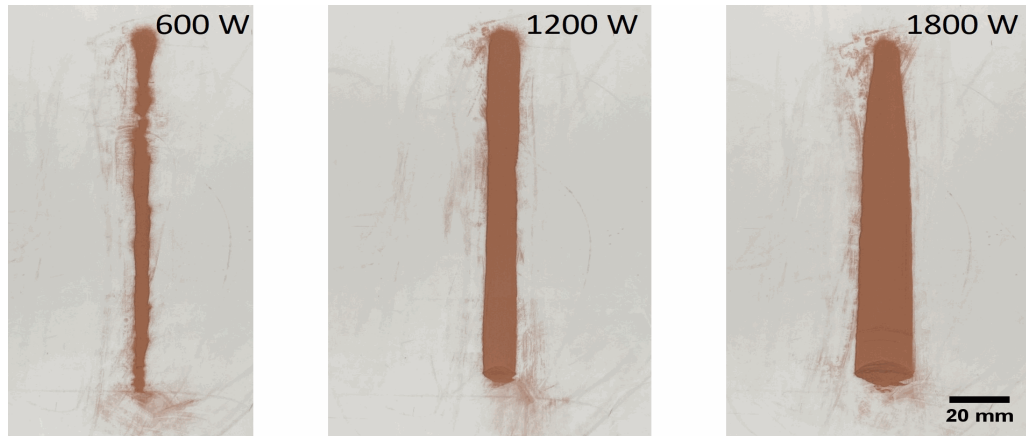


Figure 4.20: A visual illustration of the powder heap shape and consistencies resulting from the examination of three diverse ultrasonic power levels, utilizing the 1 mm deposition nozzle at a speed rate of 10 mm/s.

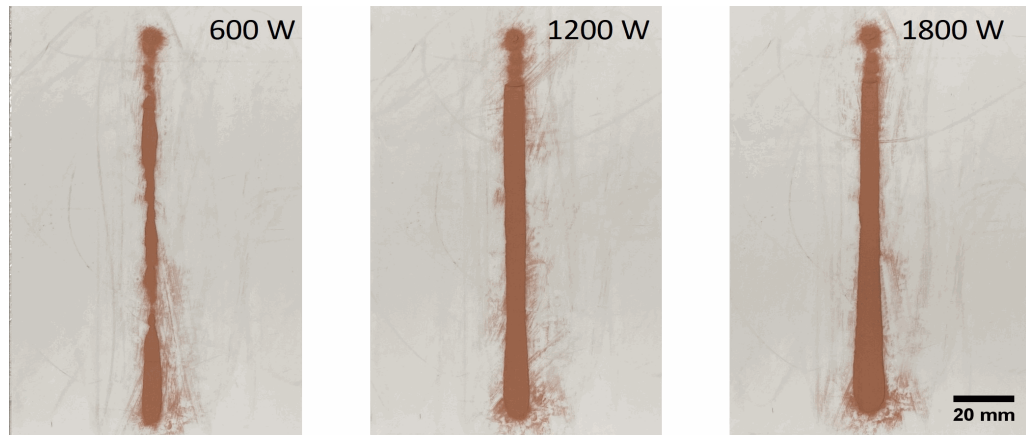


Figure 4.21: A visual illustration of the powder heap shape and consistencies resulting from the examination of three diverse ultrasonic power levels, utilizing the 1 mm deposition nozzle at a speed rate of 30 mm/s.

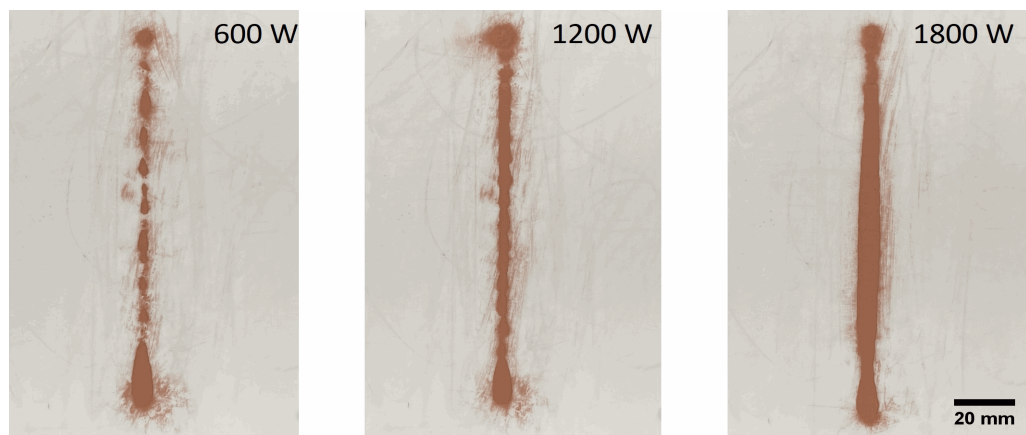


Figure 4.22: A visual illustration of the powder heap shape and consistencies resulting from the examination of three diverse ultrasonic power levels, utilizing the 1 mm deposition nozzle at a speed rate of 50 mm/s.

The findings extracted from the subsequent series of experimental trials, depositing powder with the use of a flattening wiper, offer insights into the interplay of deposition parameters on powder heap characteristics. Employing a 1 mm nozzle diameter, the attainment of a consistently desirable heap line pattern hinges on the application of ultrasonic power and head movement speed. Specifically, an ultrasonic power setting of 1200 W, coupled with either a 10 mm/s or 30 mm/s head movement speed, demonstrates good outcomes, yielding heap widths of 11 mm and 7.2 mm, respectively. This underscores the significance of tailoring deposition parameters to nozzle specifications to achieve optimal results.

Conversely, when utilizing the 0.8 mm nozzle, the reliability is realized through the use of an ultrasonic power level of 1800 W with a measured head movement speed of 10 mm/s. This precise configuration begets a dependable heap line pattern with a width of 9.8 mm, further underscoring the relationship between nozzle dimensions and deposition conditions.

4.2.2 Comparison of Deposited Heap Results with and without Flattening Wiper.

4.2.2.1 Utilizing a 1 mm nozzle

Figure 4.23 presents a comparative analysis of heap width variations derived from two distinct experimental paradigms: one incorporating the use of a round flattening wiper during the powder deposition process, and another conducted without such a wiper. The lines' widths have been measured for three different samples for each parameter arrangement by a vernier calliper. The measurement have taken place at the middle part of the deposited line. The average value of the three readings has been chosen as the parameter arrangement's value. In Figure 4.23(a-c), the visual representation distinctly illustrates that the absence of a wiper during powder deposition results in a discernibly thinner heap width.

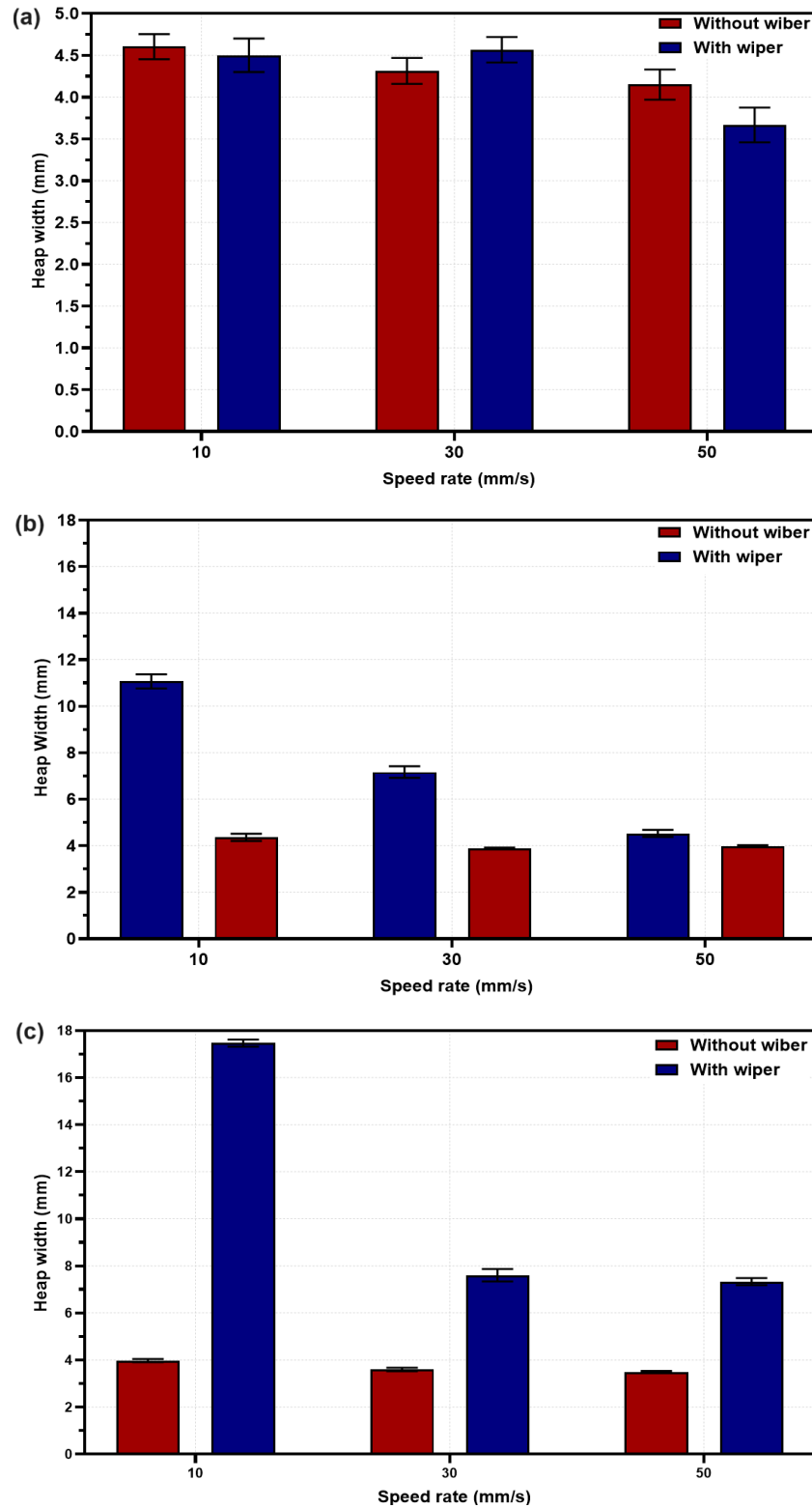


Figure 4.23: The distinctions in powder deposition patterns, comparing the utilization of a flattening wiper to its absence, are investigated across varied ultrasonic power levels, specifically at (a) 600 W, (b) 1200 W, and (c) 1800 W.

This phenomenon can be ascribed to the inherent lack of external forces that would otherwise aid in the homogeneous spreading of the deposited powder situated at the peak of the powder heap. However, it is important to note that this reduction in heap width is concomitant with an elevation in heap height, a parameter with potential ramifications for subsequent layer-building processes, as detailed in Table 4.5. This supplementary mechanism offers precise control over layer thickness, obviating the necessity for external tools such as a rolling spreader. This is particularly relevant in scenarios where thin heap width is not an essential requirement. Conversely, when the 3D printing process requires a small heap width, the deployment of the multi-material deposition system without the round flattening wiper, yet using a levelling roller, is deemed a preferable course of action. This thorough balance between heap width and height considerations forms an integral aspect of optimizing the efficacy of the multi-material deposition system.

	10 mm/s		30 mm/s		50 mm/s	
	Without wiper	With wiper	Without wiper	With wiper	Without wiper	With wiper
Width (mm)	4	17.5	3.6	7.9	3.5	7.3
Height (μm)	760	150	562	150	365	150

Table 4.4: Disparities in width measurements investigated in the context of powder deposition using a 1 mm nozzle and ultrasonic power of 1800 W, comparing instances where a wiper was employed to those where it was not.

4.2.2.2 Utilizing a 0.8 mm nozzle

In this comparison, the configurations involving a movement speed of 50 mm/s coupled with a 0.8 mm nozzle diameter were deliberately omitted from further consideration as outlined in chapter 4.2.1.2. This decision was grounded in the antecedent finding that such a configuration had consistently yielded suboptimal deposition lines across a spectrum of ultrasonic power levels. Furthermore, a discerning analysis of the experimental outcomes revealed instances of powder discontinuities at the commencement of deposited lines when employing lower ultrasonic powers (600 and 1200 W) at both 10 mm/s and 30 mm/s speeds. Hence, in the context of the 0.8 mm deposition nozzle, a singular ultrasonic power level is employed, specifically set at 1800 W. The lines' widths have been measured for three different samples for each parameter arrangement by a vernier calliper. The measurement have taken place at the middle part of the deposited line. The average value of the three readings has been chosen as the parameter arrangement's value. Figure 4.24 serves as a visual representation, shedding light on the alterations in heap width when employing a 0.8 mm deposition nozzle and subjecting it to the highest ultrasonic power settings. The ensuing comparative analysis between the two experimental cohorts yields valuable insights: the introduction of a round flattening wiper leads to widths that demonstrate a substantial twofold or even threefold increase in magnitude when juxtaposed against scenarios where such a wiper is not engaged. This noteworthy outcome can be traced back to the force exerted on powder particles strategically positioned at the peak of the powder heap. The wiper's action makes these particles undergo side displacement, resulting in their systematic removal as the deposition head traverses the building platform.

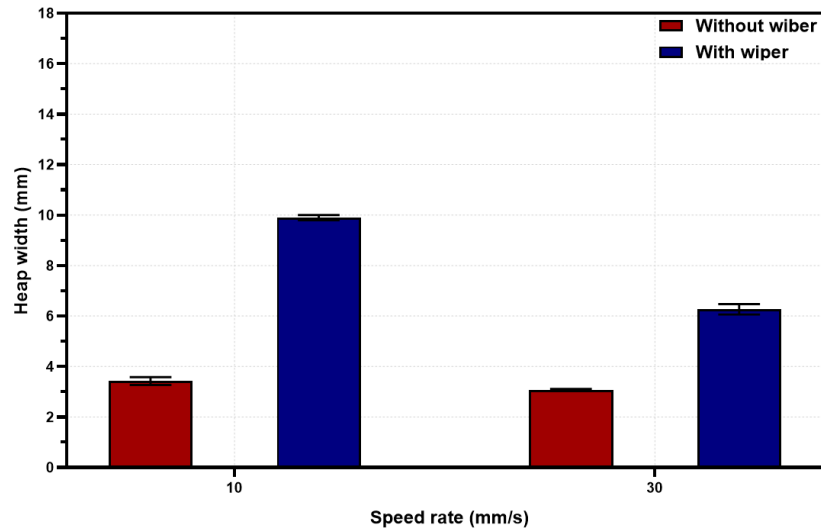


Figure 4.24: The distinctions in powder deposition patterns, comparing the utilization of a flattening wiper to its absence, are investigated across the ultrasonic power level of 1800 W.

A set of measurements is provided in Table 4.6 for detailed scrutiny and quantification of these observed effects.

	10 mm/s		30 mm/s	
	Without wiper	With wiper	Without wiper	With wiper
Width (mm)	3.4	9.8	3.1	6.2
Height (μm)	350	150	315	150

Table 4.5: Disparities in width measurements investigated in the context of powder deposition using a 0.8 mm nozzle, comparing instances where a wiper was employed to those where it was not.

4.2.3 Full Factorial Analysis

The full factorial analytical design approach has been employed in this study, and its analysis was performed using Minitab software to ascertain the effects of the selected parameters. The deployment of correlation analysis serves as a methodological factor, offering an understanding of the relationships characterizing these fundamental process variables and their impact on the dimensions of the heap. Thus, the Pearson correlation coefficient has been systematically employed to ascertain and articulate the quantitative nature of the relationships among the three critical process parameters—namely, Nozzle Diameter, Speed Rate, and Power Level—each known to exert a direct influence on the resultant heap width and height outputs within the experiment. The presentation of correlation outcomes, as seen in Table 4.7, affords a description defining the magnitude and directionalities of the correlations among the stipulated parameters and heap dimensions.

	Nozzle Diameter (mm)	Speed Rate (mm/s)	Power Level (W)
Heap Width	0.728	-0.479	-0.412
Heap Height	0.711	-0.557	0.199

Table 4.6: The correlation coefficients serve as numerical indices delineating the linear relationships among the three fundamental process parameters, namely Nozzle Diameter, Speed Rate, and Power Level. These coefficients contribute valuable insights into both the magnitude and directionality of the associations, thereby affording a thorough comprehension of the interdependencies among these variables within the system.

Noteworthy within this context is the prominence of nozzle diameter, which emerges as the paramount contributor, exhibiting the strongest correlation with both heap width and height outputs. This statistical discernment underscores the fundamental role played by nozzle diameter in shaping the dimensions of the heap. In addition, the identified positive correlation between nozzle diameter and the dimension of the heap implies a direct proportion, interpreting that an increase in nozzle diameter is accompanied by a commensurate increase in heap width and height.

Conversely, the analysis reveals a distinctive pattern concerning the Speed Rate parameter, which shows a moderate negative correlation with both heap width and height outputs. This inverse correlation implies a reduction in heap dimensions concurrent with an escalation in speed rate.

On a parallel note, scrutiny of the Power Level parameter exposes a negative moderate correlation with heap width, signifying a diminishing trend in width as Power Level increases. Intriguingly, the Power Level parameter exhibits a concurrently positive, though low, correlation with heap height, suggesting that an elevation in Power Level may result in increased heap height, although to a lesser extent.

The visual depiction in Figure 4.25 and Figure 4.26 functions as an illustrative supplement to the previously mentioned numerical data, providing a graphical synthesis of these subtle correlations.

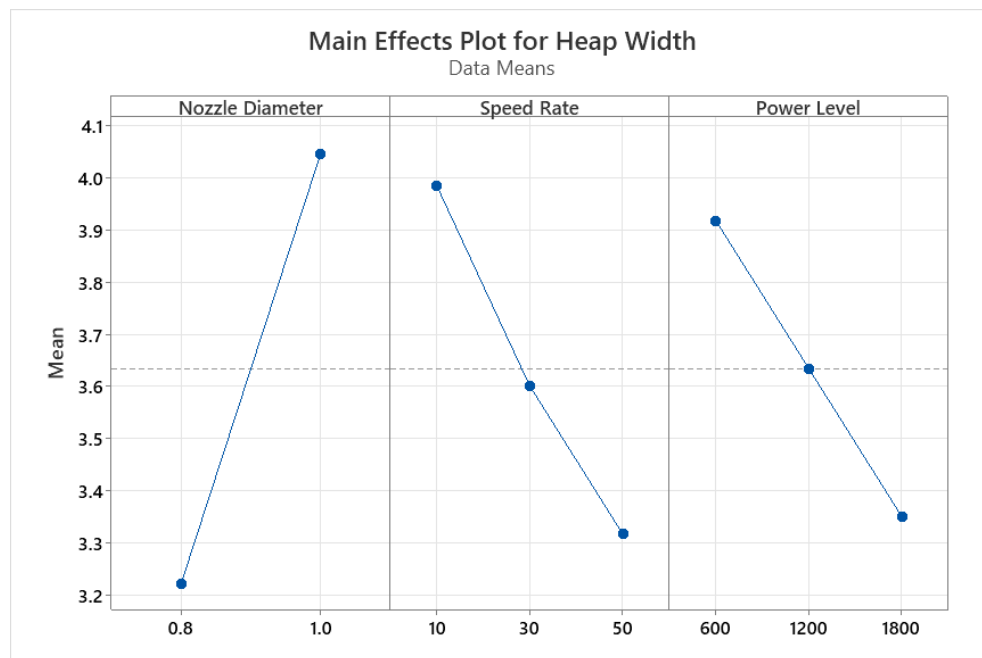


Figure 4.25: The Main effect showing the linear relationships between the three critical process parameters (Nozzle Diameter, Speed Rate, and Power Level) and the width of the deposited powder heap.

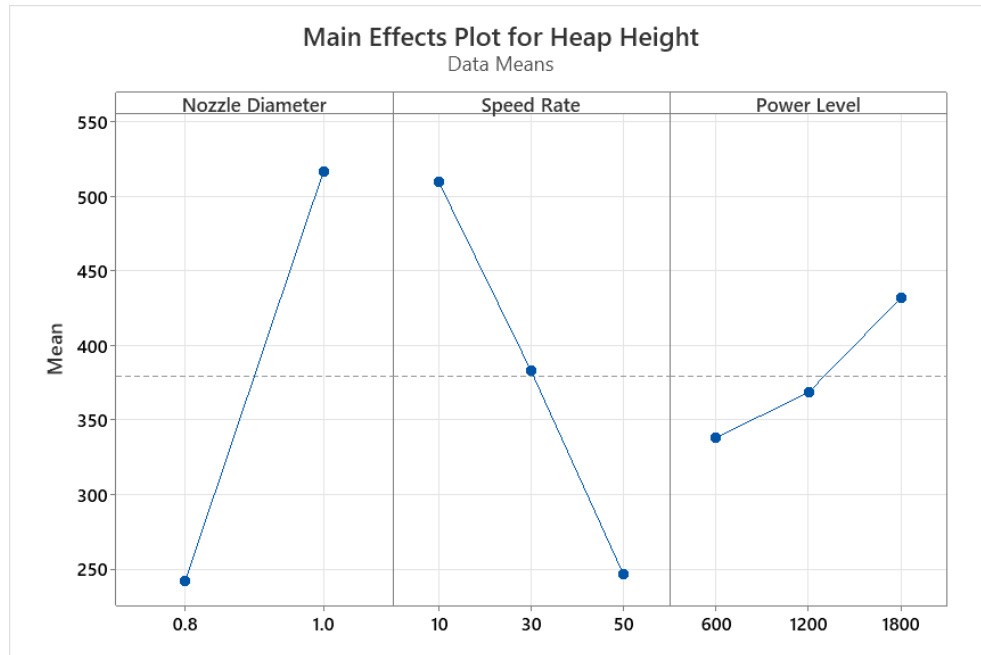


Figure 4.26: The Main effect showing the linear relationships between the three critical process parameters (Nozzle Diameter, Speed Rate, and Power Level) and the height of the deposited powder heap.

In pursuit of process optimization, a linear regression model has been developed for the purpose of refining the process parameters in attaining the desired powder heap width. The heap width assumes heightened significance as a determinant factor in shaping the resultant 3D-printed structure. Addressing the exigencies inherent to multi-material 3D printing, the emphasis is on minimizing the heap width within a prescribed range. This range is carefully delineated to strike a balance, ensuring that the width remains within acceptable limits while concurrently accommodating the requisite structural. Furthermore, the developed regression model assumes the role of a predictive model. Its efficacy extends to interpreting the impact the parameters on prospective outcomes, thereby signifying its potential as a predictive instrument. Based on the regression analysis conducted for the deposited powder width in the experimental trials, the following multiple linear regression equation was derived:

$$\text{Heap Width} = 0.983 + 4.144 \text{ Nozzle diameter (mm)} - 0.01669 \text{ Speed rate (mm/s)} - 0.0004 \text{ Power level (W)}$$

The intercept term (0.983) represents the expected value of the deposited powder width when all independent variables are set to zero. The coefficient for Nozzle diameter (4.144) suggests that, on average, a one-unit increase in nozzle diameter is associated with a 4.144-unit increase in width, holding other factors constant. Conversely, the Speed coefficient (-0.01669) indicates that for every one-unit increase in speed rate, the heap width is expected to decrease by 0.01669 units. Similarly, the Power level coefficient (-0.0004) suggests that a one-unit increase in power level corresponds to a decrease of 0.0004 units in heap width. It is essential to scrutinize the statistical significance of the coefficients and evaluate the general goodness-of-fit of the model to ascertain its reliability in predicting deposited powder width concerning the selected independent variables. Table 4.7 shows the significance level of the coefficients of the equation. Nonetheless, the regression analysis has produced a model distinguished by a predicted coefficient of determination (R^2 -pred) of 91.6 percent. Furthermore, the validation of the linear regression model has been undertaken to deepen the comprehension of the model's performance.

Term	Coefficient	P-Value
Constant	0.983	0.0000160290820872
Nozzle diameter (mm)	4.144	0.0000000000000000
Speed rate (mm/s)	-0.01669	0.0000000000000000
Power level (W)	-0.000479	0.0000000000000084

Table 4.7: The significance level of the coefficients of the predicted equation.

4.2.4 Regression Validation

An examination for the validation of the linear regression assumptions has been conducted to enhance the comprehensiveness of the model's validity. During this validation process, the deposited powder heap width was assumed to be 2 mm, and variations in nozzle diameter and ultrasonic power levels were considered. The model equation was subsequently rearranged to emphasize the influence of the speed rate. Four distinct parameter sets were established for analysis as seen in Table 4.8.

	Nozzle Diameter (mm)	Power Level (W)	Heap Width (mm)
First set	0.8	1200	2
Second set	0.8	1800	2
Third set	1	1200	2
Fourth set	1	1800	2

Table 4.8: The four distinct parameter sets were established for analysis to conduct the validation of the linear regression assumptions.

The detailed calculations of the speed rate associated with each parameter set are provided in appendix 11.5 for reference. The width of the lines was measured using a vernier calliper for three samples under each parameter arrangement. Measurements were conducted at the midpoint of the deposited line. The average of the three readings was selected as the value for the parameter arrangement. Figure 4.27 and Figure 4.28 provide a visual representation in the form of laboratory images showcasing deposited lines under the previously specified parameters, serving as a visual validation of the regression model. Figure 4.27a presents the deposited line width of 2.36 mm, as evidenced in the regression model validation outcomes. Similarly, Figure 4.27b reveals an observed deposited line width of 2.17 mm. In the context of Figure 4.28a, the recorded width of the deposited line is established at 2.05 mm, while Figure 4.28b exhibits a deposited line width of 1.95 mm, providing thorough documentation of the experimental results.

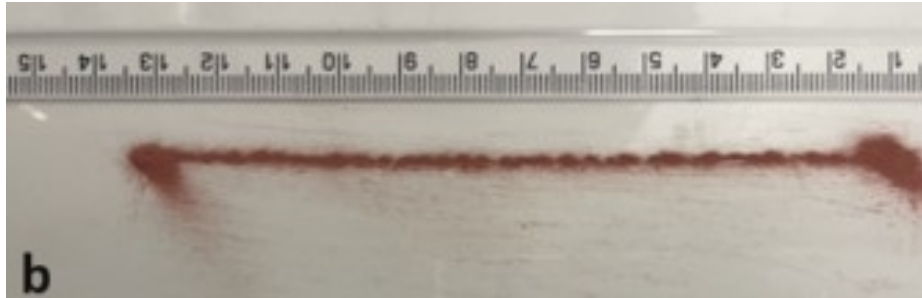
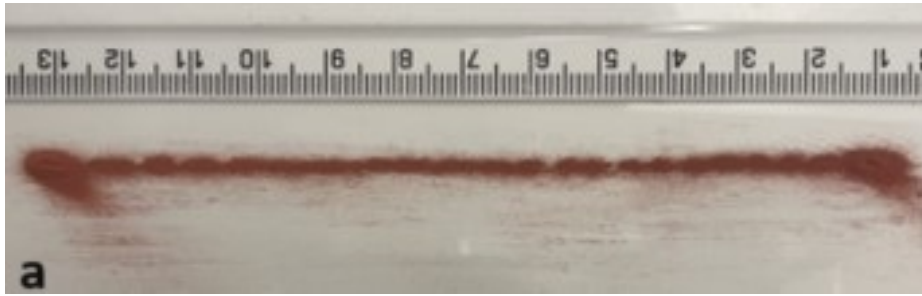


Figure 4.27: The validation of the regression equation of the deposition of a 2 mm heap width was conducted under the conditions of (a) 0.8mm nozzle diameter, 1200 power level, and speed rate of 109 mm/s. (b) 0.8 mm nozzle diameter, 1800 power level, and speed rate of 94.5 mm/s.

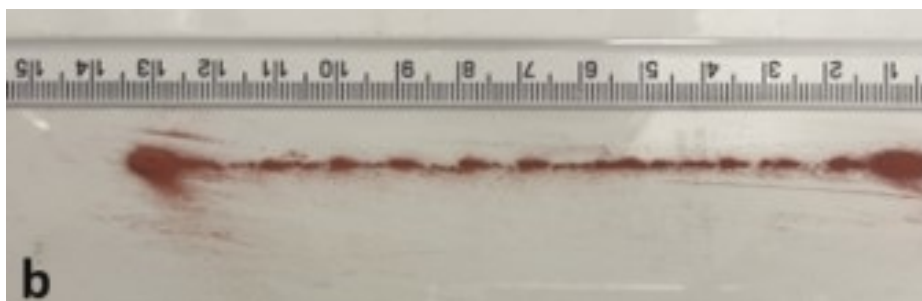
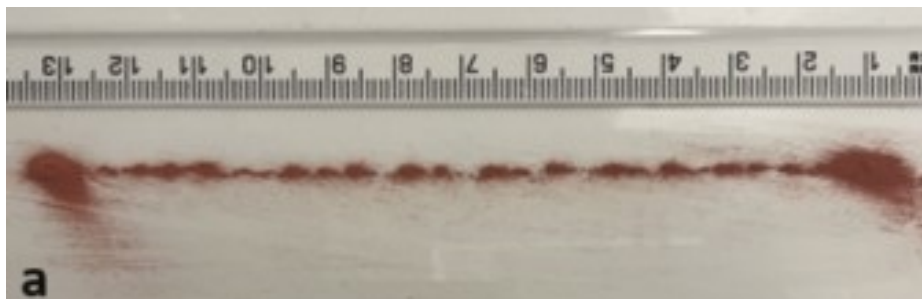


Figure 4.28: The validation of the regression equation of the deposition of a 2 mm heap width was conducted under the conditions of a 1 mm nozzle diameter, 1200 power level, and speed rate of 158.5 mm/s. (b) 1 mm nozzle diameter, 1800 power level, and speed rate of 144 mm/s.

Figure 4.29 : Quantification of the accuracy of the regression relation, considering the error of the prediction compared to the observation. The plot represents the performance of the regression model that has been utilized to achieve a target heap width of 2. It features a scatter plot where each point corresponds to one of the four experimental sets, and the actual outcomes. It illustrates the error associated with each measurement. The Root Mean Square Error (RMSE) calculated as 0.202 quantifies the average magnitude of the errors between the predicted and actual outcomes. This value provides a concise numeric summary of the model's accuracy, indicating that on average, the predictions deviate from the actual values by approximately 0.202.

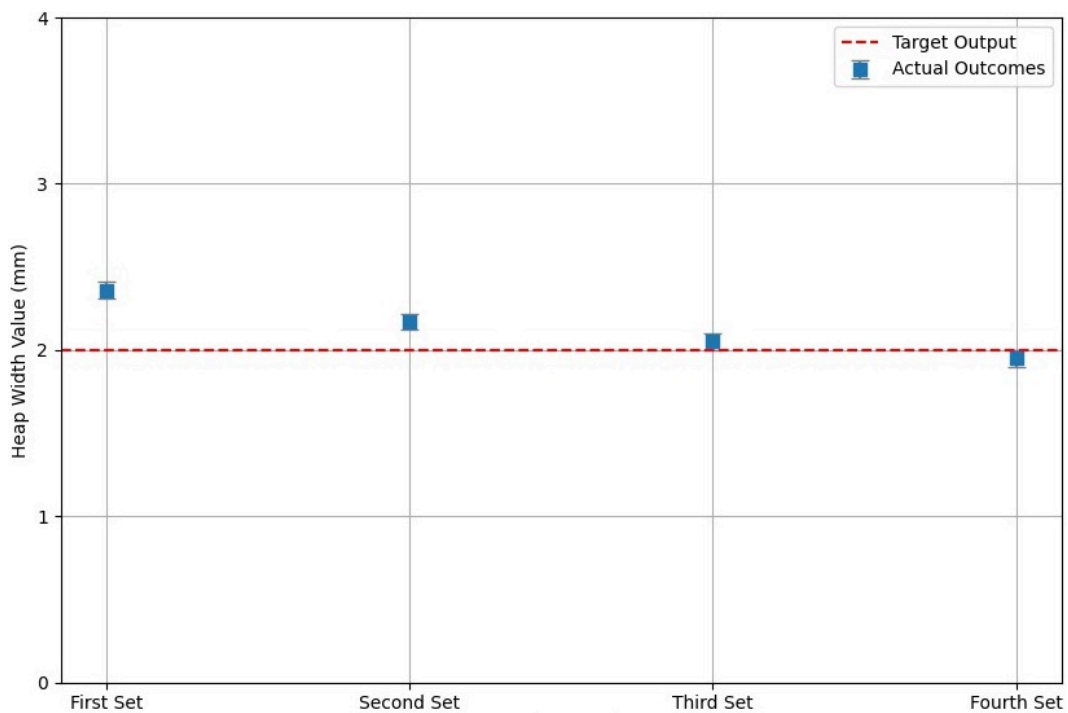


Figure 4.29: Quantification of the accuracy of the regression relation, considering the error of the prediction compared to the observation with a root mean squared error of 0.202.

4.3Conclusions

This chapter focuses on the optimization of the powder deposition system for precise powder distribution. The study examined the effects of three key parameters: nozzle diameter, head movement speed, and ultrasonic power level on powder deposition resolution. Notably, it was found that a 0.6 mm deposition nozzle, even with varying ultrasonic power levels, caused powder jamming and hindered proper ejection, suggesting the inability of the powder to pass through such a narrow orifice. Furthermore, the results indicated a proportional relationship between ultrasonic power levels and powder heap height. As ultrasonic power increased, heap height increased. The study also highlighted a negative correlation between ultrasonic power levels and heap width, the power levels increases when the heap width decreases. Additionally, the research emphasized the impact of movement speed on heap height and width as faster speeds led to narrower and shorter powder heaps. The second phase of experimental trials introduced a round flattening wiper to the deposition system, designed to spread the deposited powder at a well-defined height of 150 μm . The primary focus of these experiments was on the width of the powder heaps, as the heap height was fixed. Like the initial trials, the parameters under consideration were the same, however certain inputs were excluded due to unsatisfactory results from the first testing round. It became evident that ultrasonic power levels had a direct influence on the width of the powder heaps when the wiper was employed. Specifically, as the ultrasonic power level increased, the heap width expanded. Also, the study showed that head movement speed had an inverse relationship with heap width at the second phase of experimental trials. The comparison between deposition trials with and without the wiper revealed significant differences in the width of the deposited powder heaps. It became apparent that depositing powder without a wiper led to thinner heap widths. Finally, it was observed that best combination of parameters is diameter of 0.8 mm, head speed of 30 mm/s, and power level of 1800 W without the use of the wiper. The rationale behind these specific parameters lies in the necessity to achieve a thinner heap width essential for the building process.

Chapter 5. Binder Selection and Characterisation

5.1 Introduction

Polyvinyl alcohol, commonly referred to as PVA, represents a synthetic polymer discovered by Hermann Staudinger in 1924. PVA is characterized by its colourless, tasteless nature and its solubility in water. This versatile polymer finds applications in various industries, including textiles and the specialized field of biomedicine industry (37). When used as a binder in concentrations around 5% by weight, PVA is ecologically benign and non-toxic. Commercially, PVA is available in granular form, with molecular weights spanning the range of 10,000 to 200,000 g/mol (38). Moreover, PVA comes in varying degrees of hydrolysis, which is a measure of its water solubility. The ease of dissolution inversely correlates with the degree of hydrolysis, with highly hydrolysed PVA, often referred to as "fully hydrolysed" PVA, exhibiting higher dissolution temperatures exceeding 80°C and longer dissolution times, especially for high-molecular-weight PVA. In the context of binder spreadability, the strength of hydrogen bonding between the hydroxyl (OH) groups in the PVA polymer chain and water molecules significantly influences the outcome. After complete dissolution, fully hydrolysed PVA forms hydrogen bonds with water molecules, unlike PVA with lower degrees of hydrolysis. For the BJ process, an ideal binder material should exhibit excellent infiltration capabilities. The surface tension and viscosity of the binder are critical factors that determine the lateral and vertical penetration during the powder bed processing of materials, and these properties can be directly impacted by the molecular weights of PVA (39).

In a study has made by Paul et al (40), three different PVA-based liquid binders with distinct molecular weights—low, medium, and high (10,000, 25,000, and 84,000 g/mol, respectively)—were subjected to Sessile drop testing. Sessile drop testing is a technique commonly used to assess the wetting behaviour and surface tension of a certain liquid. In the context of evaluating PVA as a binder material, this testing method provides insights into how well the PVA solution infiltrates or spreads on the surface of a substrate material. The viscosity, surface tension, and wetting behaviour of PVA can be influenced by its molecular weight. Thus, investigating PVA solutions with varying molecular weights allows to assess how these characteristics impact the binder's ability to infiltrate the substrate material. As a result of the different molecular weights investigation, the medium molecular weight PVA-based binder exhibited the most favourable performance, displaying the lowest contact angle of 27 degrees with the powder. This was attributed to the optimal polymer chain structure of the medium molecular weight PVA and the comparatively lower viscosity of the binder's water base, which enhanced its wetting action compared to other PVA-based binders (40).

Consequently, PVA granules with a molecular weight of 26,000 g/mol and a 95% degree of hydrolysis were utilized in this research for the printing process, procured from Alfa Aesar [Heysham, UK]. The PVA aqueous solution, employed as the liquid binder, was prepared by dissolving medium molecular weight PVA particles in deionized water. The solution was agitated using a hot surface stirrer (UC152 Hot Stirrer, Stuart, Northants, UK) at a controlled temperature for a specified duration. The PVA particles, with molecular weights of 26,000 g/mol and a degree of hydrolysis of 95%, were measured and placed in a beaker. A precise volume of deionized water was then added to the mixture, and the beaker was positioned on a hot plate equipped with a magnetic stirring function. The solution was heated to 85°C, with the rotary stirrer operating at 300 RPM to facilitate thermal agitation for 45 minutes. Figure 5.1 illustrates a schematic representation of the setup employed for the preparation of the PVA binder in this study. After complete dissolution, the apparatus

was disassembled, allowing the PVA solution, now serving as the binder, to cool to the processing temperature.

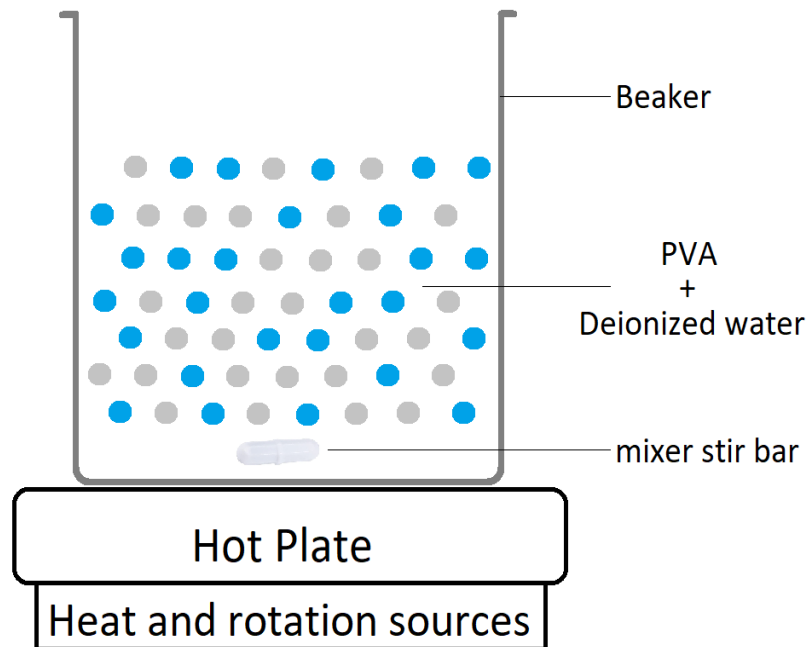


Figure 5.1: An illustrative representation is provided herein depicting the experimental apparatus employed for the formulation of the liquid binder. The procedure entailed the thorough blending of the requisite weight percentage of the binder substance with deionized water. This amalgamation was carried out utilizing a precision hot plate stirrer, calibrated to ensure accurate mixing and uniform distribution of the components.

5.1.1 PVA Concentration and Wettability Analysis

The assessment of both the quality of the printed green body and the structural integrity of the printed components was conducted through these experimental investigations aimed at understanding the influence of the liquid binder's composition on these critical aspects. To ensure that the printed green component possesses adequate green strength, precise binder quantities were judiciously administered. Three distinct weight-based concentrations of polyvinyl alcohol (PVA) within the binder were subjected to scrutiny to ascertain the optimal green strength of the printed part. To evaluate the printability of the prepared binder, a drop-on-demand (DOD) approach was employed. The liquid dispensing system utilized in these trials featured a deposition dispensing nozzle affixed to a Fisnar liquid dispensing pen, seamlessly integrated with a digital liquid dispensing controller (Fisnar DC50 Benchtop Digital Liquid Dispensing System, Intertronics, England, UK). The dispensing controller was equipped with an input air inlet for pressured air, sourced from an air compressor. Figure 5.2 illustrates the configuration of the dispensing system employed in these experimental investigations.

To the protection of the structural integrity of the green body, which is crucial for maintaining its strength under Mechanical Testing, an experiment was planned and executed. This experiment revolved around the thorough examination of three distinct PVA concentration percentages, each of which is outlined in Table 5.1. The primary objective was to reach a harmonious balance between preserving the green body's physical form and enhancing its ability to endure various forms of mechanical pressure. The green body, in this context, refers to the initial stage of a product, typically in the manufacturing process, where it retains a relatively soft. It is during this stage that needs to ensure that its structural integrity is upheld, as it will undergo further processing.

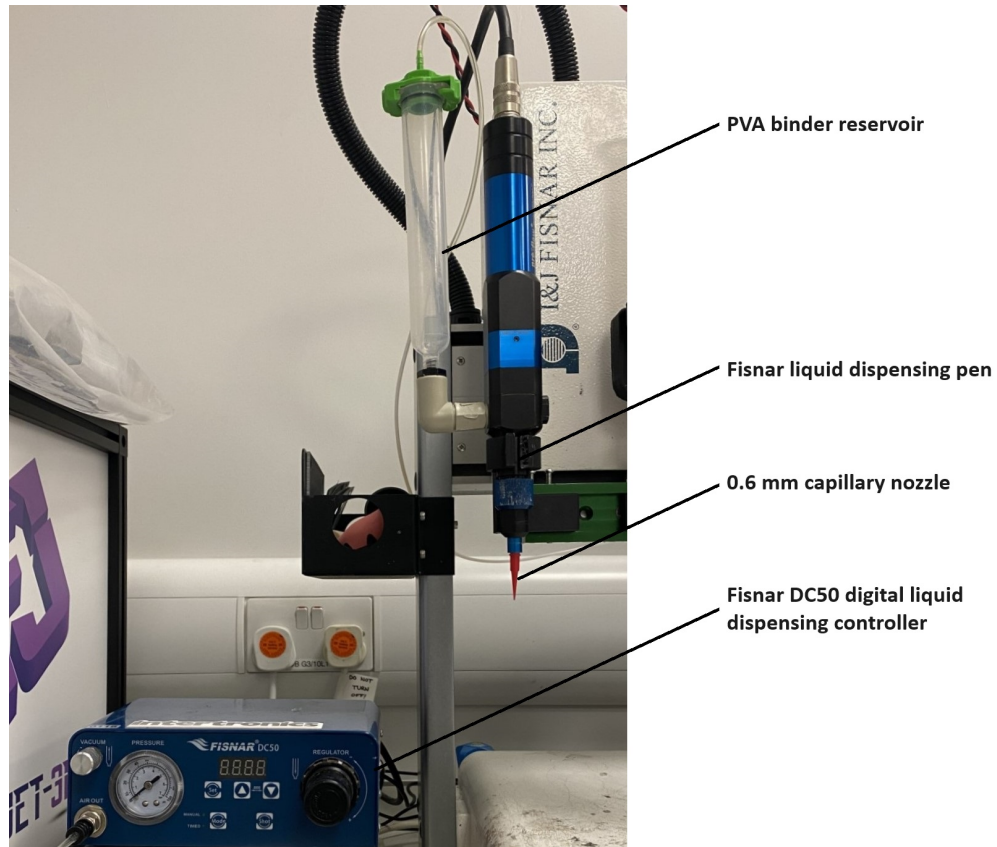


Figure 5.2: The equipment used in this study to deposit the PVA binder and evaluate the printability using a drop-on-demand approach. A deposition nozzle was connected to a Fisnar liquid dispensing pen, controlled by a digital liquid dispensing system (Fisnar DC50). This system utilized pressurized air from an external compressor.

Test	PVA concentration
Experiment 1	3%
Experiment 2	5%
Experiment 3	7%

Table 5.1: Three different levels of PVA concentration used in the test experiment were carried out to ensure the overall strength and durability of the green body. The aim was to maintain the structural integrity of the green body while also ensuring its mechanical resilience. This study sought to attain a balance between preserving the green body's form and enhancing its ability to withstand structural stress.

In addition, the role of the binder in the fabrication of well-structured green components within the BJ process is of paramount importance. The characteristics of the binder are instrumental in determining whether a binder droplet can effectively wet the surface of the powder bed and facilitate the cohesive bonding of powder particles. When a binder droplet encounters a powder layer, it shows two discernible behaviours, specifically, radial spreading resulting from the reduction in the liquid droplet's surface tension, and penetration into the powder bed, driven by capillary forces and gravitational attraction (40).

Studies investigating the interaction of capillary action with the powder bed surface have yielded insights into the division of the spreading phenomenon into primary and secondary behaviours. This delineation occurs after the initial contact between the liquid droplet and the powder bed surface. Primary spreading transpires when the sessile volume is greater than zero, whereas secondary spreading arises when the sessile volume equals zero (138) and (139). Upon contact, it has been observed that three surface tension vectors concurrently interact with one another, as depicted in Figure 5.3, where γ_{SV} is the solid-vapor (air), γ_{SL} is the solid-liquid and γ_{LV} is the liquid-vapor interfacial energies (140).

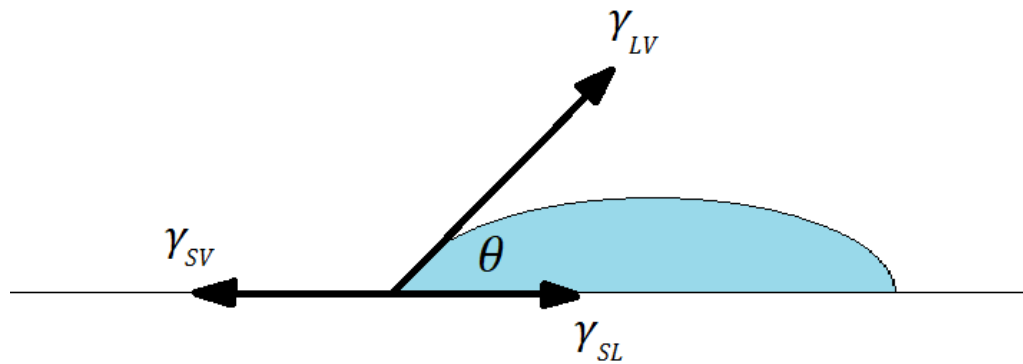


Figure 5.3: representation of the droplet upon contact between the droplet and the substrate, the interplay of three surface tension vectors becomes evident. Specifically, γ_{SV} is the solid-vapor (air), γ_{SL} is the solid-liquid and γ_{LV} is the liquid-vapor interfacial energies.

5.1.2 Thermal Characterisation of the Prepared Binder

Thermogravimetric analysis (TGA), a highly valuable analytical technique, played a fundamental role in this research. TGA is a technique that measures changes in the weight of a material as it is heated or cooled. In essence, TGA tracks the weight of a sample as it undergoes temperature variations under a controlled atmosphere. A TGA setup includes a sample pan supported by a precision balance, situated within a furnace where heating or cooling occurs. Throughout the experiment, the mass of the sample is continually monitored. Additionally, a sample purge gas, which can be inert or reactive, regulates the sample environment by flowing over the sample and exiting through an exhaust (141). TGA served as a tool for characterizing the thermal properties of the materials involved, shedding light on the burnout temperature of the binder, and ensuring the absence of undesired carbonaceous residues. This detailed thermal analysis not only contributed to the understanding of the materials but also underscored the importance of precise temperature control in various scientific and industrial applications.

First and foremost, TGA was employed to determine a critical parameter: the temperature at which the PVA particles within the samples began to thermally decompose. This specific temperature, referred to as the burnout temperature of the binder material, is of paramount importance in many applications, especially in the field of materials science. Knowing this temperature is crucial for the sintering processes, where the removal of the binders is a prerequisite for achieving the desired material properties. Additionally, this study utilized TGA to investigate whether any extraneous carbonaceous substances were generated during the experimental procedures. This facet of the analysis was particularly relevant in assessing the purity and integrity of the materials under examination. Specifically, the focus was on determining if the sintered specimens produced any unintended carbon byproducts, which could result from processes like soot formation or the charring of the material during thermal treatment.

5.2 Results and Discussions

5.2.1 PVA Concentration and Wettability Analysis

In this experiment, three different PVA concentrations dissolved in deionized water have been tested. These three concentrations were 3, 5, 7% by-weight PVA content. The samples for these tests were printed by depositing 316L stainless steel powders without the wiper, followed by levelling to a layer height of 200 microns. Subsequently, the binder material was dispensed onto the top of the deposited powder. The process was repeated 25 times to achieve a sample height of 5 mm. The temperature of the binder during dispensing was at the room temperature. In the first test, an insufficient quantity of binder material was employed, which subsequently gave rise to an undesirable outcome wherein the printed object exhibited partial structural failure under its weight. This failure stemmed from the inability of the 3% PVA concentration in the binder to provide adequate adhesion to the powder particles. On the contrary, when the PVA concentration was increased to 7% in the third test, it gave rise to a binder solution characterized by elevated viscosity. This high viscosity, while intended to enhance adhesion, presented an unforeseen challenge by impeding the smooth ejection of the binder from 0.6 mm binder dispensing nozzle as it is a bigger nozzle diameter when compared to 0.1mm. As a result, the excessive viscosity hindered the precise and controlled application of the binder during the printing process, further emphasizing the delicate balance that must be achieved in binder composition to ensure optimal printing outcomes. In concordance with the observations made in the second test, the printed object exhibited a favourable response to a PVA concentration of 5%. This concentration demonstrated an enhanced ability to retain the powder particles within the green body. The selection of this particular concentration was supported by its good performance in conferring enhanced structural integrity to the resulting green component when compared to alternative concentrations see Figure 5.4. Likewise, a study conducted by Paul et al (40) has investigated BJ process employing PVA binders

with varying concentrations. The study's findings have substantiated the effectiveness of an aqueous binder, particularly in combination with a 5% by-weight PVA content. Consequently, the 5% PVA concentration is deemed to represent an optimal proportion within the binder formulation, ensuring an appropriate balance between adhesion and viscosity, thereby contributing to the attainment of good and well-structured green parts.

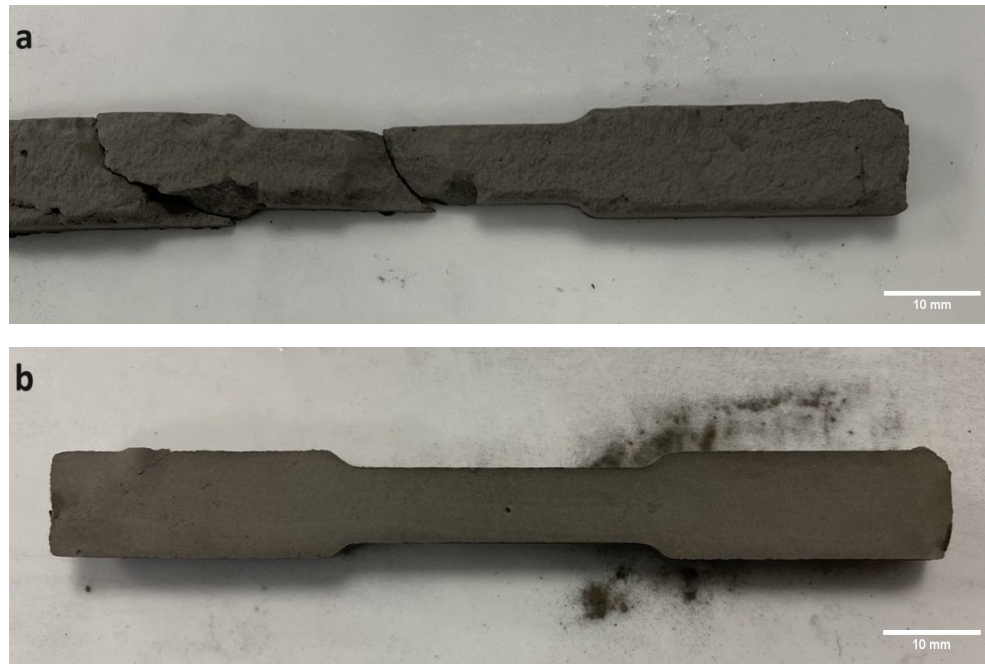


Figure 5.4: The variation in using two different PVA concentrations. (a) suboptimal binder quantity led to partial structural failure in the printed object due to inadequate adhesion resulting from a 3% PVA concentration within the binder. (b) The printed object displayed improved performance with a 5% PVA concentration, exhibiting enhanced powder particle retention within the green body, thereby confirming its efficacy.

Next, the liquid binder that included 5% PVA by weight was evaluated to see how well the droplet penetrated the powder particles in the powder bed using the Sessile Drop equipment. This evaluation, also known as wettability and contact angle analysis. In this experiment, the powder dispensing was performed manually, followed by levelling to ensure proper compaction of the powder. The results obtained from the Sessile drop experiment revealed a noteworthy phenomenon: the vanishing of the binder droplets coincided precisely with the moment of initial contact between the

liquid drop and the powder surface. Figure 5.5 shows a sequence of images, taken from a video recording during the experiment, showing the various phases of a droplet during a wettability experiment. In the initial stage (Figure 5.5a), a droplet of liquid binder makes contact with the bed of powder. As the experiment progresses, the droplet commences its entry into the powder bed, indicating the initiation of wetting (Figure 5.5b). Subsequently, the droplet continues to penetrate deeper into the powder, further demonstrating its interaction with the powder particles (Figure 5.5c). Finally, the droplet becomes fully incorporated into the powder bed, effectively disappearing within the particle matrix (Figure 5.5d). It was noted that despite using manual spreading and levelling of the powder, which typically leads to effective powder compaction, satisfactory penetration into the powder layer was achieved.

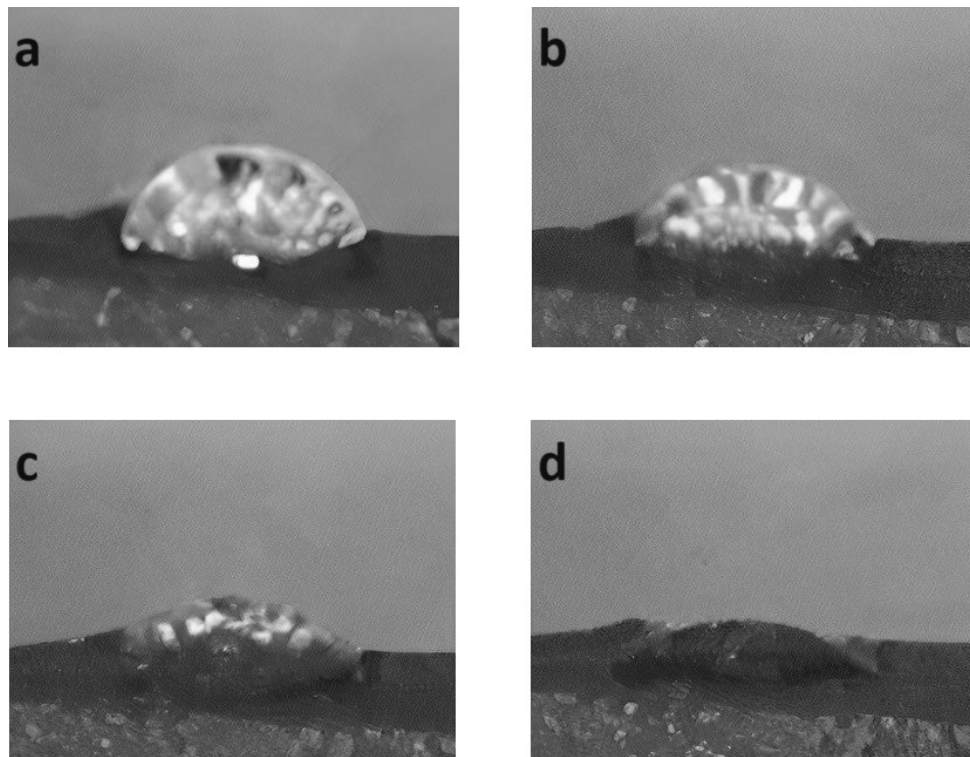


Figure 5.5: Sessile drop experiment: (a) binder droplet contacts the powder bed. (b) droplet starts to penetrate the powder bed, marking the onset of wetting. (c) the droplet advances deeper into the powder bed, illustrating its interaction with the powder particles. (d) the droplet fully integrates into the powder bed.

5.2.2 Thermogravimetric Analysis of the Prepared Binder

In the course of the Thermogravimetric Analysis (TGA) conducted on the 5% PVA binder specimen, thorough attention was paid to several critical parameters. The initial weight of the sample was precisely measured and found to be 12.015 mg. Subsequently, the TGA protocol involved subjecting the sample to a maximum temperature of 600°C, with the temperature ramping rate deliberately set at 10°C per minute. To maintain the controlled environment essential for accurate analysis, a constant stream of argon gas was introduced throughout the process at a consistent flow rate of 20 mL per minute. Thus, the sample remained shielded from the influence of atmospheric gases. The outcomes of the TGA study are visually presented in Figure 5.6, providing valuable insights into the decomposition characteristics of the PVA binder sample along with temperature.

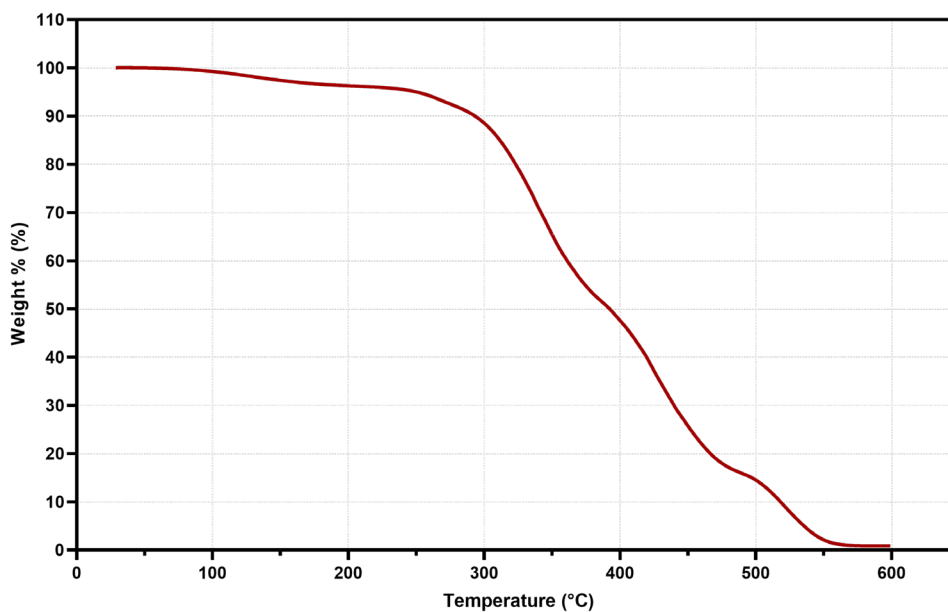


Figure 5.6: Thermogravimetric analysis of the formulated PVA binder reveals the alterations in material weight as a consequence of thermal decomposition during the temperature elevation.

The outcomes of the thermogravimetric analysis (TGA) have shown a remarkable phenomenon. Specifically, after subjecting the PVA sample to an analysis cycle that extended to a temperature of 600°C, only a small quantity (that represent 0.104 mg) of the binder material remained. This residue represents a mere 0.87% of the total weight of the initial PVA sample. This finding underscores the considerable thermal susceptibility and decomposition characteristics of the PVA binder when exposed to elevated temperatures. This serves the crucial purpose of ensuring the complete decomposition of the binder from the sample during the sintering process of the 3D-printed specimen.

5.2.3 Binder's Viscosity

The liquid binder of 5% PVA by weight of the medium molecular weights was prepared to evaluate the viscosity at various temperatures since this property plays a crucial role in the vertical infiltration of the binder after it has made contact with the powder bed. The dynamic viscosity of prepared binders, 5% PVA by weight, was determined using a Modular Compact Rheometer (MCR 502e, Anton Paar GmbH, Virginia, United States). This parameter was tested at various temperatures ranging from 25 to 45°C, at 25, 30, 35, 40, and 45°C. Figure 5.7 depicts the rate of change that occurs in dynamic viscosity as a function of temperature for the prepared PVA binder that comprised 5% medium molecular weights. Ordinary water was used for the benchmarking and these results are according to The International Association for the Properties of Water and Steam (IAPWS) (42) (43). The noticeable change was a drop of almost 34 percent in the viscosity of the deionized water from 25 to 45°C.

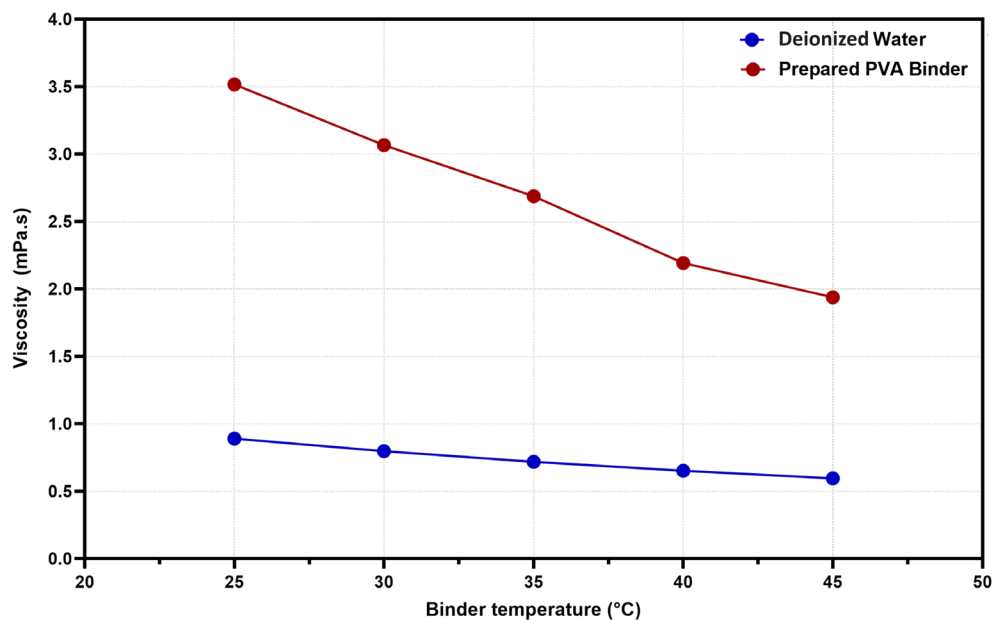


Figure 5.7: Dynamic viscosity measurements were conducted on the 5% PVA binder in conjunction with deionized water. These measurements reveal a notable reduction in viscosity values as a direct consequence of elevated temperatures.

Over the same range of temperature, ranging from 25 to 45°C, the prepared binder's viscosity has fallen from 3.5 to 1.9 mPa.s, which represents almost a 45% drop. Due to the low viscosity at 45°C, the binder will likely be able to penetrate the powder particles in the powder bed more effectively. However, one thing that should have raised some warning flags was the fact that the values of viscosity that were measured for the PVA material throughout a variety of temperatures and different PVA molecular weights did not accord with the analogous work that was available in the published research. For instance, a study has been done by Vikingsson et al (142) have shown that the viscosity of 4% by weight PVA solution that added to other polymer-based materials is 56 mPa.s at the temperature of typically around 20°C. This difference in the viscosity outcomes is the result of adding other polymer materials to the prepared PVA solution. Another study has been done, by Salaoru et al (143), has indicated that the viscosity of the aqueous PVA solutions that were created was found to be 5.4 mPa.s at room temperature. The PVA concentration was 4% by weight and it has a high molecular weight, but the solution has an addition of Mono Propylene Glycol, this justifies the change of the value of the viscosity. In addition, a PVA-based solution was the subject of research conducted by Monne et al (144) who found that the viscosity of a 4.5% PVA solution was 8.8 mPa.s at room temperature. To compare these values with the viscosity values that have been provided by the Rheometer, it can be notable that the Rheometer's values are almost half the values achieved in the previous works. In contrast, the PVA samples utilised in all of these investigations had substantially larger molecular weights than those of the PVA employed in this research, which has been used in this investigation.

5.2.4 Binder's Surface Tension

The surface tension of the finished binder sample was an additional element that was investigated and analysed. Tensiometer [BP100, Krüss, Hamburg, Germany] was used in the evaluation process so that accurate results could be obtained. The procedure of measuring begins with the first step of calibration. During this phase, the value of the capillary diameter is determined by calculating the surface tension of a calibration liquid using a known value. At a constant temperature of 25°C, the calibration was carried out using deionized water in liquid form. The effect that changes in temperature have on the surface tension of the prepared binder can be seen in Figure 5.8. The results of the binder surface tension tests suggest that the binder exhibits a slight change in surface tension from a temperature of 25°C to 45°C, from 44.5 to 42.2 mN/m. The values of surface tension were found to be approximate with values of prior PVA studies by Bhattacharya et al (145) and Monne et al (144) as the values of 4% by weight PVA solution were between 39 and 45 mN/m.

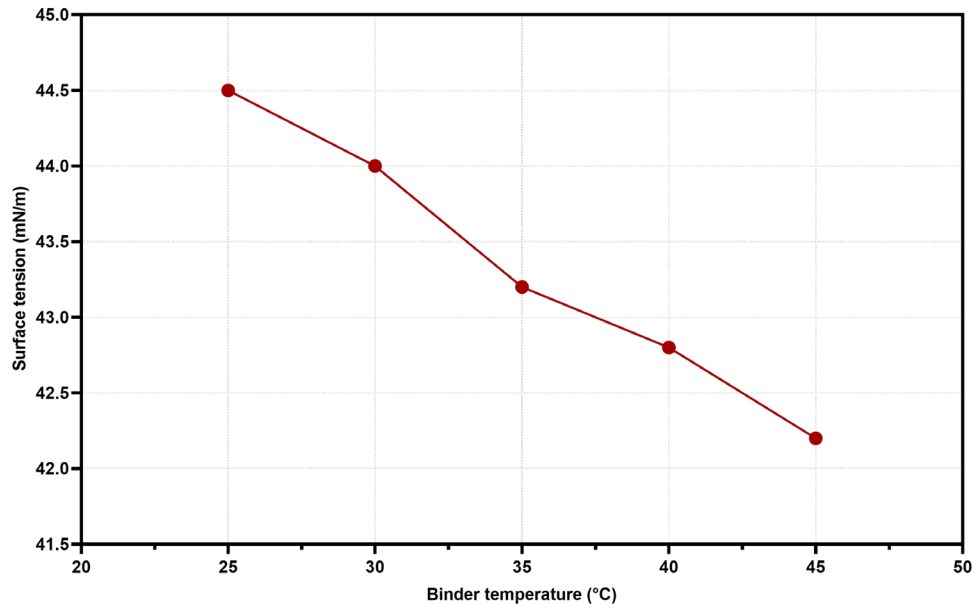


Figure 5.8: The impact of temperature variations on the surface tension of the prepared PVA binder of 5%.

5.2.5 Ohnesorge Number

The Oh number has been calculated using the formula explained in chapter 2.2.1.2. Notably, at an initial examination conducted at room temperature, the Oh number for the PVA binder with a 0.6 mm nozzle was determined to be 0.0197. Subsequently, as the temperature was elevated, the value exhibited a gradual reduction, reflecting the dynamic relationship between this key parameter and temperature. Likewise, when analysing the PVA binder with a 0.1 mm nozzle diameter, the initial Oh number, observed under room temperature conditions, was measured at 0.0483. As the temperature was increased to 45°C, the value ultimately reached 0.0274. The Oh number for the different deposition nozzles can be seen in Figure 5.9. The observed decline in the Oh number with increasing temperature can be attributed to the decrease in the dynamic viscosity of the binder. This behaviour is consistent with the fundamental relationship that ties the Oh number to the viscosity values, signifying the fundamental role of temperature in influencing these interrelated parameters.

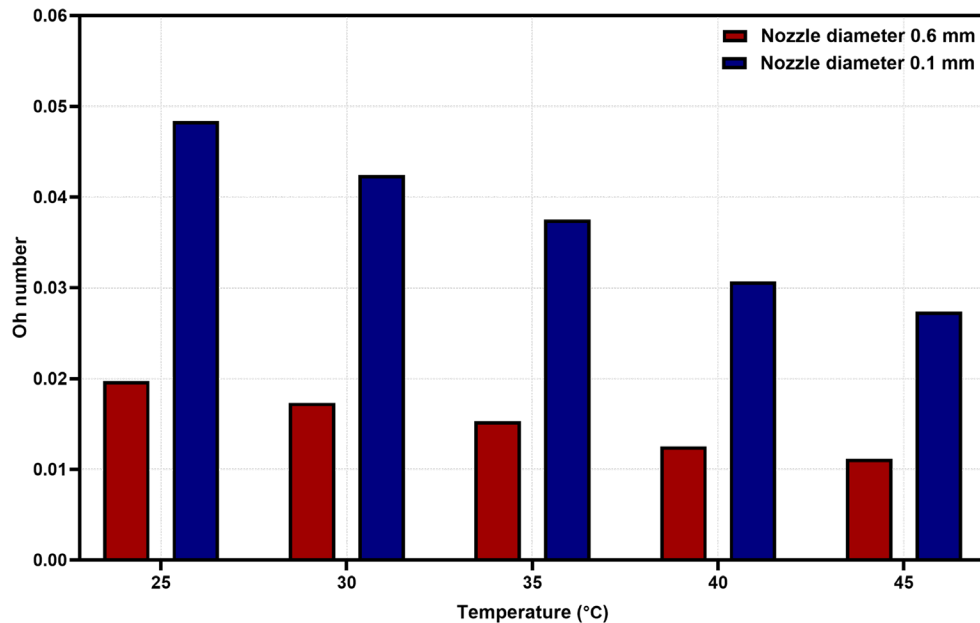


Figure 5.9: Ohnesorge number of the prepared binders comprised of 5% molecular weights of PVA dissolved in deionized water for the binder deposition nozzle of 0.1 and 0.6 mm.

5.2.6 Z-number

After obtaining the Oh number, another factor that depends on the Oh number should be determined which is the Z number. Figure 5.10 displays the results of the Z number values calculation for the PVA binder, concerning the two different binder deposition nozzles of 0.1 and 0.6 mm, that have been used in the work. The binders' Z numbers, when measured at various temperatures, reveal a range that is greater than the maximum dischargeable value of the Z number proposed by Derby et al (47) as a good measure of reliable jetting.

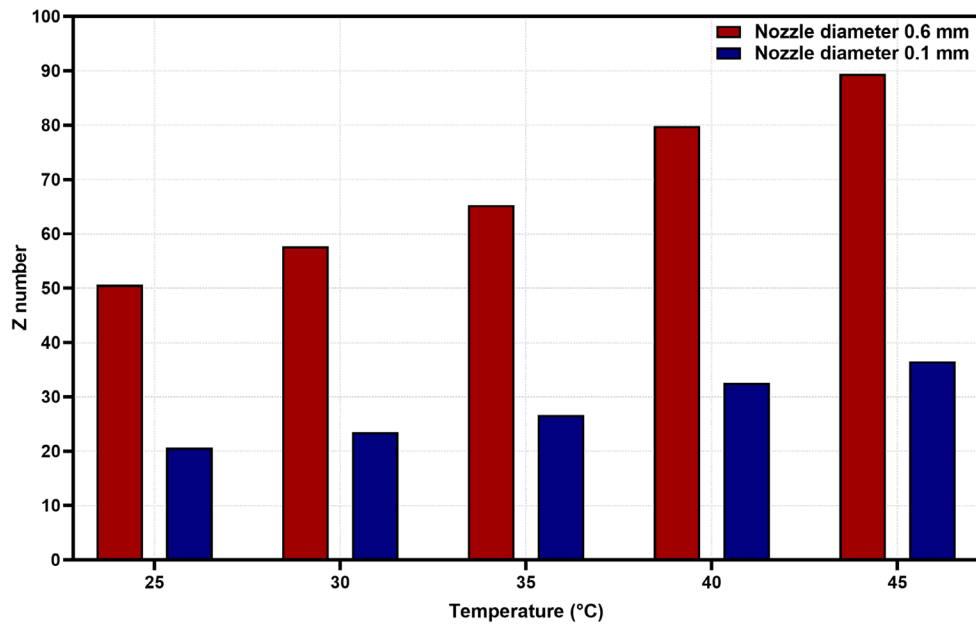


Figure 5.10: The Z number of the developed binders consisted of 5% molecular weights of PVA dissolved in deionized water at elevated temperatures for the binder deposition nozzle of 0.1 and 0.6 mm.

5.3 Conclusions

In this chapter, the initial phase of the experimental investigation focused on the PVA concentration. A 3% by-weight PVA content proved inadequate, leading to structural failure of the printed body under its weight due to insufficient adhesion to the powder particles. Conversely, a 7% by-weight PVA content resulted in a high-viscosity liquid that posed challenges in terms of ejection from the binder dispensing nozzle. However, the best concentration appeared to be a 5% by-weight PVA content, which exhibited favourable characteristics. This concentration was deemed suitable, as it demonstrated improved powder particle retention within the green body. Next, the ability to penetrate the powder bed of the 5% by-weight PVA content has been tested. The outcomes of the wettability experiment showed an observation: the binder droplets disappeared almost instantly upon contact with the powder surface. This phenomenon suggests that the binder exhibited an ability to readily infiltrate and disperse within the powder bed, ensuring efficient and effective binding of powder particles. Subsequently, TGA of the 5% PVA binder sample has been performed with an initial sample weight of 12.015 mg with a maximum temperature limit of 600°C. It was evident that approximately 0.87% of the PVA remained following the completion of the TGA cycle, ending at the high temperature of 600°C. Next, the viscosity over a temperature range from 25 to 45°C has been evaluated, which showed a 45% reduction. The research then focused on examining the impact of temperature variations on the surface tension of the prepared binder. The results of the surface tension indicate that the surface tension of the binder exhibited only minor changes between 25°C and 45°C, ranging from 44.5 to 42.2 mN/m. After, in this chapter, the Oh number was calculated to assess the behaviour of a PVA binder with two distinct nozzle diameters, 0.1 mm and 0.6 mm, under varying temperature conditions.

After the PVA concentration tests and rheological characterisation had been completed, the liquid binder that included 5% PVA by weight was evaluated to see how well it flowed through the 0.1 and 0.6 mm binder deposition nozzles. These two nozzles have been used to show the difference in the droplet size once it penetrates the powder bed. It was discovered that, despite the high Oh and Z number values of the binders that have been calculated, all of the binders were gettable and could be dispensed reliably over a while without the issue of droplet jamming or uneven droplet formation at room temperature from the 0.6 mm nozzle. Due to the high viscosity of the binder with regards to using a small orifice nozzle diameter and a temperature of 25°C, the binder could not be dispensed from the 0.1 mm nozzle. The same phenomenon occurred while heating the binder to temperatures of 30 and 35°C, in which binder jamming was detected. Meanwhile, good binder deposition was seen when the binder was at temperatures between 40°C and effective dispensing has been observed around 45°C. The Oh and Z number values of the binders that have been calculated have showed that the unreliability of the theory that suggests that $10 > Z > 1$ represents a reliable domain for droplet formation discussed in the published literatures.

Chapter 6. Binder Jetting Process and Printing Parts

6.1 Introduction

In order to enable the successful implementation of the Binder Jetting process with multi-materials, a specialized system was specifically designed and developed for this study. The Fisnar robotic adjustment was configured for deployment as a multifunctional Binder Jetting (BJ) system, adept at handling multiple materials. This setup involved the integration of the Fisnar liquid dispensing pen and the Multi-material powder dispensing system, both affixed to a holder capable of movement along the X and Z axes. Additionally, the building platform exhibited motion along the Y-axis, contributing to the three-dimensional printing capabilities of the system see Figure 6.1. To control the liquid binder droplet, a DC50 Benchtop Digital Liquid Dispensing Controller from INTERTRONICS, UK was employed.

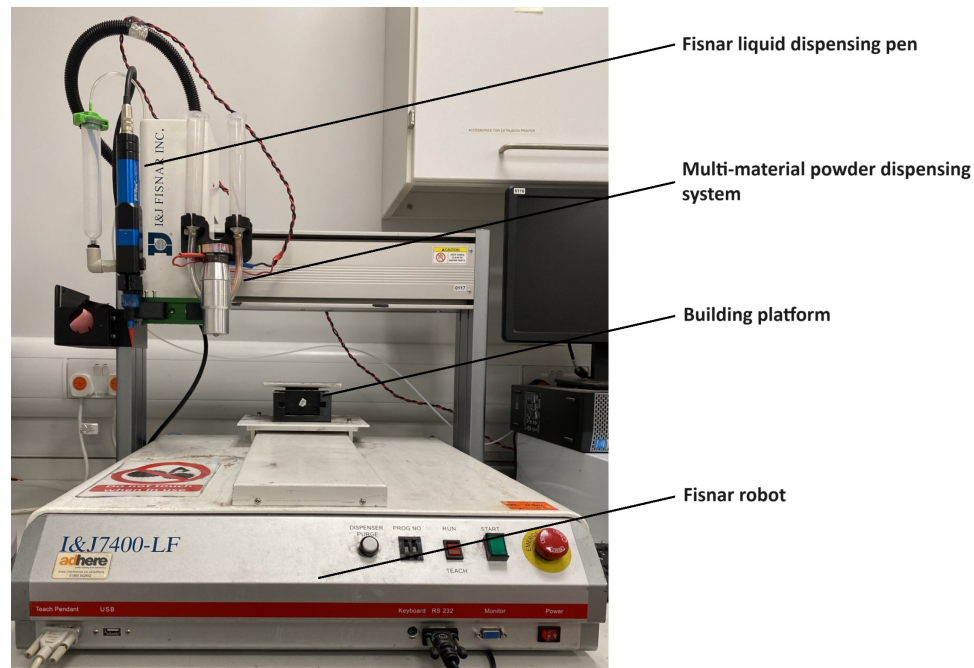


Figure 6.1: The Fisnar robotic system used for multi-material BJ processing with the integration of a liquid dispensing pen and a multi-material powder dispensing system in a versatile holder allowing movement along the X and Z axes. The building platform featured Y-axis motion, enhancing the system's three-dimensional printing capabilities.

In the context of the printing process, a drop-on-demand mechanism was employed to precisely deposit the prepared binder at user-defined locations. A distinctive feature of the liquid dispensing system is the inclusion of a pressurized air attachment. The system is integrated with an electronic controller, specifically the Fisnar DC50 Benchtop Digital Liquid Dispensing system, manufactured by Intertronics, England, UK. Notably, the pressure valve can be actuated through a foot pedal incorporated into the pressure controller. Upon depressing the foot pedal, the pressure valve opens, generating a pressure wave that propagates through the tubing. This wave subsequently transmits pressure to the syringe barrel and then to the liquid dispensing pen. This setup ensures precise and controlled discharge of a singular binder droplet from the printing equipment to the desired location. It is important to highlight that the experiments utilized two binder deposition nozzles, with dimensions of 0.1 mm and 0.6 mm, as depicted in Figure 6.2, for the controlled deposition of the binder.

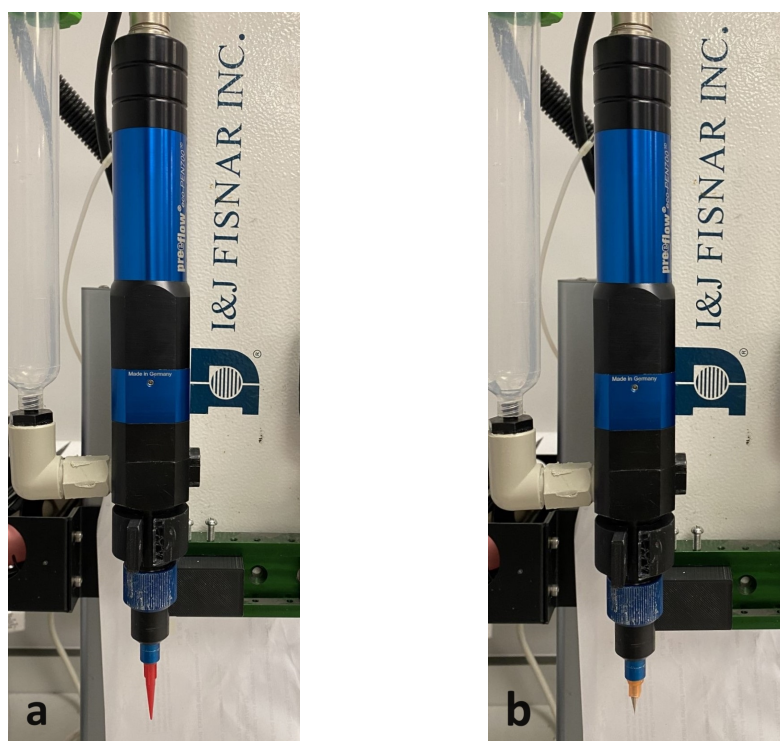


Figure 6.2: Binder dispensing pen with the two different deposition nozzles (a) 0.6 mm and (b) 0.1 mm.

In Figure 6.3, two distinct multi-material building structures have been fabricated, illustrating the results of this research and manufacturing efforts. These structures highlight the innovative capabilities and versatility of the multi-material BJ system in creating multi-material components. At the first approach, the production of multi-material structures commences with a sequential layering process, which entails the deposition of powdered material A, followed by the subsequent deposition of material B onto the pre-existing layers of material A. This methodology is referred to as "multi-material printing in the Z-axis". This approach allows for the construction of multi-material components along the vertical (Z) axis. With each successive layer, the contribution of individual layers to the overall structure is progressively enhanced, adding to its structural integrity. The second category of multi-material structures employs a sequential process, involving the initial deposition of powdered material A, followed by selective deposition of material B onto specific locations within material A within the same layer. This strategy facilitates the fabrication of multi-material components in the X-Y plane, with both materials coexisting within the same layer.

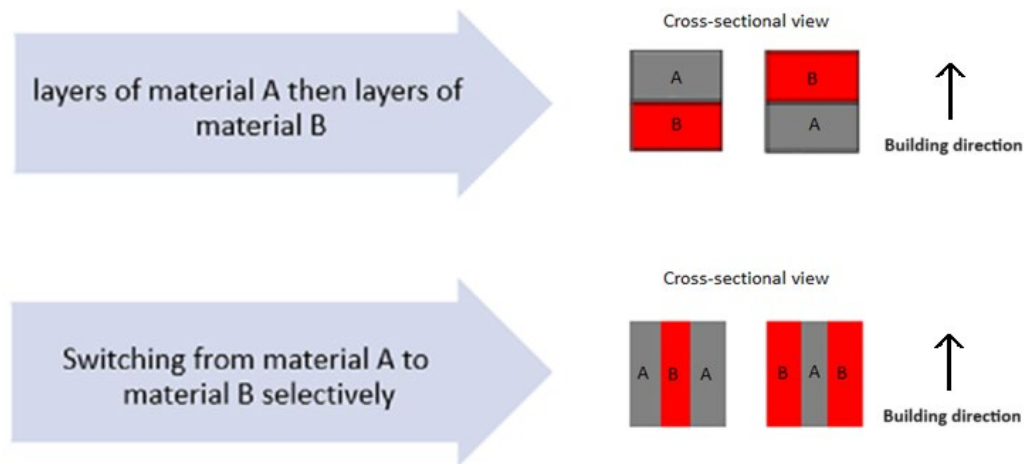


Figure 6.3: Different multi-material structures approaches. In the first approach, multi-material structures are produced through sequential layering, depositing material A powder, followed by material B onto existing material A layers. The second approach, depositing material A initially and selectively adding material B to specific locations within the same layer.

6.1.1 Printing Process

In the Z-axis printing mode, the process commences with the thorough deposition of the first layer, comprising 316L powder, onto the building platform. This initial layer establishes the foundation for subsequent layers. A powder levelling mechanism, equipped with blades, is subsequently employed to ensure the uniform distribution of the powder material, and achieve a targeted layer thickness of 200 micrometres. This critical step plays a fundamental role in promoting proper bonding and adhesion during the following stages of the manufacturing process. The subsequent crucial phase involves the dispensation of a liquid PVA binder. A specifically directed nozzle releases PVA binder droplets onto the desired regions, permeating the powder bed and initiating the bonding process among individual powder particles. The binder serves as an adhesive agent, effectively facilitating the fusion of powder particles and strengthening the overall structure of the object. These processes are iteratively conducted to successfully fabricate the final layers of 316L. Subsequently, Cu powder material is deposited on top of the previously printed 316L layers. A powder levelling device is used again to ensure uniform powder spreading, targeting the same layer thickness. Following this, liquid PVA binder droplets are dispensed, penetrating the powder bed, and initiating the bonding process. These processes are repetitively executed until the final length of the sample is achieved.

The sequential manufacturing process for multi-material components in the x-y axis falling within the scope of this investigation is illustrated in Figure 6.4. Commencing with Step 1, the procedure initiates with precise dispensing of material A powders onto the building platform at predefined locations. Subsequently, in Step 2, powders of the secondary material are judiciously distributed within a delineated area to effectively fill voids left by the initial powder deposition. Step 3 involves the use of a powder levelling blade to attain the desired layer thickness and ensure uniform dispersion of the powder across the layer. Upon levelling the powder bed, Step 4 entails positioning the binder nozzle over the targeted geometric region and then dispensing the binder. This action prompts the expulsion of binder particles that

permeate the powder bed, facilitating powder cohesion. To continue the fabrication process, the powder and binder nozzle holder is elevated to a height corresponding to the layer thickness, thereby establishing a new powder layer for further processing. These sequential operations are iteratively repeated to achieve successful 3D model fabrication.

Notably, the Binder Jetting system lacks dedicated software tools for the creation of multi-material components. In response to this limitation, a data preparation technique and tool were developed to address this deficiency. Multi-material components are conceptually treated as assemblies of single-material components during the data preparation phase. For each material, the geometry is sliced and translated into G code for each layer, a decision guided by the preceding statement. Moreover, the motion of the binder nozzle, representing the final stage of building the multi-material layer is expressed as G code to enhance production efficiency.

The building process parameters used in this investigation to 3D print the multi-material samples are presented in Table 6.1. The powder nozzle' tip diameter, powder nozzle speed, and ultrasonic power parameters were figured out through the primary optimisation of the system processes that have been done in chapters 4 and 5 experiments that were carried out to achieve the best possible building efficiency. The binder saturation level parameter was chosen as per the recommendation suggested in the published research (146), (147), (148) and (149). The samples will be built in a rectangular shape that has a length of 20 mm, a width of 8 mm, and a thickness of 5.2 mm (2.6 mm of 316L SS and 2.6 mm of Cu).

Parameter	value
Powder nozzle's tip diameter	0.8 mm
Powder nozzle speed	30 mm/s
Ultrasonic power	1800 W
Layer thickness	200 μm
Binder saturation level	100 %

Table 6.1: The Binder Jetting (BJ) building parameters employed in the fabrication of multi-material structures.

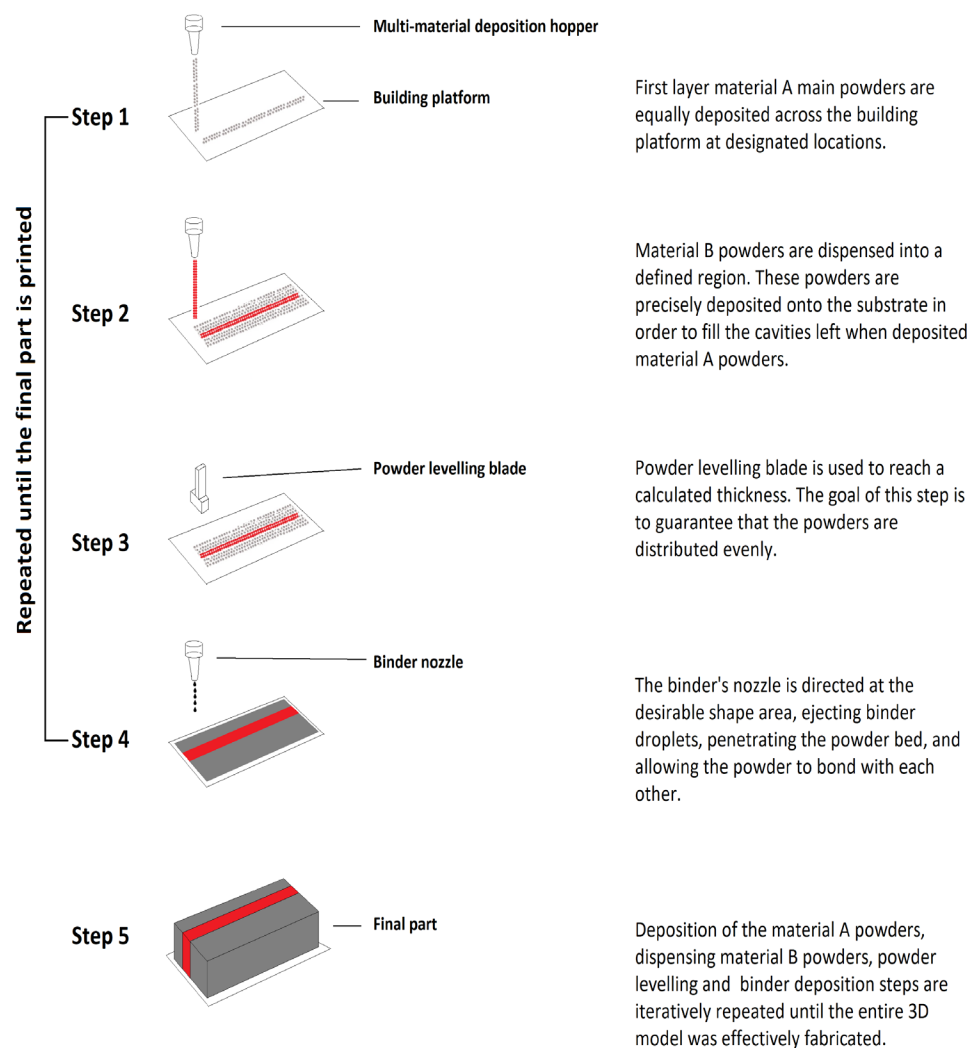


Figure 6.4: The stages of building multi-material components in the x-y axis. It begins with Step 1, where material A powders are dispensed on the platform. In Step 2, the second material powders fill the voids created by the first deposition. Step 3 uses a leveling blade to ensure even spreading. In Step 4, the binder is applied using a nozzle.

6.1.2 Sintering cycles

The post-processing steps are fundamental in BJ 3D printing. In the post-processing, the binder is burnt off and the metallic powder is sintered to fuse the lost powder to form the final shape (150). Sintering is considered the most crucial post-processing stage as it plays an essential role in the final part's density and strength (151) (152) (153). The green components were sintered in a tube furnace (STF15/180, Carbolite Gero (125)) according to a specific thermal cycle. The development of a sintering profile is of greatest significance in the field of materials processing and entails a carefully constructed procedure consisting of four unique isothermal dwell temperatures (154). The first phase, known as the initial hold, is conducted at a predetermined temperature, depending on the binder characterisations, to facilitate the curing process of the binder. The succeeding pause is also dependent on the characteristics of the binder material and requires maintaining a temperature that matches the decomposition point of the binder. This is necessary to guarantee the thorough elimination of the binder before the initiation of the sintering process. The third step, holding, plays a crucial role in regulating the heat gradient across the workpiece during heating. Typically, this temperature is set at approximately 50% of the material's melting point, marking the transition from radiation -based (as the heat environment inside the furnace) to conduction-based (as the heat transfers between powder particles). The closing hold stage is of great importance, as it is the point at which the temperature is raised to a level that effectively stimulates necking between the powder particles. This temperature is usually around 85% of the material's melting point.

To post-process the multi-material samples, an investigation of sintering cycles was conducted to optimise the quality of the interlayer connections of the two different metal materials (copper and 316L stainless steel). Each material has its characterizations such as melting temperature which are 1080°C and 1380°C for the Cu and 316L stainless steel respectively. Thus, the initial sintering cycle was designed by combining the two different single material cycles that have been reported in the published research by (155), (57), (154), (156), (157), (158), (159) and (160).

The first phase, known as the initial hold, is conducted at a predetermined temperature of 300°C, a two-hour-long binder cure phase. The succeeding phase was the binder burn-out phase and was conducted at a temperature of 600 °C according to the TGA of the binder material conducted in Chapter 5. Additionally, the second hold temperature serves as the regulation of the heat gradient over the copper side during the sintering process, which shifts from conduction-based to radiation-based heating during this temperature hold. The third step of holding is at a temperature of 900°C. at this temperature, the copper side effectively stimulates neck development, whereas the stainless-steel side is under the shift from conduction-based to radiation-based heating procedures. The final hold stage is sintering the 316L stainless steel side at 1200°C. The furnace cycles have been modified after each cycle depending on the result obtained from each cycle. The change in each furnace cycle followed a systematic methodology that changed one level at a time. The total final furnace cycles can be seen in Table 6.2. The samples are cooled inside the furnace, in the gas controlled atmosphere, until they reach the room temperature.

Cycle number	Temp (°C)	Dwell (min)	Temp (°C)	Dwell (min)	Temp (°C)	Dwell (min)	Temp (°C)	Dwell (min)	Temp (°C)	Dwell (min)
1	300	60	600	60	900	120	1080	120	1200	120
2	300	60	600	60	900	120	1080	120	1200	60
3	300	60	600	60	900	120	1080	120	1150	120
4	300	60	600	60	900	120	1080	120	1150	60
5	300	60	600	60	900	120	1080	120	1100	120
6	300	60	600	60	900	120	1080	120	1100	60
7	300	60	600	60	900	60	1080	120	-	-
8	300	60	600	60	900	120	1080	120	-	-
9	300	60	600	60	900	180	1080	120	-	-
10	300	60	600	60	900	240	1080	120	-	-
11	300	60	600	60	900	300	1080	120	-	-
12	300	60	600	60	900	360	1080	120	-	-
13	300	120	600	120	900	120	1080	120	-	-
14	300	120	600	120	900	120	1080	180	-	-
15	300	120	600	120	900	120	1080	240	-	-
16	300	120	600	120	900	120	1080	300	-	-
17	300	120	600	120	900	120	1080	360	-	-
18	300	120	600	120	900	180	1080	180	-	-
19	300	120	600	120	900	180	1080	240	-	-
20	300	120	600	120	900	180	1080	300	-	-
21	300	120	600	120	900	180	1080	360	-	-
22	300	120	600	120	900	240	1080	180	-	-
23	300	120	600	120	900	240	1080	240	-	-
24	300	120	600	120	900	240	1080	300	-	-
25	300	120	600	120	900	240	1080	360	-	-
26	300	120	600	120	900	300	1080	240	-	-
27	300	120	600	120	900	300	1080	300	-	-
28	300	120	600	120	900	300	1080	360	-	-
29	300	120	600	60	900	300	1080	360	-	-
30	300	120	600	180	900	300	1080	180	-	-
31	300	120	600	180	900	300	1080	240	-	-
32	300	120	600	180	900	300	1080	300	-	-
33	300	120	600	180	900	300	1080	360	-	-
34	300	120	600	240	900	300	1080	300	-	-
35	300	120	600	240	900	300	1080	360	-	-
36	300	120	600	300	900	300	1080	300	-	-
37	300	120	600	300	900	300	1080	360	-	-
38	300	180	600	300	900	300	1080	360	-	-

Table 6.2: The various thermal treatment cycles employed for the sintering of multi-material components

6.2 Results and Discussions

6.2.1 Printing Using 0.6mm and 0.1mm Binder Deposition Nozzle.

In the initial phase of the printing experiments, a binder deposition nozzle with a diameter of 600 micrometres was employed for fabricating three-dimensional structures. Subsequent evaluation revealed a pronounced drawback associated with this specific nozzle size. Specifically, it presented challenges in achieving precise edge resolution within the printed components, as depicted in Figure 6.5a. Furthermore, the use of a 0.6-millimeter nozzle resulted in the generation of irregularly shaped droplets, approximately 7.5 millimetres in diameter, upon the powder bed, as illustrated in Figure 6.5b. This issue significantly compromised the reliability and accuracy of the printed parts, impeding the attainment of the requisite level of geometric detail and surface quality. The non-uniform distribution of material along the perimeters of the fabricated objects had adverse repercussions on the overall dimensional accuracy. The irregular shape observed is an outcome of the substantial binder droplets produced by the larger 0.6 mm nozzle.

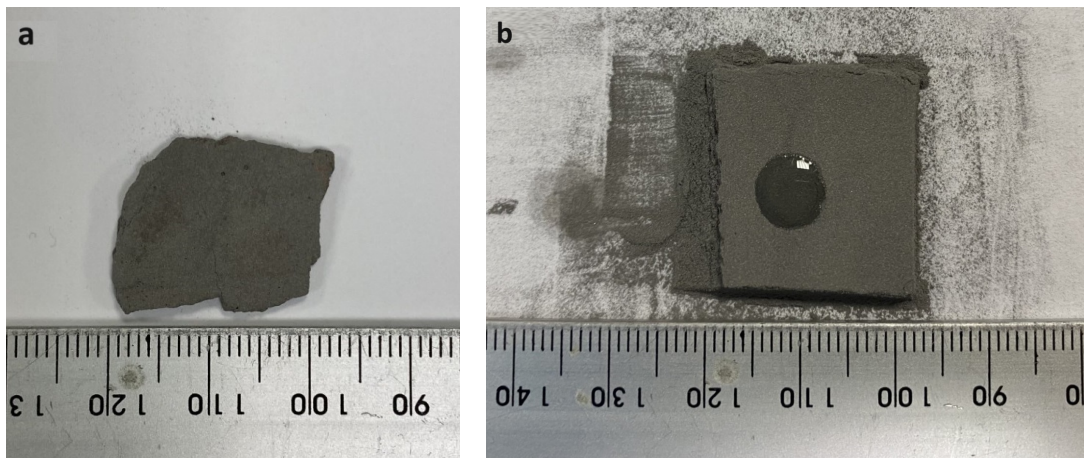


Figure 6.5: (a) Illustrating the weak geometric precision at the sample's edges achieved through the utilization of a 0.6 mm nozzle for PVA binder dispensing. (b) Quantifying the droplet spreading size resulting from the PVA binder dispensing through a 0.6 mm nozzle.

In contrast, the intent was to construct better-defined three-dimensional structures using a 100-micrometer binder deposition nozzle. Consequently, the fabrication of the green part exhibits enhanced precision in replicating details and delicate features, primarily attributable to the utilization of a smaller droplet size. This reduction in droplet size leads to minimise the spreading within the powder bed, as evidenced in Figure 6.6a. The advancement in edge resolution is chiefly ascribed to the diminutive droplet size of the 0.1 mm binder deposition nozzle and its capacity for precise spatial control, enabling more accurate material deposition with reduced dispersion due to the smaller droplet formation of 1.5 mm see Figure 6.6b. The adoption of the 100-micrometer binder deposition nozzle was necessitated by the constraints imposed by available nozzle sizes compatible with the dispensing system. However, an appreciable limitation emerged concerning this specific nozzle size, namely its incapacity to dispense the prepared PVA liquid binder. This challenge is attributed to the notably high viscosity of the liquid binder concerning the restricted outlet orifice diameter of the nozzle, which registers at approximately 3.5 mPa.s at room temperature, with a Z-factor value of 20.6 as detailed in Chapter 5.

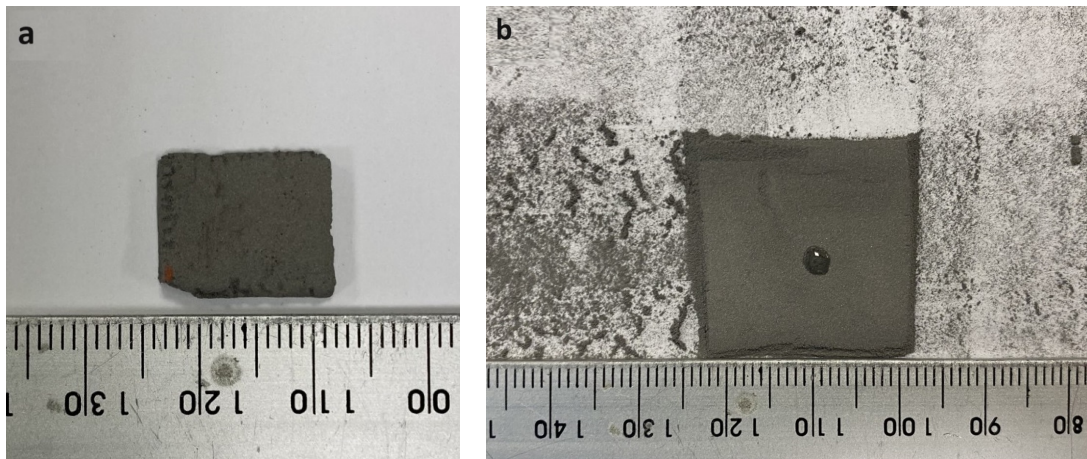


Figure 6.6: (a) Employing a 0.1 mm nozzle has yielded better geometric precision in the green part in comparison to the 0.6 mm nozzle. (b) The use of a 0.1 mm nozzle has resulted in a reduction in droplet spreading size to 1.5 mm.

To overcome this constraint, the binder was subjected to heating, raising its temperature to 45 °C, and subsequently introduced into the binder reservoir for dispensing. This modification allowed for the successful discharge of the binder into the powder bed. The success in binder deposition can be attributed to the reduced viscosity of the liquid binder at 45 °C, which measures approximately 1.9 mPa.s.

The observed irregularities, when using 0.6mm orifice size, can be attributed to the dimensions of the deposition orifice. The larger deposition orifice leads to the formation of a larger tear or bubble when compared to the smaller size, 0.1mm, before leaving the nozzle, thus resulting in a large droplet. These dimensions cause the formation of enlarged zones upon the tear of droplets when they come into contact with the powder bed. These observed irregularities can be also attributed to the phenomenon of jet instability. The term "jet instability" refers to the occurrence of an irregular or disturbed fluid flow or jet when it emerges from a nozzle. These phenomena can give rise to fluctuations, oscillations, or deviations from a state of constant flow. The size of the nozzle is a contributing component that might influence the instability of the flow (161). For this reason, the susceptibility of the PVA liquid binder to this phenomenon is increased when it flows via the large nozzle orifice since it has the potential to lead to the aggregation of larger droplets. Hence, the significant disparity in droplet sizes observed between the 0.6 mm and 0.1 mm nozzles highlights the crucial influence of jet instability on the process of droplet generation. When employing the 0.6 mm nozzle, the increased orifice diameter enabled a greater rate of flow for the PVA binder. However, it further magnified the impacts of jet instability, resulting in the creation of significantly bigger and non-uniformly formed droplets. The existence of these comparatively bigger droplets, measuring up to 7.5 mm in diameter, serves as an indication of how jet instability may have a significant influence and impede the process of droplet production when employing larger nozzles. On the other hand, the utilisation of a 0.1 mm nozzle resulted in the production of more precise and controllable jets, hence reducing the impact of jet

instability, and leading to the formation of smaller and more consistent droplets diameter of 1.5 mm.

6.2.2 Printing Parts in Different Building Directions

The process of printing in the Z axis requires the deposition of the initial layers of 316L powder onto the building platform to establish the foundation for subsequent layers. Subsequently, a levelling mechanism is employed to attain a layer thickness of 200 μm and ensure uniform dispersion of powder particles. The subsequent fundamental stage is the dispensation of liquid PVA binder. The PVA binder droplets effectively infiltrate the powder bed and establish cohesive bonds among the powder particles when being delivered through a specific nozzle. The adhesive characteristics of the binder facilitate the fusion of powder particles, hence enhancing the structural integrity of the product. To obtain the final layer numbers of 316L, it is necessary to repeat these steps. Subsequently, a coating of Cu powder is applied to the printed 316L layers. The powder levelling mechanism, equipped with blades, provides the uniform dispersion of powder by achieving a layer thickness of 200 micrometres. The binder nozzle is responsible for dispensing liquid PVA binder droplets into the powder bed, initiating the bonding process. This procedure should be iterated until the desired length of Cu is achieved. Figure 6.7 shows examples of printed green parts that followed the Z-axis building direction.

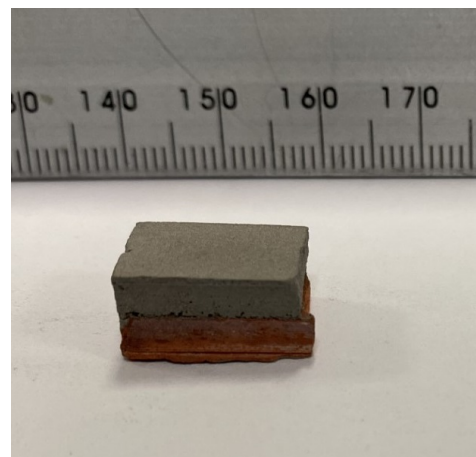
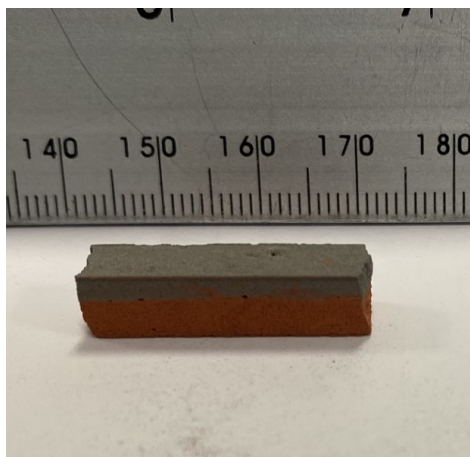


Figure 6.7: Various instances of printed green components that conform to the vertical (Z-axis) building orientation.

The second printing orientation involves the building of multi-material structures along the horizontal (X-Y) axis as seen in Figure 6.8. To initiate this process, the building platform is evenly coated with 316L primary powder material. Subsequently, Cu particles are introduced into a predefined region, strategically filling the voids created by the initial powder deposition, thereby forming a continuous and solid structure. A powder levelling blade is employed to ensure uniformity, maintaining a layer thickness of 200 μm . Proper distribution of the powder is crucial to facilitate effective bonding and adhesion in subsequent stages. The subsequent fundamental step entails the introduction of a PVA liquid binder. PVA droplets are dispensed from the binder nozzle into the designated areas, penetrating the powder bed and initiating the binding process among the powder particles. The holders for both the powder and binder nozzles are incrementally elevated to match the intended layer thickness, allowing for the gradual assembly of the object, layer by layer. This upward movement facilitates the creation of a fresh powder layer for subsequent deposition and bonding. The deposition of the primary powder material, selective dispensing of the secondary powder material, powder levelling, droplet deposition, bonding, and the controlled movement of the nozzle holders are iteratively performed until the 3D model is completely constructed.

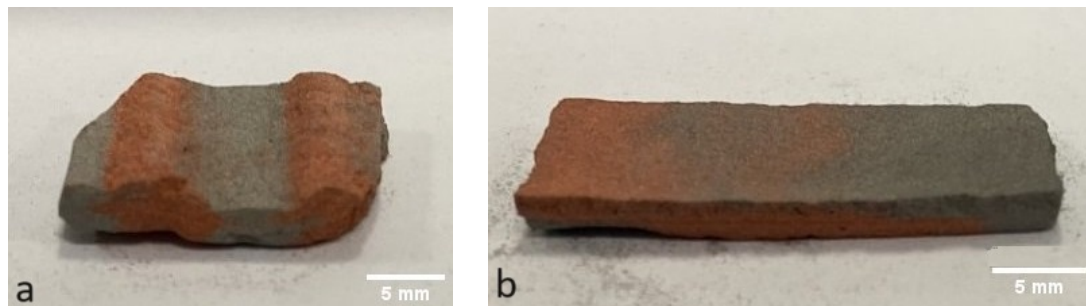


Figure 6.8: Multi-material green parts manufactured in the (X-Y-axis) orientation during. (a) Alternative lines of each material. (b) Building the copper material in a stairs shape.

6.2.3 Curing and Sintering Cycles

Table 6.3 provides a concise overview of the results obtained from an extensive series of 38 sintering cycles. The observations reveal distinct outcomes across the cycles. In cycles 1 and 2, a notable separation between the two materials is evident, with the copper component undergoing shape distortion. Similarly, in cycles 3 through 6, the copper side's structural integrity is compromised. From cycles 7 to 12, instances of material separation persist, while cycles 13 to 26 mark the emergence of incipient interlayer connections between the two materials with raw material powder in the core of the copper side. Notably, in cycles 27 and 28, a discernible improvement in interlayer connection becomes apparent. The trend continues in cycles 30 to 38, with samples displaying a more pronounced and desirable interlayer connection between the materials. Furthermore, these cycles yield promising results in terms of porosity, signifying an important step toward optimizing the sintering process.

Cycle	Geometric integrity
1-2	Separation between the two materials occurred. The copper side lost its shape.
3-6	The copper side lost its shape.
7-12	Separation between the two materials occurred.
13-26	The interlayer connection between the two materials occurred. Insufficient heat at the center of the copper side.
27-28	A better interlayer connection between the two materials occurred.
29	The copper side lost its shape.
30-38	A good interlayer connection between the two materials occurred. Good porosity results were reached.

Table 6.3: The outcomes of different sintering cycles and their impact on the geometric integrity of 3D printed sintered samples investigated in this study.

An observation emerged during the initial phase of the sintering process, where the structural morphology of the copper component underwent a discernible alteration, as illustrated in Figure 6.9a. This transformation displayed a departure from the initial form, wherein the copper material underwent a phase of fusion, subsequently ending in agglomeration, ultimately yielding a spherical copper mass. This outcome was observed to be distinctly separate from the contrasted stainless-steel component. The occurrence of the two-material separation came about as a direct result of the extremely high-temperature levels that were attained during the initial sintering cycle. The temperatures obtained during this cycle were so high that they exceeded the melting point of copper by a significant margin of 120°C. Moreover, the occurrence of this spherical shape could be attributed to the high flow of the argon gas used during the cycle. Then, the sintering cycle went through slight changes as a direct result of these results. In particular, attempts were undertaken to reduce the amount of time that the material was subjected to the highest sintering temperature. The primary purpose was to investigate the possibility that the reduction in dwelling time may affect the results that were found. Inappropriately, this modification to the sintering process has led to the production of the results that were seen during the initial sintering cycle Figure 6.9b, further reduction to the maximum sintering temperature is required.

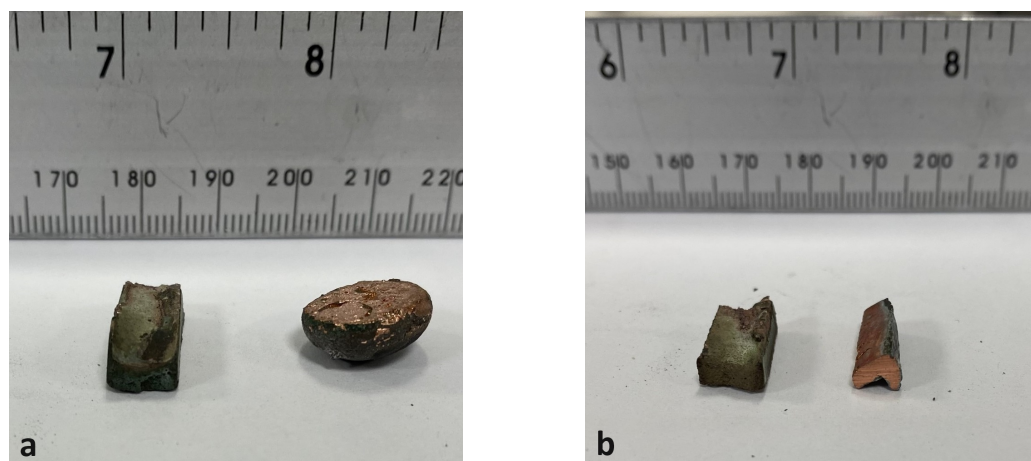


Figure 6.9: Samples subjected to sintering processes at a maximum temperature of 1200°C for varying durations: (a) a duration of two hours, and (b) a duration of one hour.

Subsequently, further refinements were introduced to Sintering Cycle Number 3. One notable adjustment pertained to the reduction of the maximum sintering temperature, which was lowered to 1150°C, and the maintenance of this temperature for a duration of two hours. Nevertheless, despite the earnest endeavours to rectify the issue, the significant problem of pronounced deformations occurring in the copper component remained unresolved, as illustrated in Figure 6.10a. Undesirably, the component underwent substantial degradation, amounting to approximately 70 percent of its original structural dimensions.

Consecutive iterations, in the form of modifications to residence time, were implemented during Cycle Number 4, to address the aforementioned issue, as demonstrated in Figure 6.10b. However, these adjustments proved ineffective in resolving the persistent deformations in the copper component. Nevertheless, the outcomes of these two cycles provide valuable insights into the relationship between the maximum sintering temperature and the structural degradation of the copper component. These experimental results underscore the fundamental role played by the maximum sintering temperature in influencing the structural integrity of the copper component.

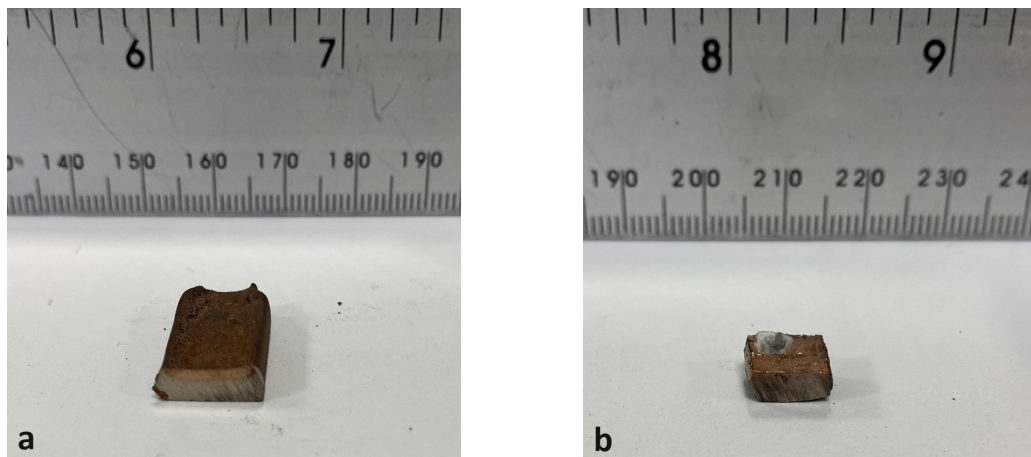


Figure 6.10: Samples subjected to sintering processes at a maximum temperature of 1150°C for varying durations: (a) a duration of two hours, and (b) a duration of one hour.

As a result of these observations, an additional refinement was introduced to the sintering process by slightly decreasing the maximum sintering temperature to 1100°C, a temperature threshold just slightly above the melting point of copper. However, it became evident that even with this adjustment, the copper component continued to undergo discernible structural alterations, resulting in an approximate loss of around fifty percent of its original form, as depicted in Figure 6.11a. These structural changes were directly attributed to the reduction in the maximum sintering temperature.

Notably, the reduction in the sintering temperature, coupled with a decrease in the material's dwell time to a mere sixty minutes, did not prove to be adequate in mitigating the undesired deformation, as illustrated in Figure 6.11b. The persistent structural changes in the copper component, despite these adjustments, underscore the relationship between sintering parameters and the preservation of the component's original form. These findings emphasize the critical importance of optimizing the sintering process to achieve the desired structural outcomes in copper components.

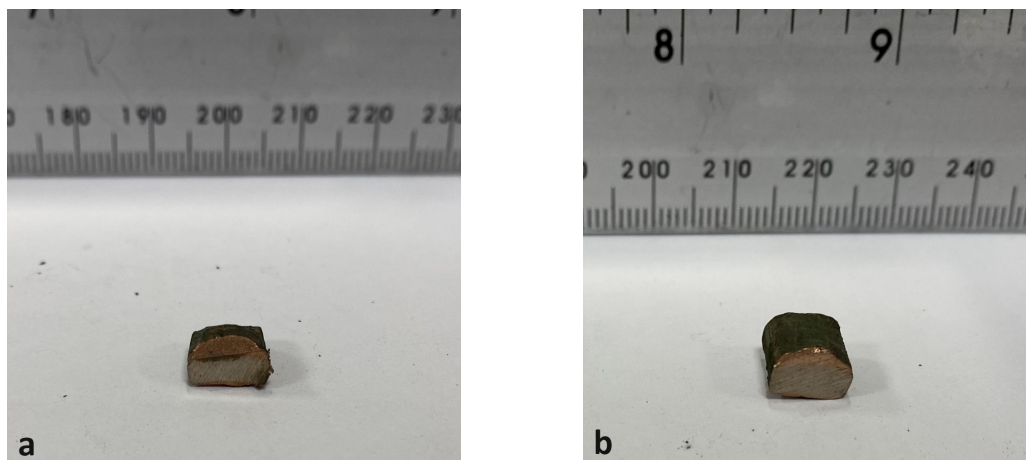


Figure 6.11: Samples subjected to sintering processes at a maximum temperature of 1150°C for varying durations: (a) a duration of two hours, and (b) a duration of one hour.

This loss of copper structural shape can be attributed to the excessive sintering phenomenon, also referred to as over-sintering. Excessive sintering is sintering the material above the melting temperature, and it can result in the collapse of the structural shape of the sintered component. This finding unequivocally highlights the presence of a limit for the sintering process, beyond which further progression is not needed. Consequently, in the subsequent cycle, an adjustment has been made by reducing the maximum attainable temperature to 1080°C. This modification aimed at preventing the undesirable consequences of over-sintering and promoting the preservation of the copper material's structural integrity.

Undesirably, the next total of six attempts to sinter the multi-material samples, spanning cycles 7 through 12, met with failure, primarily attributed to the issue of separation between the 316L stainless steel and the copper components, as visually represented in Figure 6.12. This recurrent challenge in achieving a successful sintering process underscores the complex nature of bonding dissimilar materials and the necessity for further investigation and refinement to address this critical issue.

In Figure 6.12, the predominant factor influencing the observed behaviour can be attributed to the inherent disparities in the thermal properties of copper and stainless steel. Copper exhibits a significantly higher thermal conductivity, measuring 398 W/mK, as compared to stainless steel, with a lower value of 15 W/mK (162) (163).

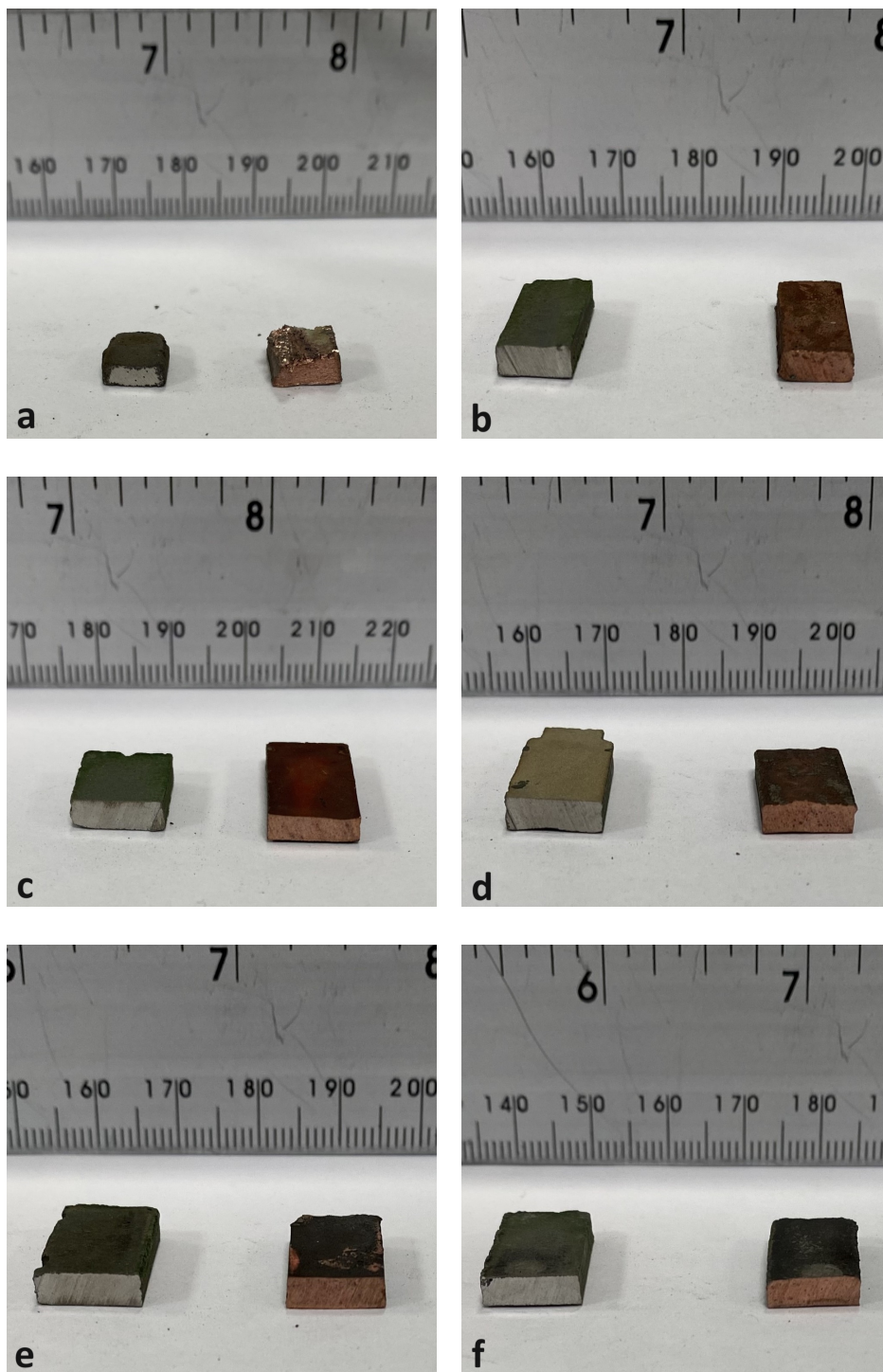


Figure 6.12: The separation of the two different materials because of low dwelling time. (a) Represents Cycle 7, where the dwell time at 900°C is set at 60 minutes. (b) Cycle 8, where the dwell time at 900°C is extended to 120 minutes. (c) Cycle 9, with a dwell time of 180 minutes at 900°C. (d) Cycle 10, with a 240-minute dwell time at 900°C. (e) Cycle 11, where the dwell time at 900°C is prolonged to 300 minutes. (f) Represents Cycle 12, with a 360-minute dwell time at 900°C.

Accordingly, these distinctive thermal properties lead to discernible variations in the thermal response rates exhibited by both materials during the sintering processes. The marked disparity in thermal conductivity between copper and stainless steel gives rise to dissimilar heating and cooling behaviours. Consequently, the intermolecular connections between these disparate materials may exhibit relatively reduced strength, thus contributing to the observed separation phenomenon.

Additionally, it is important to take into account the other phenomena of the differential thermal expansion that occurs between copper and stainless steel. These materials demonstrate different coefficients of thermal expansion, indicating that they undergo expansion and contraction at different rates in response to temperature fluctuations. When subjecting two bars—one stainless steel and the other copper—to high temperatures, a noticeable contrast emerges: the copper bar demonstrates a more pronounced thermal expansion than its steel counterpart. Accordingly, the stainless-steel component resists this differential expansion exhibited by the copper element. The difference in thermal expansion characteristics might potentially lead to the fact of separation, as the materials may fail to sustain a unified bond when subjected to these sintering cycles. Thus, in a determined endeavour to resolve the problem of the observed separation between the 316L stainless steel and the copper in the cycles 7 through 12, the residence time at 900°C was progressively increased by 60 minutes in each succeeding cycle. This was done to reduce thermal stress which involves controlling the rate of temperature change to minimize thermal gradients and the associated residual stresses that can develop in a material. It is a common strategy in materials processing to prevent deformation, cracking, or delamination due to thermal expansion and contraction disparities in dissimilar materials or components (164). Nevertheless, the structural integrity of the components that were sintered did not improve as a result of these enhancements to the extent that was intended. A later adjustment to the sintering procedure was made to address the ongoing problem of thermal stress of the multi-material samples throughout the sintering process.

In an endeavour to address the recurring challenge of separation between the copper and stainless-steel elements, a strategic modification was implemented in the sintering protocol. This modification entailed the incorporation of prolonged dwell times at two distinct temperature thresholds, namely 300°C and 600°C, which were incrementally and cyclically applied across cycles 13 through 26. This adaptive approach sought to optimize the sintering conditions to enhance the bonding between the dissimilar materials.

However, in cycle 13, it is apparent that the thermal distribution is not adequately encompass the central region of the copper component, as visually depicted in Figure 6.13. This observation highlighted a critical deficiency in the sintering process, wherein the temperature distribution failed to achieve uniformity across the entire copper component. Such non-uniform heating can significantly impact the quality and integrity of the sintered product, emphasizing the need for further refinement and optimization of the sintering methodology to attain the desired material characteristics. This non-uniform heating is caused by a rapid heat and solidification of the boundaries of the components make it hard for the heat to reach the core of it. Thus, this observed issue of non-uniform heat distribution can be attributed to a phenomenon previously explained by Bello et al (165). In their research, they expounded upon the occurrence wherein the surface temperature reaches its peak, subsequently facilitating an accelerated formation of the thermal boundary layer. This expedited thermal boundary layer development primarily stems from buoyancy effects, which are a direct consequence of the non-uniform distribution of heat within the sintering environment. Consequently, these findings underscore the critical importance of addressing non-uniform heat distribution as a fundamental aspect of optimizing the sintering process to achieve uniform material properties and structural integrity.

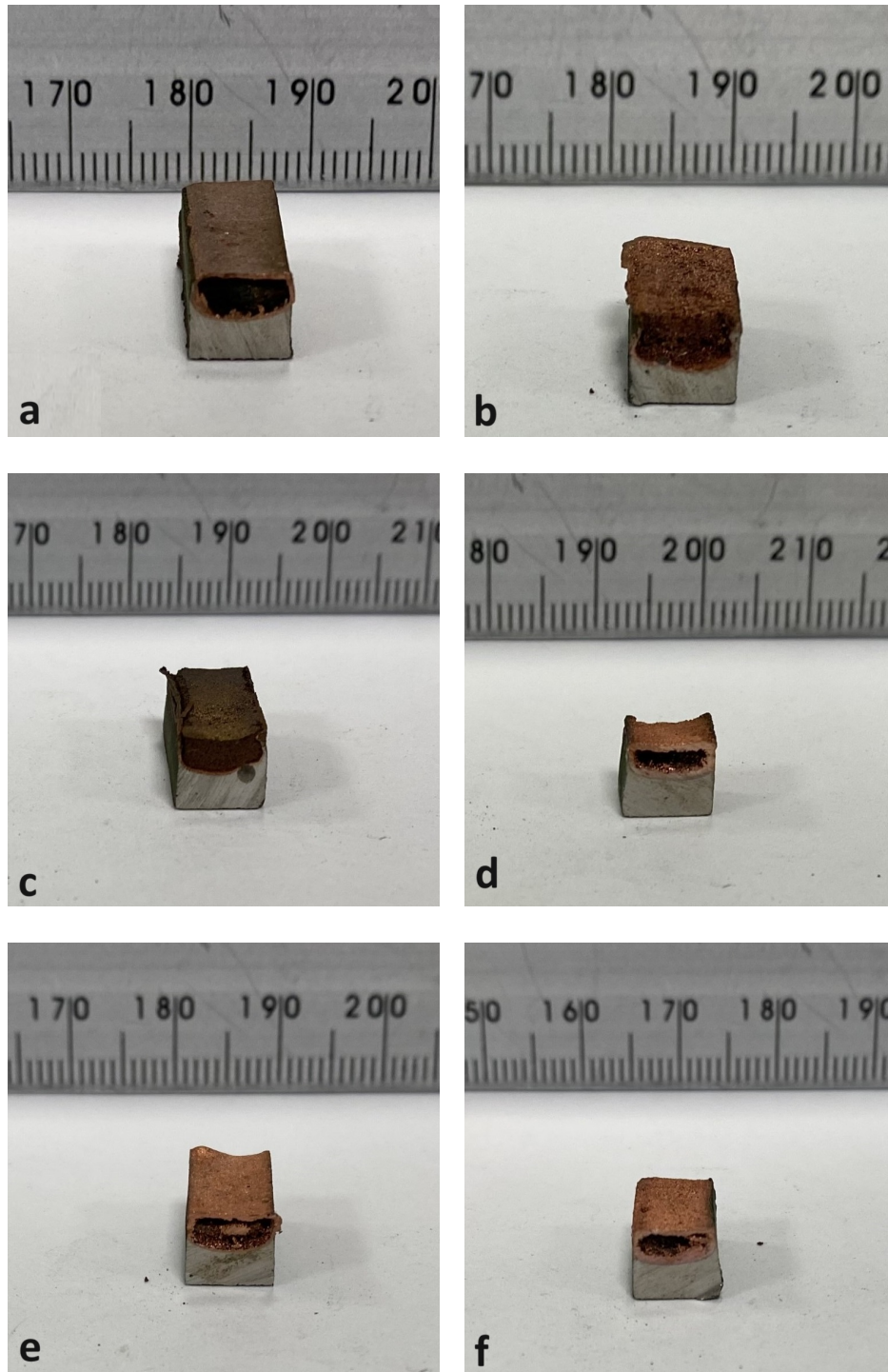


Figure 6.13: The effect of the non-uniform heat distribution on the copper side. (a) Cycle 15, with dwell times of 120 minutes at 900°C and 240 minutes at 1080°C. (b) Cycle 17, is characterized by dwell times of 120 minutes at 900°C and 360 minutes at 1080°C. (c) Cycle 19, features dwell times of 180 minutes at 900°C and 240 minutes at 1080°C. (d) Cycle 21, is marked by dwell times of 180 minutes at 900°C and 360 minutes at 1080°C. (e) Cycle 23, with dwell times of 240 minutes at 900°C and 240 minutes at 1080°C. (f) Cycle 25, is defined by dwell times of 240 minutes at 900°C and 360 minutes at 1080°C.

Next, a systematic approach was employed to address the persistent issue of uneven heat distribution in the following sintering cycles. This adjustment strategy entailed the progressive extension of dwelling times at three specific temperature thresholds: 600°C, 900°C, and 1080°C. The overarching goal of these adjustments was to ensure that the thermal energy was more effectively and uniformly distributed throughout the copper element, thereby rectifying the prior underserved regions.

Notably, it was not until the commencement of cycle 27 that these adjustments yielded significant improvements, as displayed by the successful resolution of the uniform heat distribution, as visually represented in Figure 6.14a. Cycle 28, after cycle 27, was orchestrated to improve the porosity results achieved in the preceding cycle, as represented in Figure 6.14b. Afterward, in cycle 29, an effort was made to lower the time at the temperature to 600°C in order to shorten the overall duration of the furnace cycle. Unfortunately, this adjustment proved unsuccessful, as the copper side once again lost its shape, mirroring the issue observed in the initial 6 cycles. Furthermore, the pursuit of enhanced part density prompted modifications in cycles 30 and beyond, characterized by an increase in the dwell time at 600°C to make it 180 min. This strategic augmentation was intended to further optimize the material's density and structural properties, marking a fundamental phase in the continuous endeavour to enhance the sintered components' quality and performance.

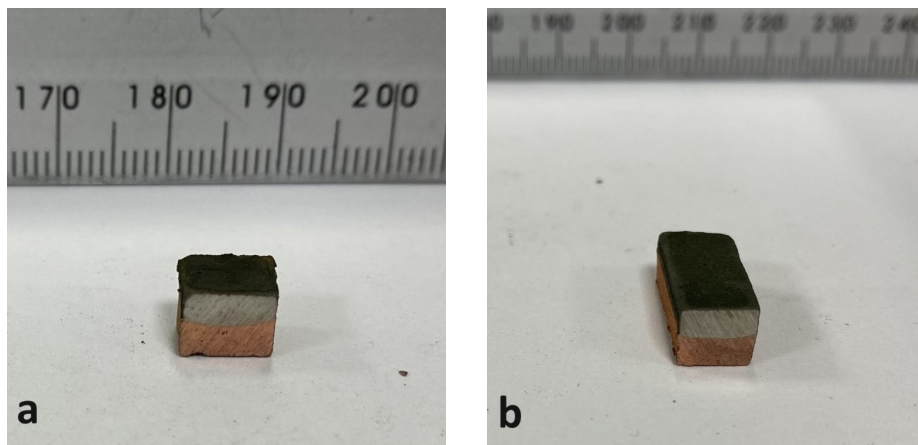


Figure 6.14: The consecutive cycles demonstrate the commitment to enhancing the quality of the components. (a) Cycle 27 marked a significant improvement in achieving uniform heat distribution. (b) Cycle 28 aimed to improve the porosity results of the previous cycle.

6.3 Conclusions

In this chapter, two separate nozzle sizes, 0.6 and 0.1 mm have been used to dispense PVA binder subjected to pressure to examine the droplet size. The nozzle with a diameter of 0.1 mm generated droplets with a diameter of roughly 2.5 mm, which is much smaller than the droplets produced by the nozzle with a diameter of 0.6 mm, which had a diameter of approximately 7 mm. Thus, the 0.1 mm nozzle has been used in building structures in different building directions and has been used in all of the 3D printing throughout this research. Furthermore, an extensive series of 38 sintering cycles undertaken in this chapter has shed light on the interplay of parameters in the sintering process, specifically concerning the interaction between copper and stainless-steel components. The initial sintering cycle exposed a phenomenon in which the copper component underwent significant structural changes, losing its original shape. This transformation was ascribed to the substantially elevated temperatures, higher than the copper's melting point by 120°C also called over-sintering. While subsequent modifications to the sintering cycle were introduced to mitigate these effects, the results showed a recurring pattern. Adjustments to temperature and dwelling times were insufficient to wholly rectify the issue, with the copper component continuing to undergo undesirable deformations, raising concerns about the structural integrity of the sintered parts. Notably, challenges of heat distribution and interlayer connection between copper and stainless steel emerged as focal points of concern. It was only through a careful and iterative process of temperature and dwelling time adjustments that the issues of heat distribution and structural integrity began to be addressed. Extended dwelling times at specific temperature points, particularly 600°C, 900°C, and 1080°C appeared to be instrumental in mitigating these concerns.

Chapter 7. Evaluation of Porosity in Sintered Parts

7.1 Introduction

Porosity is a phenomenon characterised by the presence of cavities or voids dispersed throughout the volume of a sample, resulting in affecting the final density of the sample bulk. Pores can result in stress concentration, reduction in the loading area, and the initiation and propagation of cracks (70) (71). This occurrence, of cavities and voids, has been recognised as a significant difficulty encountered in the context of various manufacturing processes (72). The formation of cavities and voids in the manufacturing processes is attributed to the entrapment of gaseous impurities released from the molten metal reservoir during solidification (73). In the BJ process, significant influence of the holding time and sintering temperature on the final parts' densities. The duration of holding time required for best results is dependent on the sintering temperature since distinct processes drive the densification process at different temperature. In addition, in some cases, when the inert gases are used in the sintering atmosphere, gases can become trapped within the material as it undergoes densification, leading to the formation of pores or voids. This gas entrapment can compromise the density of the sintered part. Therefore, adjusting sintering parameters such as temperature and dwell time can help mitigate gas entrapment.

This chapter presents an examination of the outcomes of the sintering cycles applied to the multi-material samples using the BJ. The objective of this chapter is to provide clarification on the porosity results related to the multi-material sintering. The porosity of the sintered samples that did not lose their shapes or separated in Chapter 6 will be examined. Table 7.1 shows the cycles which contribute to the porosity study. Cycles from 1 to 4 have been abandoned due to their results that show a loss of structural integrity. Furthermore, cycles from 5 to 12 have also been neglected due to the separations that occurred in these cycles. Also, cycle 29 has been overlooked due to its results as seen in Table 6.2 and Table 6.3.

Cycle number	Temp (°C)	Dwell (min)	Temp (°C)	Dwell (min)	Temp (°C)	Dwell (min)	Temp (°C)	Dwell (min)
13	300	120	600	120	900	120	1080	120
14	300	120	600	120	900	120	1080	180
15	300	120	600	120	900	120	1080	240
16	300	120	600	120	900	120	1080	300
17	300	120	600	120	900	120	1080	360
18	300	120	600	120	900	180	1080	180
19	300	120	600	120	900	180	1080	240
20	300	120	600	120	900	180	1080	300
21	300	120	600	120	900	180	1080	360
22	300	120	600	120	900	240	1080	180
23	300	120	600	120	900	240	1080	240
24	300	120	600	120	900	240	1080	300
25	300	120	600	120	900	240	1080	360
26	300	120	600	120	900	300	1080	240
27	300	120	600	120	900	300	1080	300
28	300	120	600	120	900	300	1080	360
30	300	120	600	180	900	300	1080	180
31	300	120	600	180	900	300	1080	240
32	300	120	600	180	900	300	1080	300
33	300	120	600	180	900	300	1080	360
34	300	120	600	240	900	300	1080	300
35	300	120	600	240	900	300	1080	360
36	300	120	600	300	900	300	1080	300
37	300	120	600	300	900	300	1080	360
38	300	180	600	300	900	300	1080	360

Table 7.1: The operational cycles were chosen based on their optimal geometric attributes, and their impact on porosity was systematically evaluated.

7.2 Results and Discussions

This chapter presents a thorough examination of the outcomes of the sintering cycles applied to the multi-material samples using the Binder Jetting technique. The objective of this chapter is to provide clarification on the experimental results, provide an understanding of the fundamental mechanisms involved, and provide an analysis of the difficulties and potential advantages related to multi-material sintering. This study aimed to examine and delineate the impact of diverse sintering cycles on the porosity characteristics of a multi-material specimen. The systematic evaluation of porosity variations across distinct sintering cycles was undertaken to understand the relationship between key sintering parameters and the resulting porosity profile of the material. This investigation thus sought to contribute to a deeper understanding of the interplay between various sintering conditions and the resultant material porosity, providing valuable insights for optimizing sintering processes in the context of multi-material specimens. Table 7.2 presents an overview outlining the effects of various sintering cycles on the porosity levels of the binder jetted samples that have been built using the same building parameters. To be more precise, the table presents the results of the different sintering cycles showing the porosity results for each material (316L stainless steel and copper) and the porosity results of the multi-material samples. The porosity measurements were conducted on multi-material samples. However, individual images were captured for each side to facilitate separate analysis. The Porosity maps of the cross-section have been done to delineate the locations of the pores within the objects. Three different porosity samples have been taken for each cycle to examine the porosity values. The average values of the three different samples have been taken, as shown in Table 7.2. The purpose of this presentation is to clarify the specific effects of different thermal treatment procedures on the macroscopic characteristics of the produced components.

Cycle Number	Temperature - Time Integral (°C*h)	Porosity of the 316L (%)	Standard Deviation	Porosity of the Cu (%)	Standard Deviation	Multi-material Sample porosity (%)
13	5760	32.6	0.46	90.8	0.27	63.65
14	6840	23.7	0.14	87.6	0.73	55.6
15	7920	24.9	0.19	77.7	0.28	51.3
16	9000	22.3	0.08	69.5	0.16	45.85
17	10080	21.4	0.15	34.2	0.29	27.75
18	7740	30.9	0.14	80.9	0.18	55.9
19	8820	23.4	0.30	31.3	0.25	27.35
20	9900	19.7	0.14	27.2	0.16	23.4
21	10980	17.6	0.17	24.4	0.20	21
22	8640	22.8	0.14	32.5	0.11	27.65
23	9720	19.6	0.87	27.7	0.12	23.65
24	10800	16.8	0.20	25.7	0.32	21.2
25	11880	12.2	0.14	18.4	0.18	15.25
26	10620	10.7	0.12	16.6	0.19	13.65
27	11700	8.2	0.17	10.8	0.39	9.45
28	12780	7.6	0.48	9.1	0.10	8.3
30	10140	9.2	0.14	8.7	0.14	8.95
31	11220	7.3	0.10	8.9	0.90	8.1
32	12300	7.2	0.20	7.8	0.27	7.45
33	13380	6.2	0.45	6.1	0.27	6.15
34	12900	5.5	0.36	5.1	0.34	5.25
35	13980	4.7	0.60	3.7	0.39	4.15
36	13500	4.6	0.47	3.5	0.44	4.05
37	14580	4.1	0.19	3.3	0.28	3.65
38	14880	2.4	0.30	2.7	0.17	2.6

Table 7.2: The influence of the selected sintering cycles, based on their favorable geometric integrity outcomes, on the porosity characteristics of both materials was examined.

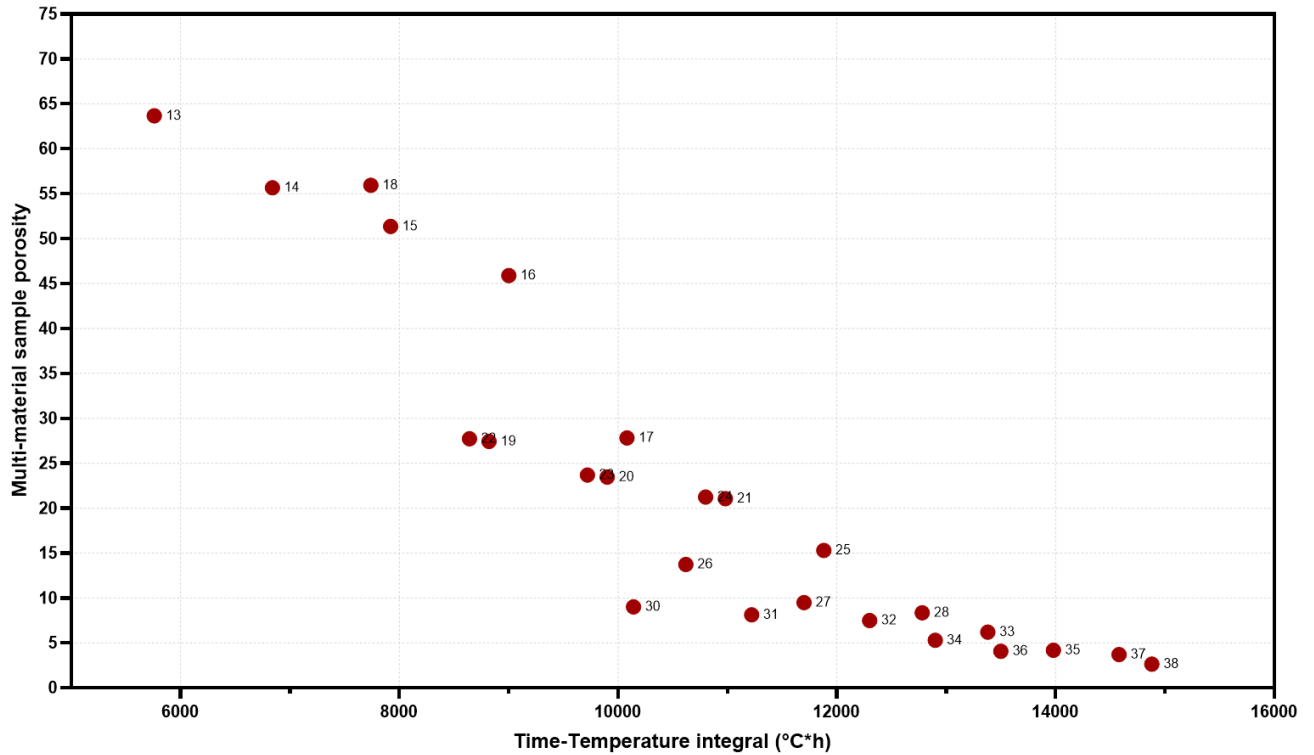


Figure 7.1: The systematic evaluation of porosity variations across discrete sintering cycles was undertaken to show the interplay between sintering parameters and the resultant porosity of the material.

Figure 7.1 illustrates the systematic examination of the full part porosity fluctuations throughout different temperature-time integral ($^{\circ}\text{C}\cdot\text{h}$). This analysis was conducted to understand the interplay between critical sintering parameters and the ensuing porosity characteristics exhibited by the material under investigation. The result of the porosity illustrates that the holding times and temperatures have a direct effect on the porosity results of the binder material as well as each metallic material. Notably, instances were observed where a reduced temperature-time integral led to an increased porosity value, contrasting with scenarios where a prolonged temperature-time integral corresponded to diminished porosity values in the context of the 3D-printed samples.

On cycle number 13, it becomes apparent that the heat distribution does not fully cover the core area of the copper surface, as seen in Figure 7.2. The observed event can be attributed to the phenomena of non-uniform heat distribution, as discussed by Bello et al (165). This phenomenon involves the achievement of maximum surface temperatures, which subsequently enhances the development of a thermal boundary layer. The rapid advancement of this layer is mostly attributed to buoyancy effects caused by the uneven distribution of heat. Thus, in cycle 13, the copper boundary layers have acted as a barrier, preventing efficient heat transfer to the centre due to the thermal conductivity. Similarly, Munitz et al (166) conducted a study to weld copper and stainless-steel tubes. The author revealed that the high thermal conductivity of the copper poses an issue when subjected to heat due to the dissipation of most of the heat input. Furthermore, Sung et al (78) have carried out an experiment where different sintering cycles have been used to sinter stainless steel specimens. The authors indicated that the sintered specimen at a temperature of 900°C represents the adhesion phase of the sintering process due to a lack of heating temperature. Thus, additional heat is required to effectively sinter the copper. In addition, the occurrence of blocking an effective flow of heat to the core of the copper side can be attributed to the binder residue that may get trapped in the middle of the material block. If there is any residual binder material trapped within the copper layers, it can hinder heat transfer and prevent proper sintering as porosity causes structural disruptions in the material that impede heat transfer, it reduces heat transfer efficiency. This happens as a result of heat-carrying particles like molecules or phonons being prevented from moving freely in porous materials by their voids. To further reduce thermal conductivity, trapped air within the pores serves as an insulator. It is of great importance that the binder material is adequately removed from the printed part before sintering. To overcome these problems, sintering parameters such as temperature and time may need to be adjusted to ensure proper heat distribution and sintering throughout the entire multi-material

sample. Experimenting with different sintering conditions could help address this issue.

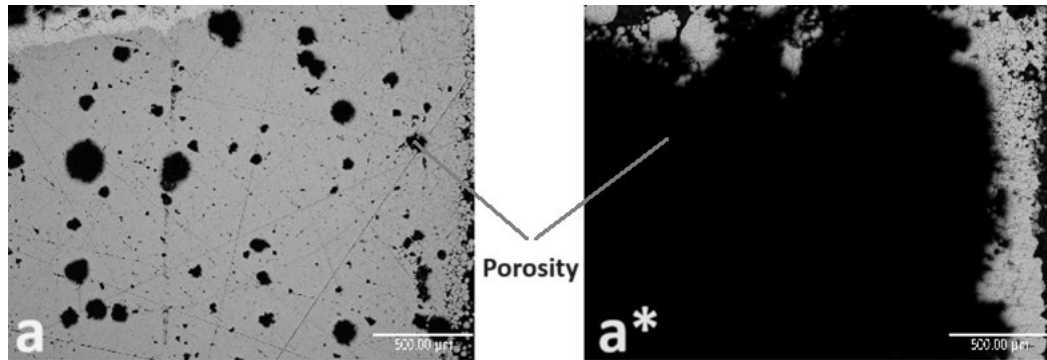


Figure 7.2: Micrographs of the sintered specimens showing the high rate of porosities as the black portions is the porosity. (a) the stainless-steel side and (a*) the copper side and the non-uniform heat distribution that prevents efficient heat transfer to the center of the copper side.

Subsequently, a systematic approach was adopted to rectify this issue by adjusting the sintering conditions in each cycle. This adjustment primarily involved extending the dwelling time at 600°C, 900°C, and 1080°C sequentially to ensure that heat diffusion reached the previously underserved portions of the copper element. It appears to be certainly possible that the issue of incomplete sintering in the central area of the copper layers has been resolved as a result of extending the dwelling time in the sintering cycle from 14 to 23 at 900°C and 1080°C Figure 7.3 and Figure 7.4. The figures show that the porosity rates at the copper side dropped from 90% to 27%, from cycle 14 to cycle 23. These high porosity results were a result of the lack of heat transfer to the middle point of the samples as the heat melts the outer surface of the sample leaving the middle powder in raw condition, which has been improved throughout the cycle adjustments. Increasing the amount of time that the material is left in a certain temperature range results in improved thermal diffusion. This is of utmost significance concerning materials such as stainless steel and copper that have different heat conductivity values. Because the sample was allowed to remain at the temperature for a longer time, the heat was able to go deeper into the material and

reach the core of the copper layers. Densification takes place as a result of the material remaining at the sintering temperature for a longer time. This is critical for creating a consistent multi-material structure and lowering the possibility of voids or incomplete sintering in the centre. It is also important for achieving a uniform structure. Additionally, temperature homogenization of longer residence durations assists in providing a more uniform distribution of temperature over the entirety of the sample. The developments in cycles 14 to 23 have assisted in ensuring that the desired sintering temperature is reached and maintained across the entirety of the sample, including the centre of the copper layers. Furthermore, extending the dwelling time at lower temperatures, such as 600°C, will help guarantee that the binder is completely burned away. There should be additional time allowed for the removal of any remaining binder residual. This is necessary to achieve effective sintering and to prevent any flaws that may occur.

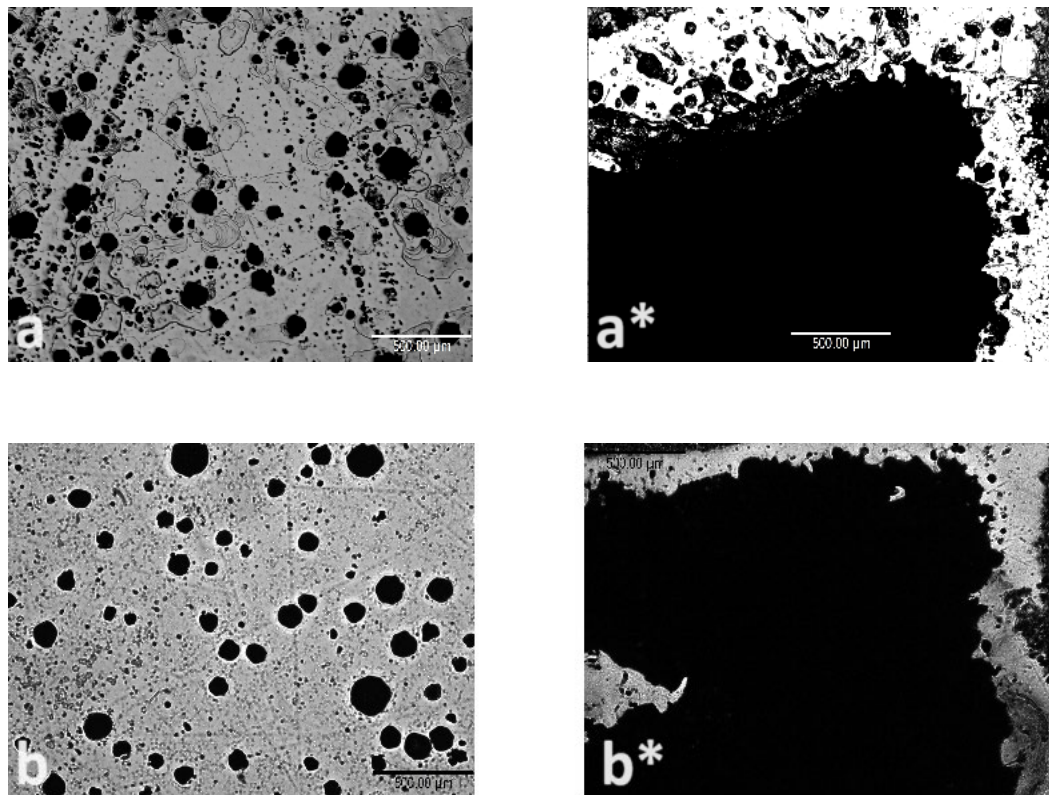


Figure 7.3: Visualization of microscopy images as the black portions is the porosity. (a, b) for the stainless-steel side and (a*, b*) for the copper side, highlights alterations in the uniformity of heat distribution achieved through the adjustment of sintering cycles. The accompanying figure additionally illustrates variations in

porosity on the copper side, transitioning from (a) with a porosity value of 90% to (b*) with a reduced porosity of 69%."*

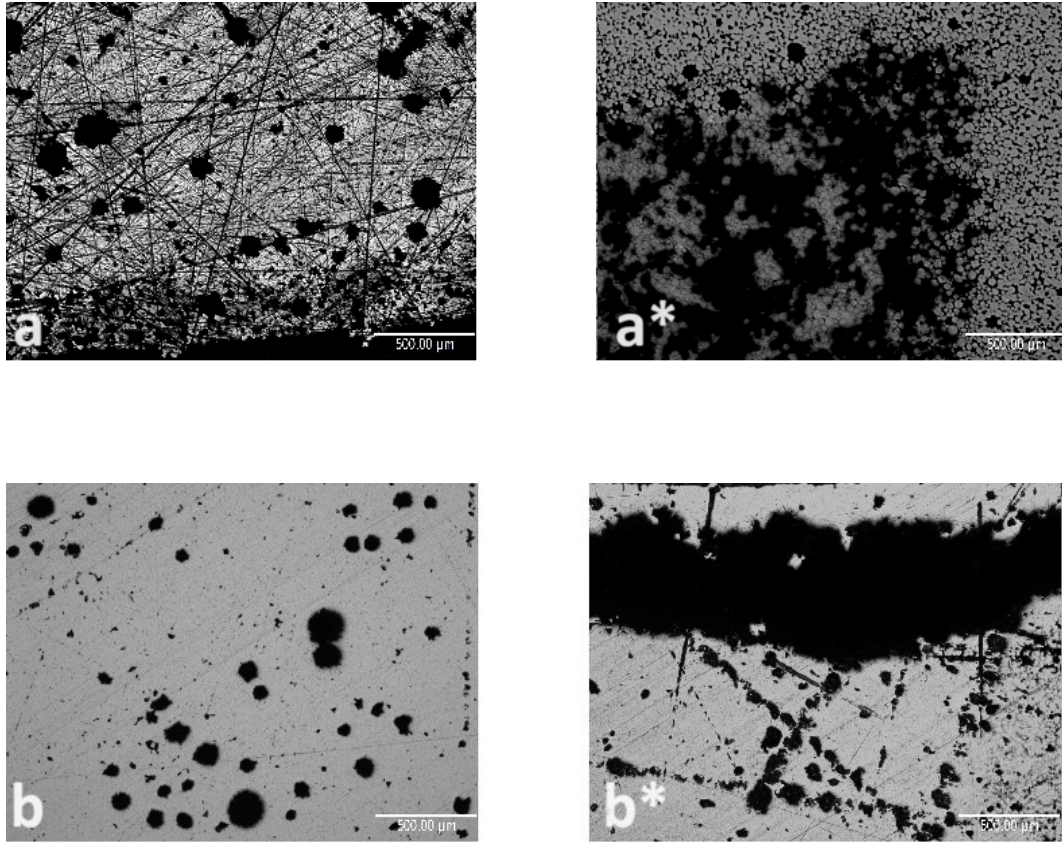


Figure 7.4: Microscopic imagery as the black portions is the porosity. (a,b) for the stainless-steel side and (a,b*) for the copper side, serves to show the enhancements in uniform heat dispersion resulting from the adjustment of sintering cycles. The presented figure further shows the consequential improvements in porosity, wherein the copper side exhibits a noteworthy transition from (a*) featuring a porosity of 34% to (b*) with a reduced porosity value of 27%.*

Figure 7.5 shows the improvement in the porosity values (a) the stainless-steel side and (a*) the copper side throughout modifying sintering cycles (cycles 24,25 and 26). Increasing the dwell time to 240 min at 900°C, and 1080°C in the previous sintering cycles provides more binder burnout, enhanced thermal diffusion, and better temperature homogeneity. It can be seen that the heat has uniformly reached the core area of the copper side resulting in fully melting powder particles. These increases in the dwelling times have allowed the sintered parts to enhance additional thorough binder burnout period, improved thermal diffusion between the two materials, and better temperature homogeneity. As a result of the previously added values working together, the sintering of the multi-material samples has been consistent and thorough, guaranteeing that the core region of the copper layers has been sintered. The accomplishment in cycle 24 onwards indicates a significant development in this study, highlighting the significance of optimising sintering conditions to enhance the interfacial interactions between materials that are different in nature. The use of solid-state diffusion principles presents a promising approach to attain good bonding and minimise porosity in sophisticated manufacturing techniques, hence holding prospective consequences for diverse industrial sectors that want dependable and long-lasting material connections. As a result of the adjustments to the cycles, a notable achievement can be seen in lowering the porosities values from 16.8% to 10.8% and from 27% to 16.6% for the stainless-steel side and the copper side respectively. The findings of the aforementioned study match the work made by Kumar et al (149) on copper. Specifically, the authors were able to achieve a porosity level of 16.4% by subjecting the binder jetted sample to a sintering cycle at a maximum temperature of 1075°C for three hours.

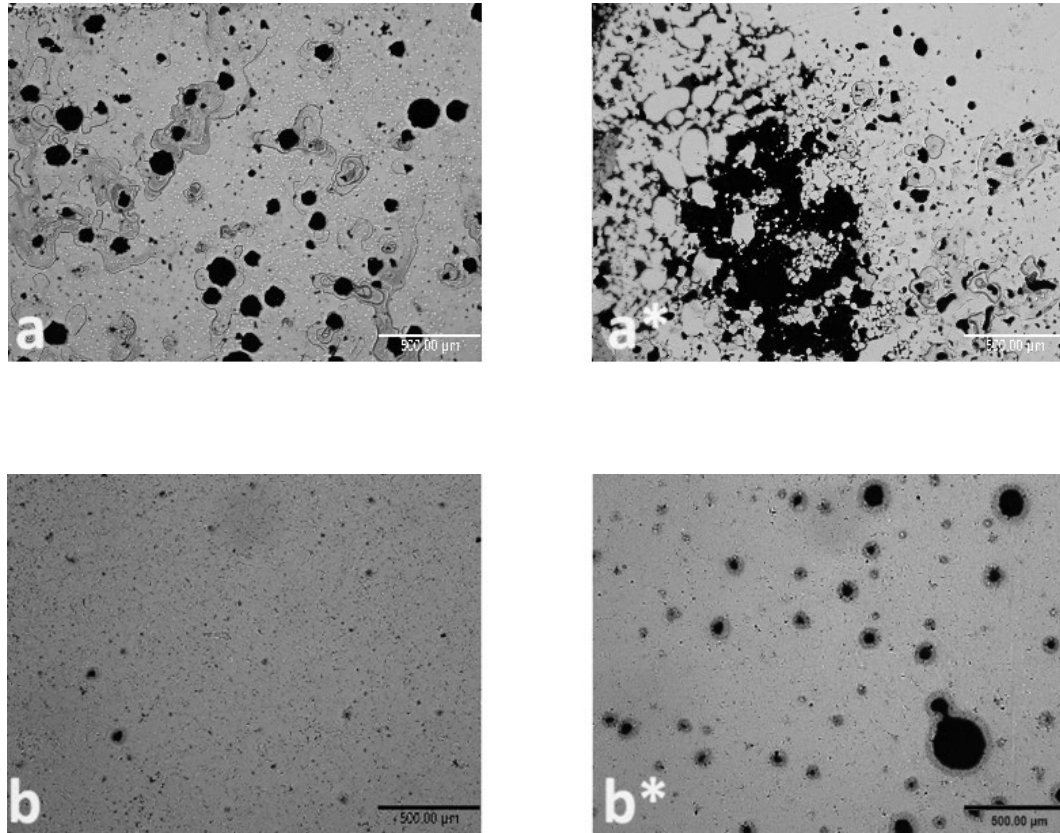


Figure 7.5: Consequent to the modifications made to the operational cycles, a significant reduction in porosity levels is discernible as the black portions is the porosity, with values decreasing from 16.8% in (a) to 10.8% in (b) for the stainless-steel side and from 27% in (a*) to 16.6% in (b*) for the copper side.

In the progression of the sintering cycles, a noticeable improvement in addressing the issue of uneven heat distribution became more evident in cycle 27, as observed in Figure 7.6. This amelioration has demonstrated a milestone in the resolution of the heat distribution problem where the porosity values have decreased from 10.8% to 8.1% and from 16.6% to 10.8% for the stainless-steel side and the copper side respectively in cycle 27. In response to the adjustment in the dwelling duration, which has been lengthened from 240 to 300 minutes, at the highest temperature of 1080°C, these changes have been applied. Because of this change, there is now more time for an even distribution of heat throughout the multi-material component, as well as an extended period to improve thermal diffusion. Similarly, bai et al (157) have explored the sintering temperature and hold time of binder jetted copper parts. The result of

porosity when sintering the copper at 1080°C for four hours was 9% which is relatively close to the porosity result in cycle 27. Additionally, Pan et al (167) have conducted a study to investigate the influence of holding time during the sintering process. The study concluded that there is an inverse relationship between the sample porosity values and the holding time during the sintering process. When the authors tested six different holding times at the maximum temperature that was used, the porosity value of the highest holding time was reported as the lower porosity value among the six samples due to the uniform heat distribution.

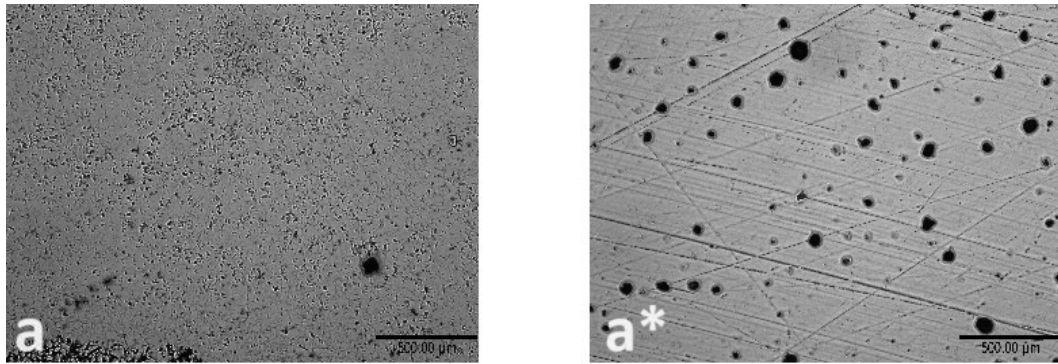


Figure 7.6: Microscopy pictures showing the improvement in the porosities as the black portions is the porosity. (a) the stainless-steel side and (a*) the copper side throughout modifying sintering cycles.

The subsequent cycle 28, which followed the successful adjustments of the previous cycle 27, was specifically designed to yield better porosity results, as depicted in Figure 7.7. The difference that the results of cycle 28 have made is slight improvements in the porosity values, decreasing from 8.1% to 7.6% and from 10.8% to 9% in the stainless-steel side and the copper side respectively. These enhancements have been made as a result of a change in the dwelling time, which has been increased from 300 to 360 minutes at the maximum temperature of 1080°C. This has led to an increase in the amount of heat distribution within the multi-material part as well as a more enhanced thermal diffusion. This improvement in outcomes, which was observed, is in agreement with the findings that were obtained

by Pan et al (120), which showed that an increase in holding time correlates with a reduction in porosity. Therefore, to achieve a more reduced part density, a deliberate extension of the duration at 600°C was characterised by cycles 30 and beyond. This was done to achieve more time to guarantee a complete binder burnout before moving on to the temperature at which the copper is sintered.

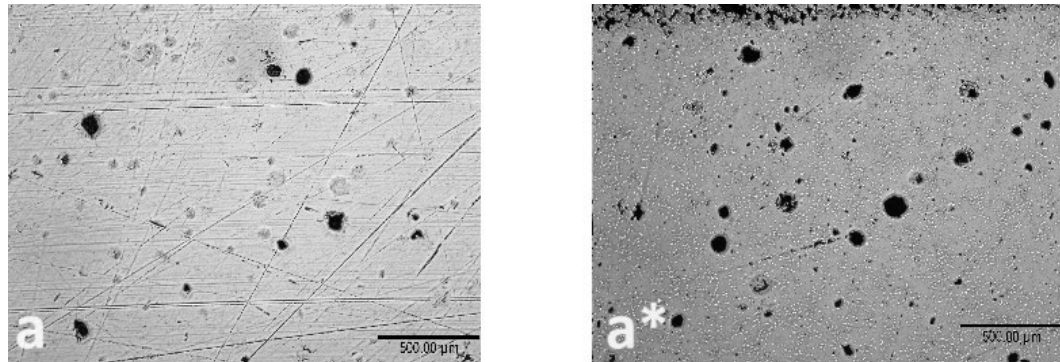


Figure 7.7: Microscopy micrographs of the sintered specimens showing the reduction in the porosity values in (a) the stainless-steel side and (a*) the copper side.

The results of cycle 30 were very similar to the patterns that were observed in cycles 27 and 28, with only very slight variations from the pattern that was anticipated. By giving careful consideration to the dynamics of the sintering process, it is possible to shed light on these variations. A reduction in the maximum temperature's holding duration from 360 to 180 minutes may be responsible for the higher porosity that was observed on the stainless steel side. This change in the dwelling time had a direct impact because it reduced the amount of time during which stainless steel could experience significant particle rearrangement and densification, which led to an increase in porosity in the end.

On the other hand, the fact that the copper side had a lower porosity than the previous cycle indicated a sintering response that was more favourable. Copper, being a material with a lower melting temperature than stainless steel, may have adapted better to the altered temperature holding duration, allowing for enhanced particle bonding and reduced porosity. This was made possible by the material's ability to

reduce porosity. These differences in porosity can be seen in Figure 7.8, which also demonstrates how the dwell time influences the sintering outcomes.

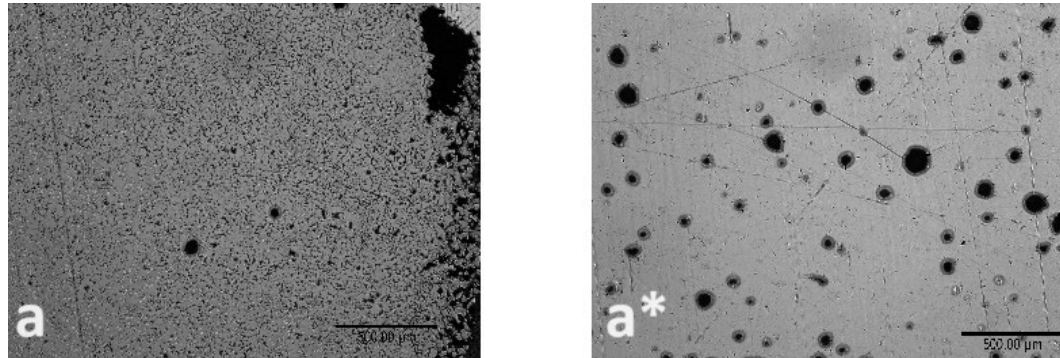


Figure 7.8: Microscopy micrographs of the sintered specimens showing the (a) higher porosity on the stainless-steel side due to the reduction in the maximum reached temperature from 360 to 180 minutes, (a*) the porosity on the copper side was lower.

Next, a significant and noteworthy decrease in porosity values was achieved for both the stainless steel and copper sides during the sequential cycles that were numbered 31 through 38. This was the case for both the stainless steel and copper sides. These distinct variations in porosity are depicted in Figure 7.9 and Figure 7.10, which also illustrate how the dwell time plays a role in determining the sintering outcomes. This trend that has been observed can be explained by the purposeful extension of dwell times at each holding temperature that is included in these cycles. An extension of this kind was purposefully carried out to simplify several important procedures. In the first place, it made it possible to burn out the binder. Because the dwell times were made to last longer, there was more time available for the breakdown of the substance and the elimination of any remaining binder residuals. This is necessary to lessen the amount of voids in the sintered material and to improve its structural integrity.

Second, the extended dwelling times encouraged greater thermal convection throughout the samples. Keeping the material at the specified temperature for longer periods enables a more efficient transfer of heat within the material. Additionally, this

enhanced thermal diffusion plays a critical role in facilitating uniform particle rearrangement and densification, which ultimately results in a reduction in porosity.

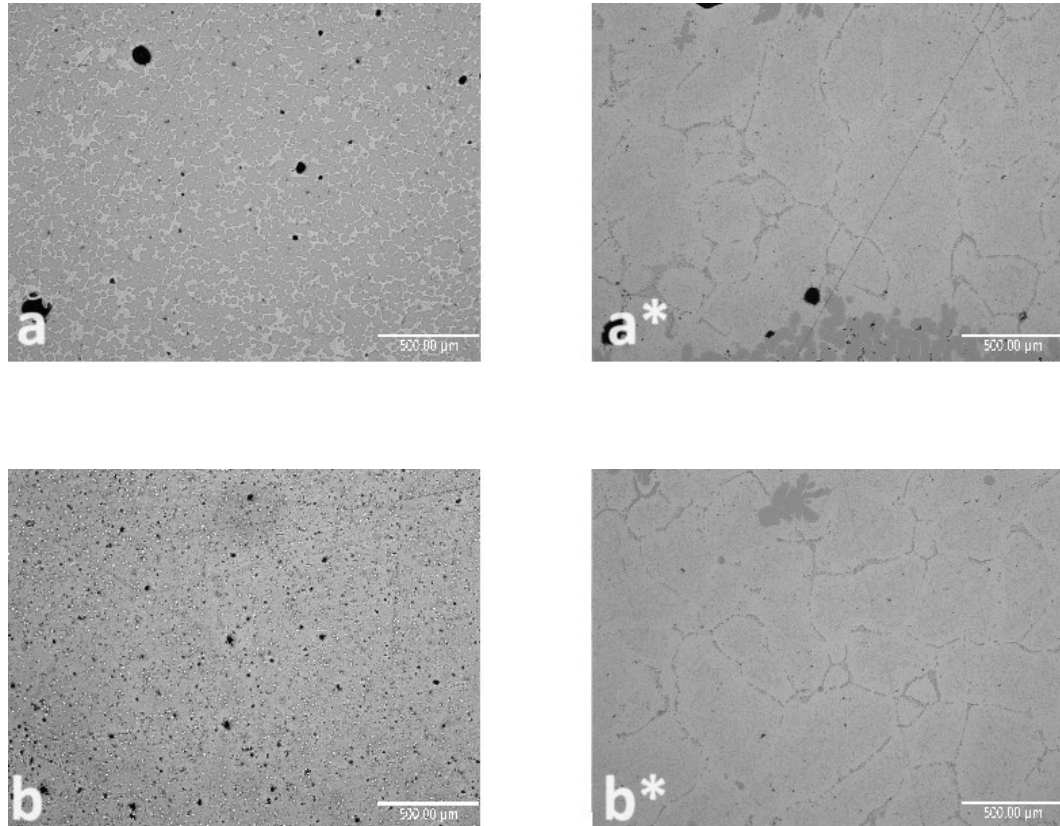


Figure 7.9: The micrographic representations visually capture the enhancements achieved through a deliberate alteration of the sintering cycles, transitioning from 31 to 34 cycles. This transformation resulted in a notable reduction in porosity, specifically from 7.3% in (a) to 5.5% in (b) for the stainless-steel side, and from 8.9% in (a*) to 5% in the copper side(b*).

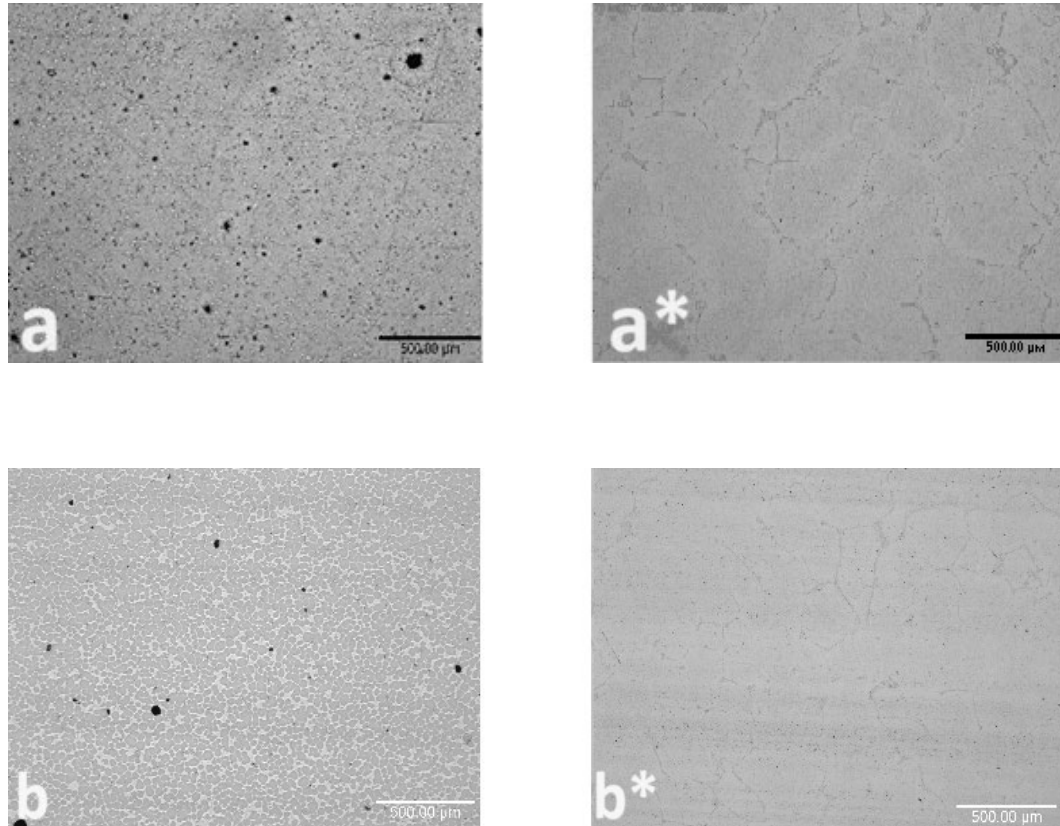


Figure 7.10: The micrographic representations visually capture the enhancements achieved through a deliberate alteration of the sintering cycles, transitioning from 31 to 34 cycles. This transformation resulted in a notable reduction in porosity, specifically from 4.6% in (a) to 2.4% in (b) for the stainless-steel side, and from 3.7% in (a*) to 2.6% in the copper side(b*).

The porosity values have been shown to gradually decrease as a result of these cycles that have been adjusted. Specifically, the porosity decreased from 8.9% to 2.8% on the copper side and from 7.3% to 2.4% on the stainless-steel side as the transition occurred from cycle 31 to cycle 38. This reduction in porosity occurred on both sides of the material. This eloquently demonstrates the positive impact that longer dwell times have on the sintering process and the consequent reduction in porosity that comes about as a result of this process. The result of the copper side matches the result of a study has been done by Kumar et al (159) where a porosity of 1.88 has been achieved by sintering the binder jetted sample at 1075°C.

Ultimately, the findings from this study underline the complexity of sintering processes and highlight the need for precise control of the parameters to achieve desired outcomes. This investigation provides valuable insights into the critical relationship between temperature, dwelling times, and material interactions in sintering processes. Finally, the results revealed that cycle number 38 consistently produced the highest bond quality as can be seen in Figure 7.11. This cycle has resulted in sintered samples with a high density, indicating excellent particle packing and solid-state diffusion at the interface when compared to other cycles.

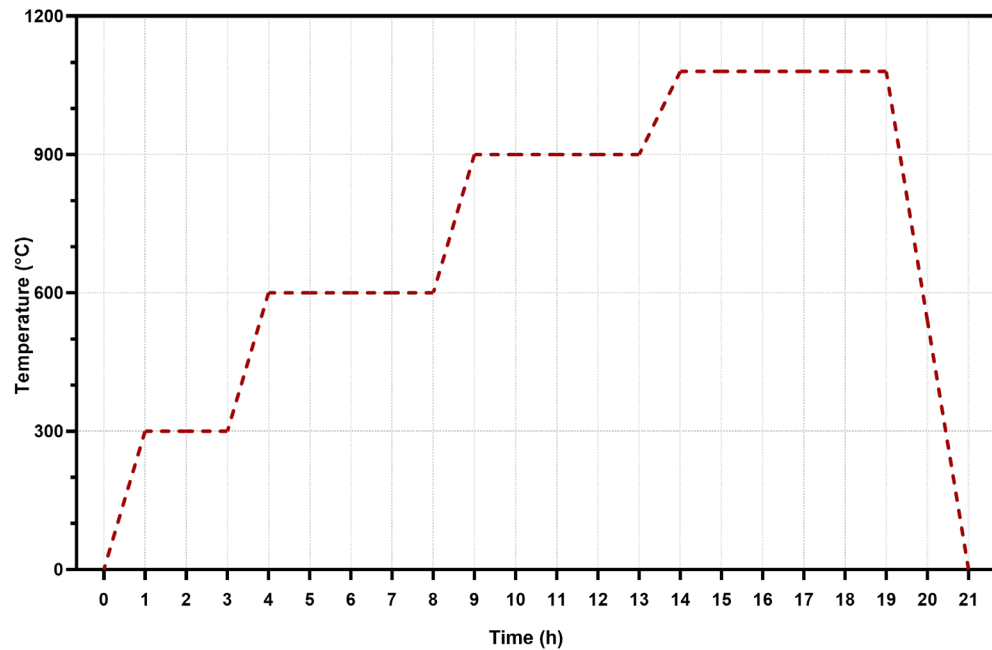


Figure 7.11: Temperature distribution and dwelling time of the best sintering cycle to the green parts that enhance the best structural quality and lower porosity values.

7.3 Conclusions

This chapter has provided an analysis of the sintering cycles applied to multi-material samples using the BJ technique. The primary objectives were to clarify the experimental findings, understand the underlying mechanisms, and analyse the challenges and potential advantages associated with multi-material sintering. In addition, the chapter presented an overview of how various sintering cycles affected the porosity levels in binder jetted multi-material samples constructed with consistent parameters. This data illustrated the impact of different thermal treatment procedures on the macroscopic characteristics of the fabricated components. The results revealed that holding times and temperatures directly influenced porosity in both the binder material and the individual metallic materials. Notably, the early cycles, exhibited issues with heat distribution, particularly affecting the core of the copper surface attributed to the non-uniform heat distribution phenomenon. This issue caused a thermal boundary layer to develop more rapidly, primarily due to buoyancy effects from uneven heat distribution. Extending dwell times at various temperatures have helped to rectify the heat distribution problem. This adjustment allowed for better heat diffusion and temperature homogenization. Binder residue could further block effective heat flow, preventing proper sintering. Therefore, ensuring complete binder burnout before sintering is crucial. Subsequent adjustments in the sintering cycles significantly improved porosity values, emphasizing the importance of optimizing sintering conditions for different materials. Longer dwell times allowed for more thorough binder burnout enhanced thermal diffusion, and better temperature uniformity. The results presented in this chapter suggest that cycle 38 represents the most optimized operational configuration within the scope of this research. Consequently, cycle 38 has been selected as the preferred configuration for producing samples throughout this research. This choice is based on the observed good performance of cycle 38, which aligns with the research objectives and ensures the validity and reliability of the ensuing experimental investigations.

Chapter 8. Interlayer Connection and Tensile Properties of the Multi-material Sintered Parts

8.1 Introduction

In this section, SEM in combination with EDS was employed to explore the interlayer connectivity and chemical distribution within the 3D-printed multi-material components. The primary objective of these analyses was to provide insights into the structural integrity and chemical composition of the 3D-printed components. The utilization of SEM served the purposes of the assessment of bonding quality, and the evaluation of the uniformity of the interfaces in the 316L and Cu binder jetted printed parts. Augmented by the capabilities of EDS, SEM allowed for elemental mapping, facilitating the identification and visualization of distinct element distributions at the material interfaces. The SEM spot size was set at 3.5, and the beam intensity was adjusted to 20 kV to acquire high-resolution images at a working distance of 10 mm under x2500 magnification. Furthermore, in accordance with the stipulations outlined in the BS EN ISO 6892-1:2016 Standards (132), dog-bone-shaped tensile test specimens were fabricated. These specimens were intended for assessing the tensile properties of the multi-material composition consisting of copper (Cu) and 316L stainless steel (SS) at ambient room temperature. The evaluation of tensile strength was carried out using a universally recognized testing apparatus, the Model H5K from Tinius Olsen Ltd equipped with a maximum load of 5 KN as specified by the manufacturer. Conforming to the protocols outlined in the BS EN ISO 6892-1:2016 Standards, the determination of strain rate was carefully executed and accurately maintained within a range of 2 mm per minute. To ensure the reliability of the results, the tensile tests were performed in triplicate for each material, enabling the calculation of average values and standard deviations, which serve to enhance the precision of the acquired data.

8.2 Results and Discussions

8.2.1 Interfacial Characteristics

Scanning Electron Microscopy (SEM) imaging was employed in the investigation of the 316L and Cu bonding interface within the multi-material sample. The sample that has been examined was constructed using the modified multi-material Binder Jetting (BJ) system with a 5% weight of PVA, 200 μm , and sintered using cycle number 38. The examination, as depicted in Figure 8.1, revealed visible separations between regions enriched in 316L stainless steel and those dominated by copper, providing valuable insights into the spatial distribution of these constituent materials.

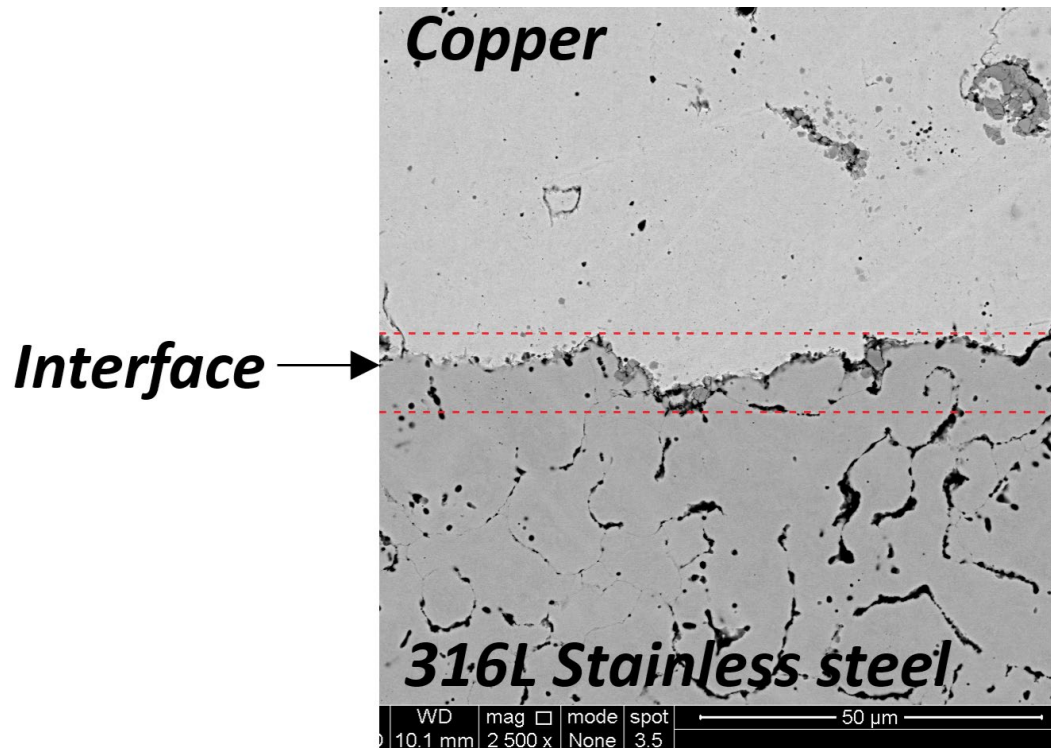


Figure 8.1: SEM image illustrating the 316L and Cu bonding interface in the multi-material sample produced by the modified Binder Jetting (BJ) system. The red dotted lines represent the borders of the transitional region between the two materials.

The SEM examination of the 316L and Cu specimen, as illustrated in Figure 8.1, shows a good metallurgical bonding at the interface between 316L and Cu. The fused Cu region exhibited structural coherence without discernible defects. In contrast, the region featuring 316L powder displayed instances of porosity and cracks. This consolidation not only substantiates the integrity of the interface but also suggests a seamless integration between the distinct materials, fostering a cohesive and well-integrated multi-material structure. The sintering process of stainless steel and copper led to the formation of shared melt regions, delineating areas where a blend of stainless steel and copper is prevalent at the interface. Notably, the interface reveals discernible cracks along specific segments, signifying structural irregularities. The genesis of these cracks is linked to the dissimilar heat interactions experienced by copper and stainless steel. Disparities in thermal coefficients between these materials induce non-uniform expansion and contraction during the solidification phase of the sintering process, thereby precipitating the formation of cracks. Additionally, the creation of intermetallic compounds at the interface may contribute to the development of brittleness, exacerbating the propensity for crack formation.

Furthermore, an assessment of the compositional transition width along the interface was conducted, revealing a calculated average distance of approximately 11 μm . This measurement corresponds to almost 5.5% of the layer thickness, underscoring that elemental diffusion at the 316L and Cu multi-material interface predominantly transpires within the initial layer of the construction, emanating from the top material. Likewise, an observation shows fluctuations in the composition profiles at the interface, hinting at a potential association with the dynamics of partial mixing between the two metal powders throughout the printing process. The discernible fluctuations in composition profiles serve as indicators of the material rearrangements occurring during the critical initial layers of the printing process. This phenomenon is linked to the interaction of the PVA lipid binder droplet with the powder bed. As the PVA lipid binder droplet makes contact with the powder bed, it could reposition the metal powders within the droplet during the printing of the first

layer of the second material on top of the first material. Other cause to the fluctuations can be attributed to solid-state diffusion. During the sintering process, there is a possibility of atomic or molecular diffusion between adjacent layers. This diffusion can result in the mixing or redistribution of elements at the interface, leading to the observed fluctuations in composition profiles.

To delineate the extent of diffusion between the 316L stainless steel and copper within the interlayer connection region, the Energy Dispersive Spectroscopy (EDS) mapping analysis was conducted at the interface of the steel/Cu sample, as presented in Figure 8.2. The qualitative determination of microconstituent compositions within the multi-material Binder Jetted samples was conducted through an analysis employing EDS mapping. The resultant elemental mapping exhibited a well-incorporated distribution of mainly iron (Fe), chromium (Cr), nickel (Ni), molybdenum (Mo), phosphorous (P), Oxygen (O), silicon (Si), and copper (Cu). This observation is indicative of a thorough intermingling of some elements within the interlayer connection region. Figure 8.2 also illustrates a discernible distribution of copper predominantly located in the upper region of the multi-material sample. Concurrently, the lower section of the sample exhibits a notable prevalence of 316L elemental compositions, encompassing constituents such as iron, chromium, nickel, molybdenum, phosphorous, and silicon. Additionally, distinct isolated dark zones, as seen in Figure 8.1 within the Cu powder area, merited attention. The subsequent scrutiny through EDS in Figure 8.2 disclosed the chemical composition of these zones as predominantly 316L, signifying the diffusion of 316L stainless steel elements into the copper-rich area. Consequently, the initial layer of the copper melt exhibits a heightened proportion of stainless steel in comparison to successive layers. This fine distribution arises from the intermingling of the two distinct materials during the sintering and remelting procedures. This occurrence is likely attributed to the transaction between the 316L powder to the copper layer during the building process, leading to a residual blending of 316L powder with subsequently deposited Cu powder, and the interaction of the PVA lipid binder droplet with the powder bed.

Moreover, the chemical composition map reveals the incidental presence of phosphorous, oxygen and some instances areas of silicon, alongside copper and 316L elements. These silicon and oxygen component is attributed to the use of colloidal silica during the polishing process of the cross-section, where the colloidal silica can be trapped in the voids (168). Phosphorous can be one of the 316L elements that found in a small percentage (169).

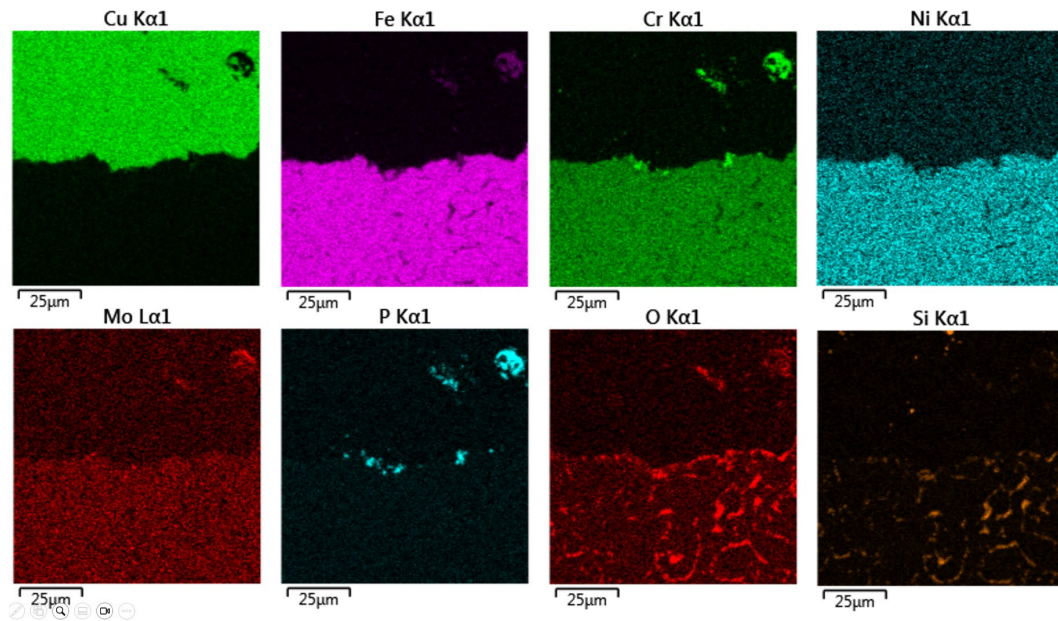


Figure 8.2: EDS mapping analysis revealing microconstituent compositions in multi-material Binder Jetted samples of 316L stainless steel (top part) and copper (lower part), highlighting element distribution within the specimens.

To attain a more quantitative assessment of the compositional variations of chemical elements spanning the interface, EDS line scans were executed at distinct positions along the interface, each scrutinized at a high magnification. The resultant outcomes, in conjunction with corresponding microstructures, are presented in Figure 8.3. The horizontal yellow line in the figure delineates the region subjected to the line scans, and the graphical representation below illustrates the discernible fluctuations in Cu (blue) and Fe (orange) elemental compositions. The interface is distinctly partitioned, with copper displayed on the left and 316L stainless steel (SS) on the right.

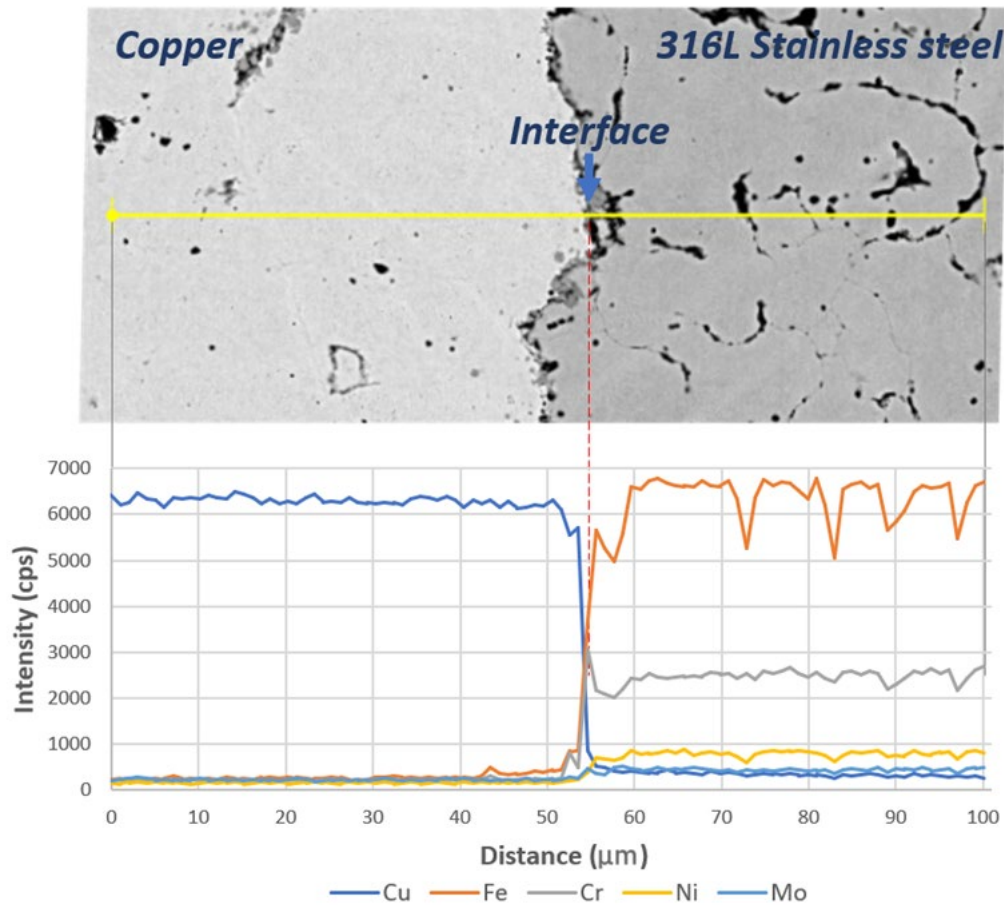


Figure 8.3: Quantitative EDS Line scans Illustrating compositional variations of Cu and Fe elements along the interface in the Binder-Jetted Multi-Material sample. The horizontal yellow line designates the scanned region, with Cu (blue) and Fe (orange) elemental compositions plotted below.

Traversing from the copper to the 316L SS side, the Cu concentration exhibits stability on the left side (counts per second (cps) of 6375 ± 50), experiences a gradual decline within the narrow transition region at the interface, and subsequently stabilizes on the right side (cps of 350 ± 15). Conversely, the Fe concentration shows an opposing trend, escalating from the Cu side (cps of 250 ± 25) towards the 316L SS side (cps of 6650 ± 50). The inferred compositional transition width at each position along the interface is deemed to be less than one layer thickness. This observation suggests that the predominant diffusion of elements at the binder-jetted multi-material interface transpires within the initial layer during the sintering process.

Figure 8.3 further reveals discernible fluctuations in the iron line composition profiles, potentially attributed to voids originating from insufficient heat application on the 316L SS side during the sintering process of the multi-material sample, as discussed in Chapter 7.

The insights provided by SEM and EDS techniques contribute to an enhanced understanding of the microstructural complexities and elemental diffusion dynamics inherent in the 316L and Cu specimen. Such analyses are required for refining multi-material additive manufacturing protocols and advancing the reliability and integrity of the multi-material components.

8.2.2 Tensile Properties

The image in Figure 8.4 provide a visual representation of the tensile test samples, that have been made in the stipulations outlined in the BS EN ISO 6892-1:2016 Standards to perform the Ultimate Tensile Strength (UTS) on three multi-material samples. In addition, Table 8.1 presents the Ultimate Tensile Strength (UTS) values for the various materials under consideration. This tabulated data serves to provide an overview of the mechanical properties of the examined materials, facilitating a comparison and analysis of their UTS characteristics. Specifically, the UTS values were measured, in this study, at 156 ± 5 MPa for the steel/Cu multi-material as seen in Figure 8.5. Moreover, studies examining the Ultimate Tensile Strength (UTS) values of individual materials have reported a mean of UTS values of 536 MPa for sintered 316L stainless steel (316L SS) samples (170), (171), (172), (173) and (174). In the context of Ultimate Tensile Strength (UTS) evaluations for copper-based materials, extant studies have demonstrated that the UTS value for copper components is measured around 344 to 350 MPa for casting (175), from 129 to 135 MPa for HIPed parts and from 82 to 115 MPa for sintered parts (149). These UTS values are fundamental in characterizing the mechanical performance of these materials in tension.



Figure 8.4: The tensile test coupons fabricated under the specifications outlined in the BS EN ISO 6892-1:2016 Standards. These specimens have been prepared to undergo Ultimate Tensile Strength (UTS) testing.

Sample	Ultimate Tensile Strength (MPa)	References
Single material samples (Sintered 316L stainless steel)	536	(170), (171), (172) and (173)
Single material samples (Sintered Pure Copper)	82 -115	(149)
Multi-material samples (Sintered 316L stainless steel and Copper)	152-161	This study

Table 8.1: A summary of the Ultimate Tensile Strength (UTS) values of the diverse array of materials under investigation. This tabular presentation offers a valuable reference for assessing and contrasting the mechanical strength attributes inherent to each of the considered materials.

The observation of the fractured tensile bars suggests that the bond strength at the interface between the steel and copper layers improves the mechanical strength of the copper material itself. The interface demonstrates a good interface bond, as evidenced by its bond strength, thus contributing significantly to the overall strength of the multi-material samples. However, despite the strength exhibited by the steel and Cu bonding, it is essential to acknowledge that the tensile strength of the steel and Cu laminate is found to be significantly lower, approximately 70% less, than that of the standalone stainless-steel component. An influential factor that can impact the tensile strength of the multi-material component is the adequacy of the sintering process, particularly in the 316L stainless steel area. As highlighted by Kurgan et al (176) an inadequate sintering process can give rise to weak bonds within powder grain boundaries. This occurs due to the incapacity of the original powder particles to form precise bonds with each other. Consequently, sharp-edged shapes and angular porosities are demonstrated in the structure, predisposing the component to

fractures occurring in intergranular necks where precise conjunctions are absent. This underscores the critical role of optimal sintering conditions in ensuring the structural integrity and mechanical performance of multi-material components. Similarly, Molinari et al (177) have revealed that subjecting alloyed 316L steel samples to sintering temperatures exceeding the eutectic temperature, with a slight elevation beyond 1200 °C, results in notable enhancements in both ultimate tensile strength and elongation at failure. Moreover, Yoon et al (178) conducted experiments to investigate the tensile and fatigue properties of metal injection-moulded 316L stainless steel under various sintering conditions. The findings of the study indicated a significant influence of sintering conditions on tensile strength and elongation. The observed insensitivity of yield strength to porosity variations was primarily ascribed to the counteracting effects of reduced porosity and simultaneous grain coarsening.

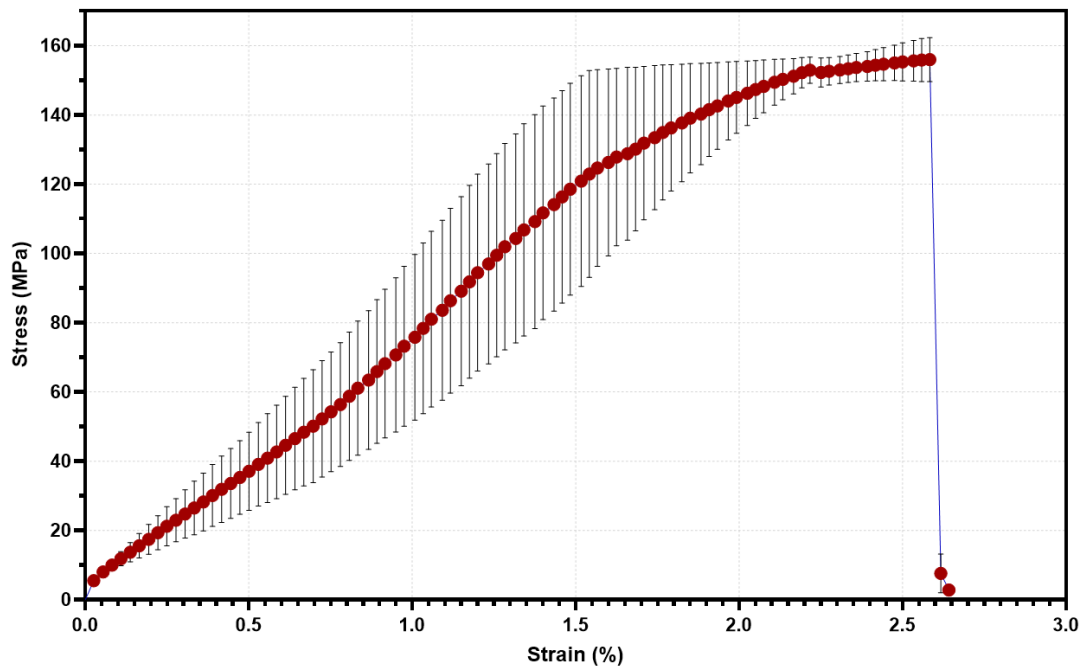


Figure 8.5: Stress versus strain analysis of the multi-material tensile specimen fabricated through the binder jetting approach. The graph shows the maximum UTS value that the multi-material specimen can stand before breakage occurs.

Further scrutiny of the fracture surface of 316L and Cu multi-material components after tensile testing, as illustrated in Figure 8.6, offers an understanding of the mechanical behaviour under stress. An examination of the tensile fracture and associated strain values reveals an unexpected appearance of brittleness, contrary to the anticipated ductile response. This brittleness is evident in the limited plastic deformation observed during the tensile test, characterized by a modest elongation of approximately 2.5% of the total length. The observed brittleness phenomenon is, at least in part, attributed to an insufficient sintering process, particularly impacting the stainless-steel side of the multi-material component. Ineffectual sintering conditions result in inadequate melting during the sintering process, leading to compromised bonding among the 316L powder particles within the microstructure. This brittleness is further underscored by the identification of weak bonds within powder grain boundaries, a phenomenon explained by Kurgan et al (176) The inability of original powder particles to establish precise bonds, due to insufficient sintering heat, contributes to the formation of sharp-edged shapes and angular porosities in the microstructure, thereby predisposing the multi-material component to fractures occurring in intergranular necks where precise conjunctions are absent.

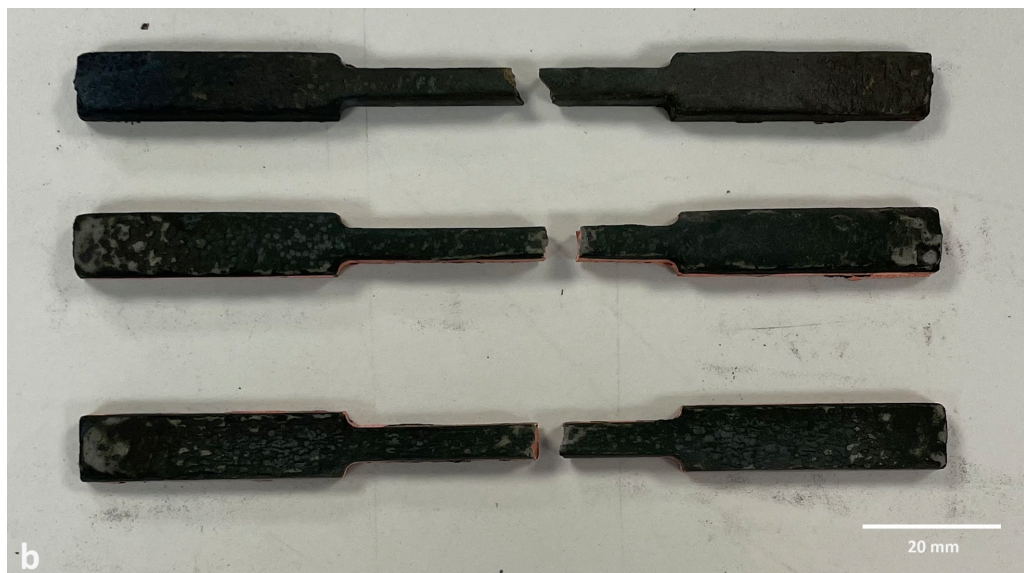
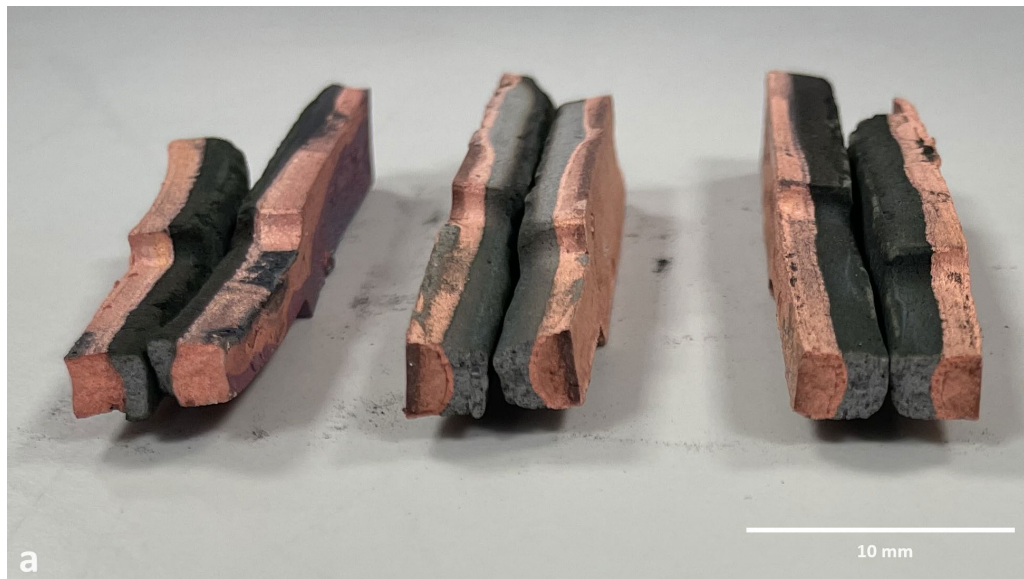


Figure 8.6: The fractured samples analysis of 316l and cu multi-material components post-tensile testing. The picture illustrates the features of the tensile bars, highlighting unexpected brittleness and limited plastic deformation, attributed to an insufficient sintering process.

8.3 Conclusions

In this chapter, the investigation into the 316L and Cu bonding interface within the multi-material sample, produced using a modified multi-material BJ system, was conducted through SEM imaging. SEM analysis of the 316L and Cu specimen showed good metallurgical bonding at the interface between 316L and Cu. The fused Cu region exhibited structural coherence, while the 316L powder region displayed some porosity and cracks. The sintering process resulted in shared melt regions, indicating a blend of stainless steel and copper at the interface. However, discernible cracks along specific segments suggested structural irregularities, attributed to dissimilar heat interactions and intermetallic compound formation. Further assessment of the compositional transition width revealed diffusion predominantly within the initial layer, constituting almost 7.5% of the layer thickness. Fluctuations in composition profiles hinted at partial mixing between the metal powders during the printing process, influenced by the interaction of the PVA lipid binder droplet with the powder bed and the solid-state diffusion. EDS mapping further displays the interlayer connection region, showing a well-incorporated distribution of iron, chromium, nickel, molybdenum, phosphorous, oxygen, silicon, and copper. Notably, distinct zones of 316L diffusion into the copper-rich area were observed, indicating a fine distribution resulting from the intermingling of materials during sintering. Also, an EDS line scan quantitatively assessed compositional variations along the interface, indicating stable Cu and Fe concentrations on each side. Fluctuations in Fe line profiles were attributed to voids from insufficient heat on the 316L SS side during sintering.

Moreover, UTS values was measured at 156 ± 5 MPa for the multi-material samples, indicate the bond strength at the interface between steel and copper layers, improving the strength of copper. Despite the good bond strength, the tensile strength is approximately 70% less than the standalone stainless-steel component as compared to the literature. Also, an unexpected brittleness in the tensile behaviour of the multi-material components has been observed and this brittleness can be attributed to insufficient sintering, particularly on the stainless-steel side.

Chapter 9. Conclusions and Future Work

9.1 Conclusions

One of the research objectives is dedicated to developing a multi-material powder deposition system for precise powder distribution, primarily focusing on binder jetting multi-material 3D printing. The system incorporates critical components and integrates with a gantry system for accurate powder deposition. Experimental investigations revolved around deposition nozzle diameter, head movement speed, and ultrasonic power levels, analysing their impacts across three levels for each factor. Statistical analysis was employed to discern principal effects and optimal factor settings. Notably, a 0.6 mm nozzle led to powder blockage, while 0.8 and 1 mm nozzles deposited powder successfully. The findings indicate a direct correlation between ultrasonic power levels and heap height, with higher power resulting in increased heap height due to faster transducer vibration. Conversely, ultrasonic power levels inversely correlated with heap width, where higher power led to narrower heaps due to focused powder streams. Head movement speed also influenced heap height and width, with increased speed resulting in narrower and shorter heaps. In the second phase, a round flattening wiper was introduced to spread deposited powder while keeping heap height constant. Ultrasonic power levels directly affected heap width when the wiper was employed, leading to expanded widths. Additionally, head movement speed inversely correlated with heap width. Comparisons between trials with and without the wiper showed significant differences in heap width, with the wiper resulting in wider heaps due to its role in spreading deposited powder.

In the next chapter, the experimental investigation was centred on the parameter of the PVA binder. A binder concentration of 3% PVA proved insufficient to hold to the shape, leading to the structural failure of the printed object due to inadequate adhesion to the powder particles. In contrast, a 7% PVA concentration resulted in a

highly viscous liquid that posed challenges in terms of extrusion from the nozzle. Nevertheless, the optimal concentration appeared to be a 5% weight percentage of PVA, which exhibited favourable structural strength. Subsequently, the evaluation extended to the behaviour of the 5% PVA binding material concerning its ability to penetrate the powder particles within the powder bed. This evaluation, encompassing wettability and contact angle analysis, was conducted through the Sessile drop experiment. The findings of the Sessile drop experiment revealed an observation: the binder droplets disappeared almost instantly upon contact with the powder surface. This phenomenon suggests that the binder material exhibited an ability to readily infiltrate and disperse within the powder bed, ensuring efficient and effective binding of powder particles. Next, Thermogravimetric Analysis (TGA) of the 5% PVA binding material sample was conducted to investigate its thermal behaviour. In the findings, it was evident that only 0.87% of the binder material remained following the completion of the TGA cycle at 600 °C. Subsequently, the study focused on the viscosity of a 5% PVA binder material with medium molecular weights under different temperatures ranging from 25 to 45°C. The results indicated a 45% reduction in viscosity of the PVA binder material from 25 to 45°C, suggesting improved penetration of powder particles at higher temperatures. In addition, the surface tension of the prepared binder was then examined using a Tensiometer under different temperatures ranging from 25 to 45°C. The results showed only minor changes in surface tension between 25°C and 45°C, ranging from 44.5 to 42.2 mN/m. Next, Ohnesorge number (Oh) and the Z number were calculated to assess the printability behaviour of the PVA binder material with two distinct nozzle diameters (0.1 and 0.6 mm) under varying temperature conditions. The Oh number decreased with increasing temperature due to the reduction in the dynamic viscosity of the binding material. The results of the Z numbers exceeded the recommended maximum dischargeable Z value proposed in the literature for reliable jetting, however the prepared binder was gettable and could be reliably dispensed through the 0.6 mm

nozzle at room temperature, without issues of droplet jamming or uneven droplet formation.

In Chapter 6, two nozzle sizes (100 and 600 μm) were used to dispense PVA binder. The smaller nozzle generated smaller droplets of 2.5 mm compared to the larger one that generated droplets of 7 mm. Consequently, the smaller nozzle was exclusively used for 3D printing the experimental binder jetted samples. The chapter also involved 38 sintering cycles to understand the interaction between 316L and Cu. Initially, the copper side underwent significant structural changes, forming a spherical mass alongside stainless steel due to elevated temperatures exceeding copper's melting point by 120°C. Despite attempts to mitigate these effects through temperature and dwelling time adjustments, concerns persisted regarding structural integrity. Challenges regarding heat distribution and interlayer connection between 316L and Cu were addressed by adjusting temperature and dwelling times, particularly at 600°C, 900°C, and 1080°C. These adjustments improved outcomes, highlighting the importance of precise parameter control in sintering processes.

Chapter 7 examines porosity as a process response in the sintered specimens. Understanding porosity not only refines the BJ process but also fosters innovative applications. The chapter analyses sintering cycles applied to multi-material samples, aiming to interpret outcomes, comprehend mechanisms, and address challenges and advantages. It reveals that holding times and temperatures directly influence porosity in individual metallic sides. Initial cycles faced challenges in heat distribution, particularly affecting the core of copper surfaces due to non-uniform heat distribution. Addressing this involved extending dwell times at various temperatures to improve heat diffusion and temperature homogenization, especially in copper layers' core. Complete binder burnout before sintering was crucial to overcome binder residue issues. Subsequent cycle modifications significantly improved porosity values, emphasizing the importance of optimizing sintering conditions. Longer dwell times facilitated thorough binder burnout, enhanced thermal diffusion, and reduced

porosity. Cycle 38 emerged as the optimized configuration, designated for sample production and further investigations to ensure research validity and reliability.

Chapter 8 examines the interface bonding, chemical composition, and tensile properties of the multi-material samples, fabricated using the modified BJ system and subjected to sintering Cycle number 38. Scanning Electron Microscopy (SEM) imaging reveals good metallurgical bonding at the 316L and Cu interface, with shared melt regions indicating a blend of stainless steel and copper. However, apparent cracks suggest structural irregularities due to dissimilar heat interactions, with compositional transition width showing diffusion primarily within the initial layer. In addition, Energy Dispersive Spectroscopy (EDS) mapping illustrates well-incorporated distribution of various elements, with distinct zones of 316L diffusion into the copper-rich area. EDS line scans reveal stable Cu and Fe concentrations on each side, with fluctuations in Fe profiles attributed to voids from insufficient sintering heat on the stainless steel side. Also, Ultimate Tensile Strength (UTS) values of 156 ± 5 MPa underscore good bond strength at the interface, albeit approximately 70% lower than standalone stainless steel components. This reduction highlights the importance of optimal sintering conditions for structural integrity, as inadequate sintering can lead to weak bonds, porosities, and fractures.

To sum up, this work establishes the first work on multi-material 3D printing through the use of BJ technology. Summary of the identified constraints and State-of-the-Art improvements can be as the follow:

1. Lack of Cost-Effective and Accessible Processing Methods: a principal challenge that has been addressed was the absence of accessible and cost-effective multi-material binder jetting processes, an obstacle that has held back the advancement and broader adoption of multi-material binder jetting technology. At the core of this work lies a novel achievement—designing a cost-effective multi-material powder deposition system.

2. Lack of Recyclability for Used Powders: Before the study, recycling of used powders was limited. Research outcomes facilitated the development of recycling methods, promoting sustainability in material usage, allowing for the exact placement of powder at designated locations on the building platform.
3. Issues with Powder Separation: Challenges with powder separation hindered process reliability. Yet, with this system, the requirement to completely cover the entire build platform with powder for the production of small parts becomes unnecessary. This efficient approach not only reduces costs but also contributes to the reduction of material waste.
4. Issues with Thermal Expansion in the 3D Printing: thermal expansion issues in some of the additive manufacturing processes have obstructed the production of multi-material parts of two materials that have different thermal coefficients of expansion. However, the exploration of sintering cycles for binder jetted multi-material parts within this study yields invaluable insights into the art of controlling the thermal expansion issue. Thus, this issue has been resolved, in the case of 316L and Cu, using the BJ technique. The controlled heating furnaces in the sintering cycle control the cooling rate, redefining the concept of thermal expansion control and enabling the creation of good functionally graded multi-material components.
5. Elevated Porosity in Final Components: Existing techniques often resulted in components with high porosity. Research interventions focused on optimizing sintering parameters to reduce porosity and enhance part quality.

Overall, the research contributed to overcoming various constraints associated with additive manufacturing, leading to improvements in performance, efficiency, complexity, sustainability, and affordability of the fabrication process and resulting components.

9.2 Proposed Areas of Future Work

One of the most important aspects of future research will be to develop and improve the multi-material powder deposition system. The development aims at achieving full automation of the deposition process, thereby enhancing efficiency and precision in the fabrication of structures. The envisioned system transcends conventional limitations by not only accommodating a two-material deposition but also by pioneering the capability to handle and deposit more than two distinct powder materials. This expansion of functionality broadens the spectrum of potential applications, enabling the fabrication of complex components with diverse material compositions in a seamless and automated manner. The automation of the system is anticipated to streamline production workflows, reduce human intervention, and minimize errors, contributing to the realization of a highly reliable and versatile additive manufacturing platform.

Moreover, leveraging the insights derived from the present investigation, prospective research endeavours should focus on the optimization of sintering cycles, strategically aiming to achieve a delicate equilibrium between reduced cycle durations and the perpetuation of optimal material properties. The current findings unequivocally attest to the efficacy of prolonged sintering cycles in realizing outcomes characterized by diminished porosity and enhanced bonding strength. Nevertheless, a fundamental avenue for further advancement lies in exploring methodologies directed toward curtailing cycle techniques while concurrently upholding the quality benchmarks of the sintering process. The pursuit of shortened cycle times in the context of sintering transcends mere expediency; it constitutes a scientific challenge necessitating an exploration of thermal dynamics, phase transformations, and material interactions.

Furthermore, in subsequent research investigations, it is crucial to systematically address the potential implications stemming from variations in relative thicknesses between 316L stainless steel and copper sections within tensile specimens to improve

the mechanical properties of the specimen. The discerned variability in mechanical properties accentuates the paramount importance of conducting geometric analyses to understand the underlying factors contributing to such variations.

Another area of future work is to investigate various multi-material combinations, specifically integrating Inconel 690 and 316L stainless steel through the multi-material binder jetting technique, which holds significant promise for advancing thermal management applications. The planned exploration aims to understand the interplay of material properties and manufacturing parameters, with a focus on optimizing the fabrication process to achieve precise control over the spatial distribution of Inconel 690 and 316L stainless steel within composite structures. This research endeavour is poised to contribute to the development of tailored solutions for thermal management, addressing the critical requirements of efficient heat dissipation, corrosion resistance, and mechanical strength.

Lastly, after observing the sintering of dissimilar metals and noting potential structural irregularities and brittleness in the multi-material components, the implementation of an inter-layer material between the 316L stainless steel and copper layers can improve the multi-material components. This inter-layer material could serve as a buffer, facilitating better bonding and mitigating the effects of dissimilar heat interactions during the sintering process. By introducing a compatible intermediary material, the homogeneity of the interface and minimize the formation of cracks and voids can be enhanced. This approach could lead to improved structural integrity and mechanical properties of the multi-material components, ultimately enhancing their performance and reliability in various applications. Further research and experimentation will be necessary to identify the most suitable inter-layer material and optimize its incorporation into the fabrication process.

Chapter 10. References

1. **The American Society for Testing and Material, (ASMT).** Committee F42 on Additive Manufacturing Technologies. *The American Society for Testing and Material*. [Online] 2010. <https://www.astm.org/COMMITTEE/F42.htm>.
2. **Hull, Charles W.** *Apparatus For Production Of Three-Dimensional Objects By Stereothography*. US4575330 1984.
3. **M. Greul, T. Pintat, M. Greulich.** *Rapid prototyping of functional metallic parts*. 1, 1995, Computers in Industry, Vol. 28, pp. 23-28.
4. **Fernández, Javier Ledesma.** *Jetting of multiple functional materials by Additive Manufacturing*. Nottingham : University of Nottingham, August 2017.
5. **Saereh Mirzababaei, Somayeh Pasebani.** *A Review on Binder Jet Additive Manufacturing of 316L Stainless Steel*. 2019, Manufacturing and Materials Processing, Vol. 3, p. 82.
6. **Asier Lores, Naiara Azurmendi, Iñigo Agote & Ester Zuza.** *A review on recent developments in binder jetting metal additive manufacturing: materials and process characteristics*. 5, 2019, Powder Metallurgy, Vol. 62, pp. 267-296.
7. **QIAN, M.** *Metal Powder for Additive Manufacturing*. 3, 2015, The Minerals, Metals & Materials Society, Vol. 67, pp. 536-537.
8. **Tugdual Amaury Le Néel, Pascal Mognol, Jean-Yves Hascoët.** *A review on additive manufacturing of sand molds by binder jetting and selective laser sintering*. 2018, Rapid Prototyping Journal.
9. **Stevenson, D.** *3D Sand Printing – Cores & Moulds for the Foundry Industry Agenda*. 2015, ExOne.
10. **Rao, TV Ramana.** *Metal Casting: Principles and Practice*. 1. New Delhi : New Age International, 2003.
11. **Williams, Emanuel M. Sachs John S. Haggerty Michael J. Cima Paul A.** *Three-dimensional printing techniques*. US5204055A United State of America, 1993.
12. **Dean Snelling, Christopher Williams, Carlos Suchicital, Alan Druschitz.** *Fabrication Of Cellular Cordierite Preforms Via Binder Jetting* 2015, VT Tech Department of Materials Science and Engineering, pp. 1434-1449.
13. **B Verlee, T Dormal, J Lecomte-Beckers.** *Density and porosity control of sintered 316L stainless steel parts produced by additive manufacturing*. 4, 2012, Powder Metallurgy, Vol. 55, pp. 260-267.
14. **Arghavan Farzadi, Mehran Solati-Hashjin, Mitra Asadi-Eydivand, Noor Azuan Abu Osman.** *Effect of Layer Thickness and Printing Orientation on Mechanical Properties and Dimensional Accuracy of 3D Printed Porous Samples for Bone Tissue Engineering*. 9, s.l. : PLoS ONE, 2014, Vol. 9.

15. **S.M. Gaytan, M.A. Cadena, H. Karim, D. Delfin, Y. Lin, D. Espalin, E. MacDonald, R.B. Wicker.** *Fabrication of barium titanate by binder jetting additive manufacturing technology.* 5, s.l. : Ceramics International, 2015, Vol. 41.
16. **Mohsen Ziaee, Nathan B. Crane.** *Binder jetting: A review of process, materials, and methods.* : Additive Manufacturing, 2019, Vol. 28.
17. **Meet Upadhyay, Tharmalingam Sivarupan, Mohamed El Mansori.** *3D printing for rapid sand casting—A review* : Journal of Manufacturing Processes, 2017, Vol. 29.
18. **Hoosier Pattern Inc.** *3D Sand Printing - Benefits of Additive Manufacturing.* Hoosier Pattern Inc. [Online]
19. **Jason Walker, Evan Harris, Charles Lynagh, Andrea Beck, Brian Vuksanovich, Brett Conner, Eric MacDonald, Rich Lonardo, Jerry Thiel, Kirk Rogers.** *3D PRINTED SMART MOLDS FOR SAND CASTING.* International Journal of Metalcasting, 2018, Vol. 12.
20. **Haolong Shangguan, Jinwu Kang, Chengyang Deng, Yongyi Hu, Tao Huang.** *3D-printed shell-truss sand mold for aluminum castings.* Journal of Materials Processing Tech., 2017, Vol. 250.
21. **Dean A. Snelling, Christopher B. Williams, Alan P. Druschitz.** *Mechanical and material properties of castings produced via 3D printed molds.* Additive Manufacturing, 2019, Vol. 27.
22. **Mohsen Ziaee, Nathan B. Crane.** *Binder jetting: A review of process, materials, and methods.* Additive Manufacturing, 2019, Vol. 28.
23. **Ashwath Kumar, Yun Bai, Anders Eklund, Christopher B. Williams.** *Effects of Hot Isostatic Pressing on Copper Parts Fabricated via Binder Jetting.* LA : 45th SME North American Manufacturing Research Conference, 2017.
24. *Powder bed binder jet 3D printing of Inconel 718: Densification, microstructural evolution and challenges.* **Current Opinion in Solid State and Materials Science**, 2017, Vol. 21.
25. **Özgür Özgün, H. Özkan Gülsoy, Ramazan Yılmaz, Fehim Fındık.** *Microstructural and mechanical characterization of injection molded 718 superalloy powders.* Journal of Alloys and Compounds, 2013, Vol. 576.
26. **Pantcho Stoyanov, Kalissa Andre, Paul Prichard, Matthew Yao, Christoph Gey.** *Microstructural and mechanical characterization of Mo- containing Stellite alloys produced by three dimensional printing.* 3rd CIRP Conference on Surface Integrity (CIRP CSI) , 2016.
27. **Yuhaowei Zhou, Yunlong Tang, Thibault Hoff, Martin Garon, Fiona Yaoyao Zhao.** *The Verification of the Mechanical Properties of Binder Jetting Manufactured Parts by Instrumented Indentation Testing.* 43rd Proceedings of the North American Manufacturing Research Institution of SME, 201.
28. **Yun Bai, Williams Christopher B.** *Binderless Jetting: Additive Manufacturing of metal parts via jetting nanoparticles.* Solid Freeform Fabrication, 2017.
29. **Han Chen, Yaoyao Fiona Zhao.** *Process parameters optimization for improving surface quality and manufacturing accuracy of binder jetting additive manufacturing process.* Rapid Prototyping Journal, 2016, Vol. 22.

30. **Shuang-Jun Huang, Chun-Sheng Ye, Huo-Ping Zhao & Zi-Tian Fan.** *Parameters optimization of binder jetting process using modified silicate as a binder.* 2019, *Materials and Manufacturing Processes*, Vol. 35, pp. 214-220.
31. **Yun Bai, Williams Christopher.** *Binder jetting additive manufacturing with a particle-free metal ink as a binder precursor.* 2018, *Materials and Design*, Vol. 147, pp. 146-156.
32. **Ben Utela, Duane Storti, Rhonda Anderson, Mark Gantera.** *A review of process development steps for new material systems in three dimensional printing (3DP).* 2008, *Journal of Manufacturing Processes*, Vol. 10, pp. 96-104.
33. **Yang, Xiaohong Yang · Weiling Zhu · Qiao.** *The Viscosity Properties of Sodium Silicate Solutions.* 2008, *Journal of Solution Chemistry*, Vol. 37, pp. 73-83.
34. **Dean Snelling, Christopher Williams, Alan Druschitz.** *A Comparison Of Binder Burnout And Mechanical Characteristics Of Printed And Chemically Bonded Sand Molds.* 2014, *SFF Symposium*, pp. 197-209.
35. **Yin, Y.X., Hu, R.J., Liu, W.Q., Yue, M., Zhen, Z.** *Comparisons and Analysis of Sodium Silicate and Epoxy Bond NdFeB Magnets.* 2016, *Materials Science Forum*, Vol. 852, pp. 136-141.
36. **W.Q. Liu, R.J. Hu, M. Yue, Y.X. Yin, D.T. Zhang.** *Preparation and properties of isotropic Nd-Fe-B bonded magnets with sodium silicate binder.* 2017, *Journal of Magnetism and Magnetic Materials*, Vol. 435, pp. 187-193.
37. **Havstad, Maja Rujnić.** *Plastic Waste and Recycling, Biodegradable plastics.* s.l. : Academic Press, 2020. 9780128178805.
38. **C.C DeMerlis, D.R Schoneker.** *Review of the oral toxicity of polyvinyl alcohol (PVA).* *Food and Chemical Toxicology*, Vol. 41. 0278-6915.
39. **Finch, C. A.** *Polyvinyl alcohol : properties and applications.* s.l. : Wiley, London, 1973. 9780471258926.
40. **Paul, Sourabh.** *Binder Jetting of Aqueous Polyvinyl Alcohol for Additive Manufacturing of Inconel 718.* s.l. : The University of Sheffield, 2022.
41. **GmbH, Anton Paar.** **Modular Compact Rheometer.** [Online] Anton Paar GmbH, 2024. *Anton Paar*. <https://www.anton-paar.com/uk-en/products/details/rheometer-mcr-102-302-502/>.
42. **International Association for the Properties of Water and Steam.** *Release on the IAPWS Formulation 2008 for the Viscosity of Ordinary Water Substance .* International Association for the Properties of Water and Steam, 2008.
43. **Anton Paar.** *Viscosity of Water.* Anton Paar. [Online] Anton Paar GmbH, 2008. <https://wiki.anton-paar.com/uk-en/water/>.
44. **scientific, Kruss.** **Bubble Pressure Tensiometer. Kruss .** [Online] Kruss scientific. https://www.kruss-scientific.com/en/products-services/products/bp100?gad_source=1&gclid=Cj0KCQjwqpSwBhCLARIsADIZ_Tn2A9bPVpkdRH YBIHBlXtlnMK-ZnKozTwqeZ6hZCbftQaauvSJXMq0aAj78EALw_wcB.

45. **Jiayan Tai, Hiong Yap Gan, Yen Nan Liang, Boon Keng Lok.** s.l. *Control of Droplet Formation in Inkjet Printing Using Ohnesorge Number Category: Materials and Processes.* Electronics Packaging Technology Conference, 2008. 978-1-4244-21 18-3.
46. **Florence Marcotte, Stéphane Zaleski.** *Density contrast matters for drop fragmentation thresholds at low Ohnesorge number.* Physical Review Fluids, 2019, Vol. 4.
47. **Derby, Brian.** *Inkjet printing of functional and structural materials: fluid property requirements, feature stability, and resolution.* Annual Review of Materials Research, 2010, Vol. 40.
48. **Emine Tekin, Patrick J. Smith, Ulrich S. Schubert.** *Inkjet printing as a deposition and patterning tool for polymers and inorganic particles.* Soft Matter, 2008, Vol. 4.
49. **Nicholas A. Meisel, Christopher B. Williams, Alan Druschitz.** *Lightweight Metal Cellular Structures via Indirect 3D Printing and Casting.* 2012, SFF Symposium, pp. 162-176.
50. **Truong Do, Patrick Kwon, Chang Seop Shin.** *Process development toward full-density stainless steel parts with binder jetting printing.* 2017, International Journal of Machine Tools & Manufacture, Vol. 121, pp. 50–60.
51. **Rahaman, M.N. Kinetics and mechanisms of densification.** [book auth.] Zhigang Zak Fang. *Sintering of Advanced Materials.* s.l. : Woodhead Publishing Series in Metals and Surface Engineering, 2010.
52. **Thümmeler, W. Thomma.** *The sintering process.* 1, 1967, Metallurgical Reviews, Vol. 12, pp. 69-108.
53. **German, Randall M.** *Powder Metallurgy and Particulate Materials Processing.* s.l. : The Processes, Materials, Products, Properties and Applications, 2005.
54. **Inovar.** *Powder Metallurgy Review.* [Online] [Cited: September 6, 2020.] <https://www.pmr-review.com/introduction-to-powder-metallurgy/sintering-in-the-powder-metallurgy-process/>.
55. **Nicholas McKenna, Sarat Singamneni, Olaf Diegel, Darius Singh, Thomas Neitzert, John St. George, Asimava Roy Choudhury and Prasad Yarlagadda.** *Direct Metal casting through 3D printing: A critical analysis of the mould characteristics.* Gold Coast Australia : 9th Global Congress on Manufacturing and Management, 2008.
56. **G. Goudah, Faiz Ahmad, Othman Mamat, Mohd Afian Omar.** *Preparation and Characterization of Copper Feedstock for Metal Injection Molding.* 24, s.l. : Journal of Applied Sciences, Vol. 10.
57. **Nor Shamimi Shaari¹, Muhammad Hussain Ismail, Mahfuzah Zainudin, Ros Atikah Abd Kadir, Mazyan Yahaya, Rosniza Rabilah.** *Effect of sintering parameters on Cu/CNTs using quartz tube furnace under argon atmosphere.* Proceedings of Mechanical Engineering Research, 2019.
58. **Francisco L. Serafini, Marcele Peruzzo, Israel Krindges, Michell Felipe C. Ordoñez, Daniel Rodrigues, Roberto M. Souza, María Cristina M. Farias.** *Microstructure and mechanical behavior of 316L liquid phase sintered stainless steel with boron addition.* Materials Characterization, 2019, Vol. 152.

59. **Huali Hao, Yanjing Wang, Hamid Reza Jafari Nodooshan, Yongyun Zhang, Shulong Ye, Yonghu Lv, Peng Yu.** *The effects of sintering temperature and addition of TiH₂ on the sintering process of Cu.* s.l. : Materials , 2019, Vol. 12.
60. **Chiara Zitelli, Paolo Folgarait, Andrea Di Schino.** *Laser Powder Bed Fusion of Stainless Steel Grades: A Review.* **Metals.** 9, 2019, Vol. 731.
61. **Alberta Aversa, Giulio Marchese, Abdollah Saboori, Emilio Bassini, Diego Manfredi, Sara Biamino, Daniele Ugues, Paolo Fino, Mariangela Lombardi.** *New Aluminum Alloys Specifically Designed for Laser Powder Bed Fusion: A Review.* **Materials.** 12, 2019, Vol. 1007.
62. **Richard O'Leary, Rossi Setchi, Paul Prickett, Gareth Hankins, Nick Jones.** *An Investigation into the Recycling of Ti-6Al-4V Powder Used Within SLM to Improve Sustainability.* Sustainable Design and Manufacturing. 2015, Vol. 8, 2.
63. **Zhuming Bi, Xiaoqin Wang.** *Computer Aided Design and Manufacturing.* Hoboken : Johan Wiley & Sons Ltd and ASME Press, 2020.
64. **J. Liu, E. Fearon, S.P. Edwardson, G. Dearden.** *Blown Powder Laser Cladding with Novel Processing Parameters for Isotropic Material Properties.* Austin : 8th Annual International Solid Freeform Fabrication Symposium, 2017.
65. **Metallisation.** *Laser Cladding for Critical Component Repair Duplex Stainless Steel.* [Online] Metallisation Limited. <https://www.metallisation.com/applications/laser-cladding-for-critical-component-repair-duplex-stainless-steel/>.
66. **B.Song, T.Hussain, K.T.Voisey.** *Laser Cladding of Ni50Cr: A Parametric and Dilution Study.* 2016 : Physics Procedia, Vol. 83.
67. **Simpson, Timothy W.** Additive Manufacturing via Material Extrusion. *Additive Manufacturing.* [Online] 01 2019.
<https://www.additivemanufacturing.media/blog/post/additive-manufacturing-with-material-extrusion>.
68. **Brian N. Turner, Robert Strong, Scott A. Gold.** *A review of melt extrusion additive manufacturing processes: I. Process design and modeling.* 3, s.l. : Rapid Prototyping Journal, 2014, Vol. 20. 1355-2546.
69. **N. Chawla, X. Deng.** *Microstructure and mechanical behavior of porous sintered steels.* Materials Science and Engineering: A, 2005, Vol. 390.
70. **Rice, R. W.** *Comparison of stress concentration versus minimum solid area based mechanical property-porosity relations.* s.l. : Journal of Materials Science, 1993, Vol. 28.
71. **Yiwei Mao, Chao Cai, Jinkai Zhang, Yuhua Heng, Kunhao Feng, Daosheng Cai, Qingsong Wei.** *Effect of sintering temperature on binder jetting additively manufactured stainless steel 316L: densification, microstructure evolution and mechanical properties.* s.l. : Journal of materials research and technology, 2023, Vol. 22.
72. **Rajkumar Velu, Sarat Singamneni.** *Evaluation of the influences of process parameters while selective laser sintering PMMA powders.* s.l. : Proceedings of the Institution of Mechanical Engineers, Part C: Journal of Mechanical Engineering Science, 2014.

- 73. TWI research and technology organisations.** *What is porosity and how can it be prevented?* TWI Ltd. [Online] <https://www.twi-global.com/technical-knowledge/faqs/faq-what-is-porosity-and-how-can-it-be-prevented#:~:text=Porosity%20is%20caused%20by%20the,originates%20from%20poor%20gas%20shielding>.
- 74. Seiji Katayama, Naoki Seto, Masami Mizutani and Akira Matsunawa.** *Formation Mechanism of Porosity in High Power YAG Laser Welding* in *High Power YAG Laser Welding*. 1, s.l. : International Congress on Applications of Lasers & ElectroOptics , 2000, Vol. 2000.
- 75. Akira Matsunawa, Masami Mizutani, Seiji Katayama & Naoki Seto.** *Porosity formation mechanism and its prevention in laser welding*. s.l. : Welding international, 2003.
- 76. S. Mohammad H. Hojjatzadeh, Niranjana D. Parab, Qilin Guo, Minglei Qu, Lianghua Xiong, Cang Zhao, Luis I. Escano, Kamel Fezzaa, Wes Everhart, Tao Sun, Lianyi Chen.** *Direct observation of pore formation mechanisms during LPBF additive manufacturing process and high energy density laser welding*. *The International Journal of Machine Tools and Manufacture*, 2020.
- 77. Saad A. Khairallah, Andrew T. Anderson, Alexander Rubenchik, Wayne E. King.** *Laser powder-bed fusion additive manufacturing: Physics of complex melt flow and formation mechanisms of pores, spatter, and denudation zones*. s.l. : Acta Materialia, 2016, Vol. 108.
- 78. Hwan-Jin Sung, Tae Kwon Ha, Sangho Ahn, Young Won Chang.** *Powder injection molding of a 17-4 PH stainless steel and the effect of sintering temperature on its microstructure and mechanical properties*. s.l. : Journal of Material Processing Technology, 2002, Vols. 130-131.
- 79. Ronald Machaka, Phumlani Ndlangamandla, Mandy Seerane.** *Capillary rheological studies of 17-4 PH MIM feedstocks prepared using a custom CSIR binder system*. s.l. : Powder Technology, 2017, Vol. 326.
- 80. Mohsen Ziaee, Eric M Tridas, Nathan B Crane.** *Binder-Jet Printing of Fine Stainless Steel Powder with Varied Final Density*. s.l. : The Journal of The Minerals, Metals & Materials Society (TMS), 2017, Vol. 69.
- 81. Wenchao Du, Xiaorui Ren, Zhijian Pei, Chao Ma.** *Ceramic binder jetting additive manufacturing: a literature review on density*. s.l. : Journal of Manufacturing Science and Engineering, 2020, Vol. 142.
- 82. German, Randall M.** *Liquid Phase Sintering*. United States : Springer US, 2013.
- 83. Kang, Suk-Joong L.** *Sintering: Densification, Grain Growth and Microstructure*. Netherlands : Elsevier Science, 2004.
- 84. Nesma T. Aboulkhair, Nicola M. Everitt, Ian Ashcroft, Chris Tuck.** *Reducing porosity in AlSi10Mg parts processed by selective laser melting*. s.l. : Additive Manufacturing, 2014, Vols. 1–4. 2214-8604.
- 85. B. Verlee, T. Dormal, J. Lecomte-Beckers.** *Density and porosity control of sintered 316L stainless steel parts produced by additive manufacturing*. 4, s.l. : Powder Metallurgy, 2012, Vol. 55.

86. **Juan, Hsiang-Ling.** *effect of temperature ratio (t_s/t_m) and time on the sintering behavior of metallic 316l stainless steel coupons coupons produced using jet-binder technology.* s.l. : University of Pittsburgh, 2017.
87. **C. Anstaett, Dr.-Ing. C. Seidel, Prof. Dr.-Ing G. Reinhart.** *Fabrication of 3D Multi-material Parts Using Laser-based Powder Bed Fusion.* Austin : The 28th Annual International Solid Freeform Fabrication Symposium, 2017.
88. **K. Chockalingam, N. Jawahar, K.N. Ramanathan, P.S. Banerjee.** *Optimization of stereolithography process parameters for part strength using design of experiments.* s.l. : The International Journal of Advanced Manufacturing Technology, 2006, Vol. 29.
89. **Stone, Michelle. Meet Charles Hull, Inventor of Stereolithography.** Autodesk Inc. [Online] Autodesk Inc, December 2019. <https://www.autodesk.com/products/fusion-360/blog/meet-charles-hull-inventor-of-stereolithography/#:~:text=Hull%20is%20actually%20the%20inventor,patenting%20the%20idea%20in%201986..>
90. **T. Chartier, A. Badev, Y. Abouliatim, P. Lebaudy, L. Lecamp.** *Stereolithography process: Influence of the rheology of silica suspensions and of the medium on polymerization kinetics – Cured depth and width.* s.l. : Journal of the European Ceramic Society, 2012, Vol. 32.
91. **Jae-Won Choi, Ho-Chan Kim, Ryan Wicker.** *Multi-material stereolithography.* 1, 2011, Journal of Materials Processing Technology, Vol. 211, pp. 318–328.
92. **E. Willems, M. Turon-Vinas, B. Camargo dos Santos, B. Van Hooreweder, F. Zhang, B. Van Meerbeek, J. Vleugels.** *Additive manufacturing of zirconia ceramics by material jetting.* 10, s.l. : Journal of the European Ceramic Society, 2021, Vol. 41.
93. **Loughborough University.** About Additive Manufacturing, Material Jetting. *Loughborough University.* [Online] <https://www.lboro.ac.uk/research/amrg/about/the7categoriesofadditivemanufacturing/materialjetting/>.
94. **Frakes, Dr David H.** 3D Printing Advances Cerebral Aneurysm Research. *Solidscape.* [Online] Solidscape. https://www.solidscape.com/wp-content/uploads/2015/03/asu_advanced_research_case_study_11202012.pdf.
95. **Daniel Periard, Evan Malone, Hod Lipson.** *Printing Embedded Circuits.* Ithaca : Mechanical & Aerospace Engineering Cornell University, 2007. pp. 503-512.
96. **Jin-Hyung Shim, Jung-Seob Lee, Jong Young Kim and Dong-Woo Cho.** *Bioprinting of a mechanically enhanced three-dimensional dual cell-laden construct for osteochondral tissue engineering using a multi-head tissue/organ building system.* 8, 2012, Journal of Micromechanics and Microengineering, Vol. 22.
97. **Wei Li, Jingwei Zhang, Xinchang Zhang, Frank Liou.** *Effect of optimizing particle size on directed energy deposition of Functionally Graded Material with blown Pre-Mixed Multi-Powder.* s.l. : Manufacturing Letters, 2017, Vol. 13.

- 98. Lin Li, W.U.H. Syed, A.J. Pinkerton.** *Rapid additive manufacturing of functionally graded structures using simultaneous wire and powder laser deposition.* 4, s.l. : Virtual and Physical Prototyping, 2006, Vol. 1.
- 99. Venkata Karthik Nadimpalli, Thomas Dahmen, Emilie Hørdum Valente, Sankhya Mohanty, David Bue Pedersen.** *Multi-material additive manufacturing of steels using laser powder bed fusion.* Bilbao : The European Society for Precision Engineering and Nanotechnology, 2019.
- 100. Chao Wei, Lin Li, Xiaoji Zhang, Yuan-Hui Chueh.** *3D printing of multiple metallic materials via modified selective laser melting.* 2018, CIRP Annals - Manufacturing Technology, Vol. 67, pp. 245 - 248.
- 101. Anqi Liang, Sandeep Sahu, Xiao Zhao, Tomas Polcar, Andrew R. Hamilton.** *Interfacial characteristics of austenitic 316 L and martensitic 15–5PH stainless steels joined by laser powder bed fusion.* s.l. : Materials Characterization, 2023, Vol. 198.
- 102. Aerosint.** We Made L-PBF Dual-Metal. *Aerosint.* [Online] March 4, 2020. <https://aerosint.com/we-made-l-pbf-dual-metal/>.
- 103. Sertoglu, Kubi.** AEROSINT AND ACONITY3D DEVELOP MULTI-MATERIAL METAL 3D PRINTER. *3D Printing Industry.* [Online] 2020.
- 104. Su-Jin Lee, Hiroshi Nakamura, Yousuke Kawahito and Seiji Katayama.** *Weldability of Ti and Al Dissimilar Metals Using Single-Mode Fiber Laser.* 2, Osaka : JLMN-Journal of Laser Micro/Nanoengineering, 2013, Vol. 8.
- 105. Jean Pierre Bergmann, Franziska Petzoldt, Renè Schürer and Stefan Schneider.** *Solid-state welding of aluminum to copper—case studies.* Ilmenau : Weld World, 2013.
- 106. (DKI),** German Copper Institute. Copper-Nickel Alloys: Properties, Processing, Applications. *Copper Development Association Inc.* [Online] https://www.copper.org/applications/marine/cuni/properties/DKI_booklet.html.
- 107. Grolms, Martin.** A new copper-titanium alloy enables 3D printing. *Advanced Science News.* [Online] 2020. <https://www.advancedsciencenews.com/a-new-copper-titanium-alloy-enables-3d-printing/>.
- 108. C. Yao, J. Lu, T. J. Webster.** *Titanium and cobalt–chromium alloys for hips and knees.* s.l. : Biomaterials for Artificial Organs, 2011.
- 109. Langley Alloys.** The role of copper in improving corrosion resistance of stainless steels. *Langley Alloys.* [Online] April 2020. <https://www.langleyalloys.com/en/copper-improving-corrosion-resistance-stainless-steels/>.
- 110. Tata Steel 2021.** *Copper-plated steel.* Tata Steel Europe. [Online] 2021. <https://www.tatasteeleurope.com/ts/engineering/products/electro-plated/copper-plated-steel#:~:text=These%20high%2Dperformance%20products%20are,of%20components%20in%20demanding%20shapes..>

- 111. Shuji Matsusaka, Motohiro Urakawa, Hiroaki Masuda.** *Micro-feeding of fine powders using a capillary tube with ultrasonic vibration.* 4, s.l. : Advanced Powder Technology, 1995, Vol. 6. 0921-8831.
- 112. Xiaochun Li, Hongseok Choi, Yong Yang.** *Micro rapid prototyping system for micro components.* s.l. : Thin Solid Films , 2002.
- 113. Evans Julian RG, Yang Shoufeng.** *Solid Freeforming and Combinatorial Research.* 1, s.l. : Tsinghua Science & Technology, 2009, Vol. 14. 1007-0214.
- 114. Subhankar Roy, Jagadish.** *Design of a circular hollow ultrasonic horn for USM using finite element analysis.* s.l. : The International Journal of Advanced Manufacturing Technology, 2017, Vol. 93. 00170-016-8985-6.
- 115. Zvei.** *Ultrasonics, Power. Sonotrode design and manufacturing instructions,* handbook. www.powerUltrasonics.com. [Online] 1999.
<https://www.powerultrasonics.com/content/sonotrode-design-and-manufacturing-instructions-zvei-handbook>.
- 116. Kumar Parshad, Komal G. Dave, Samir B. Shah.** *Design and analysis of sonotrode for ultrasonic consolidation.* 5, s.l. : Journal of Emerging Technologies and Innovative Research, 2018, Vol. 5.
- 117. Fisher Scientific.** *Stainless Steel powder, -325 mesh, Type 316-L, Thermo Scientific Chemicals.* [Online] Fisher Scientific. <https://www.fishersci.co.uk/shop/products/stainless-steel-powder-325-mesh-type-316-l-3/11359259>.
- 118. M. Averyanova, Ph. Bertrand, B. Verquin.** *Studying the influence of initial powder characteristics on the properties of final parts manufactured by the selective laser melting.* 4, s.l. : Virtual and Physical Prototyping, 2011, Vol. 6.
- 119. Freshie Wind Store.** *100W 220V Ultrasonic Cleaner Power Driver Board 40KHz Transducer High Performance Efficiency Ultrasound Cleaning Circuit Board.* [Online] <https://www.aliexpress.com/i/4001069187500.html#nav-specification>.
- 120. Yong Yang, Xiaochun Li.** *Experimental and analytical study of ultrasonic micro powder feeding.* 1, s.l. : Journal of Physics D: Applied Physics, 2003, Vol. 36. S0022-3727.
- 121. S. Yang, J.R.G. Evans.** *Metering and dispensing of powder; the quest for new solid freeforming techniques.* 1, s.l. : Powder Technology , 2007), Vol. 178.
- 122. Xuesong Lu, Shoufeng Yang, Julian R.G. Evans.** *Microfeeding with different ultrasonic nozzle designs.* 1, s.l. : Ultrasonics, 2009, Vol. 49.
- 123. Shenzhen Derui Ultrasonic.** *High quality digital ultrasonic generator 600W-3000W LED window show for ultrasonic cleaner 40Khz transducers driver.* [Online] <http://www.derui-ultrasonic.com/plus/list.php?tid=7>.
- 124. Intertronics.** *Benchtop Dispensing Robots. Intertronics.* [Online] <https://www.intertronics.co.uk/product-category/robotics/benchtop-robots/>.

125. **Norrscope Ltd.** *Carbolite STF 15/180 Tube Furnace*. Norrscope. [Online] Norrscope Ltd, 2024. <https://norrscope.com/product/carbolite-stf-15-180-tube-furnace/>.
126. **Buehler Ltd.** *Simplimet® 4000 compression mounting press*. Buehler Ltd. [Online] <https://www.buehler.com/products/mounting/compression-mounting/simplimet-4000-compression-mounting-press/>.
127. **Buehler Ltd.** *Automet® 250 grinder-polisher*. [Online] Buehler Ltd. <https://www.buehler.com/products/grinding-and-polishing/grinder-polishers/automet-250-grinder-polisher-membrane/>.
128. **Nikon Instruments Inc.** *ECLIPSE LV150NA and LV150N*. [Online] Nikon Industrial Microscopy. <https://industry.nikon.com/en-gb/products/industrial-microscopy/industrial-microscopes/upright-eclipse-lv150na-lv150n/>.
129. **MA, Zavala Arredondo.** *Diode area melting use of high-power diode lasers in Additive manufacturing of metallic components*. s.l. : University of Sheffield, 2017.
130. **Laboratorio de Microscopías Avanzadas.** *SEM-Inspect. Laboratorio de Microscopías Avanzadas*. [Online] <https://lma.unizar.es/en/sem-inspect/>.
131. **Rowlands, William.** *Additive manufacturing of advanced ceramics for demanding applications*. s.l. : Loughborough University, 2019.
132. **European Committee for Standardization.** *Metallic materials - Tensile testing - Part 1: Method of test at room temperature (ISO 6892-1:2016)*. s.l. : European Committee for Standardization, 2016.
133. **Saeed Maghsoodloo, Guttekin Ozdemir, Victoria Jordan, Chen-Hsiu Huang.** *Strengths and limitations of taguchi's contributions to quality, manufacturing, and process engineering*. 2, s.l. : Journal of Manufacturing Systems, 2004, Vol. 23.
134. **Negrete, Carmita Camposeco.** *Optimization of FDM parameters for improving part quality, productivity and sustainability of the process using Taguchi methodology and desirability approach*. s.l. : Progress in Additive Manufacturing, 2020, Vol. 5.
135. **Vishal Wankhede, Darshit Jagetiya, Akshata Joshi, Rakesh Chaudhari.** *Experimental investigation of FDM process parameters using Taguchi analysis*. 3, s.l. : Materials Today: Proceedings, 2020, Vol. 27.
136. **Zicheng Zhu, Shan Lou, Candice Majewski.** *Characterisation and correlation of areal surface texture with processing parameters and porosity of High Speed Sintered parts*. 1, s.l. : Additive Manufacturing, 2020, Vol. 36. 101402.
137. **Glen, Stephanie.** *Regression Equation: What it is and How to use it. Statistics How To*. [Online] <https://www.statisticshowto.com/probability-and-statistics/statistics-definitions/what-is-a-regression-equation/>.
138. **M. Denesuk, G.L. Smith, B.J.J. Zelinski, N.J. Kreidl, D.R. Uhlmann.** *Capillary Penetration of Liquid Droplets into Porous Materials*. 1, s.l. : Journal of Colloid and Interface Science, 1992, Vol. 158.

- 139. Markicevic, B., D'Onofrio, T. G. and Navaz, H. K.** *On spread extent of sessile droplet into porous medium: Numerical solution and comparisons with experiments.* 1, s.l. : Physics of Fluids, 2010, Vol. 22.
- 140. R. M. do Nascimento, A. E. Martinelli, A. J. A. Buschinelli.** *Review Article: Recent advances in metal-ceramic brazing.* s.l. : Cerâmica , 2003, Vol. 49.
- 141. Perkin Elmer.** *A Beginners Guide Thermogravimetric Analysis (TGA).* Perkin Elmer. [Online] 2010. https://resources.perkinelmer.com/lab-solutions/resources/docs/faq_beginners-guide-to-thermogravimetric-analysis_009380c_01.pdf.
- 142. Line Vikingsson, Alvaro Vinals-Guitart, Alfonso Valera-Martínez, Jaime Riera, Ana Vidaurre, Gloria Gallego Ferrer, Jose Luis Gómez Ribelles.** *Local deformation in a hydrogel induced by an external magnetic field.* 1, s.l. : Journal of Materials Science volume, 2016, Vol. 51.
- 143. Iulia Salaoru, Zuoxin Zhou, Peter Morris, Gregory J. Gibbons.** *Inkjet printing of polyvinyl alcohol multilayers for additive manufacturing applications.* s.l. : The Journal of Applied Polymer Science, 2016.
- 144. Mahmuda Akter Monne, Chandan Kumar Howlader, Bhagyashree Mishra, Maggie Yihong Chen.** *Synthesis of Printable Polyvinyl Alcohol for Aerosol Jet and Inkjet Printing Technology.* s.l. : Micromachines, 2021, Vol. 12.
- 145. A. Bhattacharya, P. Ray.** *Studies on surface tension of poly(vinyl alcohol): Effect of concentration, temperature, and addition of chaotropic agents.* s.l. : Journal of Applied Polymer Science, 2003, Vol. 93.
- 146. Waqas Muhammad, Rasim Batmaz a, Arunkumar Natarajan, Etienne Martin.** *Effect of binder jetting microstructure variability on low cycle fatigue behavior of 316L .* s.l. : Materials Science & Engineering A , 2022.
- 147. Hadi Miyanaji, Shanshan Zhang, Li Yang.** *A new physics-based model for equilibrium saturation determination in binder jetting additive manufacturing process.* 11, s.l. : International Journal of Machine Tools and Manufacture, 2018, Vol. 1.
- 148. Sanjay Shrestha, Guha Manogharan.** *Optimization of Binder Jetting Using Taguchi Method.* 3, s.l. : The Minerals, Metals & Materials Society, 2017, Vol. 69.
- 149. Ashwath Yegyan Kumar, JueWang, Yun Bai, Scott T. Huxtable, Christopher B. Williams.** *Impacts of process-induced porosity on material properties of copper made by binder jetting additive manufacturing.* 1, s.l. : Materials and Design, 2019, Vol. 182.
- 150. M. Qian, G.B. Schaffer. [book auth.] Zhigang Zak Fang.** *Sintering of aluminium and its alloys. Sintering of Advanced Materials.* s.l. : Elsevier Science, 2010.
- 151. O'Neill, Benedict.** *Guide to post-processing for 3D printed parts.* aniwaa. [Online] 9 2021. <https://www.aniwaa.com/buyers-guide/post-processing/post-processing-3d-printing/>.
- 152. Heide, Luca Van der.** *Guide to Post-processing for Metal AM.* Aniwaa. [Online] 10 2022. <https://www.aniwaa.com/guide/post-processing/guide-post-processing-metal-am/>.

- 153. Luis A. Chavez, Paulina Ibañez, Bethany Wilburn, David Alexander IV, Calvin Stewart, Ryan Wicker, Yirong Lin.** *The Influence of Printing Parameters, Post-Processing, and Testing Conditions on the Properties of Binder Jetting Additive Manufactured Functional Ceramics*. 1, s.l. : Ceramics , 2020, Vol. 3.
- 154. Yujia Wang, Yaoyao Fiona Zhao.** *Investigation of Sintering Shrinkage in Binder Jetting Additive Manufacturing Process*. s.l. : 45th SME North American Manufacturing Research Conference, 2017.
- 155. Truong Do, Tyler J. Bauder, Tyler J. Bauder, Kristian Rego, Junghoon Yeom, Patrick Kwon.** *Additively manufactured full-density stainless steel 316L with binder jet printing*. s.l. : The International Manufacturing Science and Engineering Conference, 2018. MSEC2018-6681, V001T01A017.
- 156. T.-Y. Chan, M.-S. Chuang, S.-T. Lin.** *Injection moulding of oxide reduced copper powders*. 2, s.l. : Powder Metallurg, 2005, Vol. 48.
- 157. Yun Bai, Christopher B. Williams.** *An exploration of binder jetting of copper*. 2, s.l. : Rapid Prototyping Journal, 2015, Vol. 21.
- 158. Meeder, Matthew Paul.** *Modeling the Thermal and Electrical Properties of Different Density Sintered Binder Jetted Copper for Verification and Revision of The Wiedemann-Franz Law*. s.l. : Virginia Polytechnic Institute and State University, 2016.
- 159. Ashwath Kumar, Yun Bai, Anders Eklund, Christopher B. Williams.** *Effects of Hot Isostatic Pressing on Copper Parts Fabricated via Binder Jetting*. s.l. : 45th SME North American Manufacturing Research Conference, NAMRC 45, LA, USA, 2017.
- 160. Ashwath Yegyan Kumar, Yun Bai, Anders Eklund, Christopher B. Williams.** *The effects of Hot Isostatic Pressing on parts fabricated by binder jetting additive manufacturing*. 1, s.l. : Additive Manufacturing, 2018, Vol. 24.
- 161. Takuji Ishikawa, Thanh-Nghi Dang, Eric Lauga.** *Instability of an active fluid jet*. s.l. : Fluid Dynamics , 2022.
- 162. Thermtest Instruments.** *Top 10 Thermally Conductive Materials*. Thermtest Instruments. [Online] <https://thermtest.com/thermal-resources/top-10-resources/top-10-thermally-conductive-materials>.
- 163. Geise, Sarah.** *Know the differences between 304 stainless steel vs 316*. Kloeckner Metals. [Online] 9 2021. [https://www.kloecknermetals.com/blog/304-stainless-steel-vs-316/#:~:text=304%20vs%20316%20Stainless%20Steel%3A%20Heat%20Resistance&text=The%20melting%20range%20of%20304,%20C%20B%20C%20\(1697%E2%84%A8\)9..](https://www.kloecknermetals.com/blog/304-stainless-steel-vs-316/#:~:text=304%20vs%20316%20Stainless%20Steel%3A%20Heat%20Resistance&text=The%20melting%20range%20of%20304,%20C%20B%20C%20(1697%E2%84%A8)9..)
- 164. Hui Ren, Guisheng Zou, Qiang Jia, Zhongyang Deng, Chengjie Du, Wengan Wang, Lei Liu.** *Thermal stress reduction strategy for high-temperature power electronics with Ag sintering*. s.l. : Microelectronics Reliability, 2021, Vol. 127.
- 165. Solomon Bello, Puzhen Gao, Samuel Abiodun Olatubosun, Yuqi Lin, John Njoroge.** *Experimental study of heat distribution in a Non-uniform heat source of a natural circulation loop*. s.l. : Annals of Nuclear Energy, 2022, Vol. 172.

166. **Munitz, Abraham.** *Metastable liquid phase separation in tungsten inert gas and electron beam copper/stainless-steel welds.* 11, s.l. : Journal of Materials Science, 1995, Vol. 30.
167. **Yu Pan, He Li, Yongsheng Liu, Yansong Liu, Kehui Hu, Ning Wang, Zhigang Lu, Jingjing Liang and Sujun He.** *Effect of Holding Time During Sintering on Microstructure and Properties of 3D Printed Alumina Ceramics.* 54, s.l. : Frontiers in Materials, 2020, Vol. 7.
168. **Ataman Kimya.** *Colloidal silica.* [Online]
<https://atamankimya.com/sayfalaralfabe.asp?LanguageID=2&cid=3&id=2868&id2=5547#:~:text=Colloidal%20silica%20consists%20of%20dense,ordered%20on%20a%20molecular%20level.>
169. **Masteel UK Ltd.** *Type 316L Stainless Steel.* Masteel. [Online] <https://masteel.co.uk/type-316l-stainless-steel/>.
170. **Saereh Mirzababaei, Brian K. Paul, Somayeh Pasebani.** *Microstructure-property relationship in binder jet produced and vacuum sintered 316 L.* Additive Manufacturing, 2022, Vol. 53.
171. **B Verlee, T Dormal, J Lecomte-Beckers.** *Density and porosity control of sintered 316L stainless steel parts produced by additive manufacturing.* 4, s.l. : Powder Metallurgy, 2012, Vol. 55.
172. **Nora Lecis, Marco Mariani, Ruben Beltrami, Lorena Emanuelli, Riccardo Casati, Maurizio Vedani, Alberto Molinari.** *Effects of process parameters, debinding and sintering on the microstructure of 316L stainless steel produced by binder jetting,.* s.l. : Materials Science and Engineering: A, 2021, Vol. 828.
173. **Punit Kumar, R. Jayaraj, J. Suryawanshi, U.R. Satwik, J. McKinnell, U. Ramamurty.** *Fatigue strength of additively manufactured 316L austenitic stainless steel.* Acta Materialia, Vol199.
174. **Anqi Liang, Sandeep Sahu, Xiao Zhao, Tomas Polcar, Andrew R. Hamilton.** *Interfacial characteristics of austenitic 316 L and martensitic 15–5PH stainless steels joined by laser powder bed fusion.* Materials Characterization, 2023, Vol. 198.
175. **Francisco Briones, Vanessa Seriacopi, Carola Martí'nez, Jose Luis Valin, Dany Centeno, Izabel Fernanda Machado.** *The effects of pressure and pressure routes on the microstructural evolution and mechanical properties of sintered copper via SPS.*s.l. : Journal of Materials Research and Technology, 2023, Vol. 25.
176. **N. Kurgan, R. Varol.** *Mechanical properties of P/M 316L stainless steel materials.* s.l. : Powder Technology, 2010, Vol. 201.
177. **A. Molinari, J.Kazior, F. Marchetti, R. Canteri, I. Cristofolini, and A. Tiziani.** *Sintering mechanisms of boron alloyed AISI 316l Stainless Steel.* 2, s.l. : Powder Metallurgy, 1994, Vol. 37.
178. **Tae Shik Yoon, You Hwan LEE, Sang Ho AHN, Jung Hwan LEE, Chong Soo LEE.** *Effects of Sintering Conditions on the Mechanical Properties of Metal Injection Molded 316L Stainless Steel.* 1, s.l. : ISIJ International, 2003, Vol. 43.
179. **V. E. Beal, P. Erasenthiran, N. Hopkinson, P. Dickens, C. H. Ahrens.** *The effect of scanning strategy on laser fusion of functionally graded H13/Cu materials.* 2006, Int J Adv Manuf Technol, Vol. 30, pp. 844–852.

- 180. Chivel, Yuri.** *New Approach to Multi-material Processing in Selective Laser Melting.* 2016, Physics Procedia, Vol. 83, pp. 891-898.
- 181. INTERTRONICS.** *Volumetric Dispensing System for 310ml Cartridges and Silicones.* [Online] 2020. [Cited: Sep 17, 2020.] <https://www.intertronics.co.uk/product/volumetric-dispensing-system-310ml-cartridges-silicones/>.
- 182. SUTRISNO, Bernard Noventio.** *Design of Ultrasonic Powder Deposition Device for 316L Stainless Steel Powders with Discrete Element Method Study Analysis.* Sheffield : The University of Sheffield, 2020.
- 183. Katayama, S.** *Laser welding of aluminium alloys and dissimilar metals.*s.l. : Welding international, 2004.
- 184. M. Mouiya, A. Bouazizi, A. Abourriche, Y. El Khessaimi, A. Benhammou, Y. El hafiane, Y. Taha, M. Oumam, Y. Abouliatim, A. Smith, H. Hannache.** *Effect of sintering temperature on the microstructure and mechanical behavior of porous ceramics made from clay and banana peel powder.* s.l. : Results in Materials, 2019, Vol. 4.
- 185. Aalco Metals Ltd.** *Copper and Copper Alloys, CW004A Sheet, Plate and Bar.* Wednesbury : Aalco Metals Ltd, 2019.
- 186. Jessirie Dilag, Tiffany Chen, Sheng Li, Stuart A. Bateman.** *Design and direct additive manufacturing of three-dimensional surface micro-structures using material jetting technologies.* s.l. : Additive Manufacturing, 2019, Vol. 27.

Chapter 11. Appendices

11.1 Building platform bed drawings

As part of designing the building platform, design drawings must be submitted to the mechanical engineering workshop. The drawings of the manufactured part by the workshop are shown in the following.

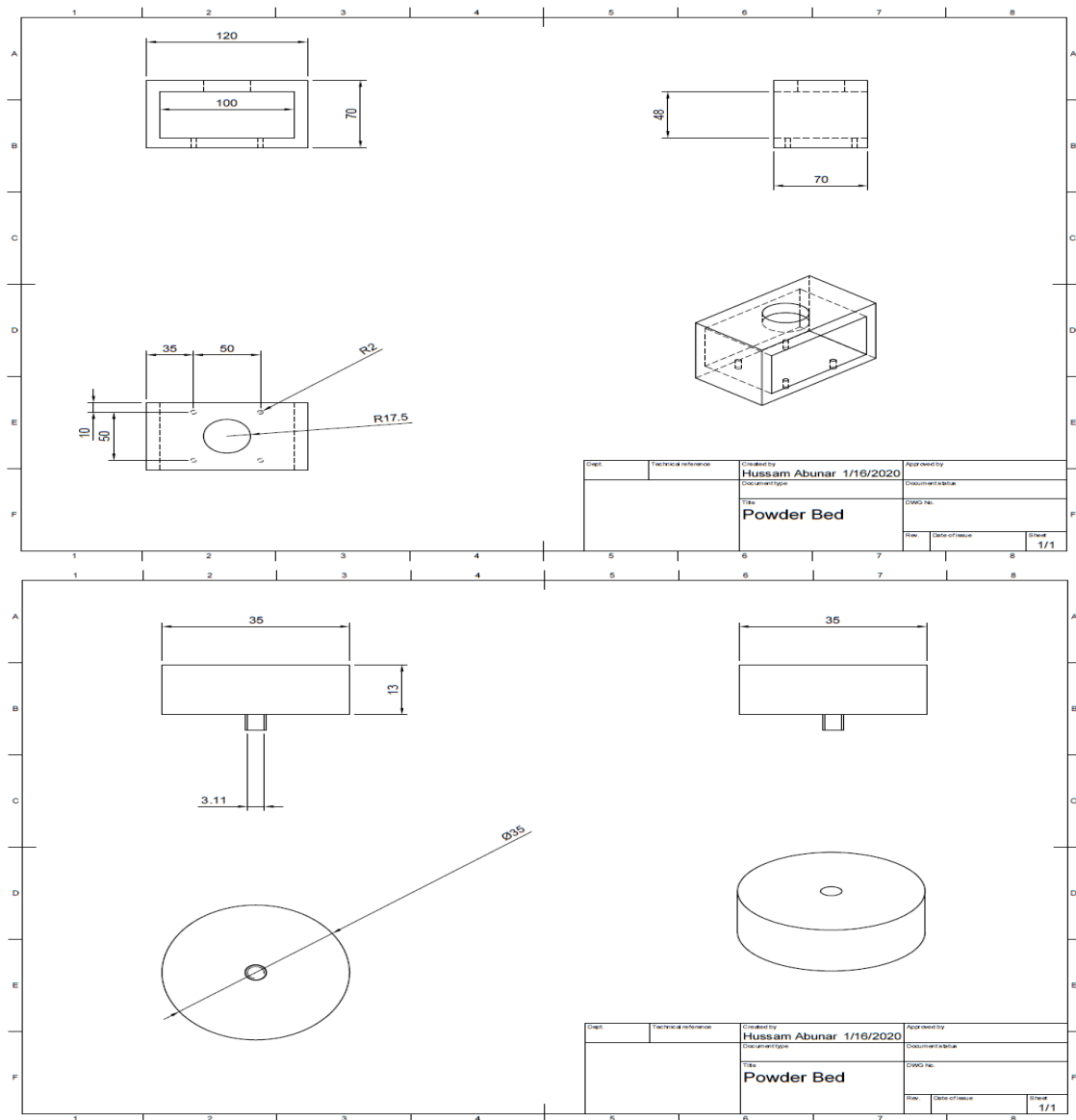


Figure 11.1: The design drawings of the manual powder bed used as a powder bed in some 3D printing buildings.

11.2 Sonotrode calculations

Variable	Equation	Value
Sonotrode Material		Aluminium 6061-T6
Sonotrode Shape		Stepped
Operating frequency (F)		40 kHz
Sound velocity (C _L)		6300 m/s
Wavelength (λ)	$\frac{CL}{F} = \frac{6,300,000}{40,000}$	157.5 mm
Calculated Sonotrode Total Length (L)	$\frac{\lambda}{2} = \frac{157.5}{2}$	78.75 mm
Amplification ratio	$(\frac{D1}{D2})^2 = (\frac{45}{39})^2$	1.4
Wavenumber (K _u)	$\frac{2 \pi}{\lambda}$	0.04
Length of the upper diameter (L ₁)	$\frac{1.5}{Ku} = \frac{1.5}{0.04}$	38.75 mm
Length of the lower diameter (L ₂)	$\frac{1.6}{Ku} = \frac{1.6}{0.04}$	40 mm

Table 11.1: A thorough and in-depth exploration of design calculations of the sonotrode's manufacturing, which offers an extensive repository of detailed information and specifications.

Technical drawing of a Sonotrode 1, showing front, top, and isometric views with dimensions and annotations.

Front View (Top): Shows a cylindrical body with a total height of 39. The top flange has a diameter of 45. A central hole is labeled "Hole d = 10". The top surface features a conical structure with a 65° angle and a 34.8 diameter. The top flange has a 2.6 thickness. The central hole is labeled "Hole d = 10". The top surface is labeled "Tapping M6X1".

Top View (Bottom): Shows a circular cross-section with a diameter of 45. A central hole is labeled "Hole d = 10". The top surface is labeled "Tapping M6X1".

Isometric View (Right): Shows the 3D structure of the Sonotrode 1. The total height is 39. The top flange has a diameter of 45. The central hole is labeled "Hole d = 10". The top surface features a conical structure with a 65° angle and a 34.8 diameter. The top flange has a 2.6 thickness. The central hole is labeled "Hole d = 10". The top surface is labeled "Tapping M6X1".

Dimensions and Annotations:

- 39: Total height of the device.
- 45: Diameter of the top flange.
- 34.8: Diameter of the conical structure.
- 2.6: Thickness of the top flange.
- 65°: Angle of the conical structure.
- Hole d = 10: Diameter of the central hole.
- Tapping M6X1: Thread specification for the top flange.
- M10X1: Thread specification for the central hole.
- R2, R3: Fillet radii.
- 18: Distance from the top flange to the bottom of the central hole.
- 76: Total length of the device.
- 45: Diameter of the central hole.
- 60: Distance from the bottom of the central hole to the bottom of the device.

Table:

Doc. No.	Technical reference	Created by	Approved by
		HUSSAM ABUNAR 04/01/2021	
		Document type	Document status
		Title	Doc. No.
		Sonotrode 1	
		Rev.	Date of issue
		1/1	

237

11.4 Round wiper drawings

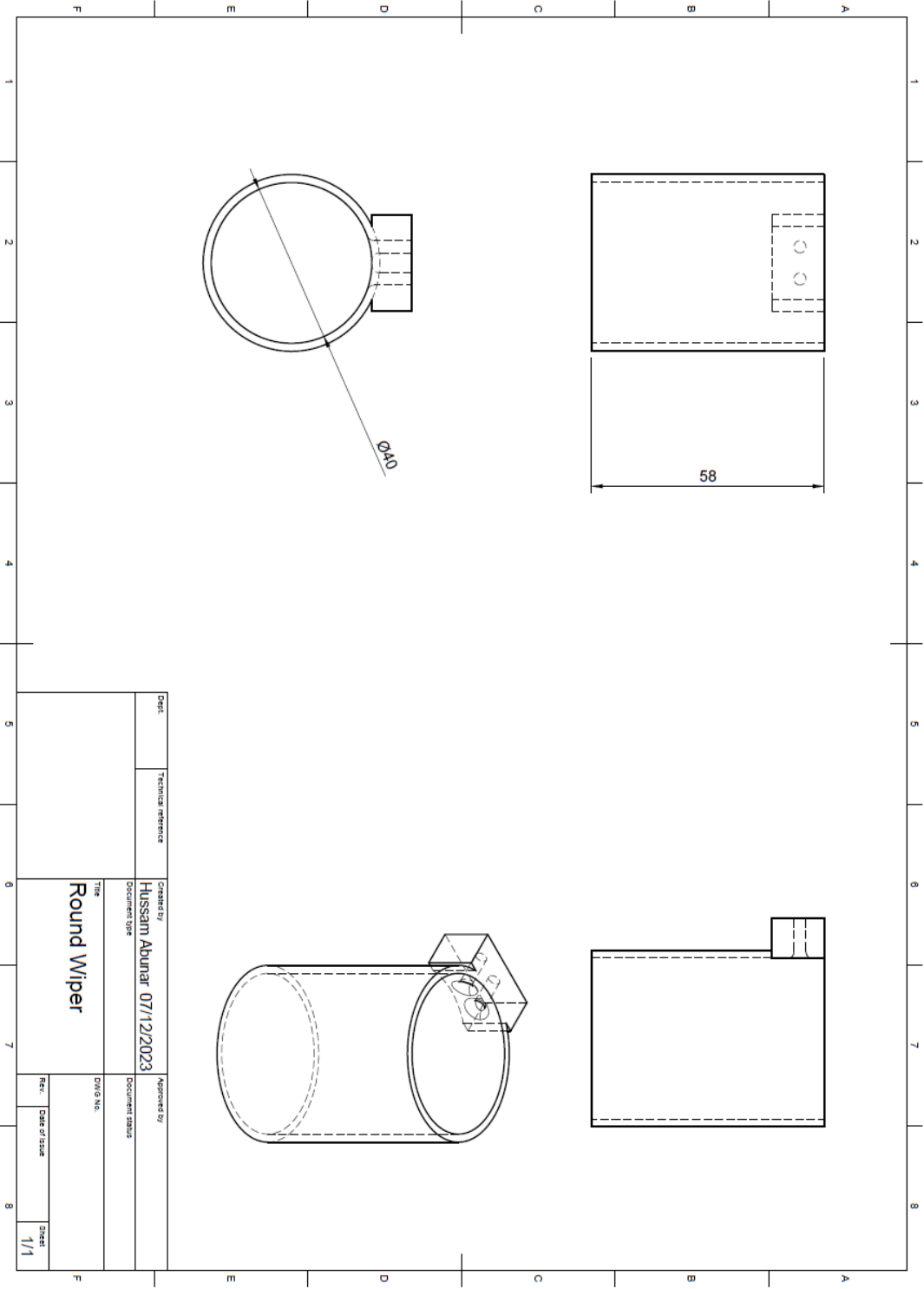


Figure 11.3: The design drawings of the sonotrode used in the multi-material powder deposition system.

11.5 Calculations of the speed rate associated with each parameter set for the regression validations.

Based on the regression analysis conducted for the deposited powder width in the experimental trials, the following multiple linear regression equation was derived:

$$\text{Heap Width} = 0.983 + 4.144 \text{ Nozzle Diameter (mm)} - 0.01669 \text{ Speed Rate (mm/s)} - 0.0004 \text{ Power Level (W)}$$

Manipulating the structure of the regression equation to isolate the speed rate variable involves a strategic rearrangement process.

$$\text{Speed Rate} = \frac{0.983 + 4.144 \text{ Nozzle Diameter} - \text{Heap Width} - 0.0004 \text{ Power Level}}{0.01669}$$

The calculations of the speed rate associated with the four-parameter sets are as follows. The first set comprised a nozzle diameter of 0.8 mm, a power level of 1200, and a heap width of 2 mm:

$$\begin{aligned} \text{Speed Rate} &= \frac{0.983 + 4.144 (0.8) - (2) - 0.0004 (1200)}{0.01669} \\ &= 109 \text{ mm/s} \end{aligned}$$

The second set featured a nozzle diameter of 0.8 mm, a power level of 1800, and a heap width of 2 mm:

$$\begin{aligned} \text{Speed rate} &= \frac{0.983 + 4.144 (0.8) - (2) - 0.0004 (1800)}{0.01669} \\ &= 94.5 \text{ mm/s} \end{aligned}$$

The third set involved a nozzle diameter of 1 mm, a power level of 1200, and a heap width of 2 mm:

$$\begin{aligned}\text{Speed rate} &= \frac{0.983 + 4.144 (1) - (2) - 0.0004 (1200)}{0.01669} \\ &= 158.5 \text{ mm/s}\end{aligned}$$

The fourth set incorporated a nozzle diameter of 1 mm, a power level of 1800, and a heap width of 2 mm:

$$\begin{aligned}\text{Speed rate} &= \frac{0.983 + 4.144 (1) - (2) - 0.0004 (1800)}{0.01669} \\ &= 144 \text{ mm/s}\end{aligned}$$

11.6 Ohnesorge number calculations for 0.1- and 0.6-mm nozzle diameters

Temperature (°C)	μ (Pa.s)	σ (N/m)	ρ (Kg/m ³)	L (m)	Oh
25	0.00352	0.0445	1190	0.0006	0.0197
30	0.00307	0.044	1190	0.0006	0.0173
35	0.00269	0.0432	1190	0.0006	0.0153
40	0.00219	0.0428	1190	0.0006	0.0125
45	0.00194	0.0422	1190	0.0006	0.0112

Table 11.2: Ohnesorge number of the prepared binders comprised of 5% molecular weights of PVA dissolved in deionized water for the binder deposition nozzle of 0.6 mm.

Temperature (°C)	μ (Pa.s)	σ (N/m)	ρ (Kg/m ³)	L (m)	Oh
25	0.00352	0.0445	1190	0.0001	0.0483
30	0.00307	0.044	1190	0.0001	0.0424
35	0.00269	0.0432	1190	0.0001	0.0375
40	0.00219	0.0428	1190	0.0001	0.0307
45	0.00194	0.0422	1190	0.0001	0.0274

Table 11.3: Ohnesorge number of the prepared binders comprised of 5% molecular weights of PVA dissolved in deionized water for the binder deposition nozzle of 0.1 mm.